Phase and Size Selective Crystal Growth of Nanoparticles under Supercritical Water

Tomoki Fujita

February 2022

Phase and Size Selective Crystal Growth of Nanoparticles under Supercritical Water

Tomoki Fujita

Doctoral Program in Physics

Submitted to the Graduate School of
Pure and Applied Sciences
in Partial Fulfillment of the Requirements
for the Degree of Doctor of Philosophy in
Science

at the
University of Tsukuba

Table of contents

1. Introduction

Physical properties of materials have a close relation with their atomic arrangement. Size, surface, interface and lattice defects of materials are relating to properties of materials such as electric and/or thermal conductivity. Fine nanoparticles below 10 nm size show interesting physical properties such as a narrower band gap or a lower melting point than bulk materials.

Supercritical hydrothermal synthesis has attracted a lot of attention as a method to synthesize fine metal oxide nanoparticles with uniform size and shape [1]. Nanoparticles are prepared in the water above its critical temperature and pressure of 673 K and 22.1 MPa. Supercritical water is placed between a liquid phase and a gas phase on the phase diagram. Density and dielectric constant of supercritical water are continuously varied with temperature and pressure. Highly functional nanoparticles with large specific surface area can be synthesized in supercritical water [2]. Complex nanoparticles can be synthesized at lower temperature than a conventional method [3]. Mass production of nanoparticles is possible due to its short reaction time. It typically takes a few seconds to one hour.

Supercritical water has superior properties as a reaction field for preparing fine nanoparticles with controllable functionality [4]. Lower solubility can suppress crystal growth through Ostwald ripening in conventional hydrothermal synthesis in a liquid phase. A higher density than that of a gas phase can prevent the collision and aggregation between nucleuses of nanoparticles which are frequently observed in gas phase reaction like a chemical vapor decomposition (CVD) method. Organic solvent can be dispersed in supercritical water due to its low dielectric constants. This makes it possible to synthesize nanoparticles with a highly reactive surface modified by organic molecules. Controlling structure of fine functional nanoparticles is possible by changing properties of a reaction field continuously.

Control of crystalline phase is one of the most important topics of supercritical hydrothermal synthesis of nanoparticle. Functional metal oxide nanoparticles have several crystalline phases. It strongly affects their physical or chemical properties [5], [6]. Phase stability depends on the size of nanoparticles and/or a precursor used in the synthesis [7], [8]. Various crystalline phases were observed for nanoparticles synthesized in supercritical water [3], [9]–[11]. Controllable parameters of synthesis are temperature, pressure, pH of solution, type of solute molecule, ionic composition of solution, and reaction time. It is difficult to carry out complete investigation for all combinations of controllable parameters.

Physical properties of nanoparticles can be changed by local defects in atomic arrangement. Disorder at interface of core-shell structure of nanoparticles attracts attention in terms of controlling optical resonance of quantum dots [12]. Strain induced at interface by lattice mismatch causes upper offset of valence band and red shift of photoluminescence spectra. The improvement of thermoelectric performance was reported for composite nanoparticles [13]. The high density of twin faulting led to higher phonon scattering and lower thermal conductivity. A figure of merit was higher by 50 % than bulk material.

Methods of structure determination in atomic-to-nanoscale are powerful tools, which can help with the development of a new area of materials science which focuses on local structure of nanoparticles. Simultaneous determination of size, shape and local defect of nanoparticles provides important clues to identify structural parameters relating to important properties of nanoparticles. Elucidating local structure in fine nanoparticles enables us to create a guideline for an improvement of nanomaterials properties which depends on local lattice defects.

Monitoring of nanoparticles structure during synthesis can provide clues to phase stability, mechanism of growth or correlation between structure of nanoparticles and physical properties of supercritical water. The critical size between polymorphs of nanoparticles is reported from observation of size and crystalline phase of nanoparticles [8]. Surface stress of nanoparticles was investigated from anomalous lattice expansion or contraction of nanoparticles [14]. The measurement at multi-temperature and pressure conditions can provide an evidence of correlation between microscopic structure and macroscopic properties of a reaction field.

This "*in-situ*" measurement of nanostructure during synthesis requires intense beam with an angstrom wavelength. An X-ray, a neutron and an electron beam are commonly used for evaluating structure of materials in atomic and nanometer scale [15]. Both X-ray and neutron beams can penetrate the reaction vessel, while electron beam is scattered by electrons on the wall of vessel. A neutron beam is a tool for evaluation of structure of materials composed with light atoms like lithium and oxygen [16]. A neutron experiment requires a sample size of the order of centimeter due to its low intensity per area. Electron diffraction and microscopy can be carried out in milliseconds due to strong interaction between electrons [17]. High vacuum should be kept around samples for preventing the electron from being scattered by air.

Synchrotron radiation (SR) is an intense X-ray source. A highly intense and parallelized X-ray are emitted by accelerated relativistic electrons in a magnetic field with GeV order energy. The brilliance at the third generation SR facility is more than 10^{10} times higher than that of an X-ray tube. The high brilliance decreases the time for collecting powder X-ray diffraction (PXRD) data which can be used for structure analysis. A large space can be assured around samples in the setup of SR-PXRD measurement, since a highly parallelized X-ray does not require optics elements such as soller slit. The various measurement systems can be installed for conducting measurement at the high temperature, the high pressure or the vacuum conditions.

SR is a powerful tool for evaluation of structure of nanoparticles. Diffraction data can be collected from samples with weight of microgram. It is possible to observe the weak scattering from nanoparticles, discriminating it with scattering from a pressure vessel. The composition of crystalline phase of nanoparticles can be identified from a set of positions of diffraction lines. The average diameter of nanoparticles can be estimated from width of diffraction profiles.

In-situ SR-PXRD measurement has been carried out for observation of nucleation and crystal growth of nanoparticles during synthesis [18], [19]. A reaction vessel or equipment for synthesis was installed at a sample position. PXRD data were collected from nanoparticles during synthesis with a second time scale. Reaction processes of various synthesis were investigated. An anatase phase of TiO_2 nanoparticle was monitored in reaction of a sol-gel method [20]. The formation of Ru nanoparticle with fcc and hcp structure was observed in solvothermal reaction with supercritical ethanol [21]. Phase transition during the mechanochemical reaction was reported for ball-milling process [22].

High quality PXRD data are required for determination of structure of nanoparticles from *in-situ* experiment. Diffraction data should be collected simultaneously from a wide range of diffraction angles. In the case of 10 nm ZrO_2, data with resolution $d > 0.6$ Å were required for determining lattice constants with 0.001 Å accuracy. The broadening of diffraction profiles due to energy dispersion should be minimized for estimating a size of nanoparticles. Crystal growth was investigated at the beamline with the 10^{-4} scale of the energy dispersion [23].

Evaluation of size and lattice constants can be complicated due to local lattice defects. For example, a shift and broadening of diffraction lines can be caused by planar defects such as twin and deformation faulting in the stacking structure [24]. Lattice defects of nanoparticles cause a greater change to PXRD data than those of bulk material, since larger fraction of atoms is related to defect structures. We found the height of 200 reflection of Ag nanosphere was almost half of the calculated data of Rietveld refinement. Several reflections of ZrO_2 nanoparticle prepared by supercritical hydrothermal synthesis were not fitted by Rietveld refinement.

Issues about reproducibility of parameters obtained from analysis of diffraction data of *in-situ* SR-PXRD experiment were reported by Iversen *et al*. [25]. In work presented by this group, diffraction data were collected 10 times for *in-situ* experiments of hydrothermal synthesis in identical conditions. In Rietveld refinement, the absolute value of an intensity scaling factor of diffraction data were not reproduced. It was partly due to occasional movement of nanoparticles in initial heating process, since it made difficult to control amount of samples exposed by an X-ray. The diameter of nanoparticles estimated from diffraction line width showed uncertainty of about 3 nm. Iversen *et al.* found that diffraction lines with relatively narrow width corresponding to 15 nm diameter required a careful treatment than those corresponding to the diameter of less than 10 nm. The time dependence of an intensity scaling factor and that of the diameter were qualitatively reproduced for 10 times of experiments.

The methods have been developed for analyzing powder diffraction data of nanoparticles. Leonardi *et al.* reported effect of dislocation to PXRD data for the rod-shaped nanoparticle of iridium and palladium [26]. Bertolotti et al. investigated atomic arrangement of colloidal nanoplatelet [27]. Parakh *et al.* reported high pressure study about gold nanoparticles structure [28]. Atomic arrangements were modeled by using a combination of diffraction data calculation and a molecular dynamics simulation. Some of these studies were performed on the large-scale parallel computing platform.

In the present study, we carried out *in-situ* SR-PXRD experiment to investigate the crystal growth of nanoparticles in supercritical water. The measurement system was developed for *in-situ* SR-PXRD experiment at the beamline BL02B2 of the third generation SR facility SPring-8. Powder diffraction data were collected at thirteen combinations from the synthesis of ZrO_2 nanoparticles. The analysis method was developed for analyzing powder diffraction data of nanoparticles in the reaction vessel. Debye Scattering Equation (DSE) was used for the calculation of powder profiles of nanoparticles. DSE was used for the analysis of a series of the powder diffraction data of nanoparticles by Ozawa [29]. The calculation was performed on the large-scale parallel computing platform with GPU.

The crystal growth of ZrO_2 nanoparticles in supercritical water was investigated by *in-situ* SR-PXRD experiment. The crystalline phases and the size of nanoparticles were determined from the analysis of the powder diffraction data. The relation between the crystalline phases, size of nanoparticles and synthesis conditions were investigated by the analysis.

2. Development of system for *in-situ* SR-PXRD experiment of nanoparticle synthesis in supercritical water

2.1 Necessity of the development of the system

Supercritical water is the reaction field for synthesis of highly functional nanoparticles with the uniform size and shape. The mechanism of controlling the structure of nanoparticles remains unsolved. *In-situ* experiment of the crystal growth of nanoparticles is the most effective approach to investigate the mechanism of the structure control in supercritical water. Synchrotron Radiation (SR) is essential to the *in-situ* experiment of the crystal growth in supercritical water. The atomic-scale structure of nanoparticles can be determined by the powder X-ray diffraction (PXRD) method. We developed the system for *in-situ* SR-PXRD experiment at large SR facility SPring-8. Powder diffraction data were collected from synthesis of ZrO_2 nanoparticles and HfO_2 nanoparticles in supercritical water.

Section 2.2 describes supercritical water. Section 2.3 explains the nanoparticle synthesis in supercritical water. Section 2.4 describes SR. Section 2.5 explains PXRD method. Section 2.6 describes the *in-situ* SR experiment. Section 2.7 shows the development of system for *in-situ* SR-PXRD experiment at SPring-8 BL02B2. Section 2.8 describes the nanoparticle synthesis by the developed system. Section 2.9 explains SR-PXRD experiment at SPring-8 BL02B2. *In-situ* SR-PXRD experiment was performed for the synthesis of ZrO_2 and HfO_2 nanoparticles in supercritical water. Section 2.10 summarizes this chapter.

2.2 Supercritical water

Water is the substance of fundamental importance in our life. Water is essential for many aspects of our daily life such as cooking, drinking or washing. Temperature and pressure are basic parameters for controlling the state of water. Water takes three states called a solid phase, a liquid phase and a gas phase depending on their temperature and pressure. The physical properties of water are changed for these three states. For example, a liquid phase water is transformed into a gas phase by raising temperature. The density of water is drastically decreased. This boiling phenomenon is happening when temperature and pressure are smaller than a set of values called critical point. The critical point of water is 647.3 K and 22.1 MPa. Above the critical point, no boiling or fluidization can happen by additional heating or pressurization. This region is called supercritical water.

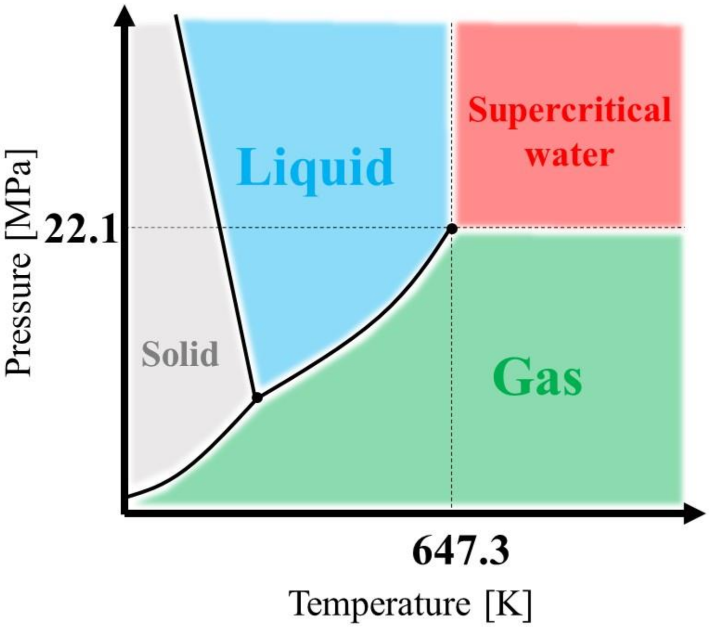

Figure 2.2.1 Phase diagram of water.

Figure 2.2.1 shows a phase diagram of water. The horizontal axis is temperature. The vertical axis is pressure. The unit of temperature is K. The unit of pressure is MPa. The gray area shows a solid phase called as ice. The blue area shows a liquid phase. The green area shows gas phase called as steam. A red area where temperature and pressure are above the critical point is called as supercritical water. Supercritical water is placed between a liquid phase and a gas phase on the phase diagram. Many questions remain unsolved about the atomic-scale structure of supercritical water. Properties of supercritical water are varied continuously and drastically with temperature and pressure.

The density of water is the weight of water per unit volume. The density of water changes drastically from a liquid phase to a gas phase. For example, density of the liquid water at room temperature and ambient pressure.is around 1.0 g/cm^3. Density of steam at 383 K and atmospheric pressure is around 6×10^{-5} g/cm^3. The International Association for Properties of Water and Steam (IAPWS) provided the internationally accepted formulations IAPWS-IF97 for the calculation of properties of water for industrial use [30]. Density of water can be calculated based on IAPWS-IF97 which is valid for temperature below 1273 K and for pressure below 1 GPa. These ranges include the wide range of supercritical water region.

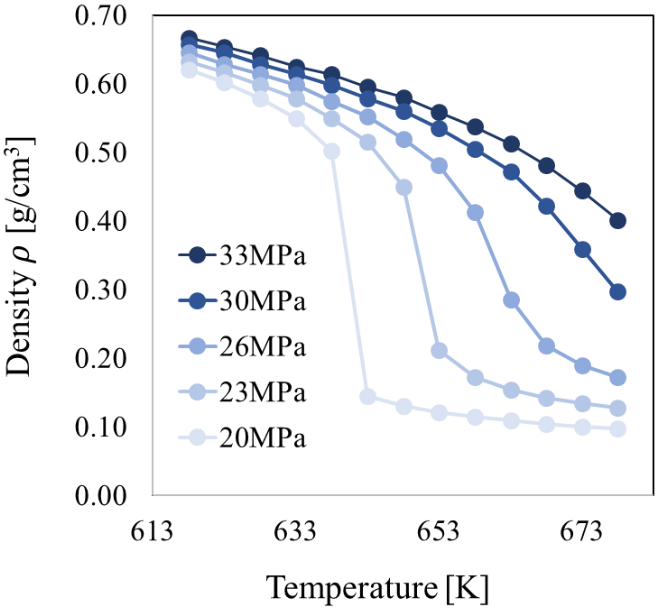

Figure 2.2.2 Temperature and pressure dependence of density of water.

Figure 2.2.2 shows the temperature and pressure dependence of density of water. The horizontal axis is temperature. The vertical axes are density of water. Density of water were calculated based on IAPWS-IF97 for pressure at 20, 23, 26, 30 and 33 MPa. Density of water at 623 K in a liquid phase was increased by 0.04 g/cm^3 by the additional 13 MPa pressure. Density of water at 623 K in supercritical water was increased by 0.34 g/cm^3 by the additional 13 MPa pressure.

Uematsu and Franck reported the equation for the calculation of dielectric constant of water by the nonlinear least square fitting of the experimental data [31]. This equation is applicable to the calculation of dielectric constant of water from 273 K to 823 K and from atmospheric pressure to 500 MPa. The equation was expressed as a function of temperature and density of water as follows:

$$\epsilon_w = 1 + \frac{A_1}{T^*}\rho^* + \left(\frac{A_2}{T^*} + A_3 + A_4 T^*\right)\rho^{*^2} + \left(\frac{A_5}{T^*} + A_6 T^* + A_7 T^{*^2}\right)\rho^{*^3} + \left(\frac{A_8}{T^{*2}} + \frac{A_9}{T^*} + A_{10}\right)\rho^{*^4} \tag{2.1}$$

where $\rho^* = \rho/\rho_0$ and $T^* = T/T_0$. ρ is density of water in kg/m^3.ε_w is dielectric constant. The coefficients of the equation are ρ_0 = 1000 kg/m^3, T_0 = 298.15 K, A_1 = 7.62571, A_2 = 2.44003 × 10^2 , A_3 = -1.40569 × 10^2 , A_4 = 2.77841 × 10 , A_5 = -9.62805 × 10, A_6 = -4.17909 × 10 , A_7 = -1.02099 × 10 , A_8 = -4.52059 × 10 , A_9 = 8.46395 × 10, A_{10} = -3.58644 × 10. Dielectric constant of water is around 80 at room temperature. This enables the electrolytes or polar molecules to be dissolved in water.

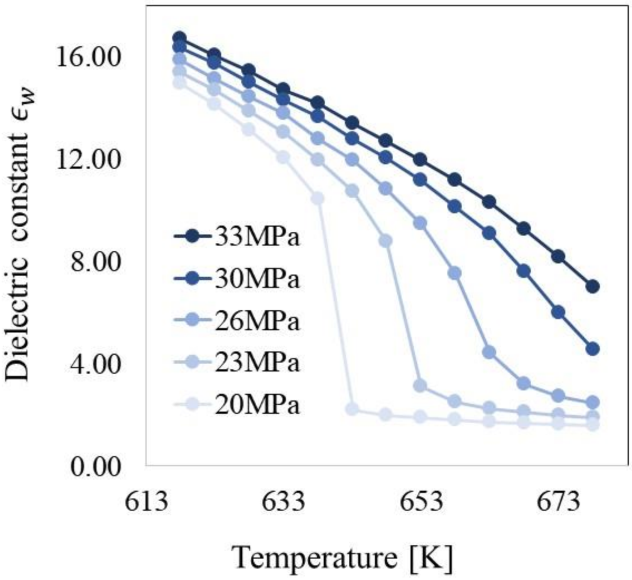

Figure 2.2.3 Temperature and pressure dependence of dielectric constant of water.

Figure 2.2.3 shows the temperature and pressure dependence of dielectric constant of water. The horizontal axis is temperature. The vertical axes are dielectric constant of water. Dielectric constant was calculated from the equation by Uematsu and Franck for pressure at 20, 23, 26, 30 and 33 MPa [31]. Dielectric constant of water at 623 K in a liquid phase was increased by 1.72 by the additional pressure of 13 MPa. The dielectric constant of water at 673 K in supercritical water was increased by 7.52 by the additional pressure of 13 MPa.

Water molecules show self-ionization reaction. A fraction of water molecules is dissociated to the hydrogen ions and hydroxide ions. A chemical formula of this reaction is expressed as follows:

$$\mathrm{H_2O} \leftrightarrows \mathrm{H^+} + \mathrm{OH^-}$$

This self-ionization is essentially related to the functionality of water as solvent. Ion product of water is the scale of self-ionization of water. This is defined as the product of concentration of hydrogen ions and concentration of hydroxide ions in pure water:

$$K_w = [\mathrm{H^+}][\mathrm{OH^-}]$$

K_w is ion product of water. Ion product of water is around 10^{-14} at room temperature. This corresponds to pH value of pure water at room temperature around seven. Marshall and Franck reported the equation for the calculation of ion product of water by the nonlinear least square fitting of experimental data [32]. This equation is applicable to the calculation of ion product of water from 300 K to 1273 K and from atmospheric pressure to 1 GPa. The equation was expressed as a function of temperature and density of water as follows:

$$\log K_w^* = A + \frac{B}{T} + \frac{C}{T^2} + \frac{D}{T^3} + \left(E + \frac{F}{T} + \frac{G}{T^2}\right) \log \rho_w^* \tag{2.2}$$

ρ_w is density of water in g/cm^3. K_w is ion product of water in mol^2 L^{-2}. Asterisks on shoulder of the variables show that these values are substituted into the equation without units. Coefficients of the equation are A = -4.098, B = -3245.2 K, $C = 2.2362 \times 10^5$ K^2, $D = 3.984 \times 10^7$ K^3, E = 13.957, F = -1262.3 K and $G = 8.5641 \times 10^5$ K^2.

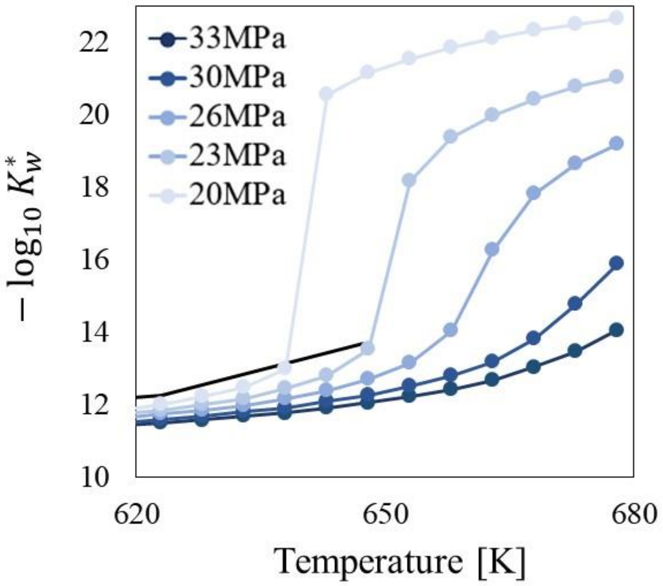

Figure 2.2.4 Temperature dependence and pressure dependence of ion product of water.

Figure 2.2.4 shows the temperature and pressure dependence of ion product of water. The horizontal axis is temperature. The vertical axis is ion product of water. The ion product of water was expressed in the common logarithmic scale. The ion product of water was calculated from the equation by Marshall and Franck for pressure at 20, 23, 26, 30 and 33 MPa [32]. The ion product of water at 623 K in a liquid phase almost doubled by additional pressure of 13 MPa. The ion product of water at 673 K and 33 MPa was 10^7 times higher than that at 673 K and 23 MPa. Properties of water are varied continuously and drastically with temperature and pressure in supercritical water.

The supercritical water is located between a liquid phase and a gas phase on the phase diagram. Widom and Fisher first predicted theoretically the existence of a line which separates the liquid-like region and the steam-like region of supercritical water by investigating the decay of pair correlation functions [33]. Nishikawa *et al.* measured small angle X-ray scattering (SAXS) of supercritical water and estimated density fluctuation of supercritical water from SAXS data [34]. They found that density fluctuation formed a ridge for temperature and density of water. This ridge was named “Nishikawa-Widom line” [35].

2.3 Nanoparticle synthesis

Supercritical water can be used as the reaction field of nanoparticle synthesis. Adschiri *et al*. developed a novel method called supercritical hydrothermal synthesis [1]. The metal salt aqueous solution is used as a precursor of nanoparticles. Metal oxide nanoparticles with the uniform size and shape can be synthesized from metal salt aqueous solution in supercritical water conditions [36]. Reactions of supercritical hydrothermal synthesis are composed of following two steps [3]:

$$\mathrm{MA}_x + x\mathrm{H_2O} = \mathrm{M(OH)}_x + x\mathrm{HA}$$

$$\mathrm{M(OH)}_x = \mathrm{MO}_{x/2} + x/2\ \mathrm{H_2O}$$

where $\mathrm{MA_x}$ is a metal salt. In the first step, hydrolysis is proceeded by heating precursor. In the second step, solubility of reaction materials becomes very low in supercritical water. Metal oxide nanoparticle is generated due to the oversaturation in the precursor.

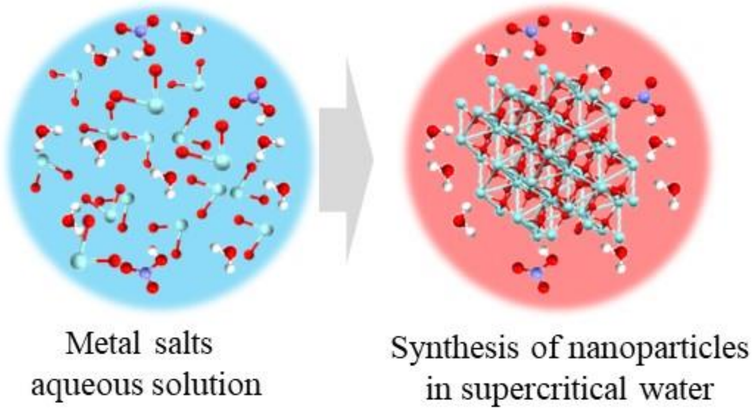

Figure 2.3.1 Schematic of the nanoparticle synthesis in supercritical water.

Figure 2.3.1 shows the schematic of nanoparticle synthesis in supercritical water. Metal salts aqueous solution is heated inside a pressure vessel. Fine nanoparticles with the diameter less than 20 nm are synthesized in supercritical water. This reaction is typically completed within one hour.

The highly functional nanoparticles can be synthesized in supercritical water by modifying those surfaces. Non-polar organic molecules can be dispersed in supercritical water due to low dielectric constant of supercritical water. The surface modification was caused by the formation of chemical bonds between organic molecules and atoms on the most reactive surfaces of nanoparticles during the synthesis. Zhang *et al.* reported the surface modification of ceria nanoparticles in the reaction field of mixture of supercritical water and decanoic acid [37]. The synthesized nanoparticles showed the shape of the truncated octahedra and exposed the reactive {001} facets.

The structure of nanoparticles such as size and shape can be flexibly controlled by synthesis conditions such as temperature, pressure or concentration of the precursor. This is probably due to the uniform reaction field by temperature or pressure. Aoki *et al*. reported the size-controlled synthesis of ceria nanoparticles by changing temperature [38]. The size of synthesized nanoparticles were around 40 nm at 623 K. The size of nanoparticles synthesized at 673 K was around 15 nm. Hakuta *et al.* reported the shape-controlled synthesis of boehmite nanoparticles by changing concentration of an aqueous solution [39]. The shape of synthesized nanoparticles was the rhombic plate by concentration of 0.01 mol/L. The shape of synthesized nanoparticles was the hexagonal plate with concentration of 0.05 mol/L. The mechanism of structure control of nanoparticles in supercritical water remains unsolved.

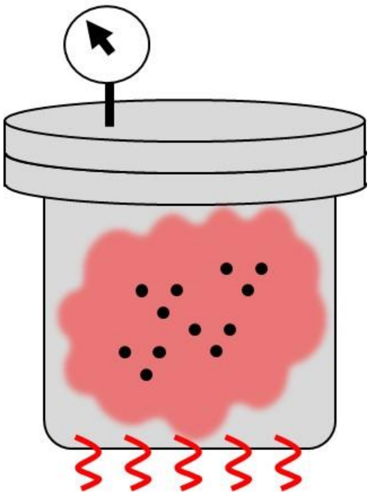

Figure 2.3.2 Schematic of batch-type reactor.

There are two types of reactors for the synthesis of nanoparticles in supercritical water. One is the batch type reactor. Another is the flow type reactor. The schematic of batch-type reactor is shown in Figure 2.3.2. This uses the autoclave as a reaction vessel with diameter of 20 to 50 mm and with height of 50 to 100 mm. The large volume of the vessel can result in a slow heating rate and non-uniform distribution of temperature inside the reaction vessel. Iversen *et al.* developed the batch type reactor by using a capillary with diameter of 0.7 to 1.6 mm [40].

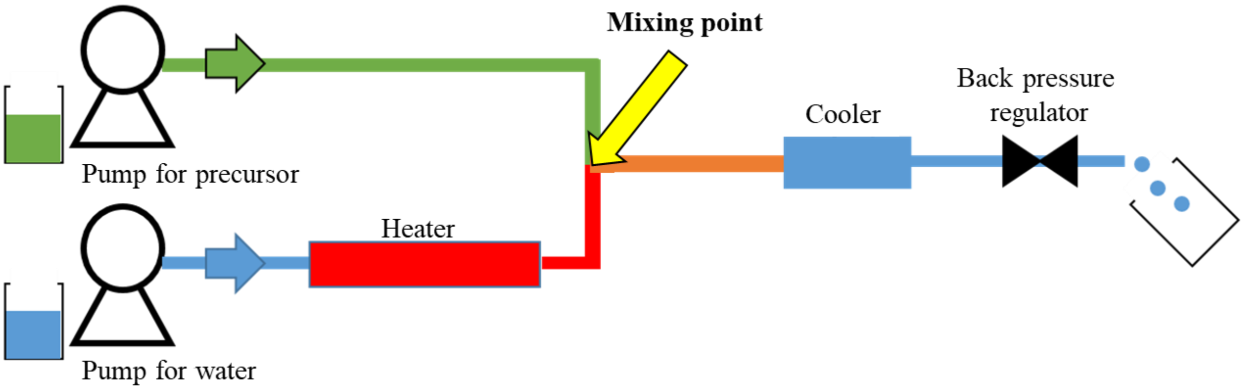

Figure 2.3.3　Schematic of flow-type reactor.

Figure 2.3.3 shows the schematic of flow type reactor. Adschiri *et al.* developed the flow-type reactor for synthesis of nanoparticles in supercritical water [1]. The basic components of this reactor are two high pressure pump, a stainless steel tube with diameter less than 10 mm, a heater and a back pressure regulator. The two pumps send water and the precursor continuously. Pressure inside the steel tube was kept at constant value by a back pressure regulator. Liquid water becomes supercritical water in the heated region of the tube. A cartridge heater or an electric heater was used as the heating device [38], [41]. The nanoparticles were synthesized at the mixing point of supercritical water and the precursor.

This flow type reactor shows several advantages to the batch-type reactor [1]. Fine nanoparticles can be synthesized during the short reaction time from several seconds to several minutes, since fast increase of temperature from a liquid phase to supercritical water results in the rapid decrease of solubility and a high nucleation rate of nanoparticles. The low solubility also suppresses subsequent crystal growth by Ostwald Ripening in a liquid phase. The small volume of mixing point is favorable to the uniform reaction field and structure control of nanoparticles. The continuous reaction scheme enables mass production of nanoparticles during short time.

2.4 Synchrotron radiation

SR is the highly brilliant X-ray beam. SR is emitted from a relativistic electron which undergoes acceleration perpendicular to the direction of motion. The brilliance of SR is more than 10^8 times higher than that of laboratory X-ray source. SR is available at large SR facilities such as SPring-8 in Japan.

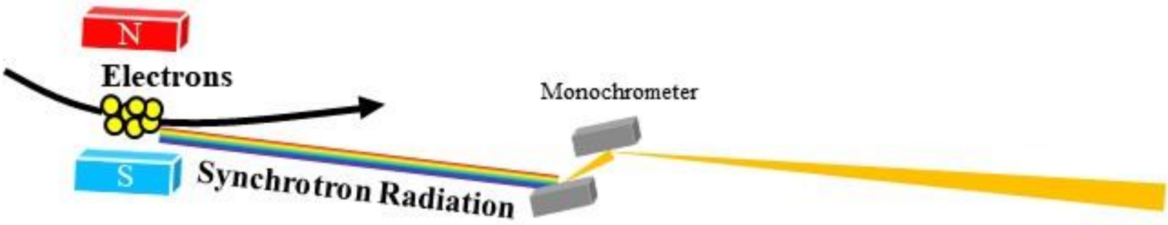

Figure 2.4.1 Schematic of emission of SR from an electron.

Figure 2.4.1 shows the schematic of emission of SR from electrons. At large SR facilities, electrons are accelerated to the relativistic speed. SR is obtained by applying magnetic field for relativistic electrons in the direction perpendicular to the orbit. Electrons are accelerated by Lorentz force and emits highly brilliant SR in the tangential direction. For example, SPring-8 provides the most powerful SR in the world from the electrons with energy of 8 GeV. This enables the highest brilliance of SR at the high-energy X-ray region around 28.9 keV.

The emitted SR is the white radiation with the continuous energy spectrum from an X-ray region to an infrared region. The photon energy of SR can be selected by using a monochromator for the experimental conditions. SR is highly parallelized electromagnetic radiation. For example, the angular divergence of SR from an 8 GeV electron is around 64 μrad. This eliminates the need for several equipment such as a soller slit which is installed for the laboratory X-ray source for reducing the divergence of X-ray. It assures the space around the sample position.

2.5 Principle of Powder X-ray diffraction

Powder X-ray diffraction (PXRD) is a method to analyze the structure of crystalline materials. This can be used for investigating the structure of a powder sample composed of the large number of crystals. PXRD data contains the information of atomic-scale structure of powder sample.

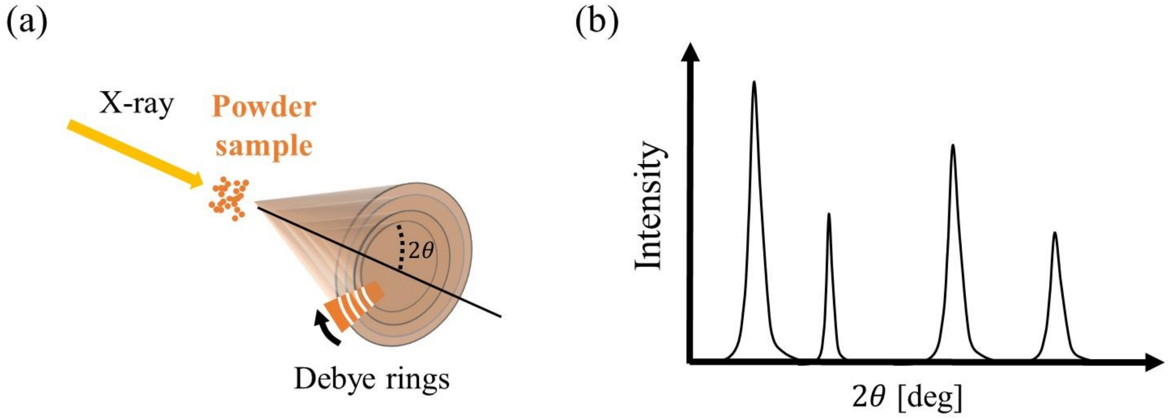

Figure 2.5.1 Schematic of PXRD experiment. (a) PXRD measurement of the powder sample, (b) powder diffraction data.

Figure 2.5.1 describes PXRD experiment. Figure 2.5.1 (a) shows the schematic of PXRD experiment. When a crystal was exposed to the monochromatic X-ray beams, strong diffracted beams are emitted to the specific diffraction angles 2θ from the direction of incident beam. The orientation of crystals in powder sample is assumed be random to all the directions in space. Diffracted beams from powder sample form a ring, since diffracted beams are emitted to all the directions which satisfy the angle 2θ from the direction of incident beam. These angles are called Bragg angles. The diffracted beams are consisted of the set of concentric rings called Debye rings. The intensity of Debye rings is measured in PXRD experiment.

Figure 2.5.1 (b) shows powder diffraction data collected at PXRD experiment. Powder diffraction data are obtained by integrating the intensity of Debye rings in radial direction as shown in Figure 2.5.1 (a). The horizontal axis of powder diffraction data is diffraction angle. The vertical axis is intensity. Powder diffraction data are consisted of the series of peaks with the finite widths. These peaks are called Bragg peaks. The intensity, diffraction angle and width of Bragg peaks can be used for the analysis of structure of crystals in the powder sample.

2.6 *In-situ* synchrotron radiation experiment

In-situ experiment of synthesis is the most effective approach to investigate the mechanism of structure control of nanoparticles. *In-situ* study enables direct monitoring of structural change during the reaction. Data measured from nanoparticles contain structural information in an atomic scale. The fast reaction in a supercritical water requires data collection within seconds or minutes.

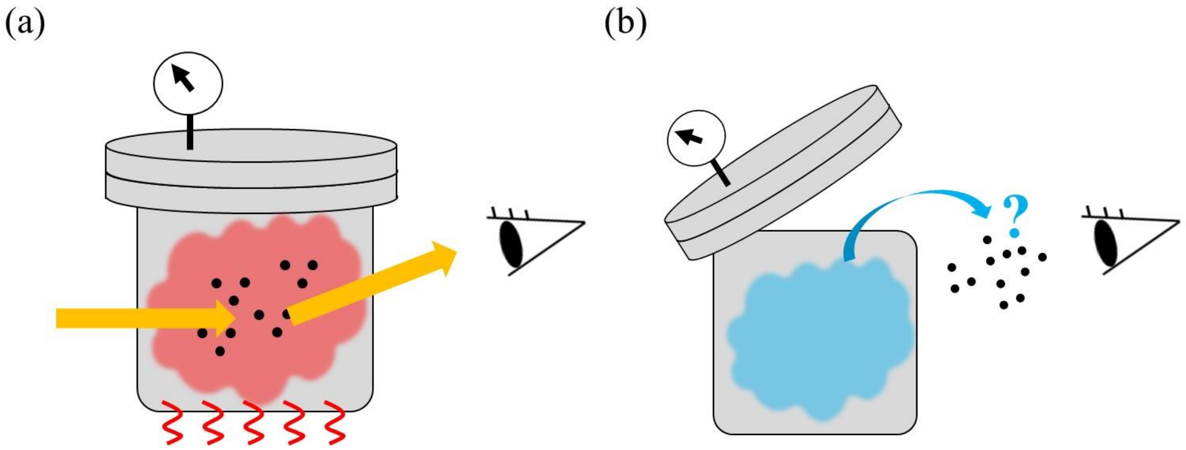

Figure 2.6.1 Two approaches to investigate the structure control of nanoparticles. (a) *In-situ* study, (b) *ex-situ* study.

Figure 2.6.1 shows two approaches to investigate the structure of nanoparticles in supercritical water. Figure 2.6.1(a) shows the schematic of *in-situ* study of nanoparticle synthesis. By *in-situ* study, data are collected from nanoparticles inside the reaction vessel. Structural change in a reaction field can be directly monitored during the reaction. Figure 2.6.1(b) shows the schematic of another approach called *ex-situ* study. Nanoparticles are synthesized in series of conditions of supercritical water. The structure of nanoparticles is characterized and compared after synthesis. In this approach, nanoparticles have to get through room temperature water after synthesis. Several characterization methods require post processing of the nanoparticles such as drying or centrifugation. These processes complicate the understanding the mechanism of structure control in supercritical water.

The structure in an atomic scale can be investigated by an electron beam, a neutron beam and an X-ray beam [16], [17], [42]. An X-ray beam is essential for the *in-situ* study of synthesis of nanoparticles in supercritical water. High-energy X-ray beam does not require high vacuum environment around sample which is required by an electron beam. An X-ray beam shows high energy per unit area and it enables the measurement of a sample whose size is 1/100 times smaller than that required for a neutron beam. Data can be collected within minutes from the sample with size less than micrometers.

SR is a powerful tool for *in-situ* study of the structural change in an atomic scale. The high brilliance of SR enables the data collection in the second time scale. The hard X-ray which can penetrate the reaction vessel can be selected from the continuous spectrum of SR. *In-situ* SR study often requires the development of measurement system for the construction of sample environment at a beamline at large SR facility. The space around the sample can be used for installation of measurement system for *in-situ* experiment. For example,_Yang *et al.* reported the *in-situ* SR study of the bimetallic oxide catalysts under the oxygen reduction reactions [43]. In the work presented by Yang group, a dedicated electrochemical cell was installed at the F-3 beamline of SR facility CHESS. The coactive site of the catalyst could be identified by monitoring the change of X-ray absorption spectrum during the cyclic voltammetry experiment.

The structural change in supercritical water has been investigated by *in-situ* SR-PXRD studies. Iversen *et al.*

developed the reactor for the *in-situ* SR-PXRD experiment of nanoparticle synthesis in supercritical reaction fields [40], [44]. They employed a fused silica or a sapphire capillary as a reaction vessel. *In-situ* SR-PXRD experiment was carried out in various SR facilities such as APS, ESRF or PETRA-Ⅲ. A major interest of Iversen group is the nucleation of nanoparticles from a precursor during several seconds to minutes. They have carried out *in-situ* SR-PXRD studies for more than a hundred of the synthesis of nanoparticle in supercritical water or supercritical alcohol [19], [45]. In other cases, O'Hare *et al.* have developed the autoclave type reactor with the large volume comparable to the equipment for the practical use [18], [46], [47]. Their interest is the reaction kinetics in supercritical water [18]. The design of their reactor was dedicated for the beamline at SR facility Diamond.

2.7 Development of the system for *in-situ* SR-PXRD experiment

This section describes the development of the system for *in-situ* SR-PXRD experiment at SPring-8 BL02B2. The system is composed of a sample holder, a pump section and a heater. Section 2.7.1 explains components and assembly of the sample holder. Section 2.7.2 describes components and assembly of the pump section. Section 2.7.3 shows the apparatus for the synthesis of nanoparticles. Section 2.7.4 describes a heater, a diffractometer and X-ray detectors at SPring-8 BL02B2. Section 2.7.5 shows the procedure of *in-situ* SR-PXRD experiment.

2.7.1 Sample holder

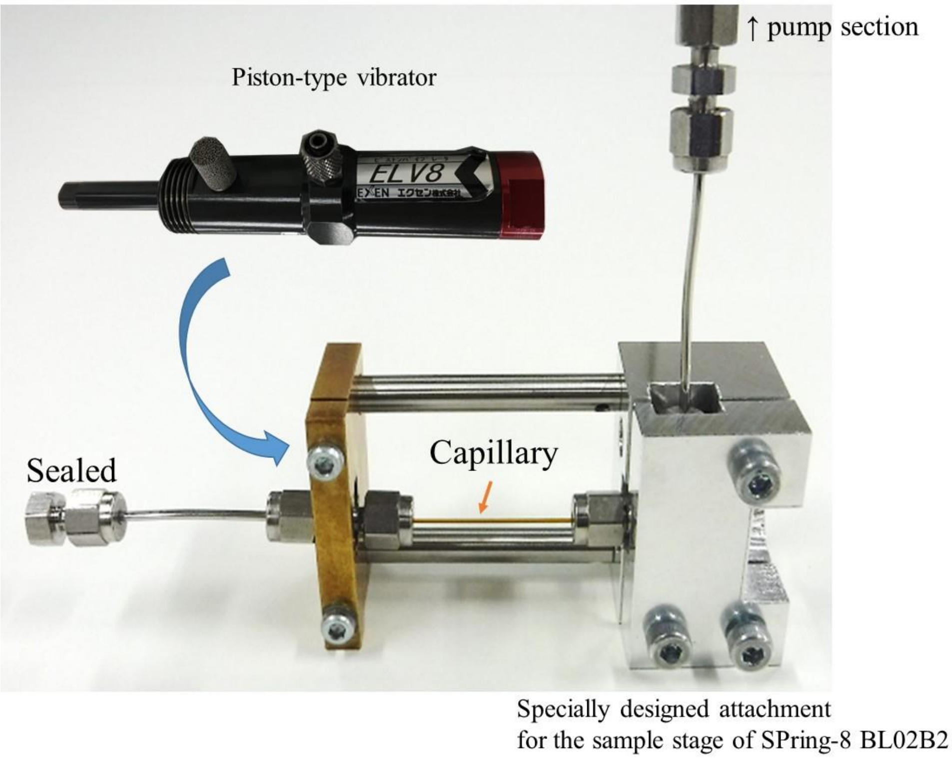

Figure 2.7.1 Sample holder.

Figure 2.7.1 shows a sample holder for SR-PXRD experiment of nanoparticle synthesis in supercritical water. The design of a sample holder was based on the reactor developed by Iversen *et al.*[40], [44]. A capillary was fixed on the sample holder as the reaction vessel. The stainless steel tube was connected on both sides of a capillary by using connectors. These connectors were sandwiched by attachment 1 and attachment 2. Two attachments were specially designed for the sample stage at SPring-8 BL02B2. Two rods sustained two attachments. The piston-type vibrator can be fixed on the side of attachment 2.

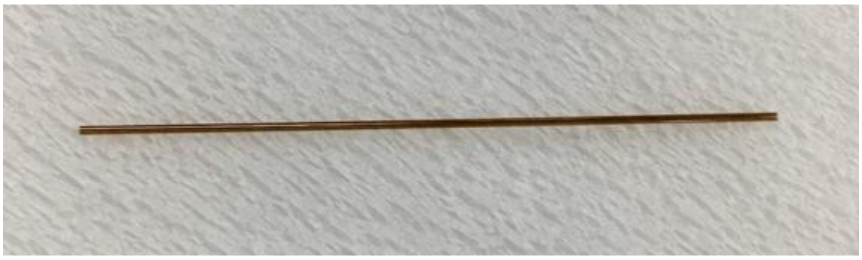

Figure 2.7.2 Fused silica capillary.

Figure 2.7.2 shows the capillary used as a reaction vessel of nanoparticle synthesis. Flexible fused silica capillary tubing by Molex Co. was used for *in-situ* SR-PXRD experiment. The material of capillary is the synthetic fused silica coated with polyimide. The inner diameter is 0.53 mm. The outer diameter is 0.68 mm. The capillary can be used under temperature of 673 K and pressure of 35 MPa. The length of capillary was typically 55 mm.

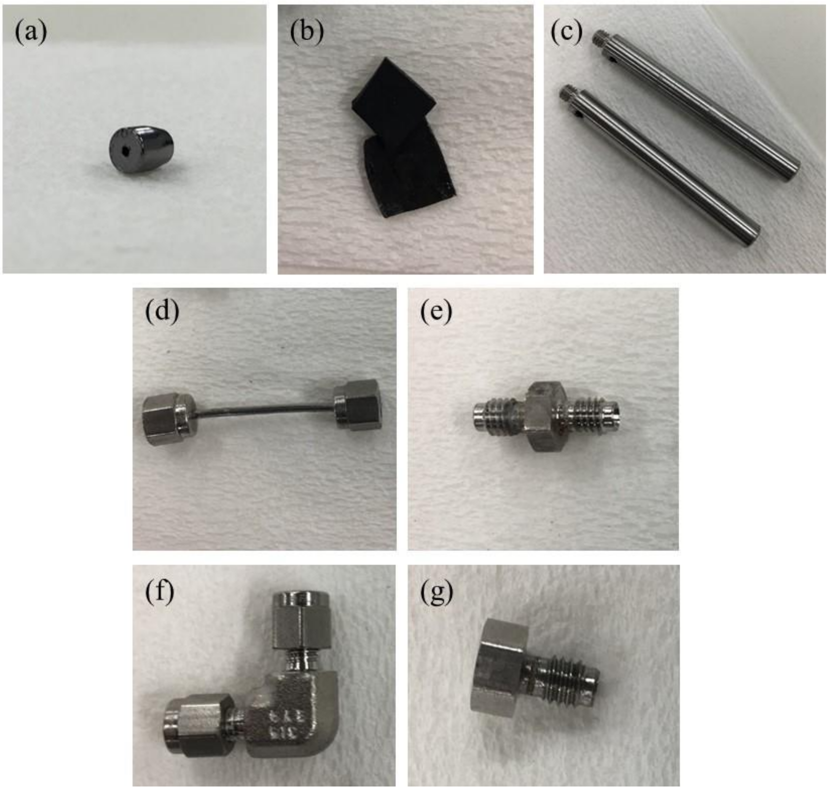

Figure 2.7.3 Components of sample holder. (a) graphite ferrule, (b) rubber sheet, (c) rod, (d) flexible tube, (e) straight connector, (f) L-shaped connector, (g) capping nut.

Figure 2.7.3 shows components of the sample holder. Figure 2.7.3(a) shows a graphite ferrule by Trajan Scientific Ltd. Two graphite ferrules were used for connection between a capillary and a stainless steel tube. Figure

2.7.3(b) shows a rubber sheet. This ensured tight fixing of a connector inside attachments. The diameter was 6 mm. The length was 50 mm.

Figure 2.7.3(d) shows a stainless steel flexible tube. The outer diameter is 1/16 inch. Stainless steel nuts and ferrules were fixed on both sides of the tube for connection. Figure 2.7.3(e) shows a stainless steel straight Swagelok connector. Figure 2.7.3(f) shows a stainless steel L-shaped Swagelok connector. Figure 2.7.3 (g) is a capping nut. This was used for sealing a stainless steel flexible tube.

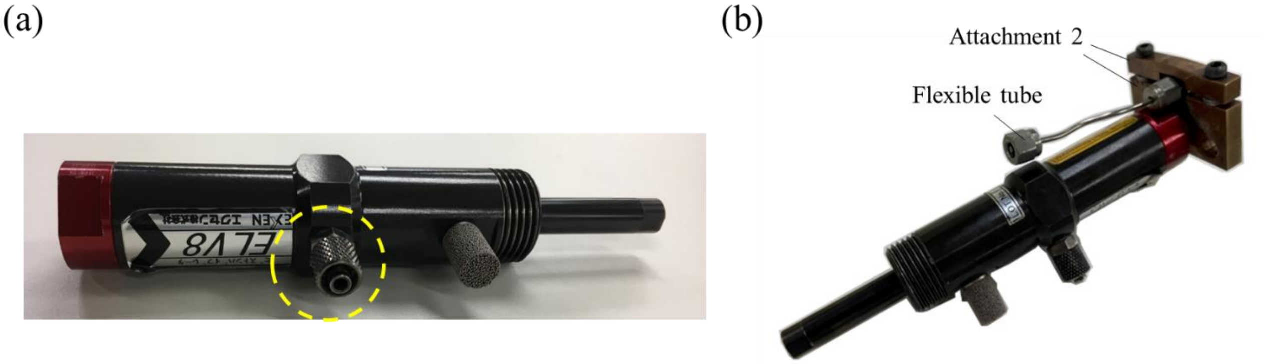

Figure 2.7.4 (a) Piston-type vibrator, (b) vibrator fixed on the attachment 2.

Figure 2.7.4 shows piston-type vibrator. Figure 2.7.4 (a) shows vibrator ELV-8 by EXEN Corp. The shape of vibrator is cylinder. The diameter is 17 mm. The height is 124 mm. The vibration is caused from the oscillation of a built-in piston by air flow from a compressor. The yellow line shows the connections for tubes through which air flow go. The frequency range is from 25 to 36 Hz corresponding to the gas pressure from 0.2 to 0.6 MPa. This was used for dispersing nanoparticles inside a reaction vessel. The vibrator can be fixed on the attachment 2. Figure 2.7.4 (b) shows vibrator fixed on the attachment 2. Vibrator is placed below the flexible tube in which a precursor is filled. Piston generates vibration by moving backward and forward along the height of cylinder.

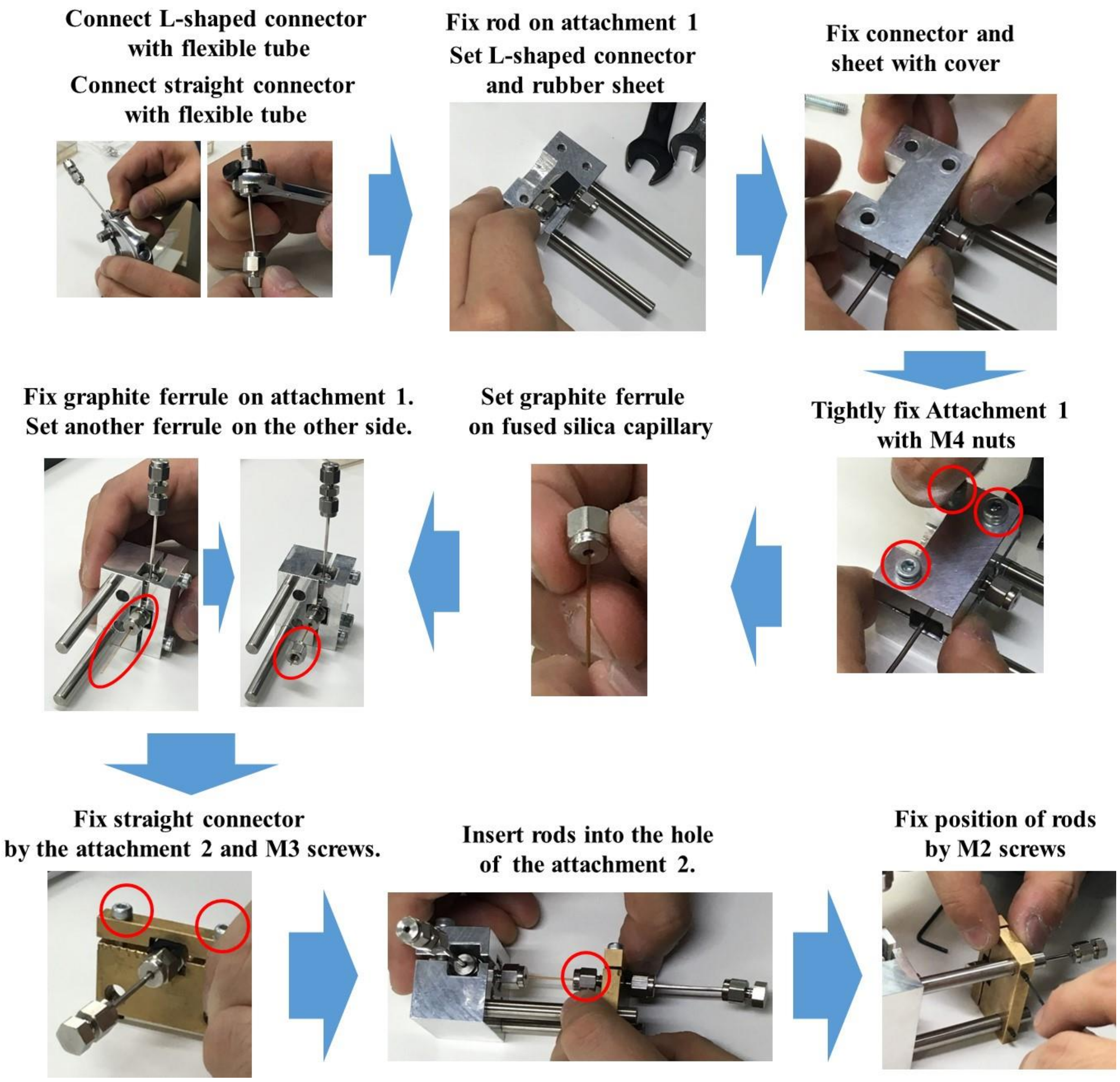

Figure 2.7.5 Procedure of assembling sample holder.

Figure 2.7.5 shows the procedure of an assembling sample holder. Firstly, an L-shaped connector and a straight connector were connected with a stainless steel flexible tube. The other side of tube with a straight connector was sealed by a capping nut. The L-shaped connector is sandwiched by attachment 1 with small pieces of rubber sheet. This will be sandwiched between parts of attachment 2. The piston-type vibrator is fixed on attachment 2 before assembly.

Two rods are screwed into the holes on the bottom part of attachment 1. These rods are fixed by hex wrench. The L-shaped connector with a flexible tube is set along groove on the bottom part of attachment 1. The rubber sheet and upper part of attachment 1 is put on the connector. The connector and rubber parts are fixed between parts of attachment by using three M4 screws. The straight connector with a flexible tube is fixed between parts of attachment 2 in the same way. Two M3 screws are used for fixing it.

Two graphite ferrules in 1/16 inch nuts and a fused silica capillary were prepared. One nut with graphite ferrule is put through the capillary. The nut is fixed on the L-shaped connector. We put another nut through capillary.

We put two rods through holes on bottom parts of attachment 2. The nut with graphite ferrule is fixed on the straight connector. The rod and attachment 2 are fixed by using two M2 screws. We can use this sample holder for synthesis of nanoparticle.

2.7.2 Pump section

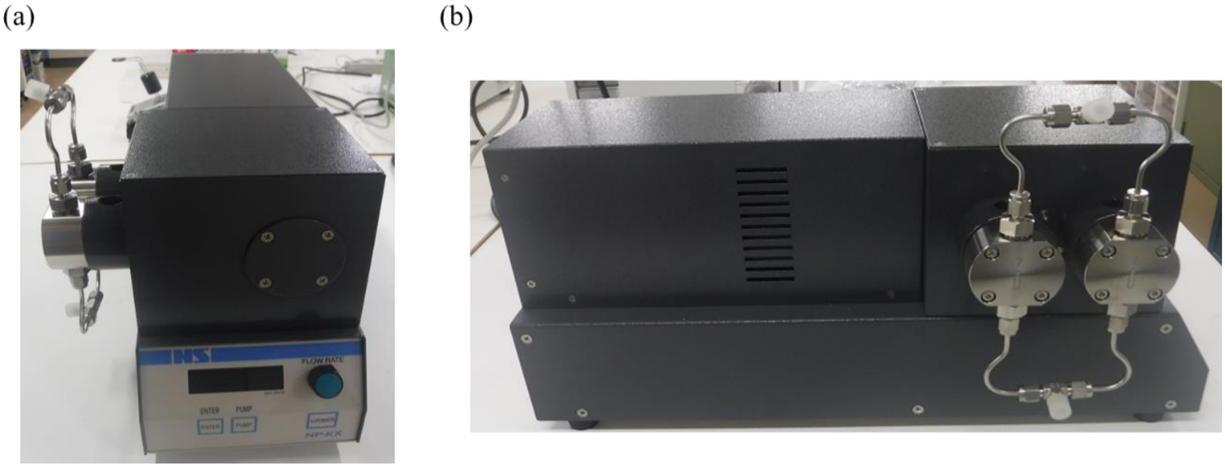

Figure 2.7.6 High pressure pump NP-KX-500. (a) Front, (b) side.

Figure 2.7.6 shows the high pressure pump NP-KX-500 by Nihon Seimitsu Co. This was used for taking up liquid and sending it with a specified flow rate. Figure 2.7.6(a) shows a front of pump. A range of flow rate is from 0.1 to 100 mL/min. Maximum delivery pressure is 35 MPa. The depth, width and height of pump is 467 mm, 215 mm and 210 mm, respectively. Three buttons, one small knob and a small display are on the front. Pressing Power button can turn on and off the pump. The flow rate can be displayed when the pump is turned on. A knob can change the setting value of flow rate. The “pump” button starts and stops the delivery of liquid with setting a value of flow rate. The “enter” button is used for adjusting the flow rate without stopping delivery of liquid. Figure 2.7.6(b) show the side of a pump. Two T-shape fittings are connected to two round shaped parts. Two plungers inside the round shaped parts move back and forth in opposite direction for sending liquid continuously.

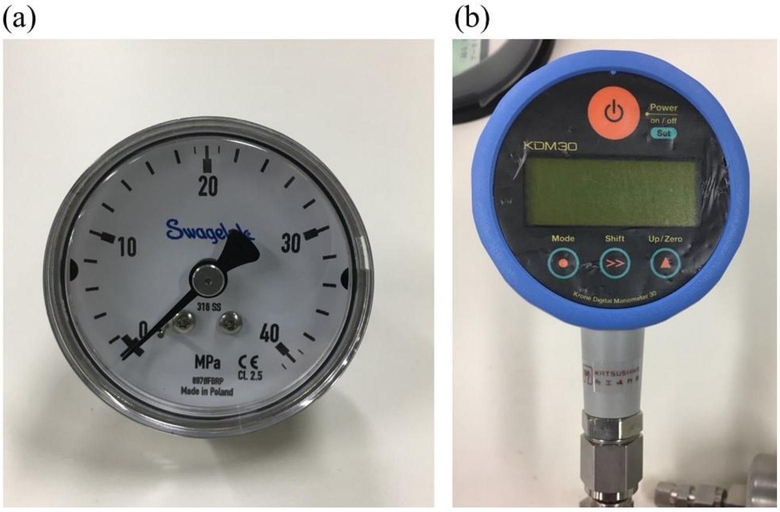

Figure 2.7.7 Pressure gauge. (a) Analog pressure gauge PGI series, (b) Digital pressure gauge KDM 30.

Figure 2.7.7 shows pressure gauges. Figure 2.7.7(a) shows analog pressure gauge PGI series by Swagelok. Scale plate shows pressure from 0 to 40 MPa. The diameter and thickness are 50 mm and 25 mm. The end connection is 1/4 inch male screw. Figure 2.7.7(b) shows digital pressure gauge KDM30 by Krone Co. Pressure is displayed on a monitor. The end connection is 1/4 inch male screw.

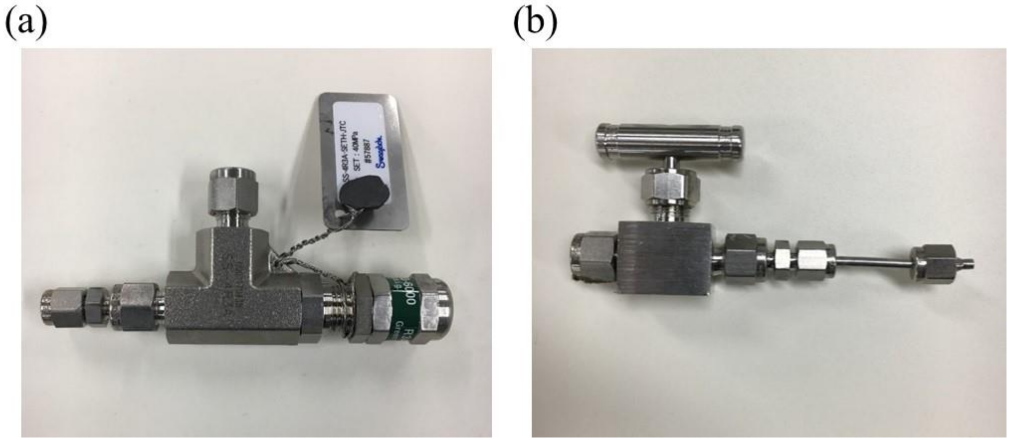

Figure 2.7.8 (a) Safety valve, (b) pressure relief valve.

Figure 2.7.8 shows a safety valve and a pressure relief valve. Figure 2.7.8(a) shows safety valve R3A series by Swagelok. Built-in spring is shrunk by pressure. A flow path was opened in direction perpendicular to spring at limit pressure of 35 MPa. The end connection is 1/4 inch male screw. Figure 2.7.8(b) shows a pressure relief valve. The stainless steel needle valve by Swagelok was used as a pressure relief valve. Pressure can be released manually by turning a handle. This can be used under pressure of 41.3 MPa. The end connection is 1/4 inch male screw.

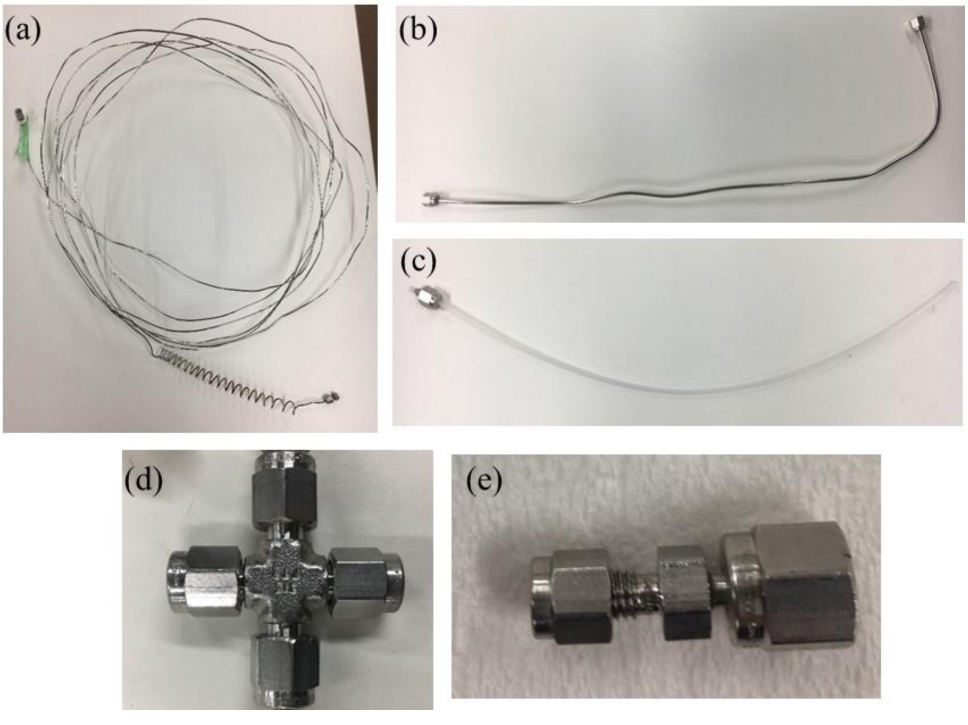

Figure 2.7.9 Components of pump section. (a) 1/16 inch flexible tube, (b) 1/8 inch tube, (c) 1/8 inch

fluorine resin tube, (d) 1/8 inch cross-type connector, (e) 1/8-1/16 inch reducer.

Figure 2.7.9 shows components of pump section. All components are products by Swagelok. Figure 2.7.9(a) shows a flexible tube with inner diameter 1/16 inch. The tube is made of stainless steel SUS316. Nuts and ferrules are connected on both sides of tube. Figure 2.7.9(b) shows a tube made of SUS316 with inner diameter 1/8 inch. Nuts and ferrules are connected on both sides of tube. Figure 2.7.9(c) shows a fluorine resin tube with inner diameter 1/8 inch. Figure 2.7.9(d) shows a SUS316 cross-type connector. Tubes with 1/8 inch in diameter can be connected in four directions. Figure 2.7.9(e) shows a SUS316 reducer. The reducer is used for connection between a 1/8 inch cross-type connector and a 1/16 inch flexible tube.

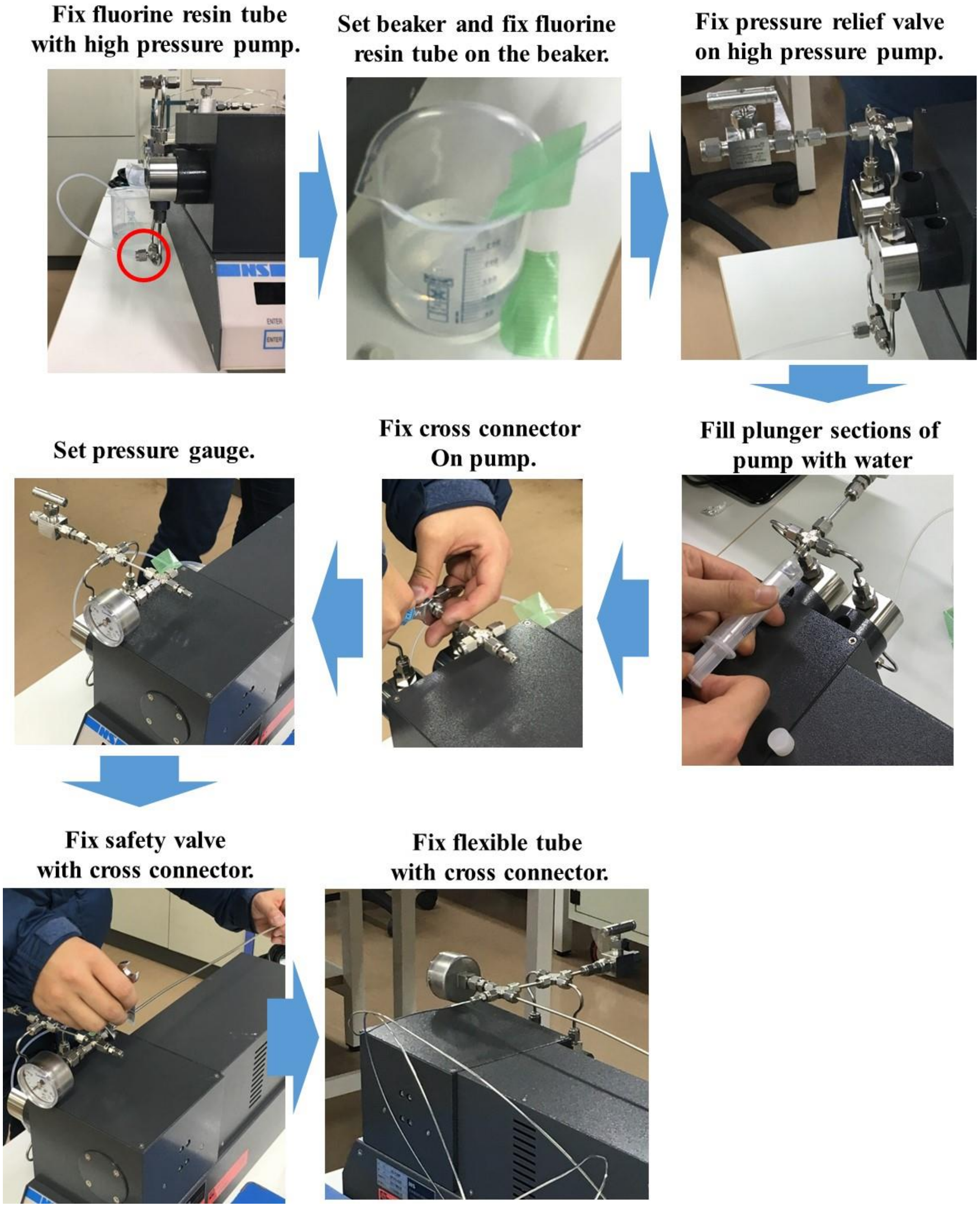

Figure 2.7.10 Procedure of assembling pump section.

Figure 2.7.10 shows the procedure of assembling pump section. A plunger pump is fixed on a stable position. The bottle is set on the side of pump. Pressure medium is put inside of the bottle. One side of the fluorine resin tube is inserted into pressure medium. We set a syringe to a connector on the pump and fill two tubes with pressure medium before using the pump. This is because air flow could break the plunger section.

A pressure relief valve is fixed to the cross-shaped connector. A 1/8 inch stainless steel tube attached to another cross connector is fixed on the other side of connection. A digital pressure gauge, a safety valve and a 1/8-1/16 inch reducer is fixed on cross connector. A reducer can be connected to 1/16 inch stainless steel flexible tube.

2.7.3 Apparatus for synthesis

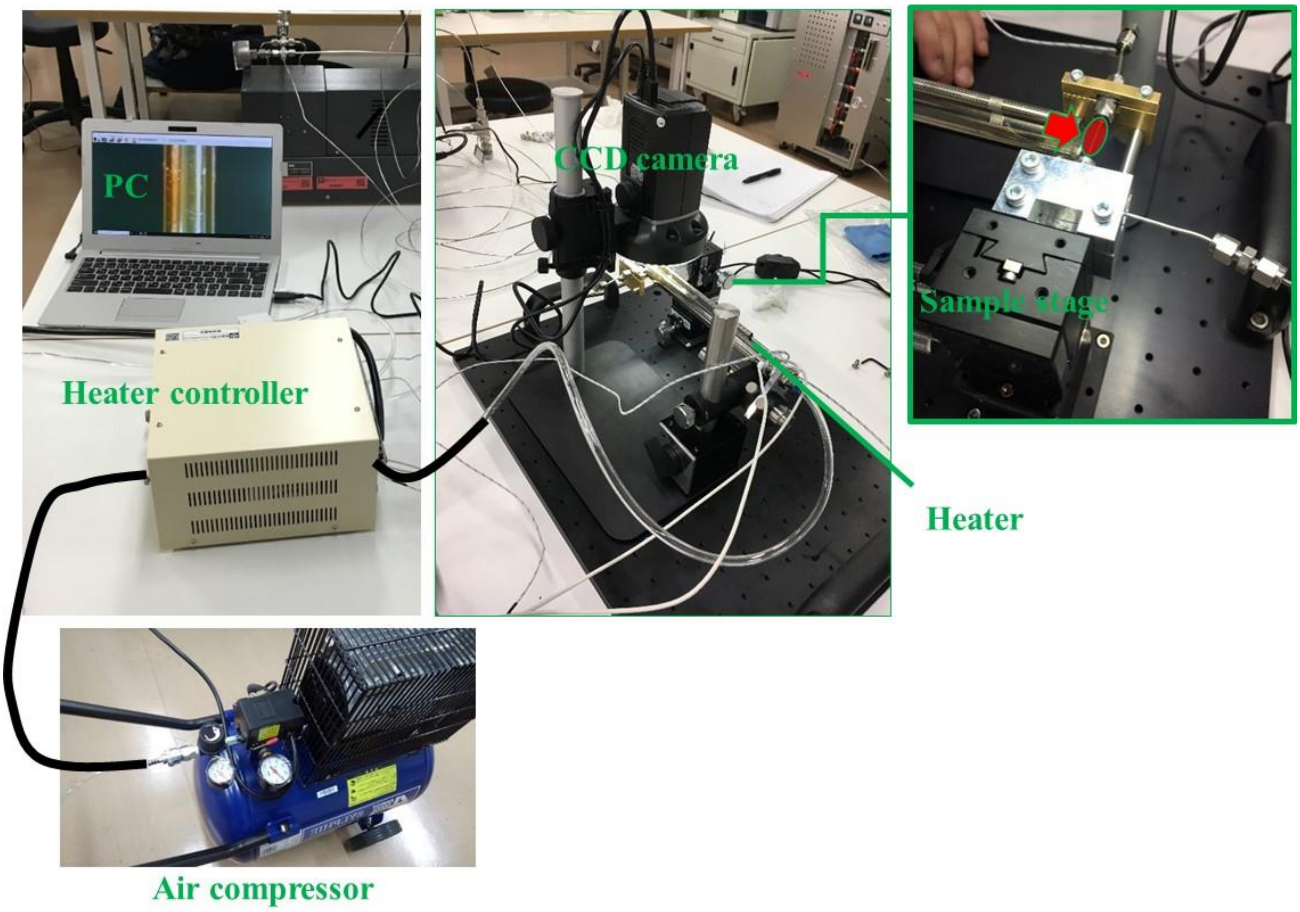

Figure 2.7.11 Apparatus for the synthesis.

Figure 2.7.11 shows the apparatus of the synthesis of nanoparticles. This was composed of a pump section, a sample holder, a stage, a heater, a heater controller, a CCD camera and an air compressor. The sample holder was mounted on the stage. Temperature of synthesis was controlled by the heater and heater controller. The heating medium was air sent by a compressor. Synthesis of nanoparticles was monitored by the CCD camera.

Figure 2.7.12 Digital microscope UM06.

Figure 2.7.12 shows a CCD camera UM06 by MICROLINKS TECHNOLOGY Co. Ltd. This is composed of a scope, a pole and a stand. The width of scope is 106 mm. The depth is 106 mm. The height is 152 mm. The length of pole is 300 mm. The width of stand is 220 mm. The depth of stand is 150 mm. The used sensor is a CMOS image sensor. The number of elements is 50,000. Magnification is 270 for an object at distance of 2 cm.

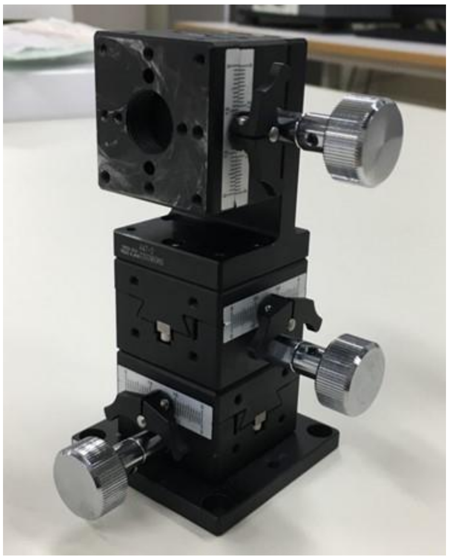

Figure 2.7.13 Manual XYZ axis stage.

Figure 2.7.13 shows a manual XYZ axis stage by SURUGA SEIKI Co., Ltd. The depth and width are 25 mm. The height is 73.5 mm. It has a square table with six holes for M3 screw. The edge of table is 25 mm. The position of stage can be shifted to directions of three axes by rotating three screws. The stroke of each axis is ±10 mm.

Figure 2.7.14 Air compressor.

Figure 2.7.14 shows an air compressor FX9731 SYLPHIE by ANEST IWATA Corp. The volume capacity of an air tank is 38 L. The maximum flow rate is 72 L/min. The rated pressure of air is 0.88 MPa. A pressure gauge monitors pressure inside the tank and outlet. Air flow is automatically stopped if pressure inside the tank is reached to 0.85 MPa.

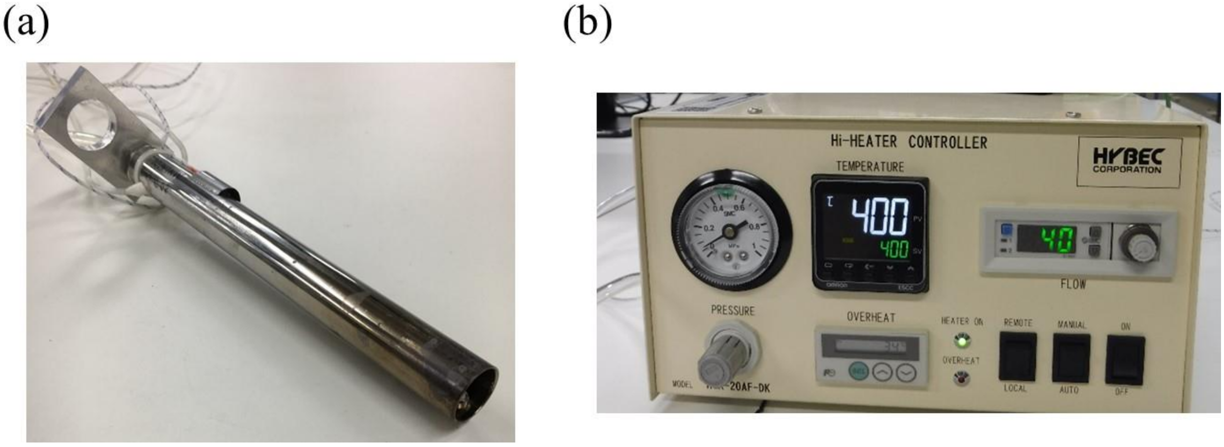

Figure 2.7.15 Heater.

Figure 2.7.15 shows the heater for the nanoparticle synthesis in laboratory. Figure 2.7.15(a) shows high power type heater SAH series by HYBEC Corp. The length is 185 mm. The heating medium goes through a quartz tube with diameter 12.5 mm. Kanthal alloy is used as a heating element. The quartz tube is covered by a stainless tube with diameter 19 mm. Temperature is measured by thermocouple around outlet. A heater can be used under temperature of 1073 K. Figure 2.7.15(b) shows temperature controller SAH series by HYBEC Corp.. The dried air or nitrogen can be used as a heating medium. Temperature is controlled by PID algorithm. It can be used under temperature of 1073 K. The range of flow rate of heating medium is from 2 to 100 L/min. The heating is automatically stopped when a controller detects overheat or the absence of flow of heating medium.

2.7.4 Diffractometer, heater and detector at SPring-8 BL02B2

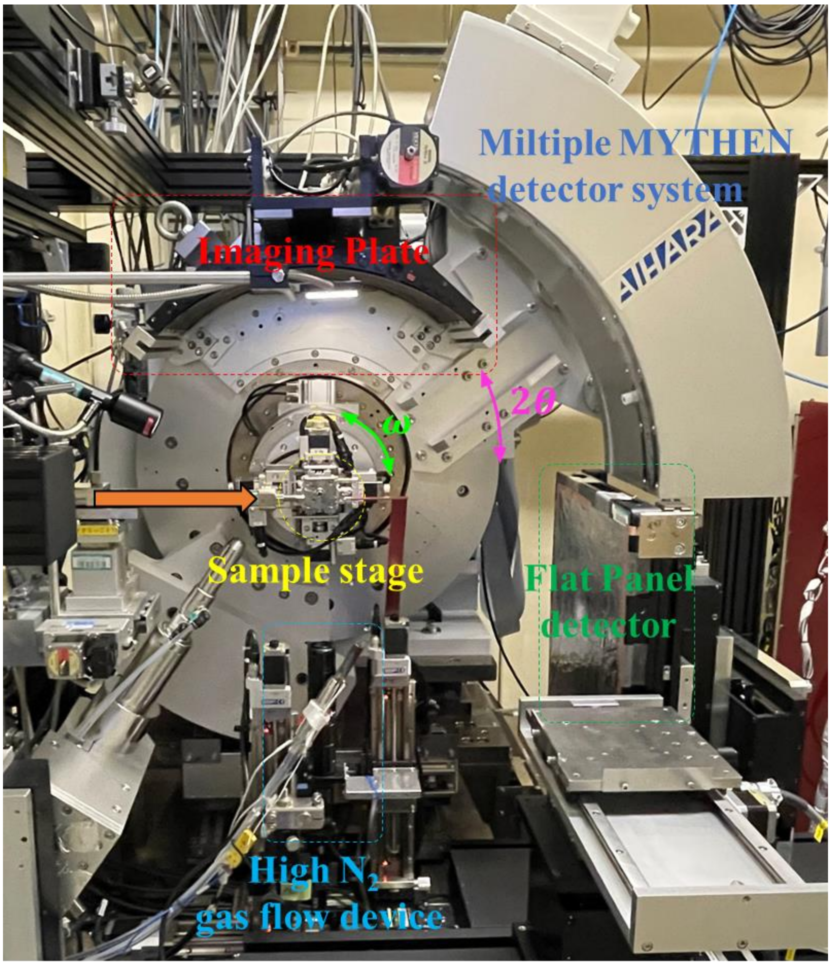

Figure 2.7.16 Large Debye-Scherrer camera at SPring-8 BL02B2.

Figure 2.7.16 shows a photograph of large Debye-Scherrer camera at SPring-8 BL02B2 [48], [49]. A two-circle diffractometer with ω and 2θ axis was installed inside the experimental hatch. The orange arrow shows the direction of the incidence of SR. The yellow line shows a five-axis sample stage on the ω-axis. Multiple MYTHEN detector systems, Imaging Plate (IP) and Flat Panel Detector can be selected as an X-ray detector. A red line shows the cassette for IP. A deep blue line shows the multiple MYTHEN detector systems. A green line shows Flat Panel Detector. These detectors can be easily switched for the measurement by moving motor-driven axes of diffractometer. IP and multiple MYTHEN detector systems are mounted on the 2θ axis. The light blue line shows a high temperature N_2 gas flow device.

Samples are mounted on a five-axis sample stage. The sample can be oscillated around the ω-axis during measurement for obtaining homogeneous intensity distribution of Debye rings. The light green arrow shows the direction of oscillation along ω-axis. A five axis sample stage is used for the automatic sample centering on the ω-axis. A high temperature N_2 gas flow device is used as a heater. Temperature range is from 300 to 1073 K. Temperature is automatically controlled within the range of ±1 K of setting value by the program installed at the beamline. The position of heater is initially away from the sample position. It can be remotely moved to sample position during the experiment.

IP is a two dimensional detector with large dynamic range and high efficiency for detecting hard X-ray. Image signals of diffracted X-ray photons are stored in a photostimulable phosphor layer on IP. The size of IP is 200×400 mm. The camera length is 286.5 mm. Powder diffraction data can be simultaneously collected by 80 ° in 2θ. Fifteen images can be collected by using a mask with 10 mm slit width. Image signals are read out by laser scanning with Fuji BAS2500 by Fuji Film installed outside of the experimental hatch. The step of diffraction angle is 0.01° in the case of readout resolution of 50×50 μm.

MYTHEN is one dimensional semiconductor detector by DECTRIS Ltd. with excellent angular resolution and short readout time. Six modules of MYTHEN were mounted on the 2θ axis. Each module are consisted of 1280 silicon micro-strips with 50 um pitch as an X-ray sensor. Readout time is in the order of milliseconds. The camera length is 477.46 mm. The step of diffraction angle is approximately 0.006 °. Powder diffraction data can be simultaneously collected by 35 ° in a single step mode, which arranges six modules in positive and negative direction of 2θ.

2.7.5 Procedure of *in-situ* SR-PXRD experiment

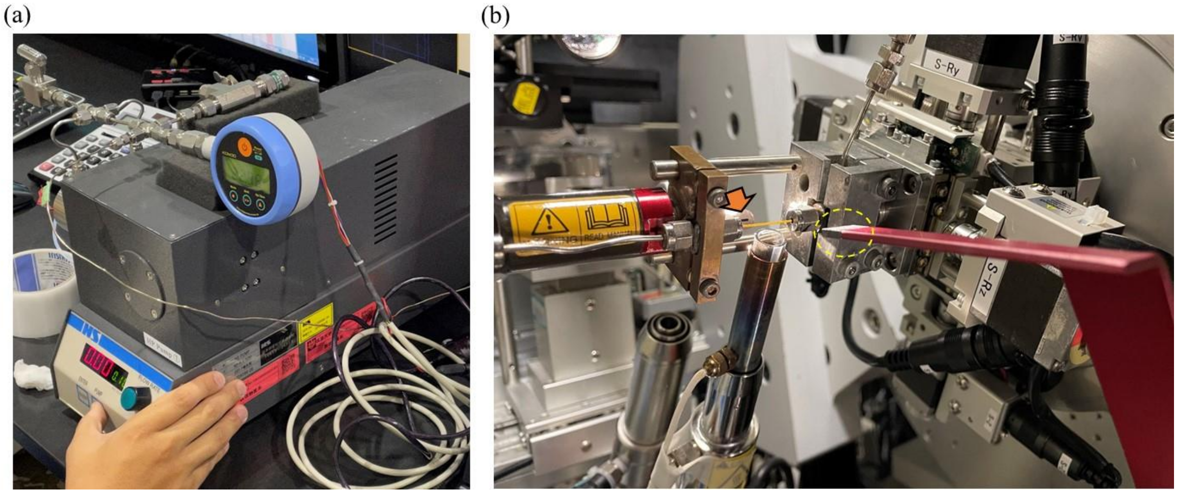

Figure 2.7.17 Experimental apparatus of *in-situ* SR-PXRD measurement. (a) pump section, (b) sample holder.

Figure 2.7.17 shows an experimental apparatus at SPring-8 BL02B2. Figure 2.7.17(a) shows a pump section. A high pressure pump was set outside of the experimental hatch. Figure 2.7.17(b) shows a sample holder fixed on the sample stage of large Debye-Scherrer camera. The orange arrow shows the collimator through which an incident X-ray comes to the sample position. The collimator size was 0.5 × 2.0 mm. The yellow line shows a beam stopper. A stainless steel flexible tube was connected to a sample holder. The other side of tube is connected to the high pressure pump.

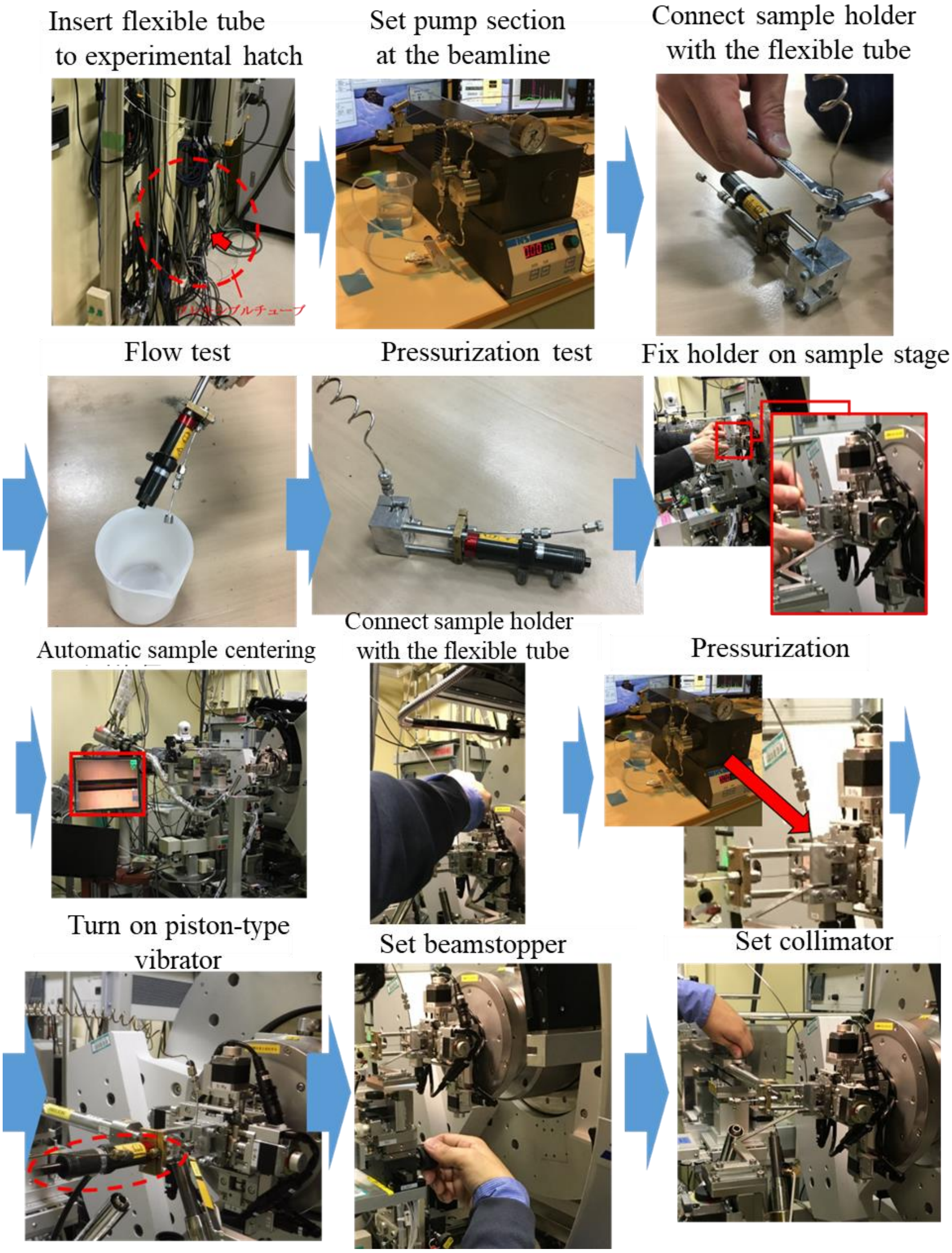

Figure 2.7.18 Procedure of *in-situ* SR-PXRD measurement.

Figure 2.7.18 shows the procedure of *in-situ* SR-PXRD measurement [50]. At first, a stainless steel flexible tube is inserted into an experimental hatch through duct space on the wall. A pump section was set at the beamline. Next, a sample holder is connected with a stainless flexible tube inside of the experimental hatch. The flow test is performed for confirming water flow. The sample holder is sealed with a capping nut. Pressure test is carried out for ensuring no leakage during pressurization. The target pressure is typically 30 MPa. Pressure is released after the test. The connection between the tube and holder and capping nut are removed temporally. Another flexible tube is connected to the sample holder. A sample solution was inserted into a capillary. The sample holder is sealed again for preventing solution from spilling out.

The sample holder is mounted on the sample stage. Automatic centering is carried out by using a program at BL02B2. This ensures the position of capillary kept at the rotation center of ω-axis during oscillation. A flexible tube is connected to the sample holder. Pressure is elevated to target value. A rubber tube is connected to a piston-type vibrator. The vibration is started by air flow from an air compressor. A beam stopper is moved to appropriate position. A collimator is set in the holder. Then experimenters leave the experimental hatch and lock door. Temperature of heater is raised to target value at the beamline. The initial position of heater is away from the sample position. The heater is approached to the sample position by using a program. Measurement is started when the heater is arrived at the sample position.

2.8 Nanoparticle synthesis in supercritical water

Synthesis of nanoparticles in supercritical water were performed by using the developed system as described in section 2.7. Section 2.8.1 shows the synthesis of ZrO_2 nanoparticles. 2.8.2 shows the synthesis of HfO_2 nanoparticles.

2.8.1 ZrO_2

A zirconia nanoparticle is one of the highly functional ceramic materials which exhibit a high strength, a high fracture toughness and a good ionic conductivity [51]. ZrO_2 nanoparticles have been used for wide applications from electrolyte of solid oxide fuel cell to biomaterials such as artificial teeth or hip joint [52].

The functionality of ZrO_2 nanomaterials highly depends on its crystalline phase. The tetragonal phase and monoclinic phase are important crystalline phases for the application of ZrO_2 nanoparticles. The tetragonal and monoclinic phases have the crucial importance for the mechanical properties of ZrO_2 nanomaterials. It is known that degradation of strength of polycrystalline material is due to phase transition from tetragonal to monoclinic phase [53]. A novel composite nanomaterial whose fracture toughness was comparable to a steel was reported by using the tetragonal-to-monoclinic phase transition [5].

Supercritical water has been used for the synthesis of ZrO_2-nanoparticles. Hakuta *et al.* synthesized ultrafine ZrO_2 nanoparticles with the diameter less than 8 nm [54]. Crystalline phases of ZrO_2- nanoparticles were tetragonal phase in high pH condition and monoclinic phase in low pH condition. Becker *et al.* reported the synthesis of ZrO_2 nanoparticles by using zirconium acetate aqueous solution as the precursor [55]. Crystalline phases of ZrO_2 nanoparticles showed the complex dependence on temperature and pressure. The relation between the crystalline phases and synthesis conditions remains unsolved for ZrO_2 nanoparticles.

Zirconium oxynitrate aqueous solution were prepared as a precursor of supercritical hydrothermal synthesis of ZrO_2 nanoparticle. $ZrO(NO_3)_2 \cdot 2H_2O$ by Sigma-Aldrich Co. LLC was dissolved into deionized water. Concentration of aqueous solution was 1.0 mol/L. Synthesis of ZrO_2 nanoparticle was performed for 5 min. Temperature and pressure of the synthesis was 673 K and 30 MPa.

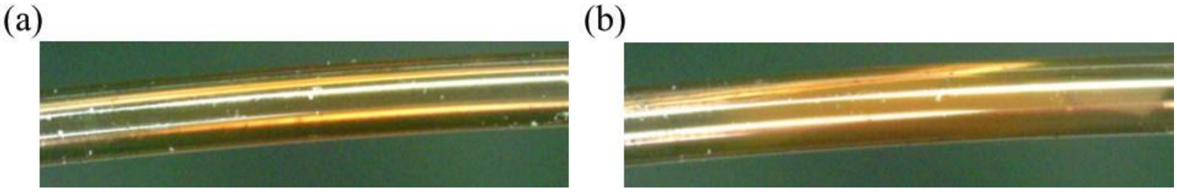

Figure 2.8.1 Synthesis of ZrO_2 nanoparticle in the capillary. (a) before and (b)5 min after start of the synthesis.

Figure 2.8.1 shows the synthesis of ZrO_2 nanoparticles. The capillary with length of 0.5 cm was monitored by the CCD camera. Figure 2.8.1(a) was the picture of capillary before start of measurement. The capillary was filled with precursors. The color was transparent. Figure 2.8.1(b) was the picture of nanoparticles after 5 min from start of synthesis. The color of precursors became white in region with length about 0.4 cm.

2.8.2 HfO_2

Hafnia nanoparticles are the functional materials which exhibits high melting point, high dielectric constant, wide band gap and high chemical stability. They have been mainly used for the dielectric layer of complementary metal oxide semiconductor (CMOS) technology or the capacitor layers in dynamic random access memory [56]. The crystalline phase is also important for the functionality of HfO_2 nanoparticles, since the most of the applications use only tetragonal phase.

Several studies were reported for the synthesis of HfO_2 nanoparticles in supercritical water. Sahraneshin *et al.* reported the synthesis of HfO_2 nanoparticles with uniform size and shape [57], [58]. $HfCl_4$ aqueous solution was used as a precursor. The crystalline phase of HfO_2 nanoparticles was the monoclinic phase. Montes *et al.* reported the synthesis of HfO_2 nanoparticles with the four types of precursors. The crystalline phase of HfO_2 nanoparticles was the monoclinic phases. The relation between crystalline phases and synthesis conditions remains unsolved for HfO_2 nanoparticles.

Hafnium oxychloride aqueous solutions were prepared as a precursor of supercritical hydrothermal synthesis of HfO_2 nanoparticle. $HfOCl_2 \cdot 8H_2O$ by Strem Chemicals, Inc. was dissolved into deionized water. Concentration of aqueous solution was 0.2 mol/L. HfO_2 nanoparticle was synthesized in supercritical water. Temperature was 673 K. Pressure was 30 MPa. Synthesis was performed for 5 min.

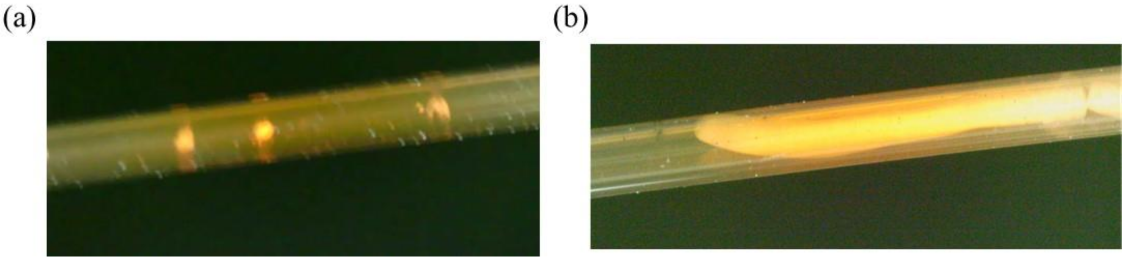

Figure 2.8.2 Synthesis of HfO_2 nanoparticle in the capillary. (a) before and (b) 5 min after start of the synthesis.

Figure 2.8.2 shows synthesis of HfO_2 nanoparticle. The capillary with length of 0.5 cm was monitored by CCD camera. Figure 2.8.2(a) was the picture of capillary before start of measurement. The capillary was filled with precursors. Three white grains were observed in the capillary. Figure 2.8.2(b) was the picture of capillary after 15 min from start of synthesis. The aggregation of particle was observed in the capillary. The length was about 0.3 cm. The width was about 0.04 cm.

2.9 Powder data measured by SR-PXRD experiments

This section describes the powder data measured by SR-PXRD experiments using the developed system. Section 2.9.1 describes the experimental conditions of SR-PXRD experiments. Section 2.9.2 shows the powder diffraction data collected from SR-PXRD experiments.

2.9.1 Experimental conditions of SR-PXRD measurement

This section summarizes the experimental conditions of SR-PXRD measurement. Powder diffraction data were collected from the reaction vessel of empty fused silica capillary. Powder diffraction data were collected from pure water at seven conditions for investigating temperature and pressure dependence of powder profiles of reaction field. This section also shows experimental conditions of SR-PXRD experiment of Ag nanoparticles by Ozawa [29]. *In-situ* SR-PXRD experiment were performed for the synthesis of ZrO_2 nanoparticles and HfO_2 nanoparticles in supercritical water.

2.9.1.1 Fused silica capillary

Powder diffraction data were collected from fused silica capillary. The empty fused silica capillary was mounted on the sample stage. The wavelength was 0.67 Å. The exposure time was 10 min. Samples were oscillated along the ω--axis during measurement. Measurements were carried out at room temperature and 600 K. IP was used as a detector.

2.9.1.2 Water

Powder diffraction data were collected from pure water. The experimental setup was identical to *in-situ* SR-PXRD experiment. Fused silica capillary was filled with deionized water. The wavelength was 0.5 Å. The exposure time was 15 min. Samples were oscillated by 2 ° along the ω-axis during measurement. IP was used as detector. Powder diffraction data of water were collected at seven combinations of temperature and pressure.

Table 2.9.1 List of measurement conditions of experiment for water.

Temperature [K]	Pressure [MPa]	Phase
300	30	Liquid
473		
573		
623		

673	30	Supercritical water
	26	
	23	

Table 2.9.1 shows a list of measurement conditions of experiment. The column shows a temperature, a pressure, and the position on the phase diagram corresponding to temperature and pressure. Seven combinations of temperature and pressure were selected for measurement. Three conditions correspond to supercritical water. For these three, temperature was kept at 673 K. Pressure values were 23 MPa, 26 MPa and 30 MPa. Other four points were liquid phase. Pressure was kept at 30 MPa. Temperature values were 623 K, 573 K, 473 K and 300 K.

2.9.1.3 Ag 10 nm nanosphere.

The powder sample of Ag nanoparticle was prepared for SR-PXRD experiment by Ozawa [29]. A 10 nm Ag nanosphere by Sigma-Aldrich Co. LLC was selected as a sample. The original sample was dispersed in water with concentration of 0.02 mg/mL. This sample dispersing liquid was centrifuged at 1350 rpm for 30 min with MCF 1350 by SAKUMA SEISAKUJO Co., Ltd. The concentrated liquid obtained from centrifugation was inserted into a glass capillary. Brown and purple colored solid particles were observed on the tip of capillary after leaving it in the fridge for more than a week. Capillary was sealed after removing unnecessary dispersing liquid. Powder diffraction data were collected at SPring-8 BL02B2. The wavelength was 0.5 Å. The exposure time was 60 min. Temperature was 100 K. IP was used as a detector.

2.9.1.4 ZrO_2

Table 2.9.2 List of measurement conditions of *in-situ* SR-PXRD measurement.

Temperature [K]	Pressure [MPa]	Phase
623	33	Liquid
	30	
	26	
	23	
648	33	Supercritical water
	30	
	23	
655	30	
673	33	
	30	
	26	
	23	
	20	Gas

Table 2.9.2 shows a list of measurement conditions of *in-situ* SR-PXRD measurement of synthesis of ZrO_2 nanoparticle in supercritical water. The column shows temperature, pressure and the position on the phase diagram

of water corresponding to combination of temperature and pressure. Thirteen conditions were selected for measurement. One condition was gas phase. Three conditions were liquid phase. Nine conditions were supercritical water. A Part of the powder diffraction data were collected by IP. Other data were collected by the single-step mode of multiple MYTHEN detectors system. Samples were oscillated by 2 ° along the ω-axis during measurement. The exposure time for collecting one frame of powder diffraction data were 5 min for IP and 20 s for MYTHEN detector system. Powder diffraction data were collected at room temperature after *in-situ* SR-PXRD experiment at 673 K and 30 MPa. Exposure time was 5 min. Other measurement conditions were identical to *in-situ* SR-PXRD experiment.

2.9.1.5 HfO_2

In-situ SR-PXRD measurement of synthesis of HfO_2 nanoparticles in supercritical water was performed at SPring-8 BL02B2. The powder diffraction data were collected at 673 K and 30 MPa. The wavelength was 0.50947 Å. Flat Panel Detector was used for measurement. The exposure time of one frame was 5 min. Samples were oscillated by 2 ° along the ω-axis during measurement. The measurement was carried out by 30 min.

2.9.2 Powder diffraction data

2.9.2.1 Fused silica capillary

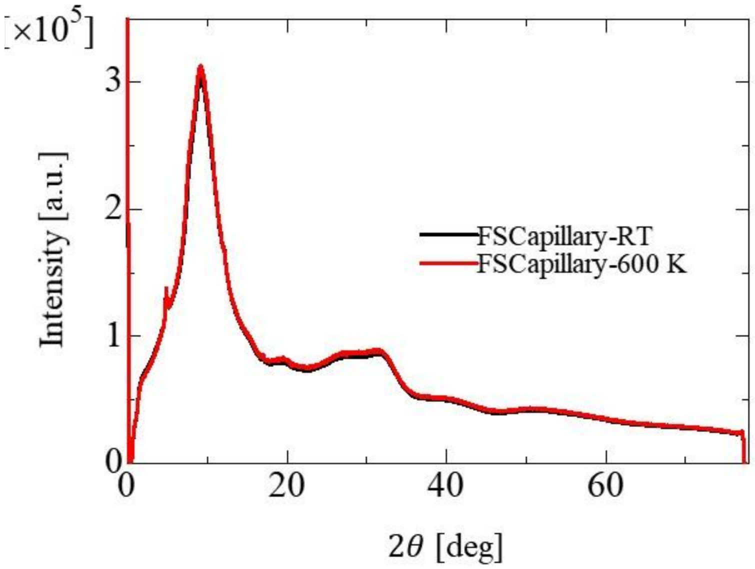

Figure 2.9.1 Powder diffraction data of empty fused silica capillary.

Figure 2.9.1 shows the powder diffraction data of empty fused silica capillary. The diffraction angle from 0 ° to 72 ° is shown. The black line shows the powder diffraction data at room temperature. The red line shows the data at 600 K. Bragg peaks were observed at 4.7 °and 12.03 °.

2.9.2.2 Water

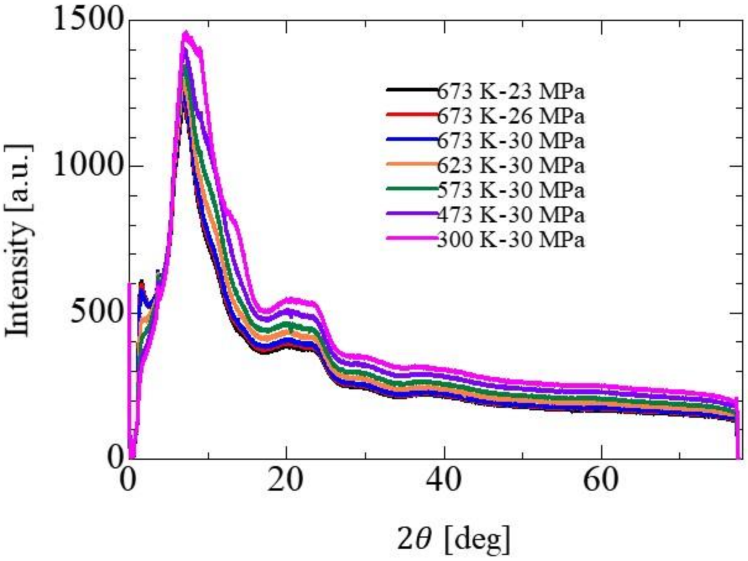

Figure 2.9.2 Powder diffraction data of water from 0 ° to 72 °.

Figure 2.9.2 shows powder diffraction data of water. The diffraction angle from 0 ° to 72 ° is shown. All of powder diffraction data showed a peak around 6.5 °. Powder diffraction data at 300 K and 30 MPa showed the second peak around 13.5 °.

2.9.2.3 Ag 10 nm nanosphere

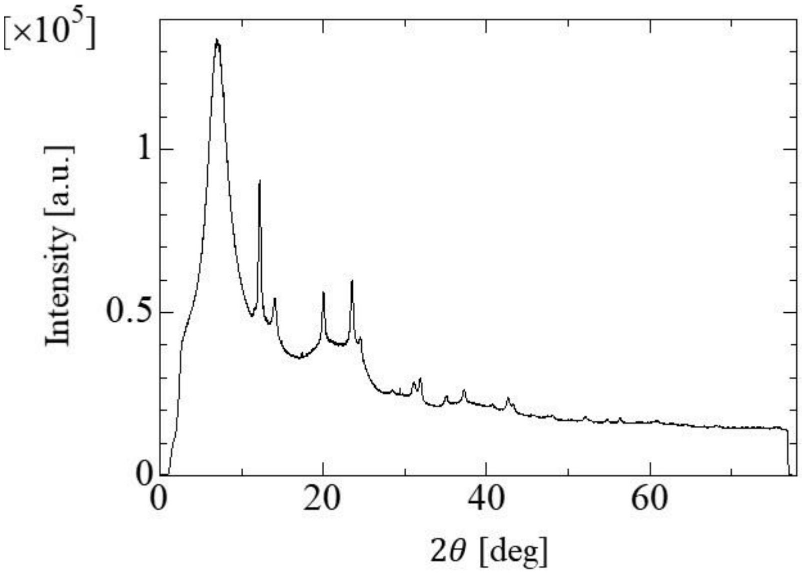

Figure 2.9.3 Powder diffraction data of Ag nanoparticles from 0 ° to 72 °.

Figure 2.9.3 shows powder diffraction data of Ag nanoparticle collected by Ozawa [29]. The diffraction angle from 0 ° to 72 ° is shown. Bragg peaks were observed from 10 ° to 60 °.

2.9.2.4 ZrO_2

(a)

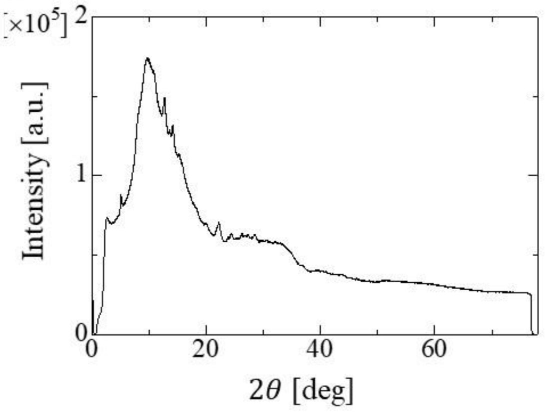

(b)

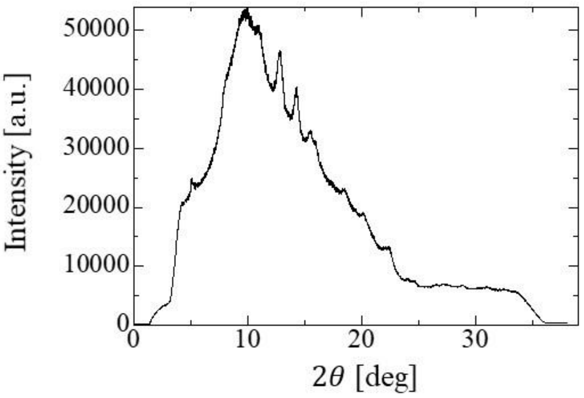

(c)

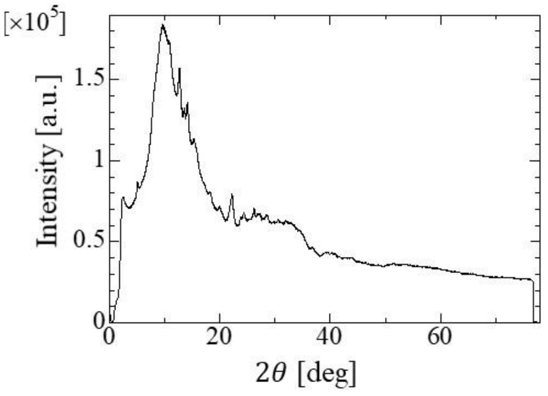

(d)

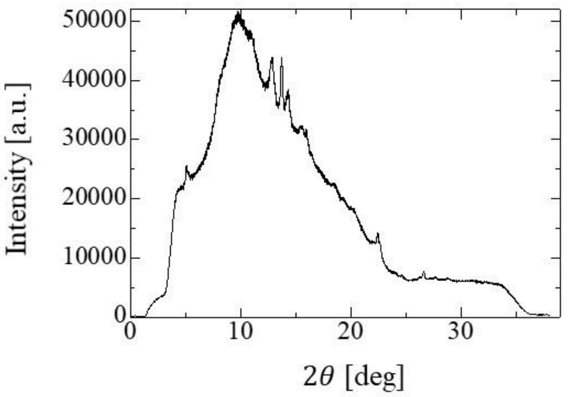

(e)

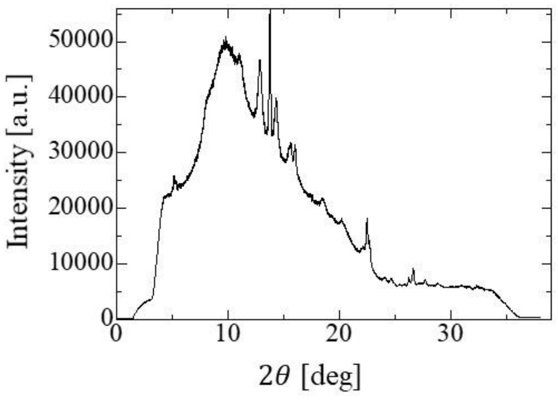

(f)

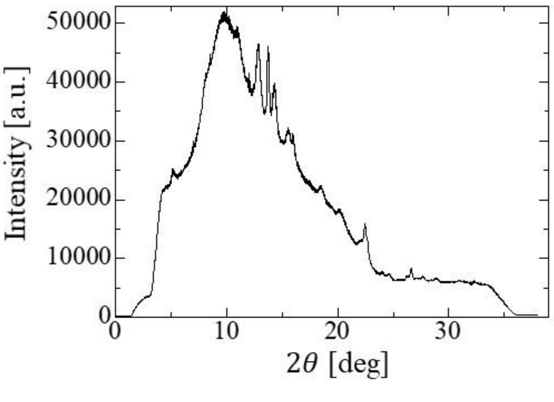

(g)

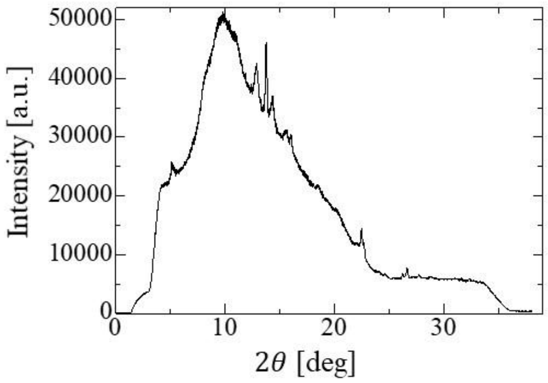
Intensity [a.u.]
50000
40000
30000
20000
10000
0
0
10
20
30
2θ [deg]

(h)

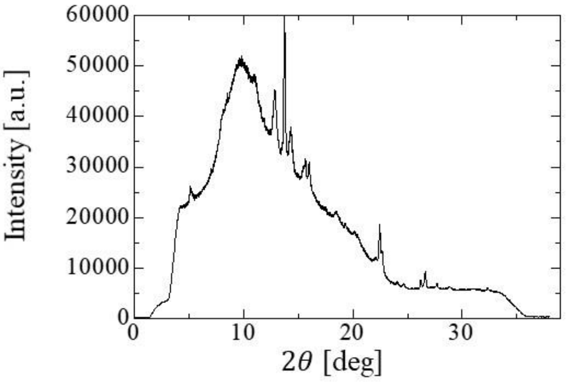
Intensity [a.u.]
60000
50000
40000
30000
20000
10000
0
0
10
20
30
2θ [deg]

(i)

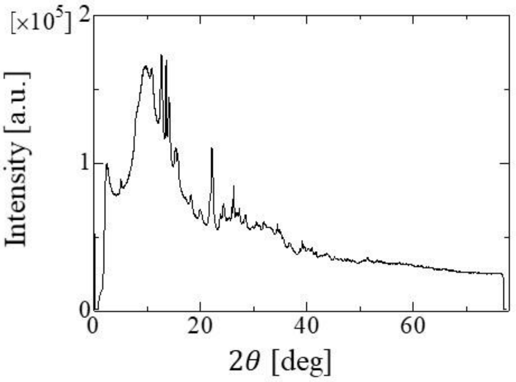
[×10^5] 2
Intensity [a.u.]
1
0
0
20
40
60
2θ [deg]

(j)

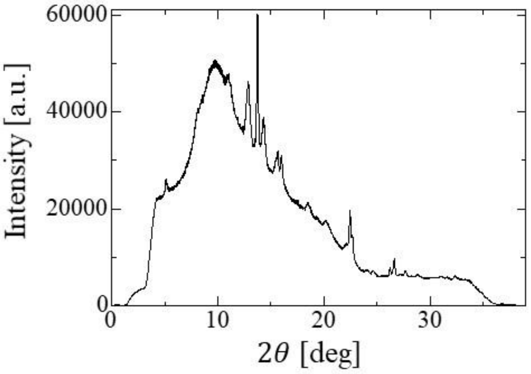
Intensity [a.u.]
60000
40000
20000
0
0
10
20
30
2θ [deg]

(k)

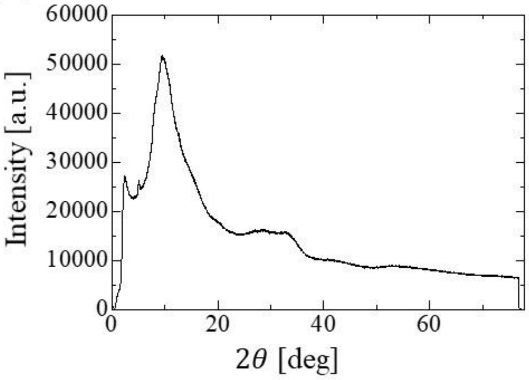
Intensity [a.u.]
60000
50000
40000
30000
20000
10000
0
0
20
40
60
2θ [deg]

(l)

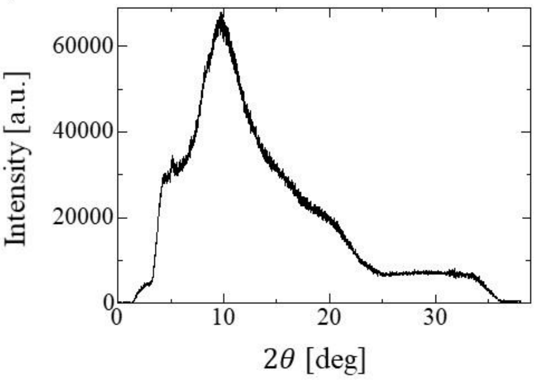
Intensity [a.u.]
60000
40000
20000
0
0
10
20
30
2θ [deg]

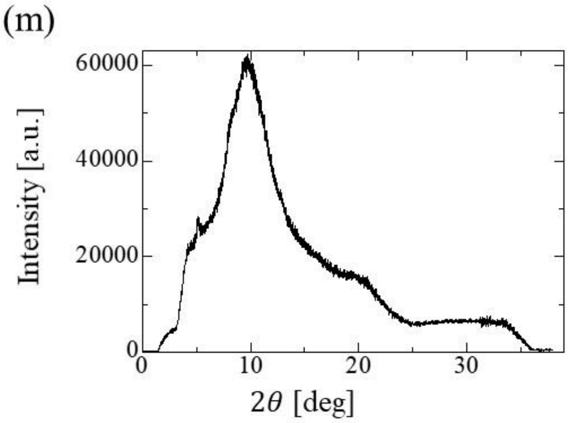

Figure 2.9.4 Powder diffraction data of ZrO_2 nanoparticles. (a) 623 K and 33 MPa, (b) 623 K and 30 MPa, (c) 623 K and 26 MPa, (d) 623 K and 23 MPa, (e) 648 K and 23 MPa, (f) 648 K and 30 MPa, (g) 648 K and 33 MPa, (h) 655 K and 30 MPa, (i) 673 K and 33 MPa, (j) 673 K and 33 MPa, (k) 673 K and 26 MPa, (l) 673 K and 23 MPa, (m) 673 K and 20 MPa.

Figure 2.9.5 shows the powder diffraction data measured at thirteen conditions. Last frame of *in-situ* SR-PXRD experiment were shown as representative. Figure 2.9.5(a) shows diffraction data at 623 K and 33 MPa. Bragg peaks were observed from 10 ° to 30 °. Figure 2.9.5(b) shows diffraction data at 623 K and 30 MPa. Bragg peaks were observed from 10 ° to 30 °. Figure 2.9.5(c) shows diffraction data at 623 K and 26 MPa. Bragg peaks were observed from 10 ° to 30 °. Figure 2.9.5(d) shows diffraction data at 623 K and 23 MPa. Bragg peaks were observed from 10 ° to 30 °. Figure 2.9.5(e) shows diffraction data at 648 K and 23 MPa. Bragg peaks were observed from 10 ° to 30 °. Figure 2.9.5(f) shows diffraction data at 648 K and 30 MPa. Bragg peaks were observed from 10 ° to 30 °.

Figure 2.9.5(g) shows diffraction data at 648 K and 33 MPa. Bragg peaks were observed from 10 ° to 30 °. Figure 2.9.5(h) shows diffraction data at 655 K and 30 MPa. Bragg peaks were observed from 10 ° to 30 °. Figure 2.9.5(i) shows diffraction data at 673 K and 30 MPa. Bragg peaks were observed from 10 ° to 30 °. Figure 2.9.5(j) shows diffraction data at 673 K and 33 MPa. Bragg peaks were observed from 10 ° to 30 °. Figure 2.9.5(k) shows diffraction data at 673 K and 26 MPa. Bragg peaks were not observed in the powder diffraction data. Figure 2.9.5(l) shows diffraction data at 673 K and 23 MPa. Bragg peaks were not observed in the powder diffraction data. Figure 2.9.5(m) shows diffraction data at 673 K and 20 MPa. Bragg peaks were not observed in the powder diffraction data.

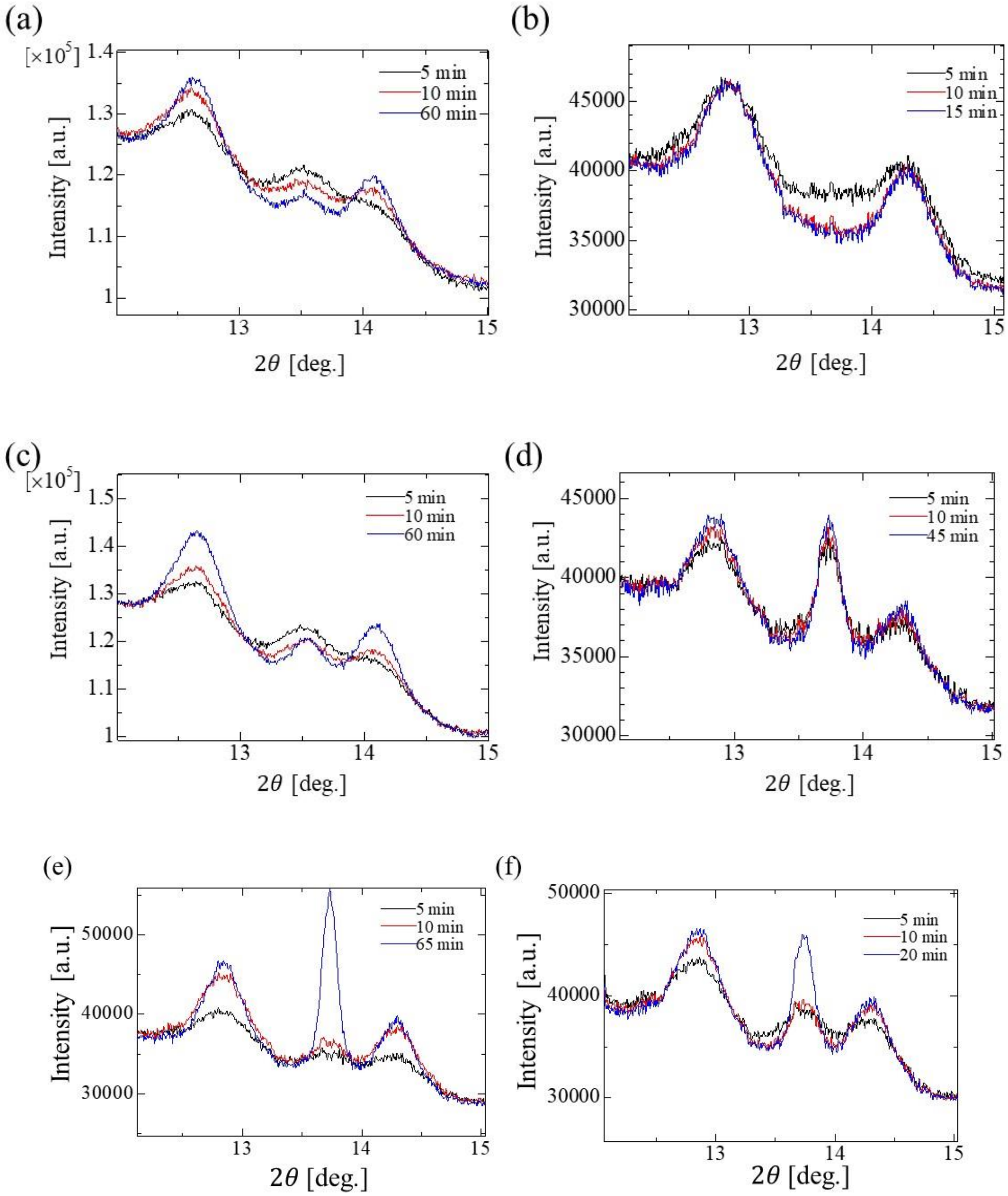
(a)
[×10^5]
1.4
1.3
1.2
1.1
1
Intensity [a.u.]
5 min
10 min
60 min
13
14
15
2θ [deg.]
(b)
45000
40000
35000
30000
Intensity [a.u.]
5 min
10 min
15 min
13
14
15
2θ [deg.]
(c)
[×10^5]
1.5
1.4
1.3
1.2
1.1
1
Intensity [a.u.]
5 min
10 min
60 min
13
14
15
2θ [deg.]
(d)
45000
40000
35000
30000
Intensity [a.u.]
5 min
10 min
45 min
13
14
15
2θ [deg.]
(e)
50000
40000
30000
Intensity [a.u.]
5 min
10 min
65 min
13
14
15
2θ [deg.]
(f)
50000
40000
30000
Intensity [a.u.]
5 min
10 min
20 min
13
14
15
2θ [deg.]

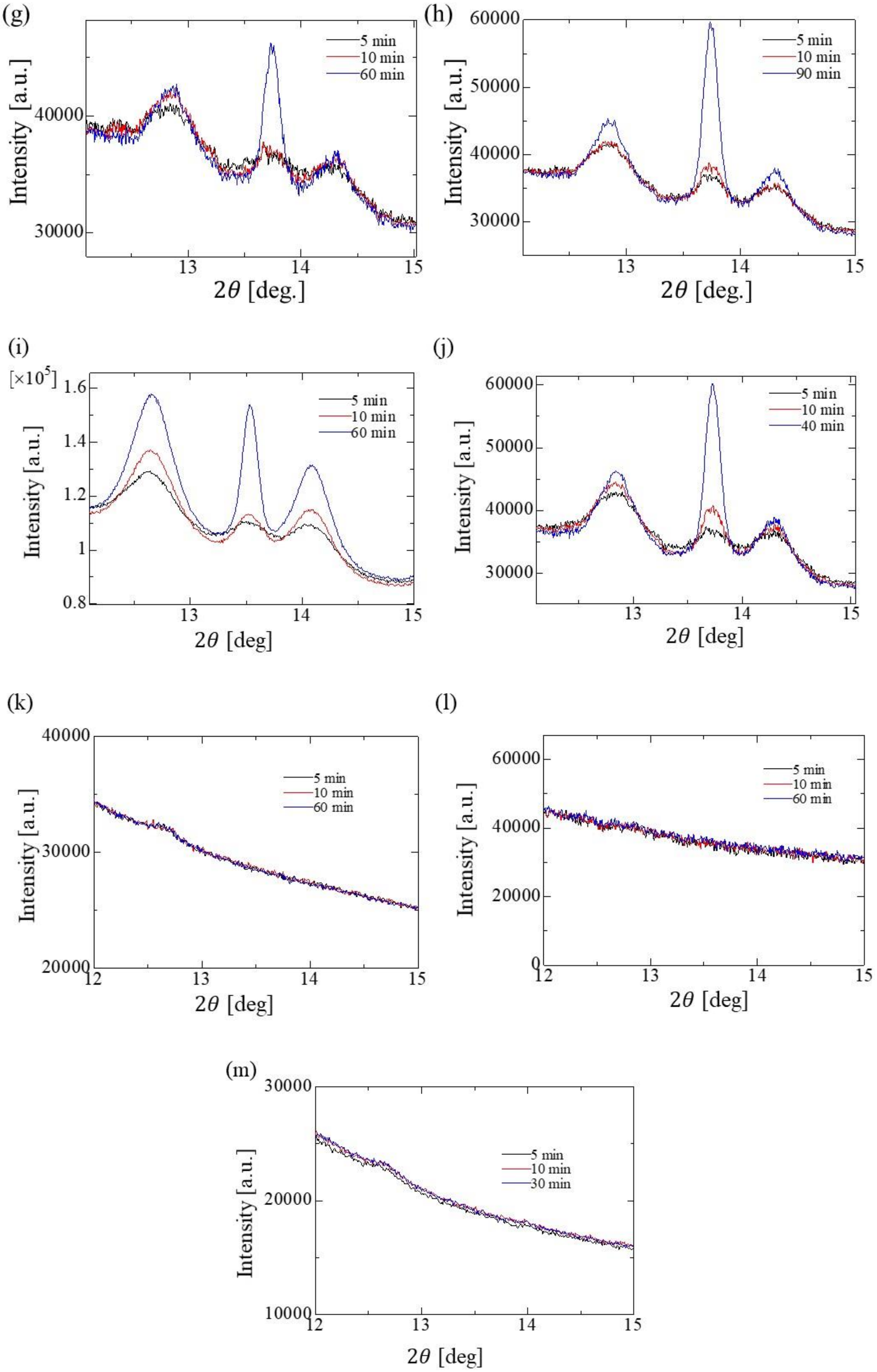

Figure 2.9.5 Powder diffraction data of ZrO_2 nanoparticles. The diffraction angle from 12 ° to 15 ° of a

frame at 5min and at 10min, and at the last frame was shown. (a) 623 K and 33 MPa, (b) 623 K and 30 MPa, (c) 623 K and 26 MPa, (d) 623 K and 23 MPa, (e) 648 K and 23 MPa, (f) 648 K and 30 MPa, (g) 648 K and 33 MPa, (h) 655 K and 30 MPa, (i) 673 K and 33 MPa, (j) 673 K and 33 MPa, (k) 673 K and 26 MPa, (l) 673 K and 23 MPa, (m) 673 K and 20 MPa.

Figure 2.9.5 shows the powder diffraction data measured at thirteen conditions. The diffraction angle from 12 ° to 15 ° is shown. Time dependence of intensity in presented by three lines. Black line shows a frame at 5 min. Red line shows a frame at 10 min. Blue line shows last frame. Figure 2.9.5(a) shows diffraction data at 623 K and 33 MPa. Bragg peaks were observed at 12.8 ° and 13.5 °at 5 min. The intensity at 12.8 ° has increased by 50000 from 5 to 60 min. The intensity at 13.5 ° has decreased by 40000 from 5 to 60 min. Figure 2.9.5(b) shows diffraction data at 623 K and 30 MPa. Bragg peaks were observed at 12.8 ° at 5 min. The intensity change at 12.8 ° was less than 1000 from 5 to 15 min. The intensity at 13.5 ° has decreased by 3000 from 5 to 15 min. Figure 2.9.5(c) shows diffraction data at 623 K and 26 MPa. Bragg peaks were observed at 12.8 ° and 13.5 ° at 5 min. The intensity at 12.8 ° has decreased by 100000 from 5 to 60 min. The intensity at 13.5 ° has decreased by 3000 from 5 to 60 min.

Figure 2.9.5(d) shows diffraction data at 623 K and 23 MPa. Bragg peaks were observed at 12.8 ° and 13.5 ° at 5 min. The intensity at 12.8 ° has increased by 2000 from 5 to 45 min. The intensity at 13.5 ° has increased by 2000 from 5 to 45 min. Figure 2.9.5(e) shows diffraction data at 648 K and 23 MPa. Bragg peaks were observed at 12.8 ° and 13.5 ° at 5 min. The intensity at 12.8 ° has increased by 7000 from 5 to 65 min. The intensity at 13.5 ° has increased by 20000 from 5 to 65 min. Figure 2.9.5(f) shows diffraction data at 648 K and 30 MPa. Bragg peaks were observed at 12.8 ° and 13.5 ° at 5 min. The intensity at 12.8 ° has increased by 4000 from 5 to 20 min. The intensity at 13.5 ° has increased by 6000 from 5 to 20 min.

Figure 2.9.5(g) shows diffraction data at 648 K and 33 MPa. Bragg peaks were observed at 12.8 ° and 13.5 ° at 5 min. The intensity at 12.8 ° has increased by 2000 from 5 to 60 min. The intensity at 13.5 ° has increased by 8000 from 5 to 60 min. Figure 2.9.5(h) shows diffraction data at 655 K and 30 MPa. Bragg peaks were observed at 12.8 ° and 13.5 ° at 5 min. The intensity at 12.8 ° has increased by 4000 from 5 to 90 min. The intensity at 13.5 ° has increased by 20000 from 5 to 90 min.

Figure 2.9.5(i) shows diffraction data at 673 K and 30 MPa. Bragg peaks were observed at 12.8 ° and 13.5 ° at 5 min. The intensity at 12.8 ° has increased by 25000 from 5 to 60 min. The intensity at 13.5 ° has increased by 48000 from 5 to 60 min. Figure 2.9.5(j) shows diffraction data at 673 K and 33 MPa. Bragg peaks were observed at 12.8 ° and 13.5 ° at 5 min. The intensity at 12.8 ° has increased by 4000 from 5 to 40 min. The intensity at 13.5 ° has increased by 20000 from 5 to 40 min.

Figure 2.9.5(k) shows diffraction data at 673 K and 26 MPa. Bragg peaks were not observed at 5 min. The intensity was not changed from 5 to 30 min. Figure 2.9.5(l) shows diffraction data at 673 K and 23 MPa. Bragg peaks were not observed at 5 min. The intensity was not changed from 5 to 30 min. Figure 2.9.5(m) shows diffraction data at 673 K and 20 MPa. Bragg peaks were not observed at 5 min. The intensity was not changed from 5 to 30 min.

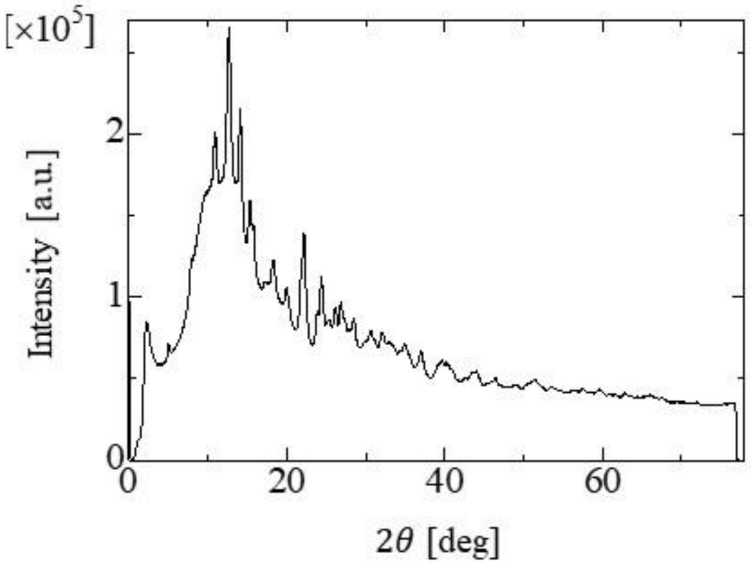

Figure 2.9.6 powder diffraction data of ZrO_2 nanoparticles at room temperature.

Figure 2.9.6 shows powder diffraction data of ZrO_2 nanoparticle at room temperature. The diffraction angle from 0 ° to 72 ° is shown. Diffraction data were collected after *in-situ* experiment at 673 K and 30 MPa. Pressure was kept at 30 MPa during measurement. Bragg peaks were observed from 10 ° to 72 °.

2.9.2.5 HfO_2

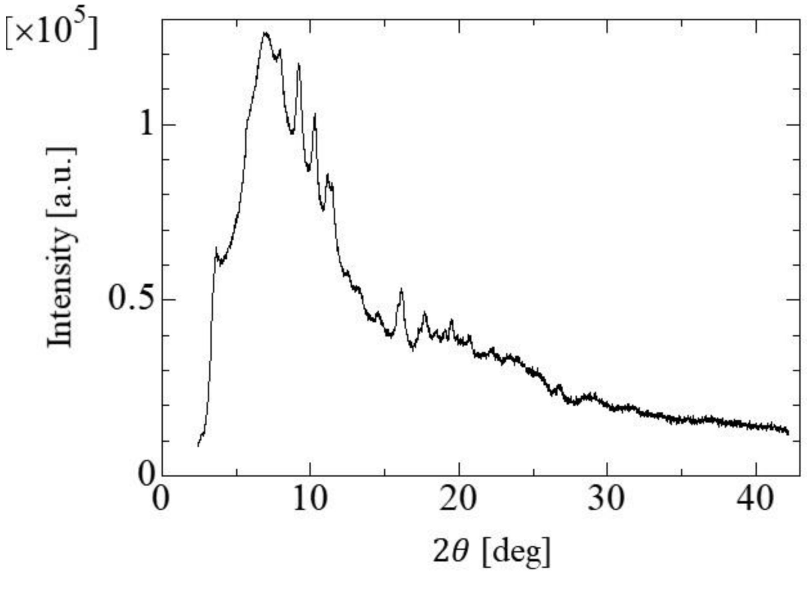

Figure 2.9.7 Powder diffraction data of HfO_2 nanoparticles.

Figure 2.9.7 shows the powder diffraction data of HfO_2 nanoparticle measured at *in-situ* SR-PXRD measurement. The diffraction angle from 0 ° to 43 ° is shown. Data were collected from 5 to 10 min of synthesis at 673 K and 30 MPa. Bragg peaks were observed from 7 ° to 30 °.

2.10 Summary

We developed the *in-situ* SR-PXRD measurement system of the nanoparticle synthesis for investigating the mechanism of the structure control of nanoparticles in supercritical water. The developed system was designed for the *in-situ* experiment at the powder diffraction beamline BL02B2 at large SR facility SPring-8. The system was composed of the sample holder, pump section and heater installed at BL02B2. The synthesis of ZrO_2 and HfO_2 nanoparticles were performed by using the system. *In-situ* SR-PXRD experiments were carried out for the nanoparticle synthesis in supercritical water at SPring-8 BL02B2. Powder diffraction data were collected from synthesized ZrO_2 nanoparticles in thirteen conditions. Powder diffraction data were also collected from the empty fused silica capillary, pure water, Ag and HfO_2 nanoparticles.

3. Development of analysis method of powder diffraction data of nanoparticle in supercritical water

3.1 Necessity of the development of the analysis method

Powder diffraction data can be used for the structure analysis of the powder sample. There are several difficulties to investigate the structure of nanoparticles from the powder diffraction data of *in-situ* SR-PXRD experiment. The diffraction of capillary and supercritical water has to be subtracted for extracting diffraction of nanoparticles from the powder diffraction data. The diffraction profiles can be shifted or broadened by small size or lattice defect of nanoparticles. We developed a method to analyze the powder diffraction data of nanoparticles in the reaction vessel. The powder profiles of capillary and supercritical water were determined for extracting diffraction of nanoparticles. The powder profiles of nanoparticles were modelled by Debye Scattering Equation (DSE).

Section 3.2 shows the principle of PXRD. Section 3.3 explains the analysis methods of the powder diffraction data. Section 3.4 describes the analysis of the powder diffraction data of nanoparticles in the reaction vessel. Section 3.5 shows the analytical representation of powder profiles of fused silica capillary and supercritical water. Section 3.6 shows the analysis of powder diffraction data of nanoparticles in reaction vessel. At first, the powder diffraction data were analyzed by Rietveld refinement. The deviations were found between powder diffraction data and powder profiles of Rietveld refinement. The effect of the size and lattice defects of nanoparticles to the powder profile were systematically studied for improving the expression of powder profiles for powder data. DSE was used for the analysis. Powder diffraction data were analyzed by powder profiles calculated by DSE. Section 3.7 summarizes the results.

3.2 Principle of the powder X-ray diffraction

The powder X-ray diffraction method can be used for the structure analysis of the powder sample. The powder diffraction data contains the structural information of the large number of crystals in the powder sample. Atomic species, lattice parameters, positions or thermal motion of atoms can be obtained from the powder diffraction data.

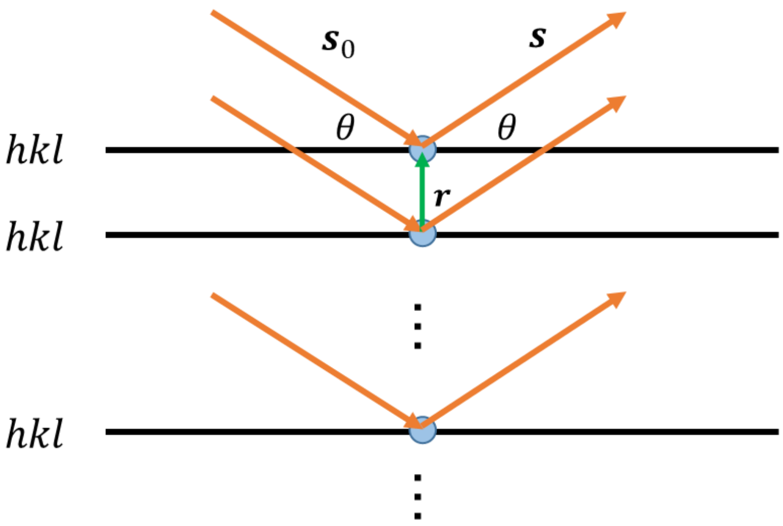

Figure 3.2.1 Schematic of the diffraction from one crystal.

Figure 3.2.1 shows the schematic of diffraction from one crystal. Spheres are atoms. Lines show lattice planes perpendicular to the *hkl* direction with interplanar spacing d_{hkl}. For convenience, it is assumed that incident beams are completely monochromatic and atomic arrangements on all the planes are identical. When this crystal is exposed to the incident X-ray beam, the diffracted beam is radiated from atoms. $\boldsymbol{s}_0$ and $\boldsymbol{s}$ show unit vectors for the direction of propagation of incident and diffracted X-ray waves. $\boldsymbol{r}$ shows the difference vector of the position of two atoms on neighboring lattice planes. The difference of the path length between these diffracted waves from two atoms is expressed as follows:

$$(\boldsymbol{s} - \boldsymbol{s}_0) \cdot \boldsymbol{r} = 2d_{hkl} \sin\theta \tag{3.1}$$

θ is the diffraction angle. When the difference of the path length matches the wavelength of X-ray, waves from two lattice planes become in phase. This also means waves from all the lattice planes are in phase, resulting in strong diffracted X-ray beam at certain diffraction angle $2\theta_{\mathrm{hkl}}$. This condition is expressed as follows.

$$\lambda = 2d_{hkl} \sin\theta_{hkl} \tag{3.2}$$

λ is the wavelength of X-ray. d_{hkl} is the interplanar spacing between two lattice planes. This equation is called Bragg's law. $2\theta_{\mathrm{hkl}}$ is called Bragg angle.

In powder diffraction experiment, Debye rings are observed from the powder sample. The schematic of PXRD experiment were shown in Figure 2.5.1. In powder diffraction method, it is assumed that a large number of crystals are oriented to all the directions in space with equal probability. The powder diffraction data are obtained by integrating the intensity of Debye rings which was radiated from all the crystals whose orientation satisfied the Bragg's law.

The structure parameters of crystals can be determined by the analysis of the powder diffraction data. The average value of interplanar spacing d_{hkl} can be estimated from the Bragg angle by Equation (3.2). The lattice parameter of the unit cell of structure can be determined by set of interplanar spacing. The integrated intensity of each Bragg peak is proportional to the following values:

$$m_{hkl}|F_{hkl}|^2(\mathrm{LP})\mathrm{e}^{-2M} \tag{3.3}$$

m_{hkl} is the multiplicity factor of Miller index *hkl*. e^{-2M} is called as temperature factor where $M = B \sin^2\theta/\lambda^2$. B is proportional to the average of the square of thermal displacement of an atom from its equilibrium position. F_{hkl} is called the structure factor of crystal, which is expressed as follows:

$$F_{hkl} = \sum_i f_i \exp\bigl(2\pi i(hx_i + ky_i + lz_i)\bigr) \tag{3.4}$$

x, y, z are the fractional coordinates of atoms in the unit cell. f is the atomic scattering factor of each atom. LP is the factor called Lorentz-Polarization factor. The Lorentz-Polarization factor is a combination of Lorentz factor and Polarization factor. The Lorentz factor is expressed as the product of three factors: the factor about the time of collecting Bragg peak from a crystal proportional to $(\sin 2\theta)^{-1}$, the effect of the number of the crystals contributing to the *hkl* reflection proportional to $\cos\theta$ and the effect of the length of Debye ring measured in the experiment proportional to $(\sin 2\theta)^{-1}$. Then the Lorentz factor is proportional to $(\sin\theta \sin 2\theta)^{-1}$.

The polarization factor corrects the angular dependence of intensity due to the polarization of the incident and diffracted beam. This depends on direction of polarization of the incident and diffracted beam at the observation point. The polarization factor is proportional to $1 + \cos^2 2\theta$ for the unpolarized incident and the diffracted beam. The Lorentz-Polarization factor with the unpolarized X-ray beam is expressed as follows:

$$\frac{1+\cos^2 2\theta}{\sin\theta\sin 2\theta} \tag{3.5}$$

In the SR-PXRD experiment, SR is linearly polarized and the diffracted beam is often collected in the direction perpendicular to the polarization of the incident beam. In this case, the directions of the polarization of the incident and the diffracted beam are always parallel. The polarization factor becomes unity for all the diffraction angles. Lorentz-Polarization factor in SR-PXRD experiment is expressed as follows:

$$\frac{1}{\sin\theta\sin 2\theta} \tag{3.6}$$

3.3 Analysis methods of the powder diffraction data

3.3.1 Rietveld refinement

Rietveld refinement is a method to calculate powder profiles from the structure models of crystals [59]. It is assumed that the powder sample is composed of bulk crystals which have a sufficiently large number of the lattice planes. The structure model of crystal is represented as a unit cell which represents the average structure of the crystal. The parameters of the structure models are refined for experimental powder diffraction data by the nonlinear least square method. Examples of the parameters of a structure model are lattice constants, fractional coordinates of atoms and temperature factors of atoms. The difference between powder diffraction data and calculated powder profiles is expressed as follows:

$$\sum_{i=1}^{N} w_i\{y_{\mathrm{obs},i} - y_{\mathrm{cal},i}\}^2 \tag{3.7}$$

$y_{\mathrm{obs},i}$ is a count of the powder diffraction data at each 2θ position. $y_{\mathrm{cal},i}$ is a count of the sum of calculated powder profiles at each 2θ position. w_i is a weighting parameter. Sum in the equation is taken for all the 2θ positions.

In Rietveld refinement, powder profiles are calculated as the sum of Bragg peaks and background. The background is calculated from the twelfth order polynomial function of the diffraction angle. The simplest case is the flat background which uses only a constant term of polynomial function. The flat background simply adds constant values of intensity in each 2θ position. The diffraction profiles of Bragg peaks are calculated from the structure model of crystal. Integrated intensity of Bragg peak is calculated by following equation:

$$I_{\mathrm{calc}} = s m_{hkl} F_{\mathrm{calc},hkl}^2 (\mathrm{LP}) \mathrm{e}^{-2M} \tag{3.8}$$

I_{calc} is the calculated integrated intensity. s is scale factor between the observed and calculated integrated intensity. F_{calc} is the structure factor of crystal calculated from the structure model.

In Rietveld refinement, the powder profile is calculated as the sum of the diffraction profiles. The profile function is assumed for the calculation of the diffraction profile. The parameters of the profile function are refined for Bragg peak by the nonlinear least square fitting. Two examples of the profile functions are the split-type pseudo-Voigt function (SPV) and the split-type PearsonⅦ function (SPVII) [60]. For example, SPV is expressed as follows:

$$f_{\mathrm{SPV}}(2\theta) = \frac{(1+A)c}{\eta + (1+\eta)(\pi \ln 2)^{0.5} + Ac} \tag{3.9}$$
$$* \left\{ \eta \frac{2}{\pi W} \left[1 + \left(\frac{1+A}{A} \right)^2 \left(\frac{2\theta - 2\theta_0}{W} \right)^2 \right]^{-1} + (1-\eta) \left(\frac{2}{W} \right) \left(\frac{\ln 2}{\pi} \right)^{0.5} \right.$$
$$\left. * \exp \left[- \left(\frac{1+A}{A} \right)^2 \ln 2 \left(\frac{2\theta - 2\theta_0}{W} \right)^2 \right] \right\}$$

where $c = [\eta + (1-\eta)(\pi \ln 2)^{0.5}]$. $2\theta_0$ is the peak position of the diffraction profile. W is the full width of half maximum (FWHM) of the diffraction profile. A is the profile asymmetry parameter. The pseudo-Voigt function is expressed as the linear combination of Lorentzian and Gaussian functions. η parameter represents the mixture of Lorentzian and Gaussian components of the diffraction profile. SPVII is expressed as follows:

$$f_{\mathrm{SP7}}(2\theta) = \frac{2(1+A)}{\pi^{1/2} \left[A \frac{\Gamma(R_l - 0.5)}{(2^{1/R_l} - 1)^{0.5} \Gamma(R_l)} + \frac{\Gamma(R_h - 0.5)}{(2^{1/R_h} - 1)^{0.5} \Gamma(R_h)} \right] W} \tag{3.10}$$
$$* \left\{ 1 + \left(\frac{1+A}{A} \right)^2 \left(2^{1/R_l} - 1 \right) \left(\frac{2\theta - 2\theta_0}{W} \right)^2 \right\}^{-R_l}$$

$2\theta_0$ is the position of profile. W is the FWHM of the diffraction profile. A is the profile asymmetry parameter. R_l and R_h are the decay rates of the profile intensity at the lower side and the higher side of the position of profile. The expression at the higher side of Bragg angle is obtained by replacing the R_l with R_h, R_h with R_l, A with $1/A$ and $1/A$ with A in equation (3.10).

The width of Bragg peaks shows an angular dependence due to several factors such as the energy resolution of an incident X-ray or the dispersion of lattice constants. In Rietveld refinement, the angular dependence of FWHM is expressed by the following equation:

$$\mathrm{FWHM} = (w + v \tan\theta + u \tan^2\theta)^{0.5} \tag{3.11}$$

The agreement between the counts of powder diffraction data and the calculated powder profiles is expressed as the reliability factor R_{wp};

$$R_{wp} = \left\{ \frac{\sum_{i=1}^{N} w_i \left[y_{\mathrm{obs,i}} - y_{\mathrm{calc,i}} \right]^2}{\sum_{i=1}^{N} w_i y_{\mathrm{obs,i}}^2} \right\}^{0.5} \tag{3.12}$$

$w_i = 1/y_{\mathrm{obs,i}}$ $w_i = 1/y_{obs,\ i}$ is the weighting factor. The agreement between the integrated intensity of powder diffraction data and the calculated powder profiles is expressed as reliability factor R_I:

$$R_{\mathrm{I}} = \frac{\sum_{j=1}^{M} \left| I_{\mathrm{obs,j}} - I_{\mathrm{calc},j} \right|}{\sum_{j=1}^{M} I_{\mathrm{obs,j}}} \tag{3.13}$$

The program synchrotron powder was used for the Rietveld refinement of the powder diffraction data [61]. SPV was used as the profile function. The flat background was used for the analysis. The scale factor, the lattice constants and the parameter w of the peak width function were optimized in the refinement. The parameter η of the profile function, the parameter v and u of the peak width function, and temperature factor of each atom were carefully selected in the analysis.

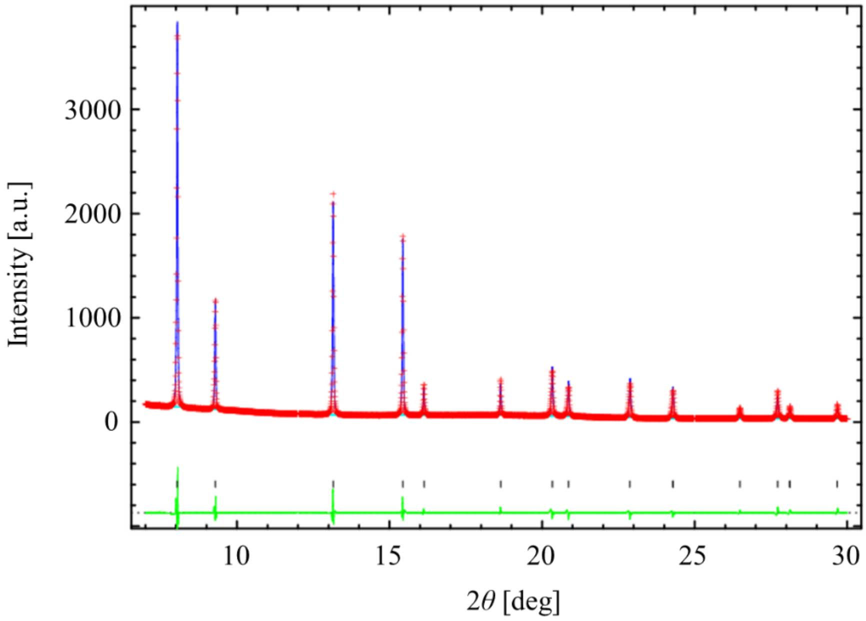

Figure 3.3.1 Example of the result of Rietveld refinement.

Figure 3.3.1 shows the example of the result of Rietveld refinement. The horizontal axis is the diffraction angle. The vertical axis is intensity. Red dots are the powder diffraction data. A blue line is the calculated powder profile of Rietveld refinement. A sky blue line is the background. A green line is the difference between the intensity of the powder diffraction data and the calculated powder profile. Small black vertical lines show the positions of the diffraction profile by Rietveld refinement. The intensity of the powder diffraction data and calculated powder profiles are divided by 100.

3.3.2 Debye Scattering Equation

DSE is the equation for calculating the powder profiles directly from the atomic arrangement of the crystal in the powder sample. The calculation of the powder profile is carried out without assuming a profile function. The structure model of atomic cluster is required instead of the average structure model in Rietveld refinement. The intensity of the powder profile is calculated as the sum of diffraction from all the pairs of atoms in the structure model. The intensity of the diffracted beam from the structure model of an atomic cluster is expressed by multiplying the sum of the amplitude of diffracted X-ray waves from all the atoms in an atomic cluster with its complex conjugate:

$$\begin{aligned} I_{eu} &= \sum_m f_m e^{\frac{2\pi i}{\lambda}(\boldsymbol{s}-\boldsymbol{s}_0)\cdot \boldsymbol{r}_m} \sum_n f_n e^{-\frac{2\pi i}{\lambda}(\boldsymbol{s}-\boldsymbol{s}_0)\cdot \boldsymbol{r}_n} \\ &= \sum_m \sum_n f_m f_n e^{\frac{2\pi i}{\lambda}(\boldsymbol{s}-\boldsymbol{s}_0)\cdot \boldsymbol{r}_{mn}} \end{aligned} \tag{3.14}$$

I_{eu} is the intensity in an electron unit. $\boldsymbol{r}_\mathrm{m}$ is the position vector of atom m in the crystal. $\boldsymbol{r}_{mn} = \boldsymbol{r}_m - \boldsymbol{r}_n$ is the difference vector between the positions of two atoms. $\boldsymbol{s}$ and $\boldsymbol{s}_0$ are the unit vectors in the direction of propagation of the incident and diffracted beam. For calculating the powder profile, it is assumed that powder sample is composed of a large number of the identical atomic clusters and that atomic clusters are randomly oriented to all the directions in space with the equal probability. Then the directional average can be taken for the exponential terms as follows:

$$\left\langle e^{\frac{2\pi i}{\lambda}(s-s_0)\cdot r_{mn}} \right\rangle = \frac{1}{4\pi r_{mn}^2} \int_0^{\pi} d\phi \, e^{iQr_{mn}\cos\phi} 2\pi r_{mn}^2 \sin\phi = \frac{\sin Qr_{mn}}{Qr_{mn}} \tag{3.15}$$

where $Q = 4\pi \sin\theta / \lambda$. ϕ is the angle between the vectors $\boldsymbol{s} - \boldsymbol{s_0}$ and $\boldsymbol{r}_{mn}$. r_{mn} is the interatomic distance between atom m and n. The intensity of the powder profile is represented as follows by replacing the exponential terms in Equation (3.14) with its average in Equation (3.15).

$$I_{eu} = \sum_m \sum_n f_m f_n \frac{\sin Qr_{mn}}{Qr_{mn}} \tag{3.16}$$

This equation is called as DSE. This was originally developed for calculating powder profiles of non-crystalline materials in 1910s [62]. It has not been used for long time for the structure analysis due to the expensive calculation cost for calculating the contributions from a millions of the pairs of atoms in a crystal. Recently, the availability of the large-scale computing platform such as multi-core CPU or GPU motivated the analysis of the powder diffraction data by DSE. Several researches were reported about the sample with the small number of atomic clusters such as nanoparticles [28], [63].

In the present study, the powder profiles of nanoparticles were calculated by DSE. Program 1dscat was used for the calculation. This program was used in the analysis of the powder diffraction data of nanoparticles by Ozawa [29]. The calculation was performed on the large-scale parallel computing platform with GPU.

3.3.3 Construction of structure models of water and nanoparticles

The structure models of nanoparticles are required for calculating the powder profiles by DSE. The coordinates, the species and temperature factors for all the atoms in a nanoparticle should be specified for the construction of the structure model. The structure models were constructed by using the software LAMMPS and PACKMOL [64], [65]. The visualization of the constructed models were performed by the software OVITO [66].

LAMMPS was used for the construction of the structure models of nanoparticles. The construction of ZrO_2 nanoparticle was shown as a representative. The unit cell was constructed at first. The lattice parameters and fractional coordinates of atoms were obtained from the analysis of the powder diffraction data by Rietveld refinement. The supercell was constructed by the repetition of the unit cell in the directions of the axes of the unit cell. The structure model of nanoparticle was cut out from the supercell with the desired dimensions.

PACKMOL was used for the construction of the structure models of water. PACKMOL was developed for constructing the initial atomic arrangements of the molecular dynamics simulation [65]. A large number of molecules are arranged in a specified region separated by a certain distance with each other. PACKMOL requires the structure of a molecule, number of molecules, shape and the size of the region for molecules to be arranged and the minimum separation between molecules for the construction of the structure model. It solves the optimization problem for obtaining the structure model which satisfies the specified conditions. The objective function of the optimization problem is expressed as follows:

$$f = \sum_{i=1}^{n\,\mathrm{mol}} \sum_{j=1}^{n\,\mathrm{atom}(i)} \left(\sum_{i'=i+1}^{n\,\mathrm{mol}} \sum_{j'=1}^{n\,\mathrm{atom}(i')} \max\left\{0, d_{tol}^2 - \left\|p^{ij} - p^{i'j'}\right\|^2\right\}^2 \right) + \sum_{i=1}^{n\,\mathrm{mol}} \sum_{j=1}^{n\,\mathrm{atom}(i)} \left(\sum_{l=1}^{r^{ij}} \max\{0, g_l^{ij}(p^{ij})\}^2 \right) \tag{3.17}$$

d_{tol} is the minimum separation between two molecules. p^{ij} is the position vector of an atom j in a molecule i. g_l^{ij} is the geometrical condition for an atom j in a molecule j. PACKMOL tries to minimize the objective function by adjusting the arrangement of a large number of molecules. When a solution was found, a structure model is obtained in which molecules are arranged with a certain separation in the specified area.

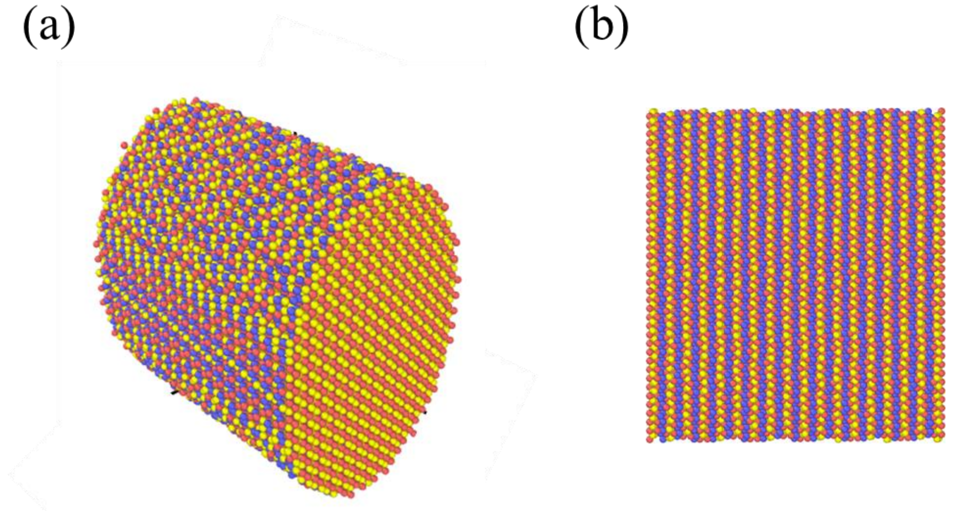

Figure 3.3.2 Example of the structure model visualized on the software OVITO. (a) structure model, (b) cutting surface.

OVITO was used for the visualization of the structure model. Figure 3.3.2 shows an example of the structure model visualized on OVITO. Figure 3.3.2 (a) shows the 3D view of structure model of ZrO_2. Spheres are atoms in the structure model. Colors of atoms show the atomic species. Red sphere shows zirconium atom. Blue and yellow spheres are oxygen atoms. OVITO provides several tools to examine and analyze the atomic arrangement in the structure model. Figure 3.3.2(b) shows the cutting surface of the structure model in the plane perpendicular to a certain crystallographic direction.

3.3.4 Profile fitting

Profile fitting is a method to analyze the powder diffraction data. Powder diffraction data are composed of the diffraction from several components such as the powder sample, sample container or air around the sample. The profile fitting explores the best expression of powder diffraction data as the sum of powder profiles of these components. Powder profiles have to be assumed as the inputs of the analysis. The intensity of powder profiles are optimized by the nonlinear least square method to minimize the difference between powder diffraction data and the sum of powder profiles. The agreement between powder diffraction data and the sum of powder profiles is evaluated by the reliability factor R_{wp}

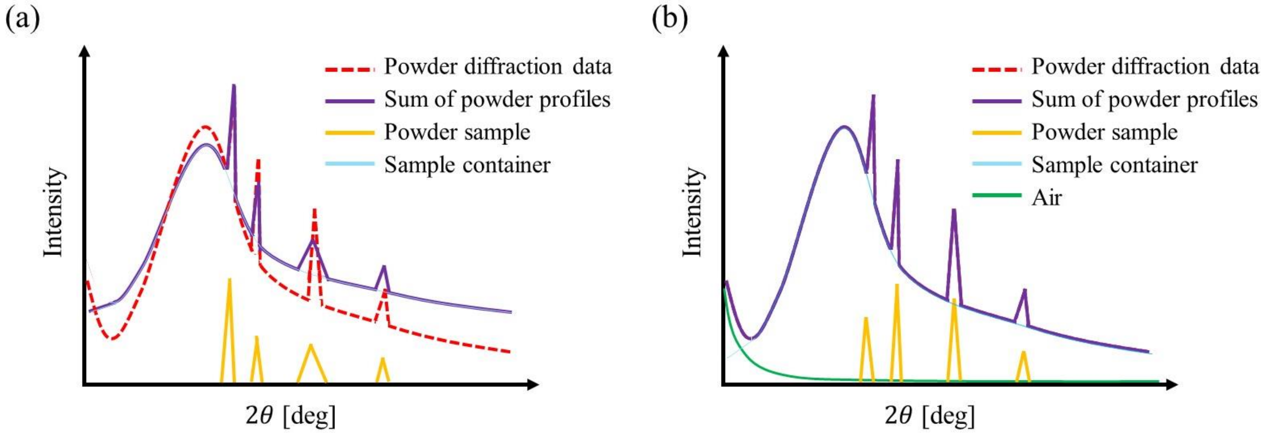

Figure 3.3.3 Examples of the profile fitting. (a) profile fitting was failed, (b) powder diffraction data were successfully expressed by the sum of powder profiles.

Figure 3.3.3 shows the schematic of the profile fitting. Figure 3.3.3 (a) shows an example of the analysis where the profile fitting of powder diffraction data were failed. A red dashed line show the powder diffraction data. The yellow lines show the powder profile of the powder sample calculated from the structure model. A blue line shows the powder profile of the sample container. A purple line shows the sum of powder profiles. The powder diffraction data were not expressed by the sum of powder profiles.

Figure 3.3.3 (b) shows an example of the analysis where the powder diffraction data were successfully expressed as the sum of powder profiles. In this case, powder profile of the powder sample was calculated by the different structure models from that in Figure 3.3.3 (a). The powder profile of air around sample was used in the analysis. A green line shows an example of powder profile of the air around sample. The powder diffraction data were represented as the sum of powder profiles of the powder sample, sample container and air around the sample.

The program synchrotron powder was used for the profile fitting of powder diffraction data. Powder profiles were assumed as background. Powder profiles of several components such as air can be expressed by the profile functions. SPⅦ was used as the profile function for diffraction from the air and for Bragg peaks which was not attributed to the powder sample. The flat background was used for the analysis. The powder profile calculated by Rietveld refinement was also used in the analysis of the several powder diffraction data. The intensity of powder profiles, parameter i and w of SPⅦ were optimized in the analysis [67].

3.4 Analysis of powder diffraction data of nanoparticles in vessel

3.4.1 Powder data from reaction field and vessel

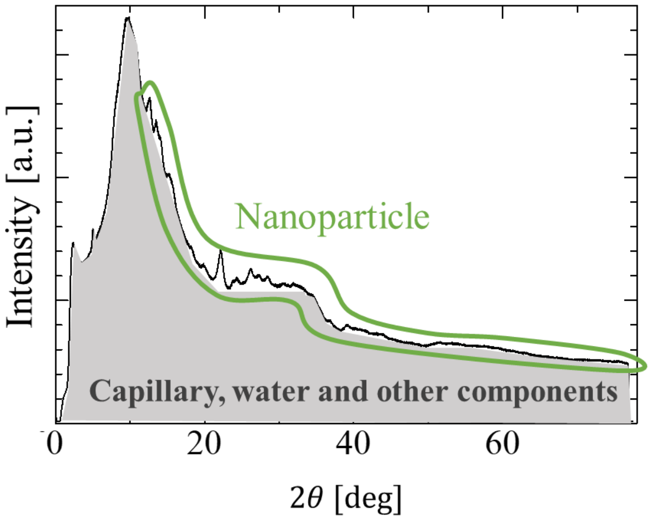

Figure 3.4.1 Powder diffraction data of *in-situ* SR-PXRD experiment.

Figure 3.4.1 shows the powder diffraction data of *in-situ* SR-PXRD experiment. Data were collected from the initial 5 min of synthesis of ZrO_2 nanoparticles. Green line shows the Bragg peaks of ZrO_2 nanoparticles synthesized in the reaction field. Gray area shows the diffraction from supercritical water, reaction vessel of fused silica capillary and other components. More than 80 % of the intensity of powder diffraction data were attributed to diffraction from supercritical water, fused silica capillary and other components. It is essential to obtain the powder profiles of supercritical water and fused silica capillary, and subtract these contributions from the powder diffraction data for extracting powder diffraction data of nanoparticles.

3.4.2 Modelling size effect of nanoparticles

Broadening of the diffraction lines can be occurred due to the small size of crystals in the powder sample. The principle of the diffraction from one crystal was described in Figure 3.2.1. In the case of bulk crystal, it is assumed that each particle in powder sample is treated as a sufficiently large crystal with the infinite number of lattice planes. Phases of diffracted waves from two planes are in phase at Bragg angle. There should be phase shift between two waves at the angle where Bragg's law is not satisfied. Shift becomes larger and reaches to half of its wavelength as the distance between two planes is increased. Then any lattice plane can always find its pair whose diffracted wave is canceled out by wave from itself. In the case of bulk material, diffracted intensity should be observed only at the neighborhood of Bragg angle. The finite width of observed diffraction line is considered as the broadening mainly due to the instrumental function.

In the case of the small crystal with the finite number of lattice planes, intensity can be observed at the wider range of the diffraction angle around Bragg angle, since not all the planes can find its pair whose diffracted wave cancels out wave from itself. Bragg peak is broadened due to the small size of crystals. Nanoparticles often have the anisotropic shape in the specific crystallographic directions. It can cause the broadening of peaks depending on the Miller indices. Such complex dependence of the peak width must be handled for the analysis of the powder diffraction data of nanoparticles.

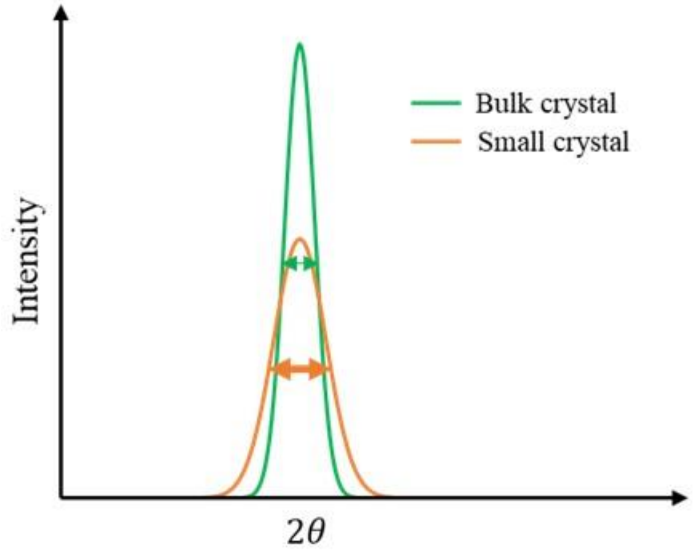

Figure 3.4.2 Broadening of Bragg peak by small size of crystal.

Figure 3.4.2 schematically shows the broadening of Bragg peak by small size of crystals. Green line shows a Bragg peak collected from bulk crystals. Orange line shows a Bragg peak collected from small crystals. FWHM of Bragg peak of the small crystals are larger than that of the bulk crystals. The width of Bragg peak can be used for the estimation of an average diameter of crystals. For example, the relation between the full width of half maximum of Bragg peak and the average diameter of crystals is expressed as follows:

$$L = \frac{0.94\lambda}{B(2\theta)\cos\theta} \tag{3.18}$$

L is the average diameter of crystals. λ is wavelength. B is FWHM. θ is Bragg angle. This equation is called Scherrer equation [68]. This equation can be applied for the evaluation of powder sample with the diameter less than 100 nm.

3.4.3 Effect of lattice defects

Powder diffraction data of nanoparticle can be largely affected by the lattice defect in the structure, since the larger fraction of atoms can relate the lattice defect than the bulk crystals. Planar defects such as the stacking fault, linear defects such as the dislocations or point defect such as the vacancies can cause the characteristic change on the powder diffraction data [69], [70]. For the bulk materials, several theories have been formulated for analyzing the lattice defect from the powder diffraction data. For example, Warren developed a method to analyze the two types of the stacking faults for the powder diffraction data of face centred cubic (fcc) metals [24].

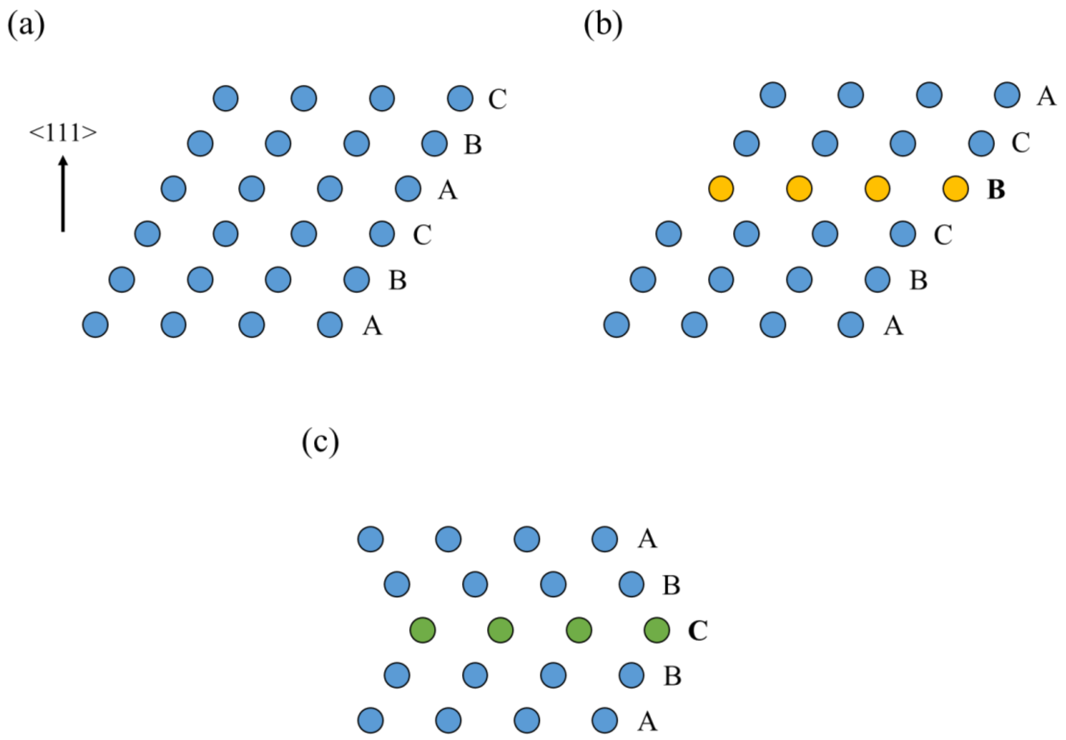

Figure 3.4.3 Stacking structures in fcc metals. (a)structure without faulting (b) deformation faulting, (c) twin faulting.

Figure 3.4.3 shows the stacking structure of fcc metals. Spheres are atoms. The vertical arrow shows the <111> direction in the fcc structure. Figure 3.4.3(a) shows the structure without stacking faults. Three types of layers A,B and C are regularly arranged as ABCABC···. Figure 3.4.3(b) shows the stacking fault called deformation faulting. One layer in the stacking sequence is skipped at the faulting. Figure 3.4.3(c) shows the twin faulting. The stacking sequence of three types of the layers are reversed on both sides of the faulting.

Warren’s theory treated the stacking fault statistically on the assumption that the faulting randomly appear in each layer with the certain level of the probability. This statistical method was successfully applied for the bulk materials which have the sufficiently large number of stacking layers of atoms [71]. The magnitude and sign of the shift and broadening has the complex dependence on Miller indices of Bragg peaks.

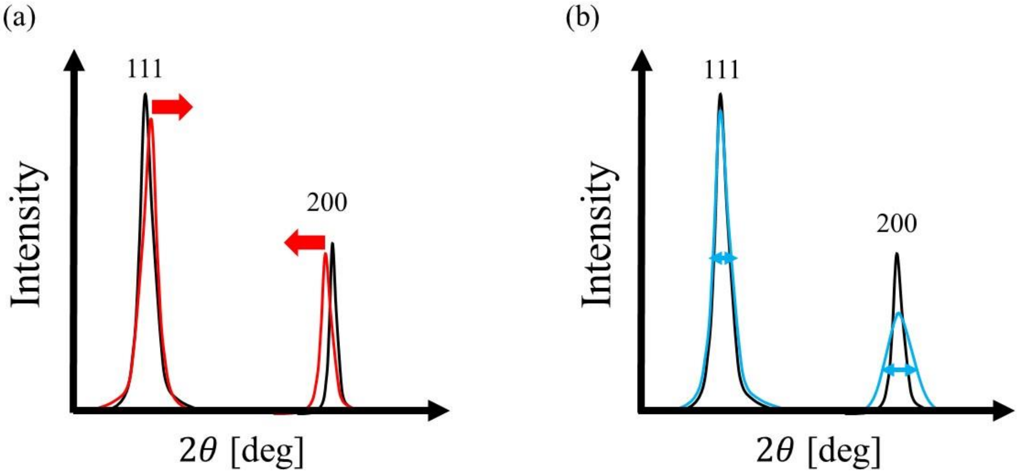

Figure 3.4.4 Effect of stacking fault to the powder profile of fcc sample. (a) peak shift by the deformation faulting, (b) peak broadening by the twin faulting.

Figure 3.4.4 shows the effect of stacking fault to the powder profile of fcc sample treated by Warren's theory. 111 and 200 reflection were shown in figures. Figure 3.4.4(a) schematically shows the effect of deformation faulting to the powder profile. The position of 111 reflection is shifted towards higher side of the diffraction angle. The position of 200 reflection is shifted towards lower side of the diffraction angle. Figure 3.4.4(b) schematically shows the effect of twin faulting to the powder profile. Twin faulting causes the broadening of 111 and 200 reflections. The broadening of 200 reflection is more than twice of that of 111 reflection.

In the case of nanoparticles, the magnitude of shift and broadening can be deviated from Warren's theory [70], [72]. For example, the fcc Ag nanosphere with the lattice parameter a = 4.09 Å and with 10 nm diameter has only 42 layers in the 111 direction. In this particle, a twin faulting at the edge of sphere would cause almost no effect to powder profile since it does very slightly change the atomic arrangement. A twin faulting at the center of sphere would cause large broadening of diffraction lines since almost 20 % of atoms in a nanoparticle belong to the neighboring two layers of twin faulting. In general, the effect of stacking fault to the powder profile are highly dependent on the size and the shape of a nanoparticle, the position of stacking faults or the distance between stacking faults in the structure. The shift and broadening of Bragg peaks due to the lattice defects must be expressed for the analysis of the powder diffraction data of nanoparticles.

3.5 Analytical representation of powder profiles of capillary and supercritical water using SPVII functions.

Powder profiles of fused silica capillary and supercritical water were determined to extract the diffraction of nanoparticles from the powder diffraction data. Section 3.5.1 shows the analytical representation of the powder profile of fused silica capillary. The powder profiles of fused silica capillary at room temperature and 600 K were determined by the profile fitting. Section 3.5.2 describes the analytical representation of the powder profile of pure water. Two approaches were employed to determine the powder profiles of water. The powder profiles of water at the seven conditions including three supercritical water conditions were determined by the profile fitting.

3.5.1 Fused silica capillary

Powder diffraction data of empty fused silica capillary collected at room temperature and 600 K were analyzed by the profile fitting. Powder profile of quartz capillary was used in the analysis. Four SPⅦ were used to express Bragg peaks of polyimide in capillary. Parameters *i*, *t*, *w*, *a* of SPⅦ were optimized in the analysis.

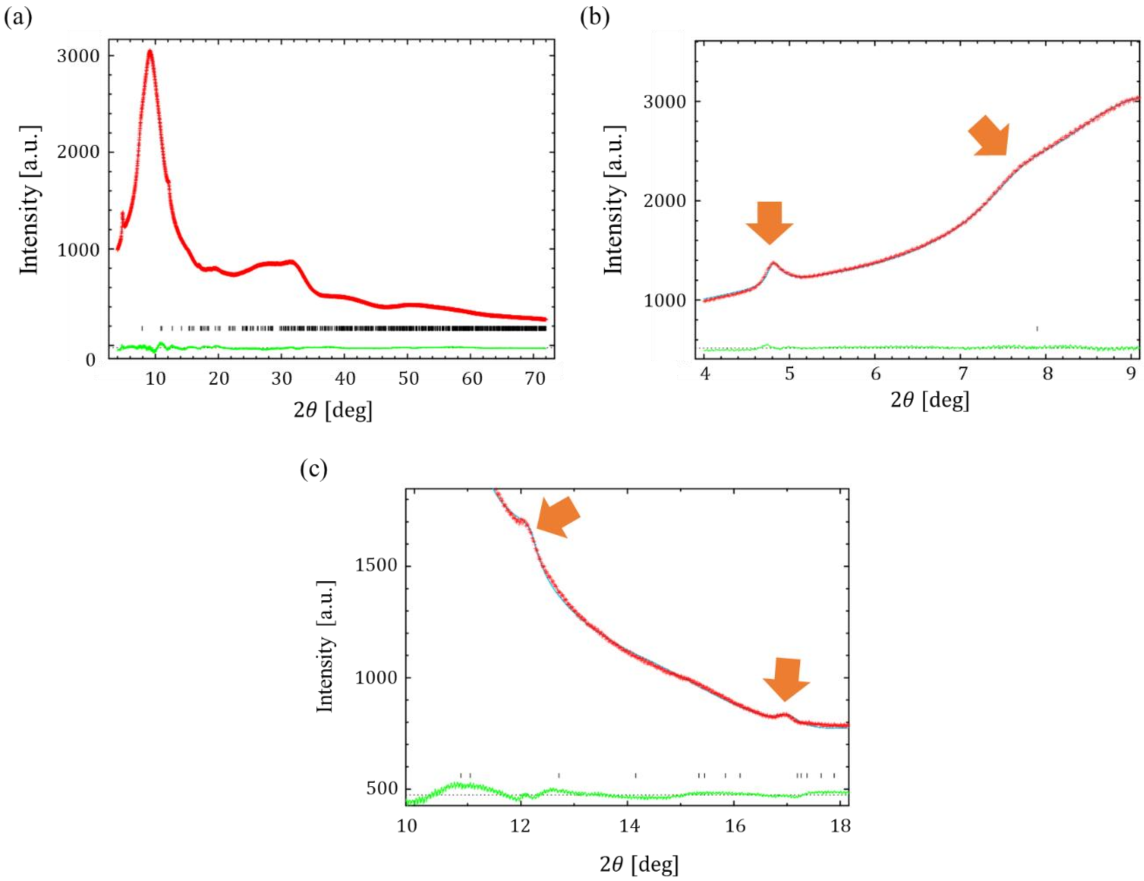

Figure 3.5.1 Powder diffraction data and the sum of powder profiles at room temperature. (a) 0 ° to 72 °, (b) 4 ° to 9 °, (c) 10 ° to 18 °.

Figure 3.5.1 shows the powder diffraction data and the sum of powder profiles. The powder diffraction data and powder profile at room temperature was shown as representative. Figure 3.5.1(a) shows the diffraction angle from 4 ° to 72 °. Difference between the powder diffraction data and sum of the calculated powder profiles were less than 50. R_{wp} was 1.09 %. Figure 3.5.1(b) shows the diffraction angle from 4 ° to 9 °. Bragg peaks of polyimide were observed at 4.8 ° and at 7.8 °. Figure 3.5.1(c) shows the diffraction angle from 10 ° to 18 °. Bragg peaks of polyimide were observed at 12.3 ° and at 17.0 °. The powder diffraction data of fused silica capillary were expressed as the sum of powder profiles of quartz capillary and the profile functions for Bragg peaks of polyimide. The powder profile of fused silica capillary at room temperature and at 600 K were extracted from the sum of powder profiles.

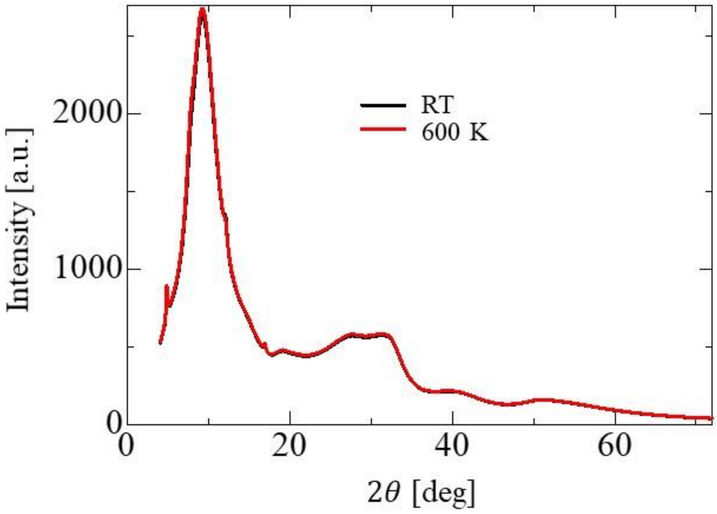

Figure 3.5.2 Powder profiles of fused silica capillary at room temperature and 600 K.

Figure 3.5.2 shows powder profile of fused silica capillary extracted from the sum of powder profiles. A black line shows the powder profile at room temperature. A red line shows the powder profile at 600 K. The difference in the intensity was very slight between the powder profiles at room temperature and 600 K.

3.5.2 Supercritical water

The modelling of the powder diffraction data of supercritical water were tried by two different approaches. The structure model of water was constructed for the calculation of the powder profile. Powder profiles of water were calculated by DSE. The calculated powder profile was not consistent with the experimental data of water at room temperature. The profile fitting was performed for the powder diffraction data of pure water collected by SR-PXRD experiment. Powder profiles of water including supercritical water conditions were determined by the profile fitting.

3.5.2.1 Structure modelling of water using PACKMOL

Modelling of the powder profile of water was tried by using the structure models of water. The structure models of water were constructed by PACKMOL for the analysis. 5000 water molecules were arranged in the cube with edge length of 53.07 Å. The density of water was 1.0 g/cm^3. Six minimum separations of the molecules were selected for the construction of the structure models. The powder profiles were calculated from the structure models by DSE.

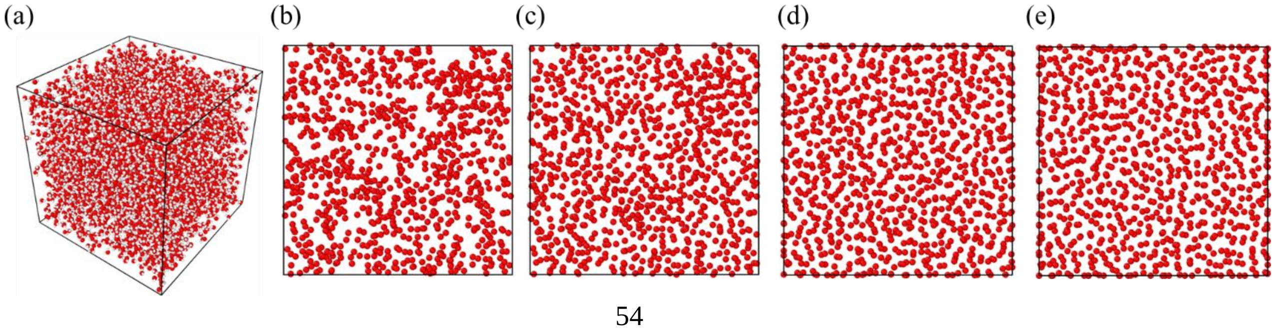

Figure 3.5.3 Structure models of water by PACKMOL. (a) Structure model of water with the minimum separation of 1.0 Å, (b-e) cutting surface of the model with the minimum separation of (b) 1.0 Å, (c) 2.0 Å, (d) 2.5 Å and (e) 2.8 Å.

Figure 3.5.3 shows the structure models of water constructed by PACKMOL. Figure 3.5.3(a) shows the structure model constructed with the minimum separation of molecules 1.0 Å. Black line shows the edge of a cube. The red spheres are oxygen atoms. The white spheres are hydrogen atoms. Figure 3.5.3(b) shows the cutting surface of the structure model with the minimum separation of molecules 1.0 Å. Thickness of the cutting surface is 10 Å. There were several clusters of the water molecules in the structure model. The size of each cluster was about 20 Å to 30 Å.

Figure 3.5.3(c) shows the cutting surface of the structure model with the minimum separation of molecules 2.0 Å. The size of dense region has decreased to about 5 Å. Figure 3.5.3(d) shows the cutting surface of the structure model with the minimum separation of molecules 2.5 Å. The water molecules are almost homogeneously distributed in the structure model. Figure 3.5.3(e) shows the cutting surface of the structure model with the minimum separation of molecules 2.8 Å. No large change was observed from the structure model with the minimum separation of molecules 2.5 Å. PACKMOL couldn't find the solution with the minimum separation of molecules 2.9 Å. The Powder profile was calculated by DSE.

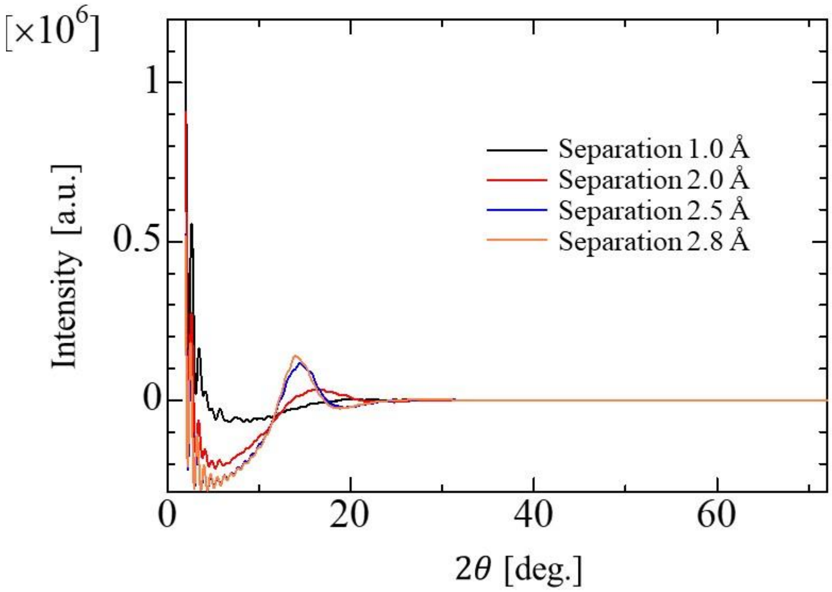

Figure 3.5.4 Powder profiles calculated from the structure models.

Figure 3.5.4 shows the powder profiles calculated from the structure models of water in Figure 3.5.3. Colored lines show the powder profiles calculated from the structure model constructed with the minimum separation of molecules 1.0, 2.0, 2.5 and 2.8 Å. The powder profile of structure model with the minimum separation 1.0 Å showed no peak from 0 to 72°. The powder profiles of other structure models showed peak in the diffraction angle from 10 °to 20 °. The shapes of powder profiles were not consistent with the experimental data at room temperature which showed the twin peaks [73]. We concluded that the structure models of water cannot be used for the modeling of powder profiles of water.

3.5.2.2 Modelling by profile fitting of the powder diffraction data of water

The profile fitting was performed for the powder diffraction data for the determination of powder profiles of supercritical water. Powder diffraction data collected at SR-PXRD experiment were used for the analysis. The powder profile of fused silica capillary was used in the analysis. Nine SPⅦ were used for extracting the powder profile of supercritical water from the powder diffraction data.

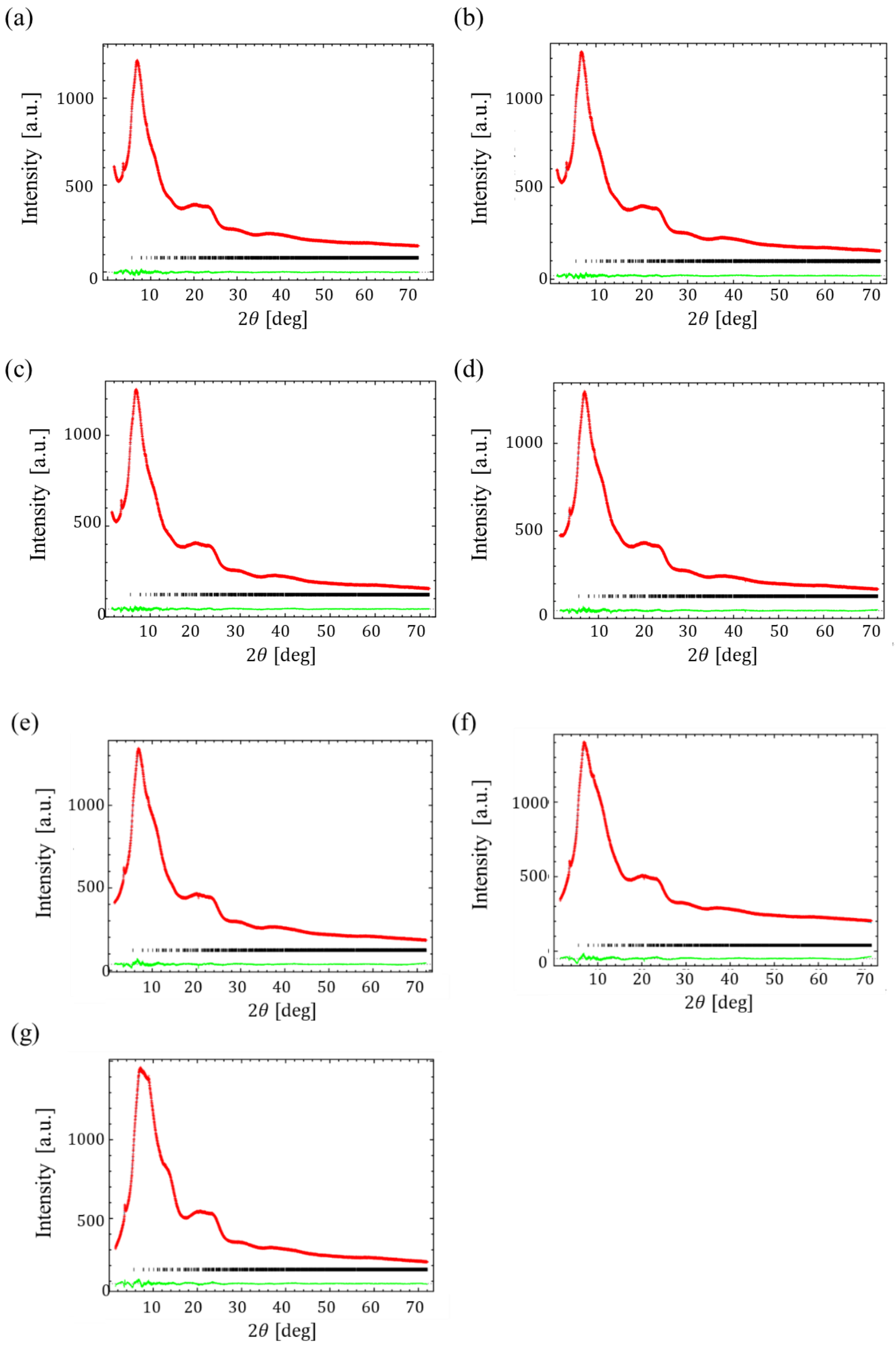

Figure 3.5.5 Powder diffraction data of water and the sum of powder profiles. (a) 673 K and 23 MPa, (b) 673 K and 26 MPa, (c) 673 K and 30 MPa, (d) 623 K and 30 MPa, (e) 573 K and 30 MPa, (f) 473 K and 30 MPa and (g) 300 K and 30 MPa.

Figure 3.5.5 shows the powder diffraction data of water and the sum of powder profiles. Figure 3.5.5(a) shows the powder diffraction data of water and the sum of powder profiles at 673 K and 23 MPa. Difference between diffraction data and calculated values were less than 30. R_{wp} was 0.76 %. Figure 3.5.5(b) shows the powder diffraction data of water and the sum of powder profiles at 673 K and 26 MPa. Difference between diffraction data and calculated values were less than 20. R_{wp} was 0.74 %. Figure 3.5.5(c) shows the powder diffraction data of water and the sum of powder profiles at 673 K and 30 MPa. Difference between diffraction data and calculated values were less than 20. R_{wp} was 0.73 %.

Figure 3.5.5(d) shows the powder diffraction data of water and the sum of powder profiles at 623 K and 30 MPa. Difference between diffraction data and calculated values were less than 20. R_{wp} was 0.81 %. Figure 3.5.5(e) shows the powder diffraction data of water and the sum of powder profiles at 573 K and 30 MPa. Difference between diffraction data and calculated values were less than 20. R_{wp} was 0.93 %.Figure 3.5.5(f) shows the powder diffraction data of water and the sum of powder profiles at 473 K and 30 MPa. Difference between diffraction data and calculated values were less than 30. R_{wp} was 1.17 %.

Figure 3.5.5(g) shows the powder diffraction data of water and the sum of powder profiles values at 300 K and 30 MPa. Difference between diffraction data and calculated values were less than 40. R_{wp} was 0.82 %. Powder diffraction data of water at seven conditions were successfully expressed as the sum of powder profiles. The powder profiles of water were extracted from the sum of powder profiles.

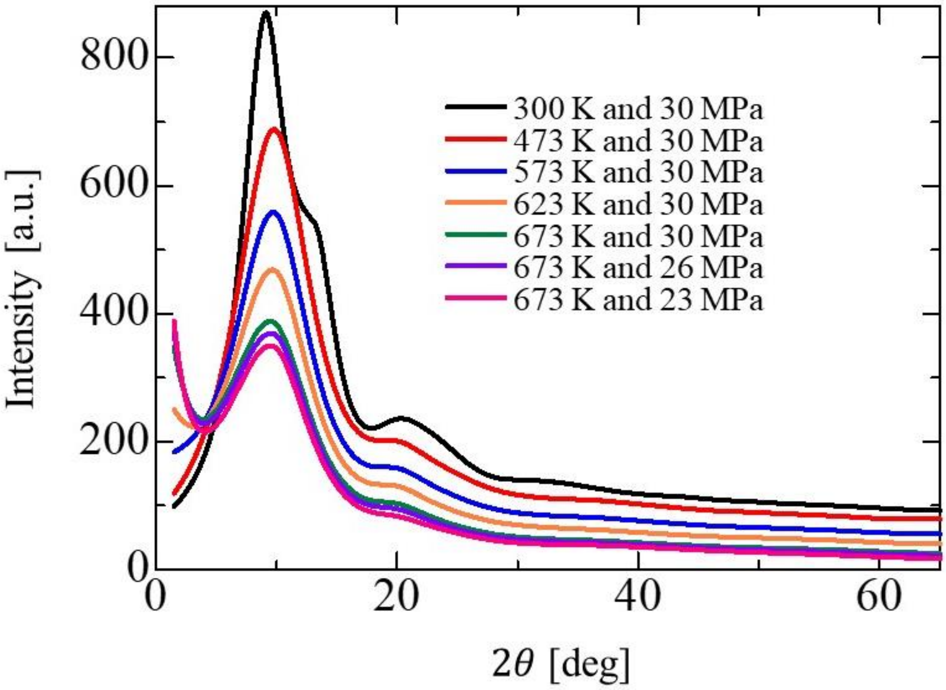

Figure 3.5.6 Powder profiles of water.

Figure 3.5.6 shows diffraction data of water extracted by profile fitting. Horizontal axis is diffraction angle 2θ. Vertical axis is intensity. Lines are powder profiles of water determined by profile fitting of powder diffraction data. Powder profile of water at 300 K and 30 MPa showed two peaks around 9.1 ° and 14.3 °. These two diffraction angle corresponded to 2.0 $Å^{-1}$ and 2.8 $Å^{-1}$ in $Q = 4\pi \sin\theta / \lambda$. The intensity and peak positions of the powder profile were same as reported experimental powder profile of water at room temperature and atmospheric pressure [73], [74]. We concluded that powder profile of water at room temperature were determined from powder diffraction data.

The intensity at 2.1 ° of powder profiles of supercritical water was larger than that of powder profiles of liquid phase water. The intensity at 2.1 ° of the powder profile at 673 K and 23 MPa was higher than that of the powder profile at 300 K and 30 MPa by 300. The intensity at 9.8 ° of powder profiles of supercritical water was lower than that of powder profiles of liquid phase water. The intensity at 9.8 ° of the powder profile at 673 K and 23 MPa was lower than that of the powder profile at 473 K and 30 MPa by 300. Similar change of the intensity of the the powder diffraction data were observed in the neutron diffraction experiment of deuterium at room temperature and supercritical water conditions [75]. We concluded that powder profile of supercritical water were determined from the powder diffraction data.

3.6 Analysis of powder diffraction data of nanoparticles

Powder diffraction data of Ag, ZrO_2 and HfO_2 nanoparticles were analyzed for the structure analysis. The powder diffraction data of nanoparticles were extracted by using the powder profiles of capillary and water. Two methods were employed for the analysis of the powder diffraction data. One is Rietveld refinement. Another one is DSE. At first, the powder diffraction data were analyzed by Rietveld refinement. The powder profiles were calculated from the average structure model of crystals. The deviations were found between the powder diffraction data and the calculated powder profiles.

DSE was used for the analysis. The effectiveness and the usefulness of DSE was investigated by the systematic study about the effect of size and the lattice defects of nanoparticles to the powder profiles. The powder diffraction data were analyzed by powder profiles by DSE. Powder profiles calculated from the structure models of nanoparticles with twin faulting showed better agreement for the powder diffraction data of nanoparticles than Rietveld refinement.

Section 3.6.1 describes a limitation in the analysis of the powder diffraction data of nanoparticles by Rietveld refinement. Section 3.6.2 shows the systematic study about the effect of size and lattice defects of nanoparticles to the powder profile. Section describes the analysis of the powder diffraction data by the powder profiles of the structure models of nanoparticles with twin faulting. Section 3.6.3 explains the developed method for the analysis of powder diffraction data of nanoparticles. Section 3.6.4 summarized this section.

3.6.1 Analysis of powder profiles by Rietveld refinement

The powder diffraction data of Ag, HfO_2 and ZrO_2 nanoparticles were analyzed by Rietveld refinement. The powder profiles of nanoparticle were calculated from the models of the average structure of crystals. Section 3.6.1.1 describes the analysis of the powder diffraction data of Ag nanoparticles. Section 3.6.1.2 shows the analysis of the powder diffraction data of ZrO_2 nanoparticles. Section 3.6.1.3 explains the analysis of the powder diffraction data of HfO_2 nanoparticles.

3.6.1.1 Ag 10 nm nanosphere

Powder diffraction data of Ag nanoparticles were analyzed by Rietveld refinement. Ozawa investigated the angular dependence of the peak widths of the powder diffraction data of Ag nanoparticles [29]. The powder diffraction data were analyzed by using the powder profiles of the powder sample and the capillary. The powder profile of sample was calculated from the structure model of fcc Ag. The powder profile of the quartz capillary was used in the analysis. Scale factor, lattice constants and parameter w of the peak width function were optimized in the refinement. The intensity of the powder profile of the quartz capillary was optimized in the analysis.

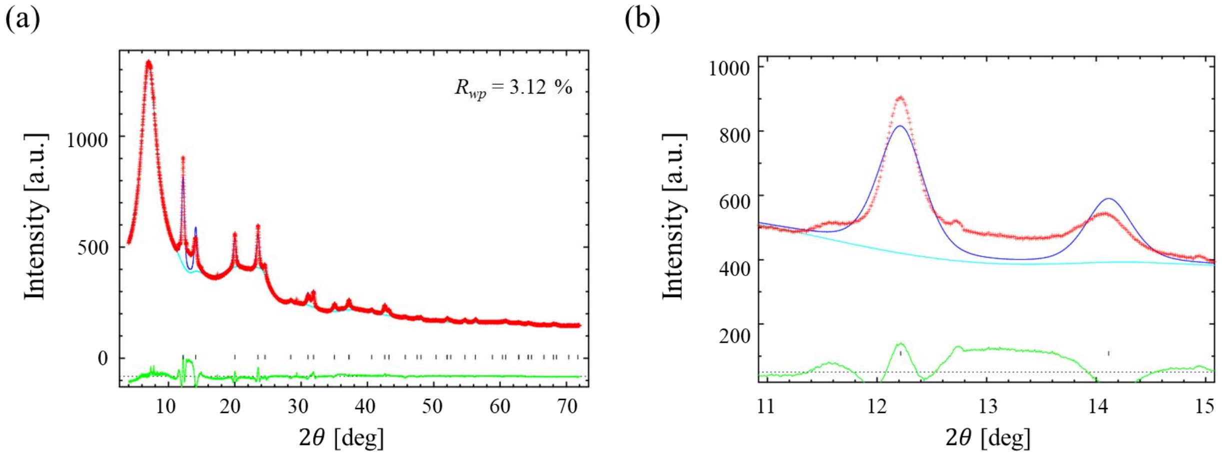

Figure 3.6.1 Powder diffraction data and calculated powder profile of Rietveld refinement. (a) 10 ° to 72 °, (b) 11 ° to 15 °.

Figure 3.6.1 shows the powder diffraction data and the powder profile of Rietveld refinement. Figure 3.6.1(a) shows the diffraction angle from 4 ° to 72 °. R_{wp} was 3.12 %. Figure 3.6.1(b) shows the diffraction angle from 11 ° to 15 °. The peak shape around 11.6 ° was not expressed by the powder profile of Rietveld refinement. The peak height of 200 reflection of the powder diffraction data at 14.2 ° was lower than that of the powder profile by 50. The difference of the peak positions of 111 and 200 reflections between the powder data and the calculated powder profile was less than 0.05 °. The peak height of 111 reflection of the powder profile was lower than that of the powder diffraction data by 100. The peak height of 200 reflection of the powder profile was larger than that of the powder diffraction data by 70. The 111 reflection and 200 reflection of Ag nanoparticles were not expressed by the powder profile of Rietveld refinement.

3.6.1.2 ZrO_2

3.6.1.2.1 Powder diffraction data collected at supercritical water condition

Powder diffraction data of ZrO_2 nanoparticle collected in supercritical water condition was analyzed by Rietveld refinement. Powder profiles of the monoclinic phase and the tetragonal phase of ZrO_2 was calculated by the structure models of Howard *et al*[76]. The powder profile of fused silica capillary and the powder profile of supercritical water at 673 K and 30 MPa were used in the analysis. Scale factor, lattice constants and peak width parameter *w* were optimized in the refinement. The intensity of powder profiles of fused silica capillary and supercritical water were optimized in the analysis.

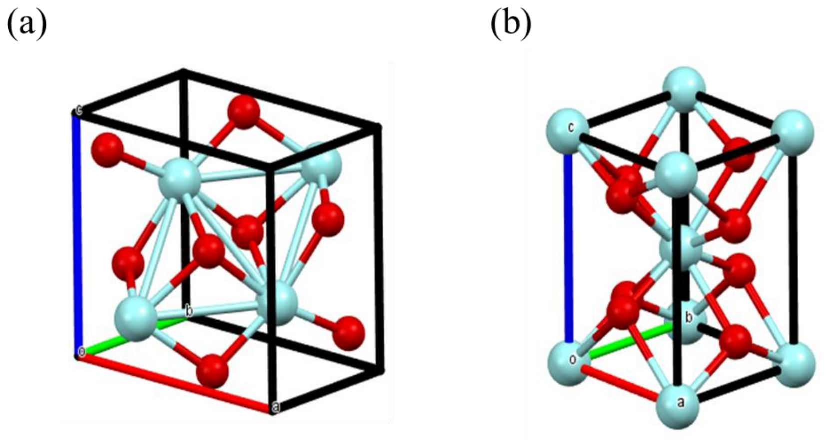

Figure 3.6.2 Unit cell of ZrO_2. (a) monoclinic phase, (b) tetragonal phase.

Figure 3.6.2 shows the unit cell of ZrO_2. The average structure models of monoclinic phase and tetragonal phase by Howard *et al.* were used for the analysis [76]. Sky blue spheres are zirconium atoms. Red spheres are oxygen atoms. Figure 3.6.2(a) shows the monoclinic phase. The unit cell was composed with four zirconium atoms and eight oxygen atoms. Figure 3.6.2(b) shows the tetragonal phase. The unit cell was composed with two zirconium atoms and four oxygen atoms.

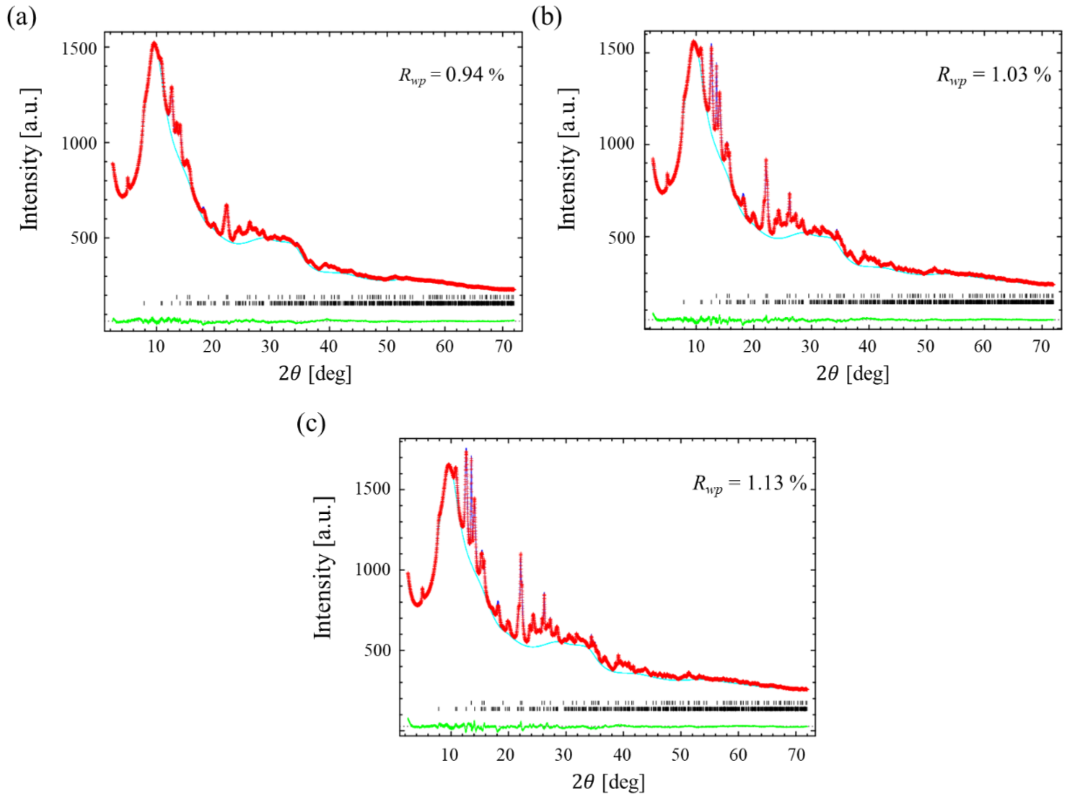

Figure 3.6.3 Powder diffraction data and the sum of powder profiles from 4 ° to 72 °. (a) Initial 5 min, (b)25

to 30 min, (c) 55 to 60 min.

Figure 3.6.3 shows the powder diffraction data of at 673 K and 30 MPa and the sum of powder profiles. The diffraction angle from 4 °to 72 ° was shown in the figure. Figure 3.6.3 (a) shows the powder diffraction data and the sum of powder profiles at initial 5 min. R_{wp} was 0.94 %. Figure 3.6.3(b) shows the powder diffraction data and the sum of powder profiles from 25 to 30 min. R_{wp} was 1.03 %. Figure 3.6.3(c) shows the powder diffraction data and the sum of powder profiles from 55 to 60 min. R_{wp} was 1.13 %.

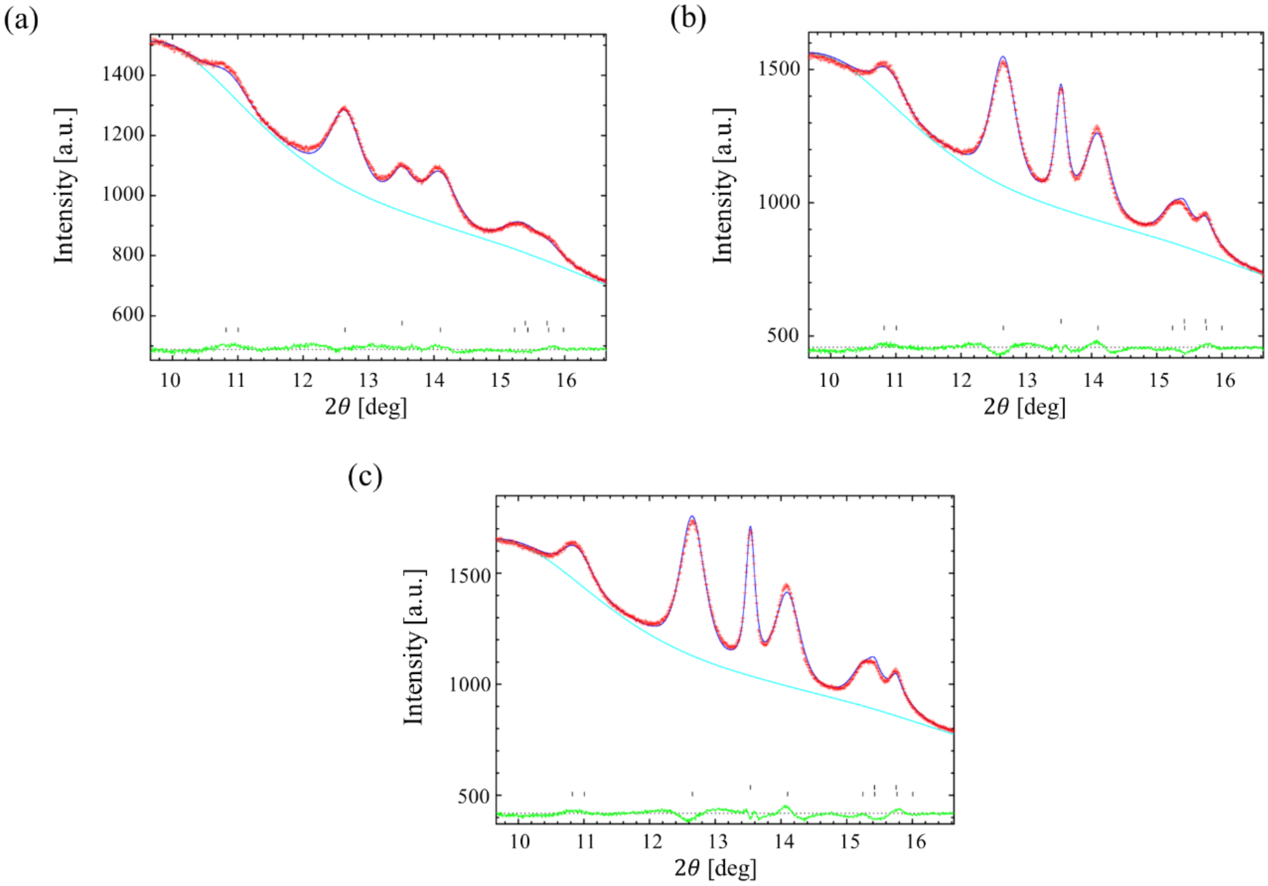

Figure 3.6.4 Powder diffraction data and the sum of powder profiles from 9.8 ° to 16.5 °. (a) Initial 5 min (b)25 to 30 min (c) 55 to 60 min.

Figure 3.6.3 shows the powder diffraction data of at 673 K and 30 MPa and the sum of powder profiles. The diffraction angle from 9.8 ° to 16.5 ° was shown in the figure. Figure 3.6.3 (a) shows the powder diffraction data and the sum of powder profiles at the initial 5 min. The difference of intensity in this angle was less than 50. Figure 3.6.3 (b) shows the powder diffraction data and the sum of powder profiles from 25 to 30 min. The difference of intensity in this angle was less than 50. Figure 3.6.3 (c) shows the powder diffraction data and the sum of powder profiles from 55 to 60 min. The difference of intensity in this angle was less than 50.

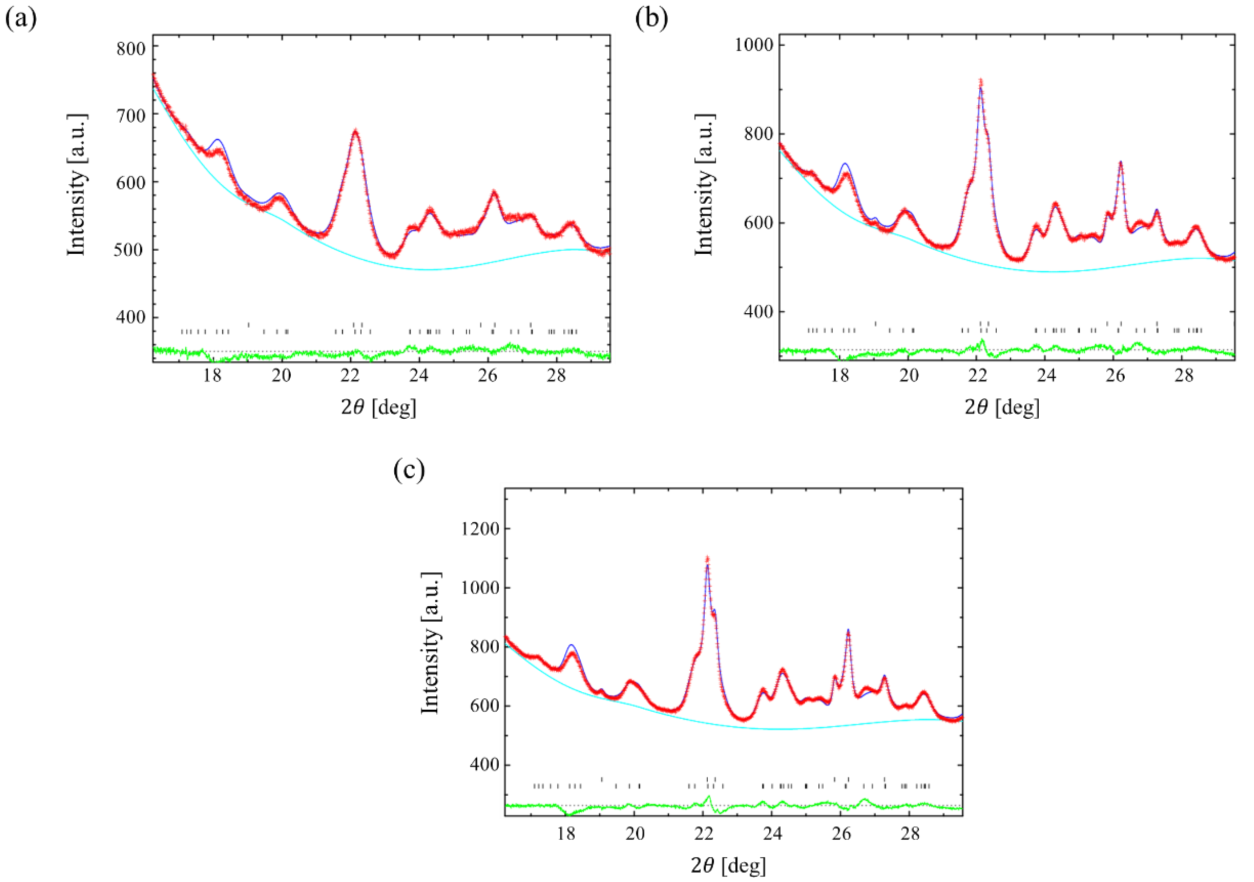

Figure 3.6.5 Powder diffraction data and the sum of powder profiles from 16.5 ° to 29.3 °. (a) Initial 5 min, (b) 25 to 30 min, (c) 55 to 60 min.

Figure 3.6.5 shows the powder diffraction data of at 673 K and 30 MPa and the sum of powder profiles. The diffraction angle from 16.5 ° to 29.3 ° was shown in the figure. Figure 3.6.5 (a) shows the powder diffraction data and the sum of powder profiles at the initial 5 min. The intensity of the powder profile at 18 ° was higher than that of the powder diffraction data by 20. The difference of intensity at 26.8 ° was less than 20. This position was around the 113 reflection of monoclinic ZrO_2.

Figure 3.6.5 (b) shows the powder diffraction data and the sum of powder profiles from 25 to 30 min. The intensity of the powder profile at 18 ° was higher than that of the powder diffraction data by 30. The intensity of the powder profile at 26.8 ° was higher than that of the powder diffraction data by 20.

Figure 3.6.5 (c) shows the powder diffraction data and the sum of powder profiles from 55 to 60 min. The intensity of the powder profile at 18 ° was higher than that of the powder diffraction data by 30. The intensity of the powder profile at 26.8 ° was higher than that of the powder diffraction data by 20. Powder diffraction data of ZrO_2 nanoparticles around 18 ° and 26.8 ° were not expressed by the powder profile of Rietveld refinement.

3.6.1.2.2 Powder diffraction data of ZrO_2 at room temperature

Powder diffraction data of ZrO_2 nanoparticle collected at room temperature was analyzed by Rietveld refinement. Powder profile of monoclinic ZrO_2 was calculated by the structure model of Howard *et al*[76]. The powder profiles of fused silica capillary and the water at 300 K and 30 MPa were used in the analysis. Scale factor, lattice constants and peak width parameter w were optimized in the refinement. The intensity of powder profiles of fused silica capillary and water were optimized in the analysis.

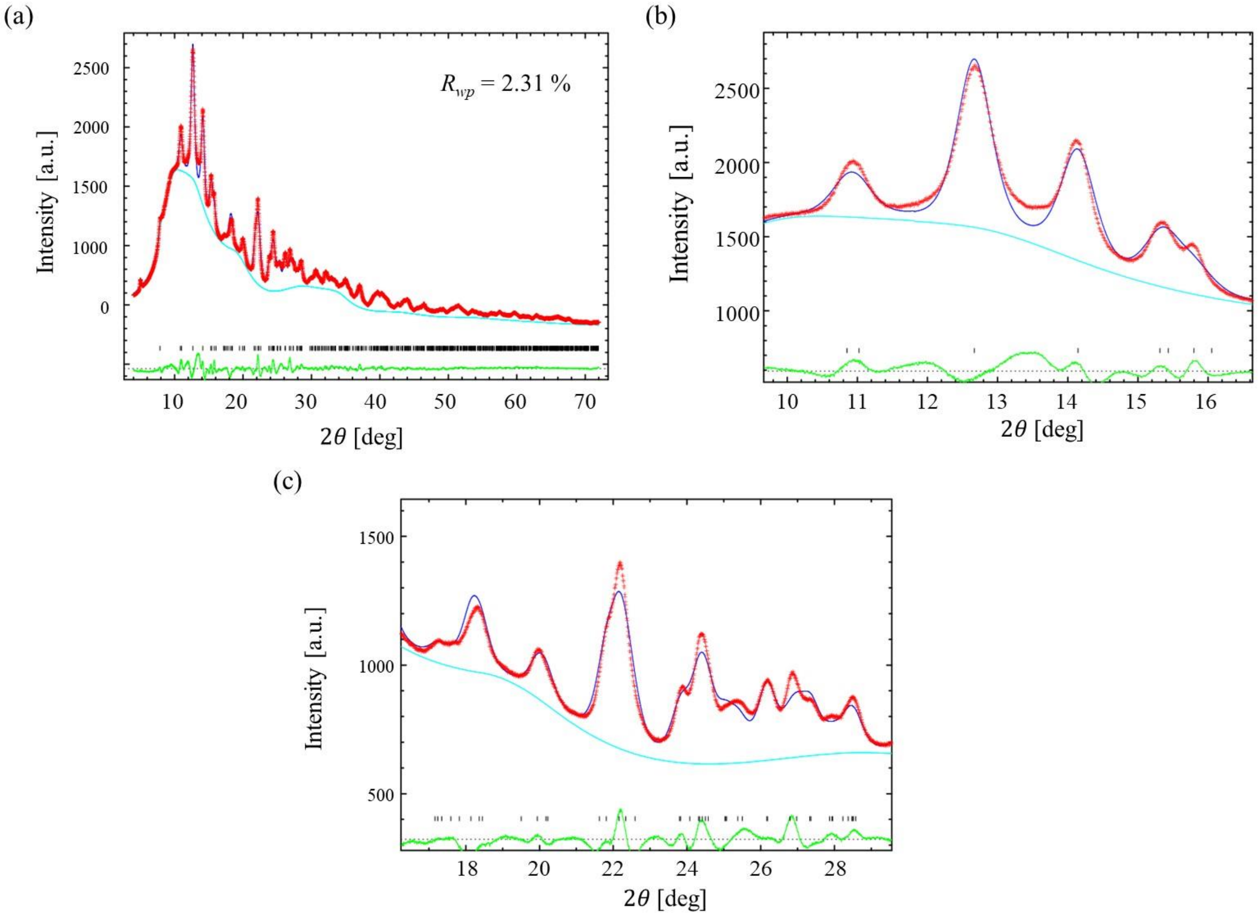

Figure 3.6.6 Powder diffraction data and the powder profile of Rietveld refinement. (a) 4° to 72 °, (b) 9.8 ° to 16.5 °, (b) 16.5 ° to 29.3 °.

Figure 3.6.6 shows the powder diffraction data and the powder profile of Rietveld refinement. Figure 3.6.6(a) shows the diffraction angle from 4 ° to 72 °. R_{wp} was 2.31 %. Figure 3.6.6(b) shows the diffraction angle from 9.8 ° to 16.5 °. The intensity of the powder profile at 11 ° was lower than that of the powder diffraction data by 100. The intensity of the powder profile at 13.5 ° was lower than that of the powder diffraction data by 150. Figure 3.6.6(c) shows the diffraction angle from 16.5 ° to 29.3 °. The intensity of the powder profile at 18 ° was higher than that of powder diffraction data by 50. The intensity of the powder profile at 26.8 ° was higher than that of powder diffraction data by 100. Powder diffraction data of ZrO_2 nanoparticles from 16.5 ° to 29.3 ° was not expressed by the powder profile of Rietveld refinement.

3.6.1.3 HfO_2

Powder diffraction data of HfO_2 nanoparticle collected at supercritical water condition was analyzed by Rietveld refinement. Powder profile of monoclinic HfO_2 was calculated from structure model by Whittle et al. [77].

The powder profile of fused silica capillary and the powder profile of supercritical water at 673 K and 30 MPa were used in the analysis. Scale factor, lattice constants and peak width parameter *w* were optimized in the refinement. The intensity of powder profiles of fused silica capillary, supercritical water were optimized in the analysis.

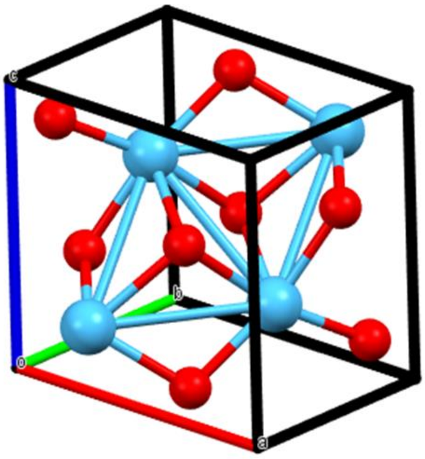

Figure 3.6.7 Unit cell of monoclinic HfO_2.

Figure 3.6.7 shows the unit cell of monoclinic HfO_2 by Whittle *et al.* [77]. Blue atoms are hafnium atoms. Red atoms are oxygen atoms. Monoclinic phase of HfO_2 has the same baddeleyte structure as the monoclinic phase of ZrO_2. The unit cell was composed with four hafnium atoms and eight oxygen atoms.

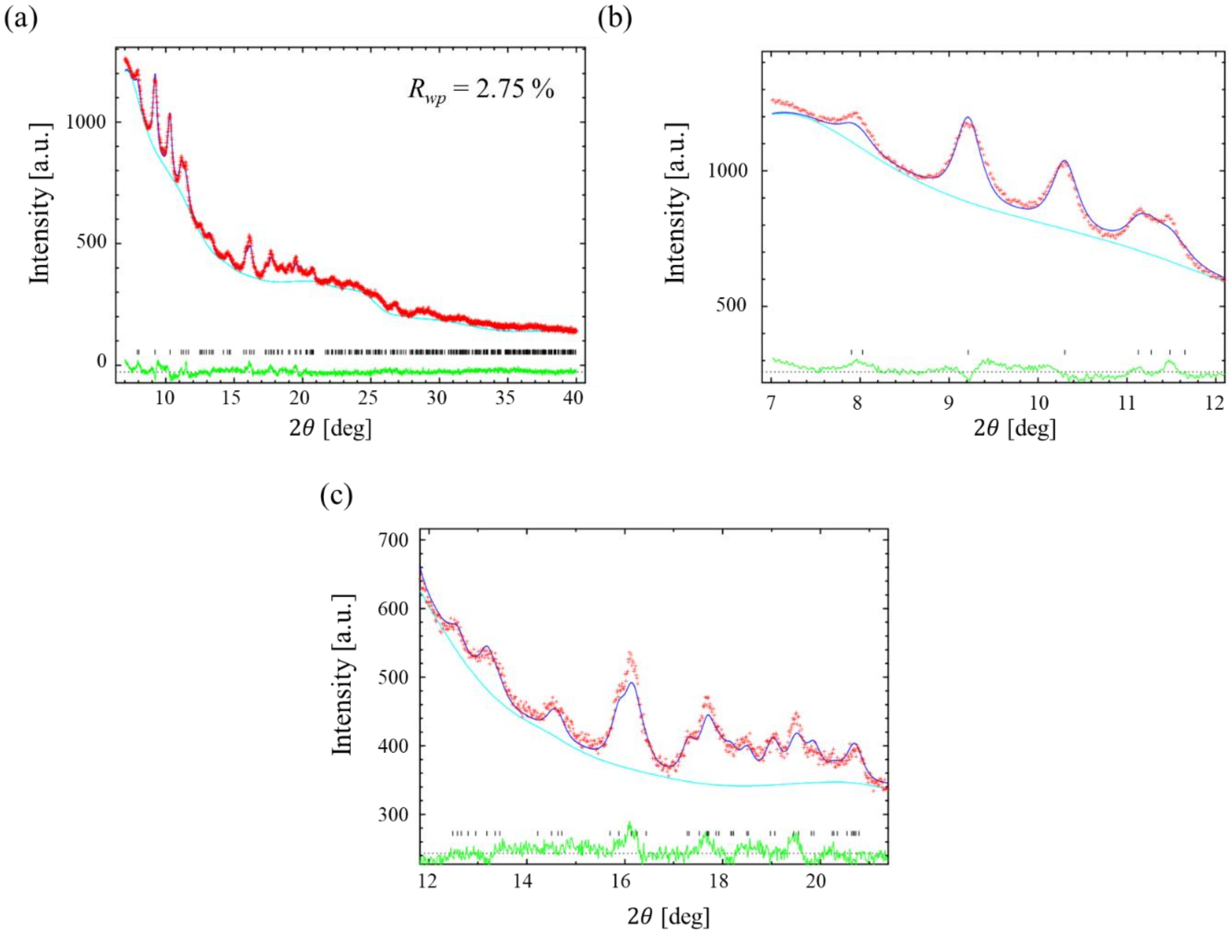

Figure 3.6.8 Powder diffraction data of monoclinic HfO_2 nanoparticle and calculated powder profile of Rietveld refinement. (a) 7 ° to 40 °, (b) 16.8 ° to 21.2 °.

Figure 3.6.8 shows the powder diffraction data and the powder profile of Rietveld refinement. Figure 3.6.8(a) shows the diffraction angle from 7 ° to 40 °. R_{wp} was 2.75 %. Figure 3.6.8(b) shows the diffraction angle from 7 ° to 12 °. The peak of 200 reflection at 11.6 ° was not appeared in the powder profile. The intensity of the powder profile at 7.9 ° was lower than that of the powder diffraction data by 40. Figure 3.6.8(c) shows the diffraction angle from 12 ° to 21.2 °. The intensity of the powder diffraction data at 17.8 ° was higher than that of the powder profile by 20. The intensity of the powder diffraction data at 19.6 ° was higher than that of the powder profile by 20. No Bragg peak was observed in the powder diffraction data at 19.8 °. The shape of the powder diffraction data of HfO_2 nanoparticles was not expressed by the powder profile of Rietveld refinement.

3.6.2 Calculation of powder profiles by Debye Scattering Equation

The powder diffraction data of nanoparticles were not expressed by the powder profiles of Rietveld refinement calculated from the average structure model of crystals. For Ag nanoparticles, the positions of 111 and 200 reflections in the powder diffraction data were consistent with the calculated powder profiles. FWHM of 200 reflection was broader than that of the powder profile. Ozawa investigated the effect of the stacking fault to the powder profile for Ag nanoparticles [29]. These results indicated the necessity of modelling the effect of twin faulting.

For ZrO_2 and HfO_2 nanoparticles, the deviation between the powder diffraction data and the powder profiles appeared for some diffraction angles. The deviations appeared mainly around Bragg peaks of monoclinic phase of ZrO_2. The dependence of the deviations on Miller index were unclear due to the serious overlap of Bragg peaks. These effects were probably due to the small size or the lattice defects in the structure of nanoparticles. The twin faulting was frequently observed in the structure of HfO_2 and ZrO_2 nanocrystals [78], [79].

We investigated the usefulness and the effectiveness of DSE for modelling the effects of the size and twin faulting to the powder profiles. The structure models of nanoparticles were constructed for calculating the powder profiles by DSE. The effects of the size and twin faulting to the powder profiles were systematically studied by comparing the powder profiles calculated from the structure models of Ag, ZrO_2 and HfO_2 nanoparticles. The effect of the number, the position, and the separation of twin faulting were also investigated for Ag, ZrO_2 and HfO_2 nanoparticles.

3.6.2.1 Ag 10 nm nanosphere

The effect of the size and twin faulting of nanoparticles to the powder profiles of Ag nanoparticles were investigated by DSE. The structure models were constructed for the analysis. The shape of nanoparticles were assumed as the sphere. The diameter of nanosphere were changed for the analysis. The structure models with twin faulting were constructed for the investigation of the effect of the lattice defect. The powder profiles were calculated from the structure models by DSE. We focused on the 200 reflection at 14.2 ° where the deviation were found in the Rietveld refinement.

3.6.2.1.1 Effect of size of Ag nanospheres

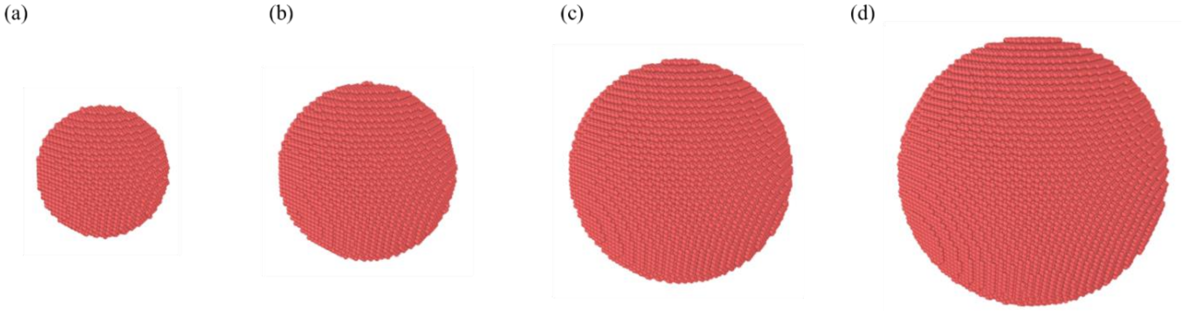

Figure 3.6.9 Structure models of Ag nanoparticle with different diameters of (a) 6 nm, (b) 8 nm, (c) 10 nm, and (d) 12 nm.

Figure 3.6.9 shows the structure models of Ag nanoparticles. The crystal structure was fcc structure. The lattice parameter was a = 4.0705 Å. The shape of models were sphere. Figure 3.6.9(a) shows the model with the diameter of 6 nm. Number of atoms in the model was 6699. Figure 3.6.9(b) shows the model with the diameter of 8 nm. Number of atoms in the model was 15947. Figure 3.6.9(c) shows the model with the diameter of 10 nm. Number of atoms in the model was 31173. Figure 3.6.9(d) shows the model with the diameter of 12 nm. The number of atoms in the models was 53741.

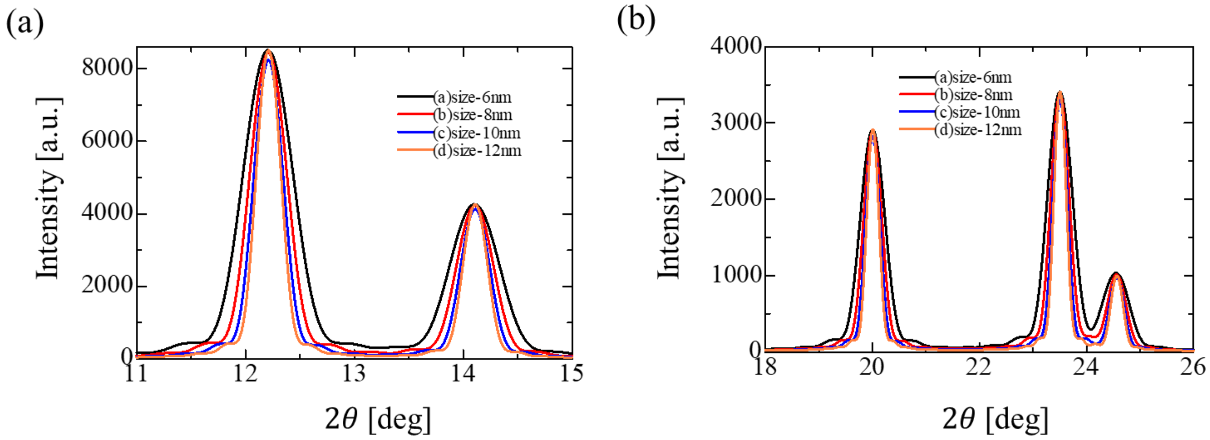

Figure 3.6.10 the powder profiles calculated from the structure models. (a) 11°to 15 °, (b) 18 ° to 26 °.

Figure 3.6.10 shows the powder profiles calculated from the structure models of Ag nanoparticle. Figure 3.6.10(a) shows the diffraction angle from 11 ° to 15 °. FWHM of 111 reflection at 12.5 ° was 0.3 ° for the structure model with the diameter 12 nm and 0.7 ° for the structure model with the diameter of 6 nm. FWHM of 200 reflection at 14.2 ° was 0.3 ° for the structure model with the diameter 12 nm and 0.7 ° for the structure model with the diameter of 6 nm. All diffraction peaks in this angle were broadened almost equally by decreasing the size of structure models.

Figure 3.6.10(b) shows the diffraction angle from 18 ° to 26 °. FWHM of 220 reflection at 20.0 ° was 0.3 ° for the structure model with the diameter 12 nm and 0.7 ° for the structure model with the diameter of 6 nm. FWHM of 222 reflection at 24.5 ° was 0.3 ° for the structure model with the diameter 12 nm and 0.7 ° for the structure model with the diameter of 6 nm. All diffraction peaks in this angle were almost equally broadened by decreasing the size of structure models.

3.6.2.1.2 Effect of twin faulting in Ag nanospheres

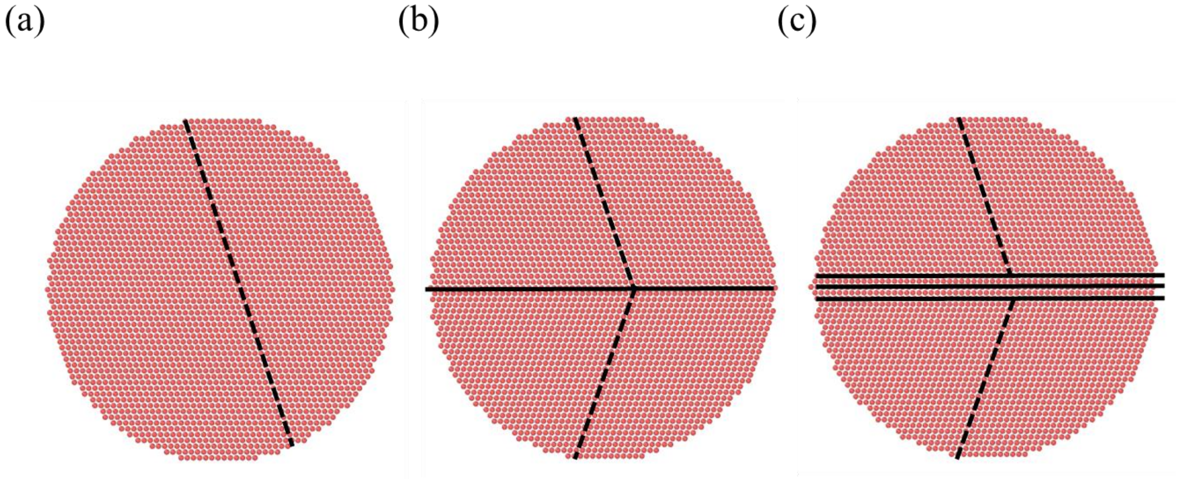

Figure 3.6.11 structure models of fcc Ag nanoparticle. (a) no faulting, (b) one layer of twin faulting, (c) three layers of twin faulting.

Figure 3.6.11 shows the structure models of Ag nanoparticle. Three structure models of Ag nanosphere were constructed for the analysis. The crystal structure of the model was fcc structure. Lattice constant was a = 4.0705 Å. The diameter of spheres was 14 nm. Twin faulting was inserted into two models. Blacked dashed lines show the direction of stacking sequence of the Ag atoms. Black lines show the positions of twin faulting. Figure 3.6.11 (a) shows the structure model without faulting. The number of atoms in the model was 85135. Figure 3.6.11 (b) shows the structure model with one layer of the twin faulting. The number of atoms in the model was 86040. Figure 3.6.11 (c) shows the structure model with three layers of twin faulting. The number of atoms in the model was 85876.

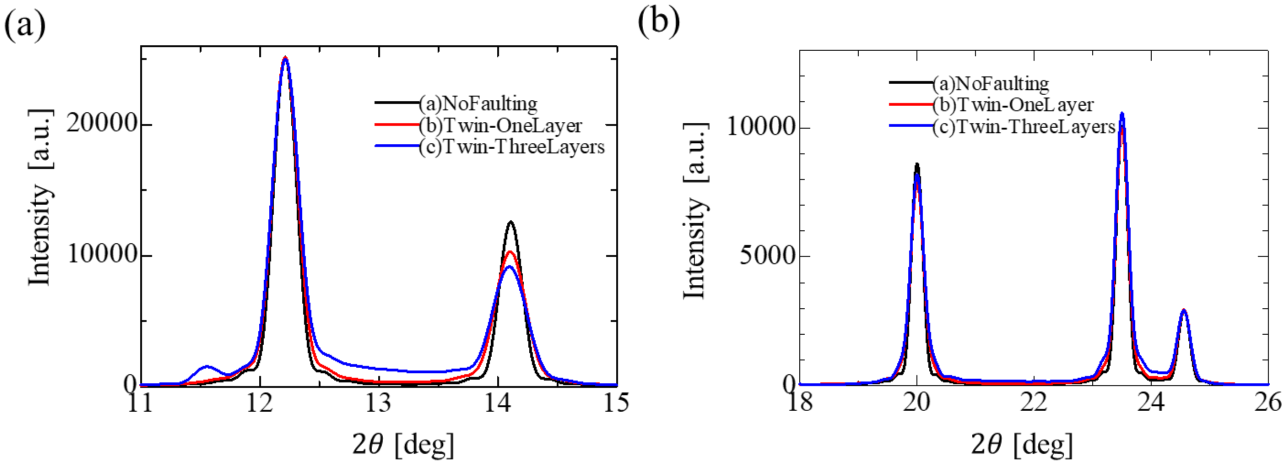

Figure 3.6.12 Powder profile of Ag nanoparticles. (a) 11° to 15 °, (b) 18 ° to 26 °.

Figure 3.6.12 shows the powder profiles of Ag nanoparticle calculated from structure models. Figure 3.6.12(a) shows the diffraction angle from 11 ° to 15 °. FWHM of the 111 reflection of the structure model with three layers of twin faulting at 12.8 ° was larger than that of the model without twin faulting by 0.02 °. Ozawa calculated the powder profile from the structure model of Ag nanosphere by DSE, and reported that the powder profile of Ag nanoparticles with stacking fault provided the broadening of 200 reflection [29]. The powder profile of the model with three layers of twin faulting showed the additional finding on Ozawa's result. Satellite peak appeared at 11.5 ° in the powder profile of the structure model with three layers of twin faulting. FWHM of 200 reflection of the structure model with three layers of twin faulting was larger than that of the structure model with one layer of twin faulting by 0.07 °.

Figure 3.6.12(b) shows the diffraction angle from 18 ° to 26 °. FWHM of 220 reflection of the structure models with three layers of twin faulting were larger than that of model without faulting by 0.02 °. FWHM of 311 reflection of the structure models with three layers of twin faulting was larger than that of the model without faulting by 0.02 °. The broadening of 200 reflection was modelled by the twin faulting in the structure models of Ag nanoparticle. The shape of 111 reflection of the powder profile of three layers of twin faulting which showed satellite peak was similar to the powder diffraction data of Ag nanoparticles.

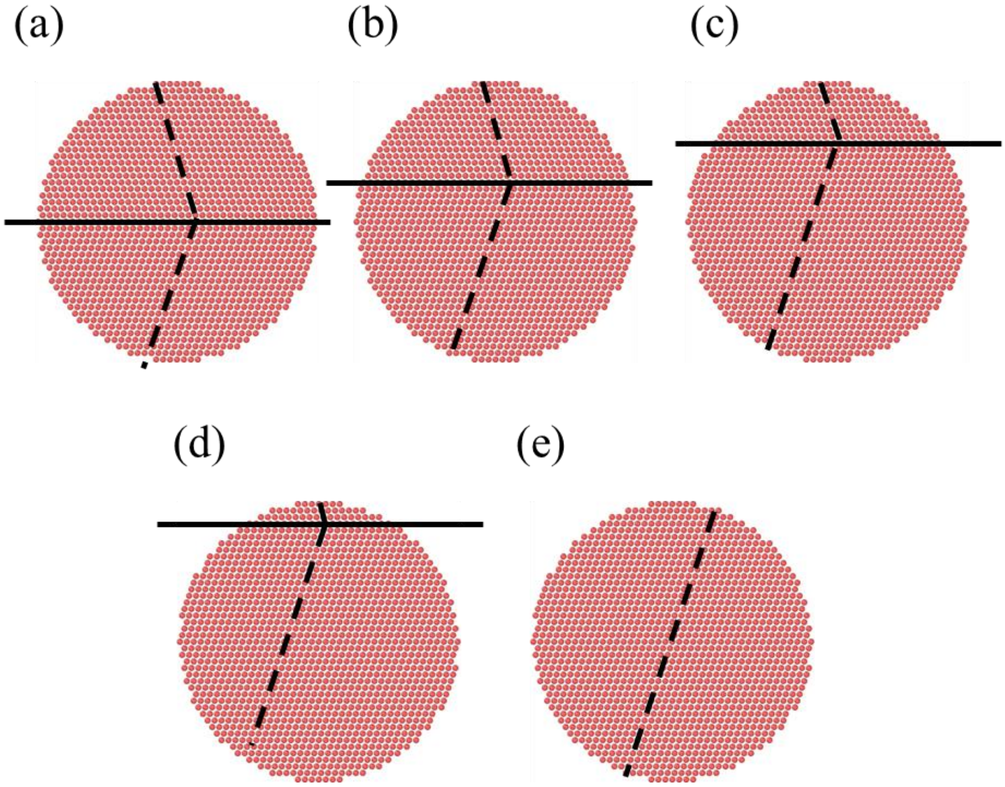

Figure 3.6.13 Structure models of Ag nanoparticle with the twin faulting in different positions. (a) Center, (b) above 6 layers from the center, (c) above 12 layers from the center, (d)above 18 layers from the center, (e)no faulting.

Figure 3.6.13 shows the structure models of Ag nanoparticle with twin faulting. Crystal structure of the model was fcc structure. The lattice parameter was $a = 4.0705$ Å. The diameter of the spheres was 10 nm. Number of the atoms in the model was 31173. One layer of twin faulting was inserted into the structure models. Position of the twin faulting was shifted upward from the center to the edge of the sphere. Figure 3.6.13(a) shows structure model with twin faulting at the center of sphere. Figure 3.6.13(b) shows structure model with twin faulting at 6 layers above from the center of sphere. Figure 3.6.13(c) shows structure model with twin faulting at 12 layers above from the center of sphere. Figure 3.6.13(d) shows structure model with twin faulting at 18 layers above from the center of sphere. Figure 3.6.13(e) shows structure model without twin faulting.

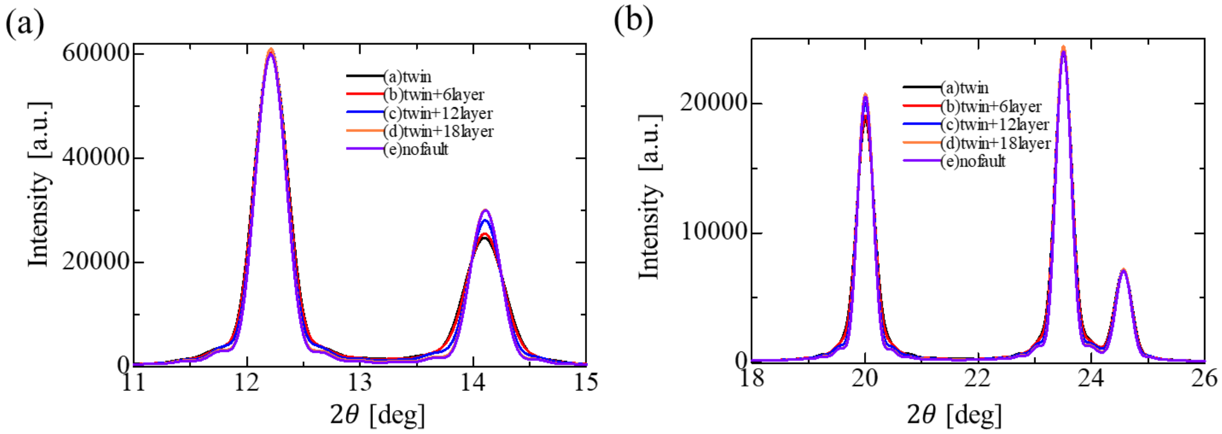

Figure 3.6.14 The powder profile of structure models. (a) 11° to 15 °, (b) 18 ° to 26 °.

Figure 3.6.14 shows the powder profile calculated from the structure models of nanoparticles. The horizontal axis is the diffraction angle. The vertical axis is intensity. The intensity of powder profiles were normalized to the peak height of 111 reflection. Figure 3.6.14(a) shows the diffraction angle from 11° to 15 °. FWHM of 200 reflection of the model with faulting at the center of the sphere at 14.2 ° was larger than that of the model without faulting by 0.05 °. FWHM of 200 reflection has decreased with the shift of the position of twin faulting from the center to the edge of the sphere. Figure 3.6.14(b) shows 18 ° to 26 °. FWHM of 220 reflection has decreased with the position of twin faulting was shifted from the center to the edge of the structure model.

The larger broadening of twin faulting at the center of the sphere was due to the larger fraction of atoms related to the structure around the faulting. The position of faulting does not mean that all the nanoparticles in powder sample have the twin faulting at the specific position. This probably reflects the fraction of nanoparticles which have the twin faulting, since the powder profiles of the structure models with faulting shifted by 6, 12 and 18 layers can be expressed as the linear combination of powder profiles of the model without faulting and the model with faulting at the center of the sphere.

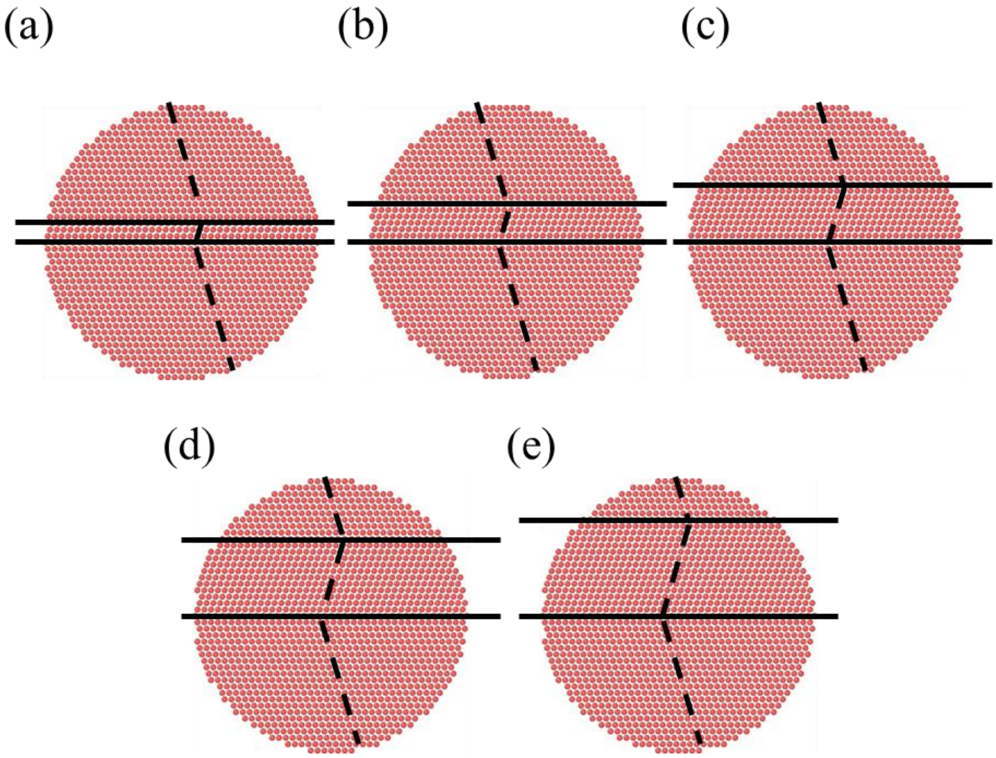

Figure 3.6.15 Structure models of Ag nanoparticle with the two layers of twin faulting separated by different distance. (a) two layers, (b) 5 layers, (c) 8 layers, (d) 11 layers, (e) 14 layers.

Figure 3.6.15 shows the structure models of Ag nanoparticle with twin faulting. The crystal structure of the model was the fcc structure. The lattice parameter was a = 4.0705 Å. Diameter of the spheres was 10 nm. Number of the atoms in the model was 31958. Two layers of twin faulting were inserted in the structure models with different separation. Figure 3.6.15(a) shows the structure models with the separation of two layers between twin faulting. Figure 3.6.15(b) shows the structure models with the separation of 5 layers between twin faulting. Figure 3.6.15(c) shows the structure models with the separation of 8 layers between twin faulting. Figure 3.6.15(d) shows the structure models with the separation of 11 layers between twin faulting. Figure 3.6.15(e) shows the structure models with the separation of 14 layers between twin faulting.

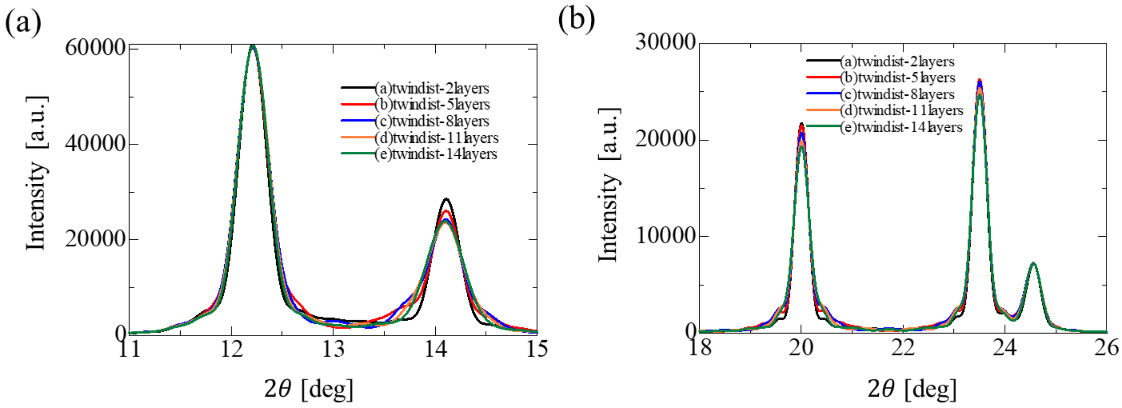

Figure 3.6.16 The powder profile of structure models. (a) 11° to 15 °, (b) 18 ° to 26 °.

Figure 3.6.16 shows the powder profiles calculated from the structure models of nanoparticles. The intensity of powder profiles were normalized to the peak height of 111 reflection at 12.8 °. Figure 3.6.16 (a) shows the diffraction angle from 11° to 15 °. The shape of the tail of 200 reflection at 14.2 ° was modulated with the increase of the separation between twin faulting. Figure 3.6.16 (b) shows 18 ° to 26 °. The shape of the tail of 220 reflection at 20 ° was modulated with the increase of the separation between twin faulting.

The effect of the size and the twin faulting to the powder profiles were systematically investigated by the powder profiles of the structure models of Ag nanoparticles. The index dependence of the broadening of Bragg peaks by twin faulting were different from those by the twin faulting. 111 reflection and 200 reflection were almost equally broadened by the size reduction. Twin faulting caused the larger broadening of 200 reflection than that of 111 reflection. A satellite peak appeared at the lower angle of the position of 111 reflection in the powder profile of the structure model with three layers of twin faulting.

3.6.2.2 ZrO_2

The effect of the size and the lattice defect of nanoparticles to the powder profile was investigated by DSE. The structure models of monoclinic ZrO_2 were constructed for the analysis. The shape of structure model was assumed as the elliptic cylinder. The height, short axis and long axis of the elliptic cylinder were changed for investigating the effect of the size. The powder profiles were calculated from the structure models by DSE. We especially focused on the intensity of powder profiles around 18.5 ° and 26.8 ° where the deviations were found in the Rietveld refinement.

3.6.2.2.1 Effect of size of ZrO_2 nanoparticles

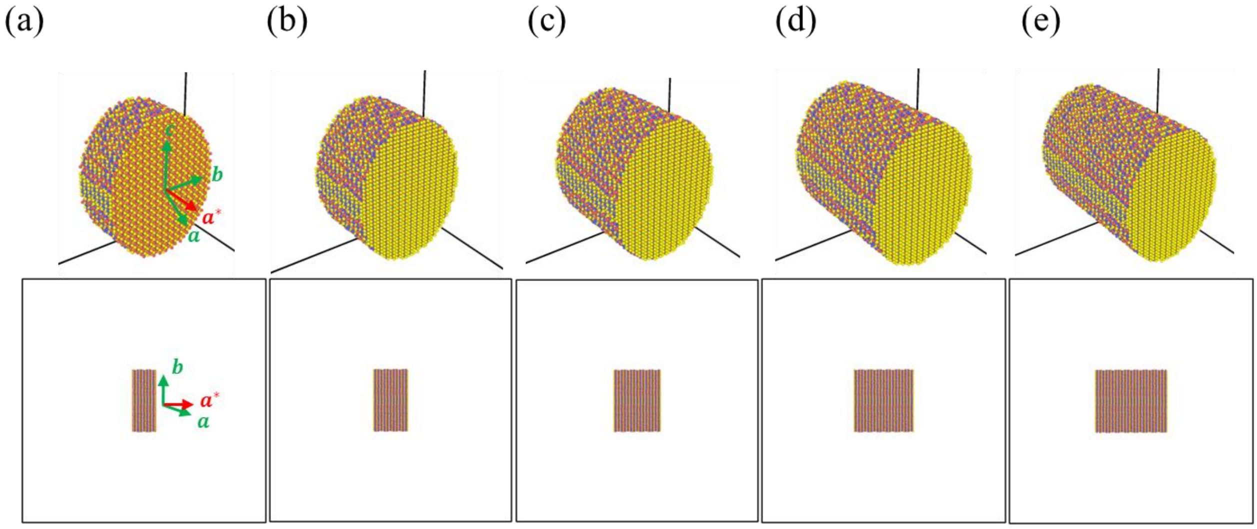

Figure 3.6.17 Structure models of ZrO_2 nanoparticle. Height of the elliptic cylinders are (a) 3.8 nm, (b) 5.8 nm, (c) 7.8 nm, (d) 9.8 nm, (e) 11.8 nm.

Figure 3.6.17 shows the structure models of ZrO_2 nanoparticle. Red spheres show zirconium atoms. Blue and yellow spheres are oxygen atoms. Green arrows show the direction of axes of the unit cell. Red arrow shows the direction of *a** axis of reciprocal lattice vector. Upper figures show structure models. Lower figures show structure models from *b* direction. Crystal structure by Howard *et al*. was used for the structure model [76]. Short axis is parallel to *b* direction. Long axis is parallel to c direction. Short axis is 8.2 nm. Long axis is 10.2 nm.

Number of atoms in the structure model with the height of 3.8 nm was 21808. Number of atoms in the structure model with the height of 5.8 nm was 32214. Number of atoms in the structure model with the height of 7.8 nm was 43612. Number of atoms in the structure model with the height of 9.8 nm was 54982. Number of atoms in the structure model with the height of 11.8 nm was 66340.

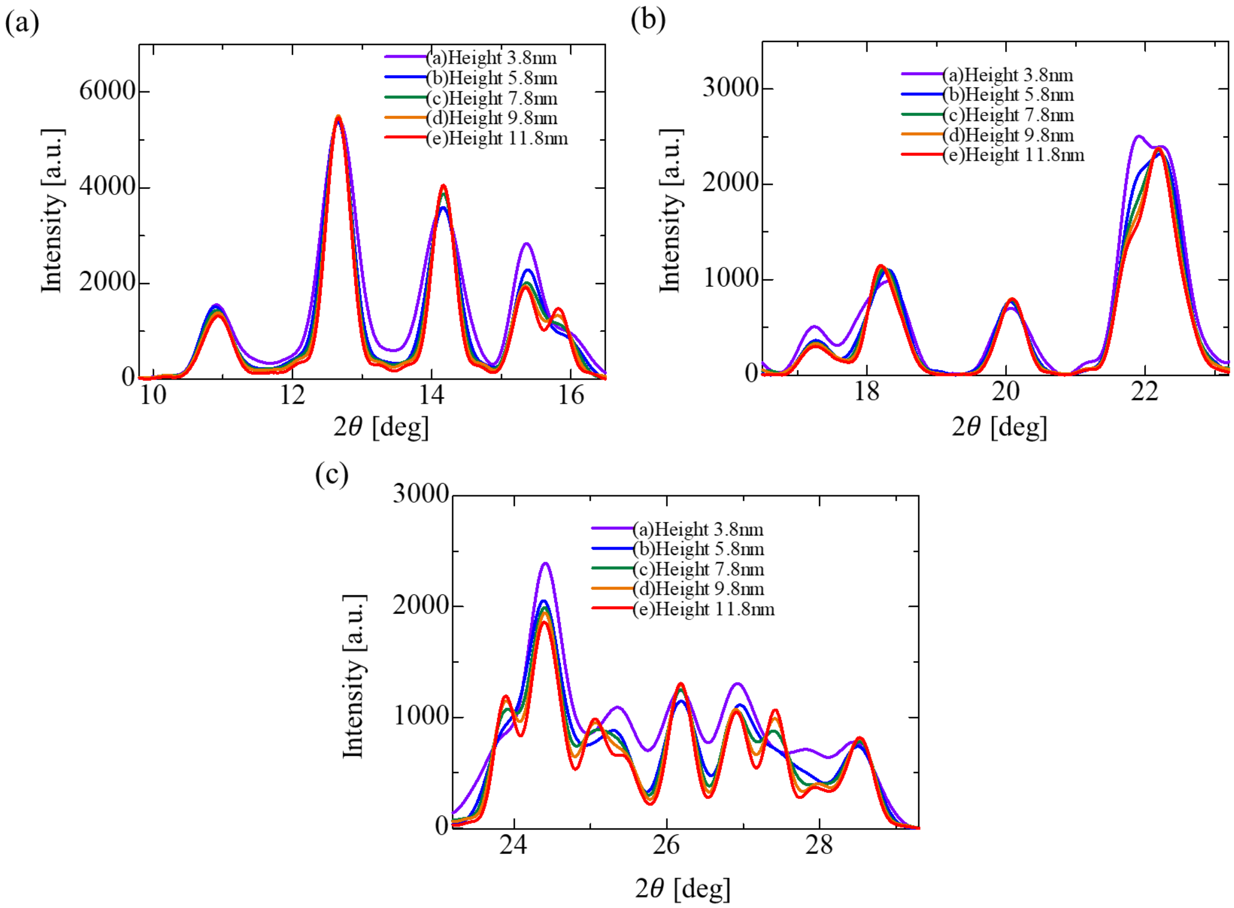

Figure 3.6.18 Powder profiles of the structure models. (a) 9.8 ° to 16.5 °, (b) 16.5 ° to 23.2 °, (c) 23.2 ° to 29.3 °.

Figure 3.6.18 shows the powder profiles calculated from the structure models. The intensity of powder profiles were normalized to the peak height of -111 reflection at 12.8 °. Figure 3.6.18(a) shows the diffraction angle from 9.8 ° to 16.5 °. The peak height of 200 reflection at 15.8 ° has increased by 500 with the increase of the height of 8 nm. Figure 3.6.18(b) shows the diffraction angle from 16.5 ° to 23.2 °. The shift of a peak around 18.5 ° was less than 0.3 ° with the change of the height. The peak height of 022 reflection at 21.8 ° has decreased by 1000 with the increase of the height of 8 nm. Figure 3.6.18(c) shows the diffraction angle from 23.2 ° to 29.3 °. The peak height of -113 reflection at 24.3 ° has decreased by 800 with the increase of the height of 8 nm. The peak height at 26.8 ° of the powder profile of the model with the height of 3.8 nm was higher than that at 26.2 ° only by 50. In this powder profile, the peak of 200 reflection hasn't appeared at 15.8 °.

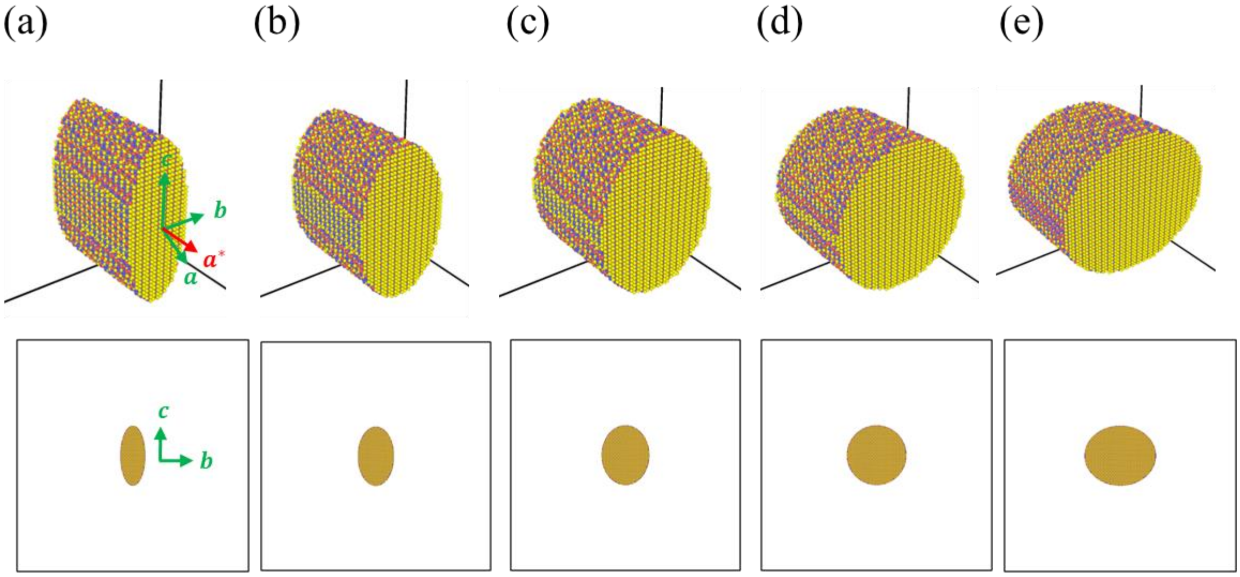

Figure 3.6.19 Structure models of ZrO_2 nanoparticle. Short axis of elliptic cylinders are (a) 4.2 nm, (b) 6.2 nm, (c) 8.2 nm, (d) 10.2 nm and (e) 12.2 nm.

Figure 3.6.19 shows structure models of ZrO_2nanoparticle. Definitions of colored spheres and arrows are the same as Figure 3.6.19. Shape and crystal structure of structure models are the same as Figure 3.6.17. Upper figures show the structure models. Lower figures show the structure models from a* direction. Height of the elliptic cylinder is 6.8 nm. Long axis is 10.2 nm.

Figure 3.6.19 (a) shows the structure model with the short axis of 4.2 nm. Number of atoms was 22328. Figure 3.6.19(b) shows the structure model with the short axis of 6.2 nm. Number of atoms was 32958. Figure 3.6.17(c) shows the structure model with the short axis of 8.2 nm. Number of atoms was 43612. Figure 3.6.17(d) shows the structure model with the short axis of 10.2 nm. Number of atoms was 54194. Figure 3.6.17(e) shows the structure model with the short axis of 12.2 nm. Number of atoms was 64794.

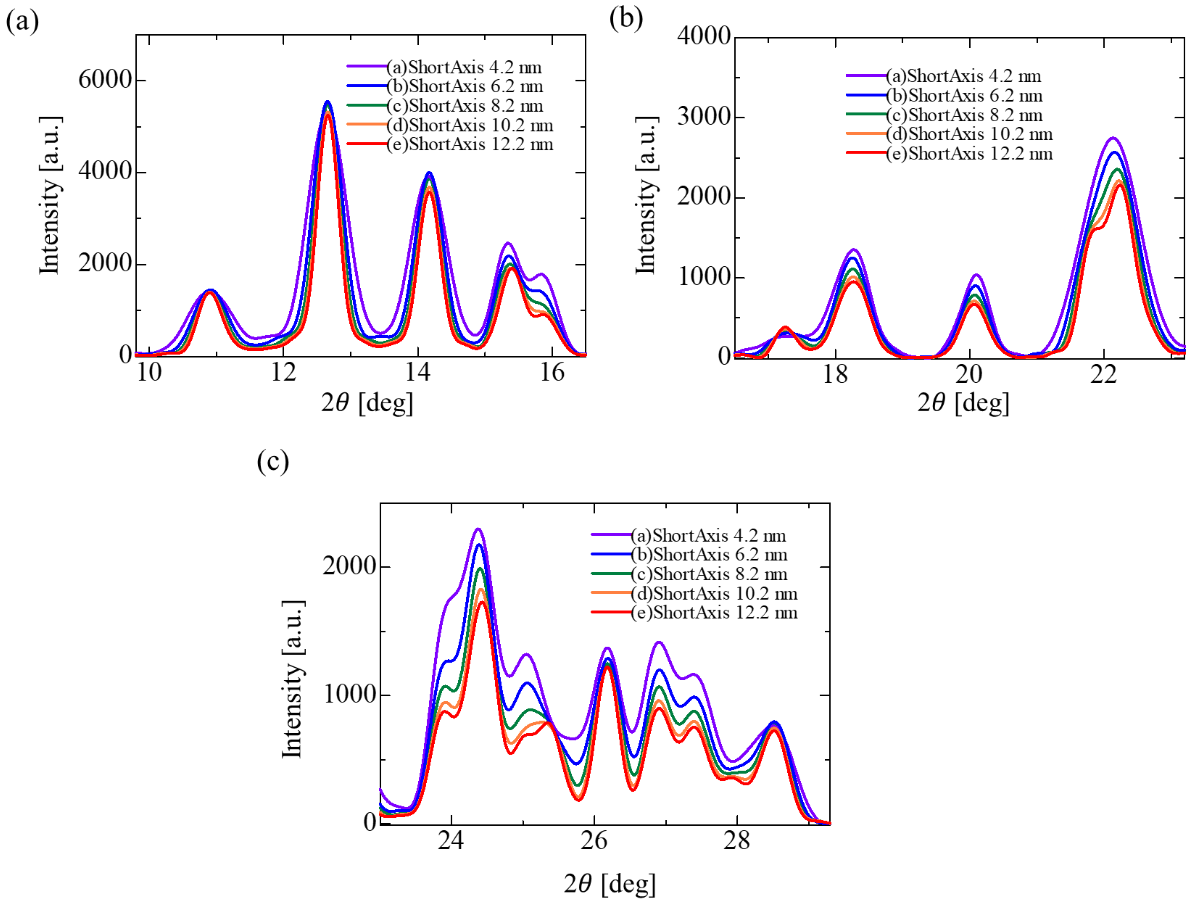

Figure 3.6.20 Powder profiles of the structure models. (a) 9.8 ° to 16.5 °, (b) 16.5 ° to 23.2 °, (c) 23.2 ° to 29.3 °.

Figure 3.6.20 shows the powder profiles calculated from the structure model. The intensity of powder profiles were normalized to the peak height of -111 reflection at 12.8 °. Figure 3.6.20 (a) shows the diffraction angle from 9.8 ° to 16.5 °. The peak height of 200 reflection at 15.8 ° has decreased by 1000 with the increasing the short axis of 8 nm. Figure 3.6.20 (b) shows the diffraction angle from 16.5 ° to 23.2 °. The peak around 18.5 ° was not shifted by changing the short axis. The peak height of 220 reflection at 22.1 ° has decreased by 1000 with increase of the short axis by 8 nm. Figure 3.6.20(c) shows the diffraction angle from 23.2 ° to 29.3 °. The peak height of 400 reflection at 23.8 ° has decreased by 700 with increase of the short axis by 8 nm. The peak height around 26.8 ° has increased by 500 with the increase of the short axis by 8 nm. In this case, the difference of intensity at 23.8 ° and 24.3° was less than 500.

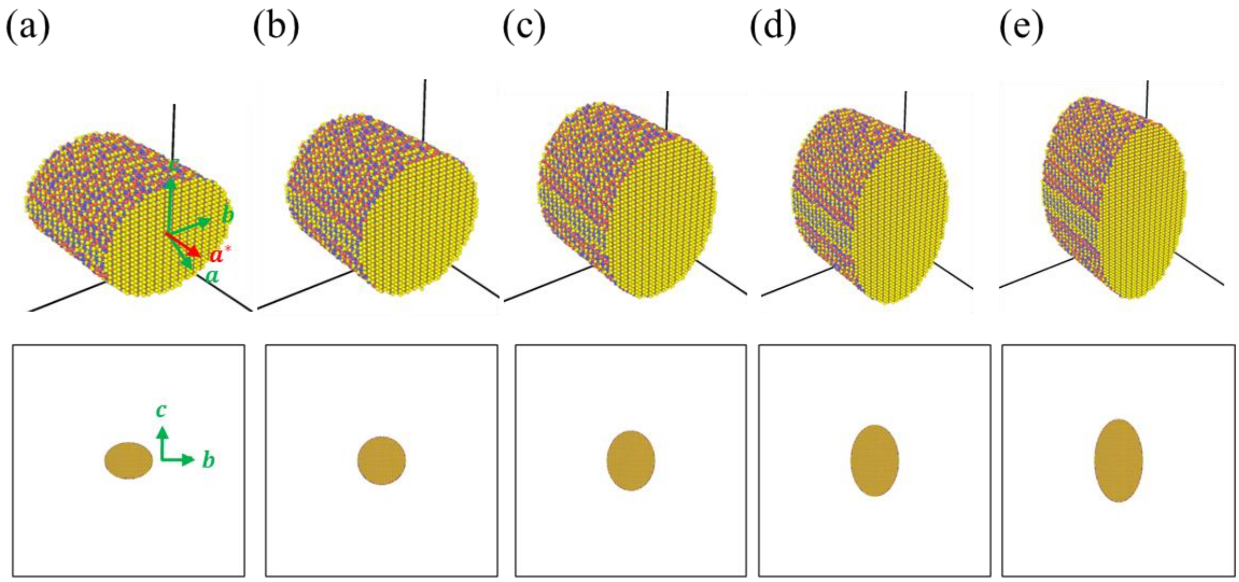

Figure 3.6.21 Structure models of ZrO_2 nanoparticle. Long axis of elliptic cylinders are (a) 6.2 nm, (b) 8.2 nm, (c) 10.2 nm, (d) 12.2 nm are (e) 14.2 nm.

Figure 3.6.21 shows structure models of ZrO_2 nanoparticle. Definitions of colored spheres and arrows are the same as Figure 3.6.21. Shape and crystal structure of structure models are the same as Figure 3.6.21. Upper figures show the structure models. Lower figures show the structure models from a* direction. Height of the elliptic cylinder is 6.8 nm. Short axis is 8.2 nm.

Figure 3.6.21 (a) shows the structure model with the long axis of 6.2 nm. Number of atoms was 26504. Figure 3.6.21(b) shows the structure model with the long axis of 8.2 nm. Number of atoms was 35044. Figure 3.6.21(c) shows the structure model with the long axis of 10.2 nm. Number of atoms was 43612. Figure 3.6.21(d) shows the structure model with the long axis of 12.2 nm. Number of atoms was 52162. Figure 3.6.21(e) shows the structure model with the long axis of 14.2 nm. Number of atoms was 60714.

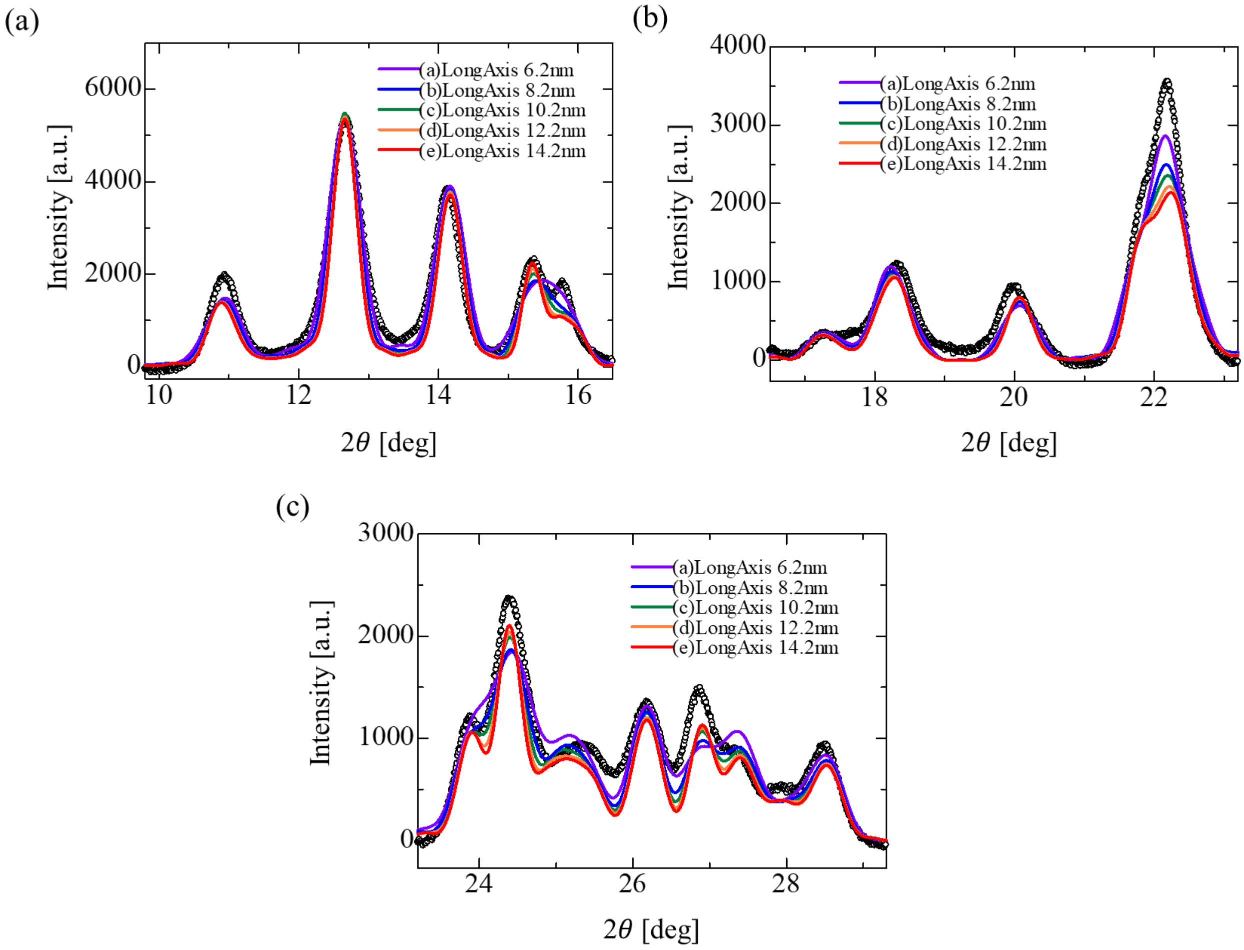

Figure 3.6.22 Powder profiles of the structure models. (a) 9.8 ° to 16.5 °, (b) 16.5 ° to 23.2 °, (c) 23.2 ° to 29.3 °.

Figure 3.6.22 shows the powder profiles calculated from the structure model. The intensity of powder profiles were normalized to the peak height of -111 reflection at 12.8 °. Figure 3.6.22 (a) shows the diffraction angle from 9.8 ° to 16.5 °. The peak height of 002 reflection at 15.2 ° has increased by 500 with increase of the long axis by 8 nm. Figure 3.6.22 (b) shows the diffraction angle from 16.5 ° to 23.2 °. The shift of peak position at 18.5 ° was less than 0.3° by the change of the long axis. The peak height of 220 reflection at 22.1 ° has decreased by 1000 with increase of the long axis by 8 nm. Figure 3.6.20(c) shows the diffraction angle from 23.2 ° to 29.3 °. The peak height of 113 reflection at 23.8 ° has increased by 200 with increase of the long axis by 8 nm. The peak height at 26.8 ° has increased by 200 with increase of the long axis by 8 nm. In this case, peak of 200 reflection at 15.8 ° hasn't appeared in the powder profile.

The size effects to the powder profiles of ZrO_2 nanoparticles were investigated by changing the length, the short axis and the long axis of the structure model. The shift of the peak at 18.5 ° was less than 0.3 ° by changing the length, the short axis and the long axis by 8 nm. The peak height at the 26.8 ° has increased by the increase of the long axis, the decrease of the short axis, or the decrease of the length of the elliptic cylinder. 200 peak at the 15.8 ° has vanished by the increase of the long axis and by the decrease of the length. The peak height at 23.8 °

became close to that at 24.3 ° by the decrease of the short axis.

3.6.2.2.2 Effect of twin faulting in ZrO_2 nanoparticles

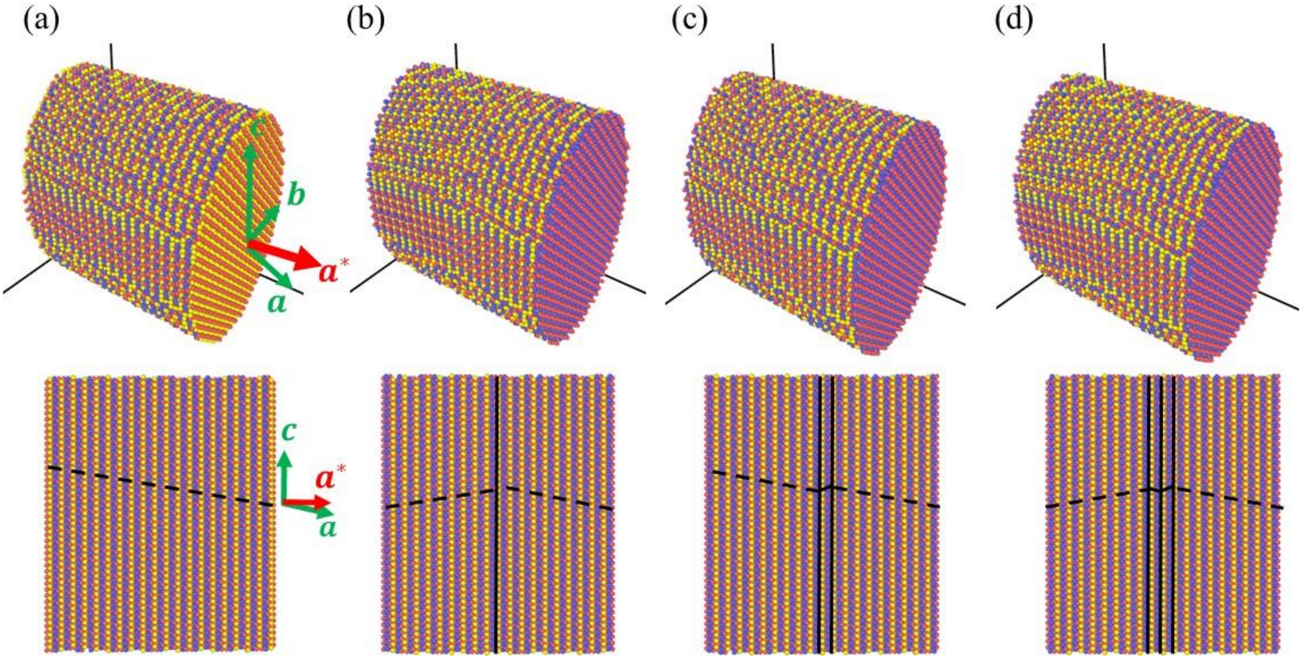

Figure 3.6.23 Structure models of ZrO_2 nanoparticle. (a) No faulting, (b) one layer, (c) two layers, (d) three layers.

Figure 3.6.23 shows the structure models of ZrO_2-nanoparticle. Red spheres are zirconium atoms. Blue and yellow spheres are oxygen atoms. Crystal structure by Howard *et al.* used for the structure model [76]. The lattice parameters were obtained from the Rietveld refinement. Green arrows show the direction of axes of unit cell. Red arrow shows the direction of *a** axis of reciprocal lattice vector. Upper figures show structure model. Lower figures show the cutting surface of structure model by ac plane. Height was 10 nm. Short axis was 8 nm. Long axis was 12 nm. Number of atom in the model was 64066.

Figure 3.6.23(a) shows the structure model with no faulting. Black dashed line shows the direction of stacking sequence of zirconium atoms. Figure 3.6.23(b) shows the structure model with one layer of twin faulting. Black line shows the position of twin faulting. Figure 3.6.23(c) shows the structure model with two layers of twin faulting. Figure 3.6.23(d) shows the structure model with three layers of twin faulting.

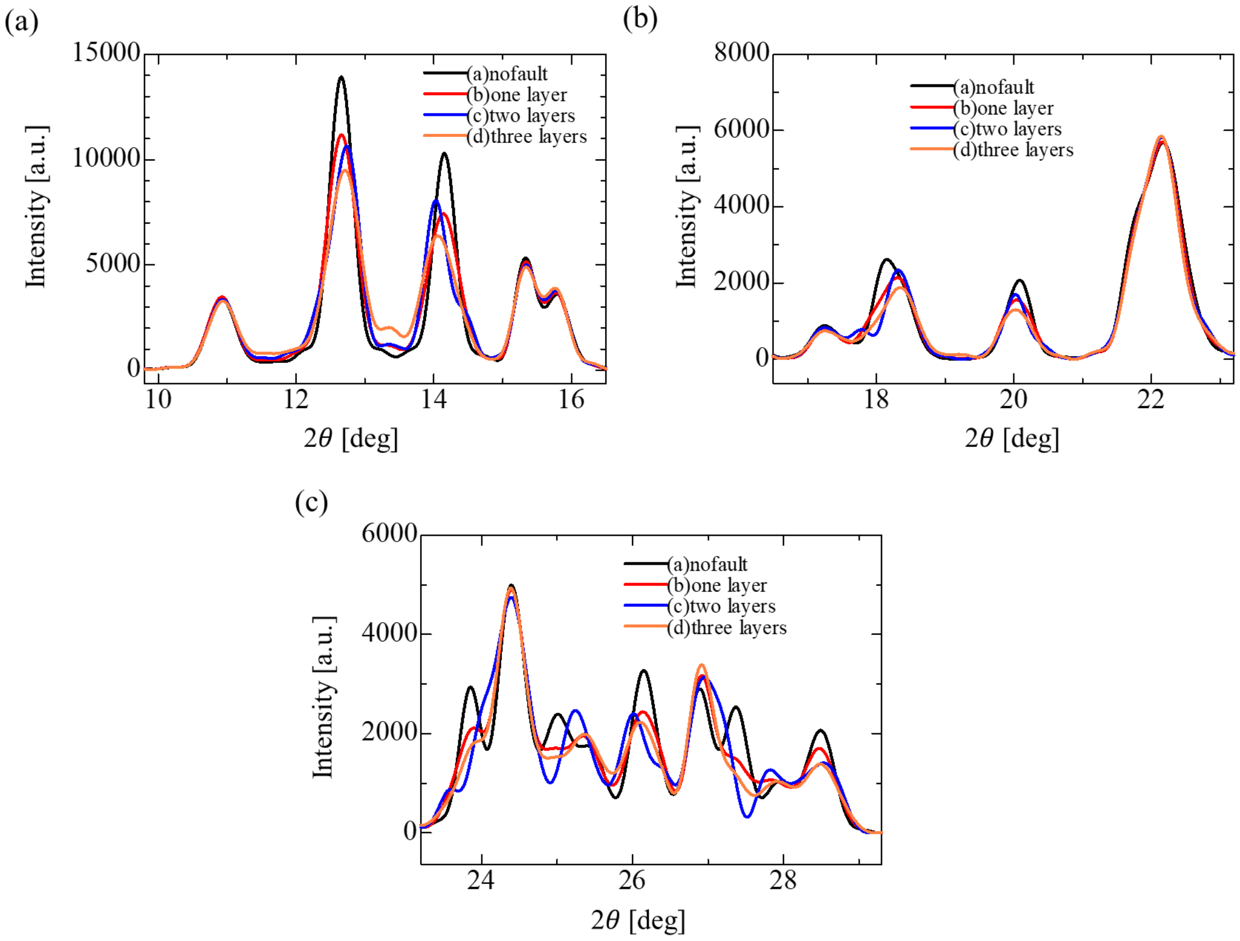

Figure 3.6.24 Powder profiles of the structure models. (a) 9.8 ° to 16.5 °, (b) 16.5 ° to 23.2 °, (c) 23.2 ° to 29.3 °.

Figure 3.6.24 shows the powder profiles calculated from the structure model. Figure 3.6.24 (a) shows the diffraction angle from 9.8 ° to 16.5 °. The positions of -111 reflection of the structure models with two and three twin faulting were shifted by 0.2 ° in the positive direction compared with that of the model without faulting. Figure 3.6.24 (b) shows the diffraction angle from 16.5 ° to 23.2 °. The positions of peak at 18.4 ° of the structure models with twin faulting were shifted by 0.3 ° in the positive direction compared with that of the structure model without faulting. Figure 3.6.20(c) shows the diffraction angle from 23.2 ° to 29.3 °. The peak height at 26.8 ° was higher than that at 26.2 ° in the powder profile of the model with one, two and three layers of twin faulting. The peak at 27.2° was not observed in the powder profiles of the structure models with twin faulting.

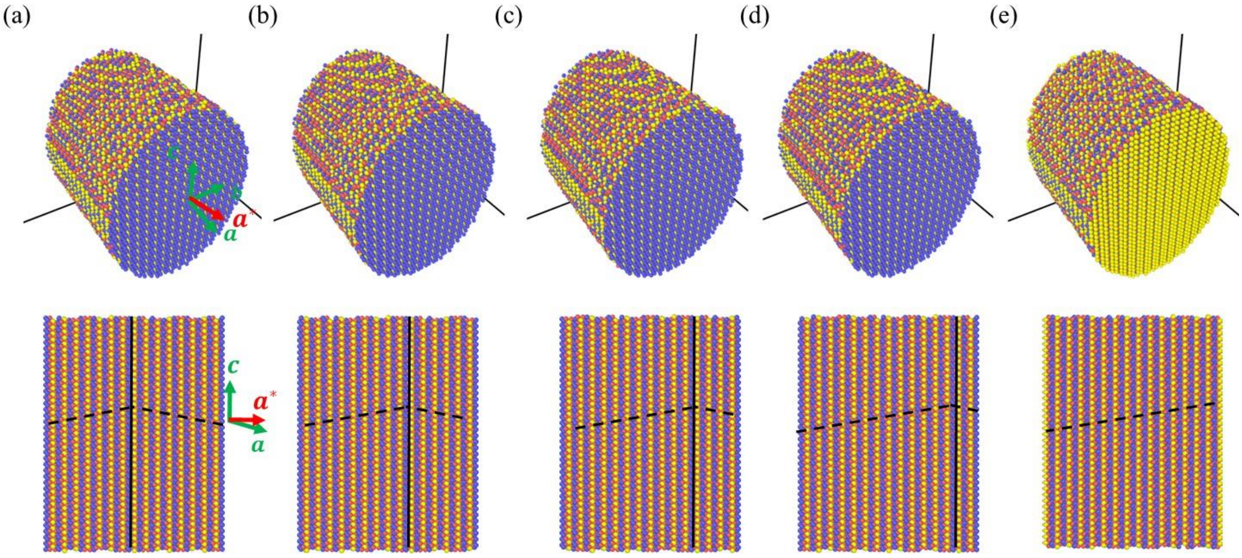

Figure 3.6.25 Structure models of ZrO_2 nanoparticle with different positions of the twin faulting. (a) Twin faulting at the center, (b) shifted by two layers, (c) shifted by four layers, (d) shifted by six layers, and (e) no faulting.

Figure 3.6.25 shows the structure models of ZrO_2 nanoparticle. Definitions of the colored spheres and arrows are the same as Figure 3.6.23. Shape and crystal structure of structure models are the same as Figure 3.6.23. Upper figures show the structure models. Lower figures show the cutting surface by ac plane. Height was 7.8 nm. Short axis was 8.2 nm. Long axis was 10.2 nm. Number of atoms was 43612.

Figure 3.6.25(a) shows the structure model with twin faulting at the center. Black lines show the direction of the stacking sequence of zirconium atoms. Black dashed line shows the position of twin faulting. Figure 3.6.25(b) shows the structure model with twin faulting. Position of the twin faulting was shifted by two layers from the center in the positive direction of a^* axis. Figure 3.6.25(c) shows the structure model with twin faulting shifted by four layers. Figure 3.6.25(d) shows the structure model with twin faulting shifted by six layers. Figure 3.6.25(e) shows the structure model with no faulting.

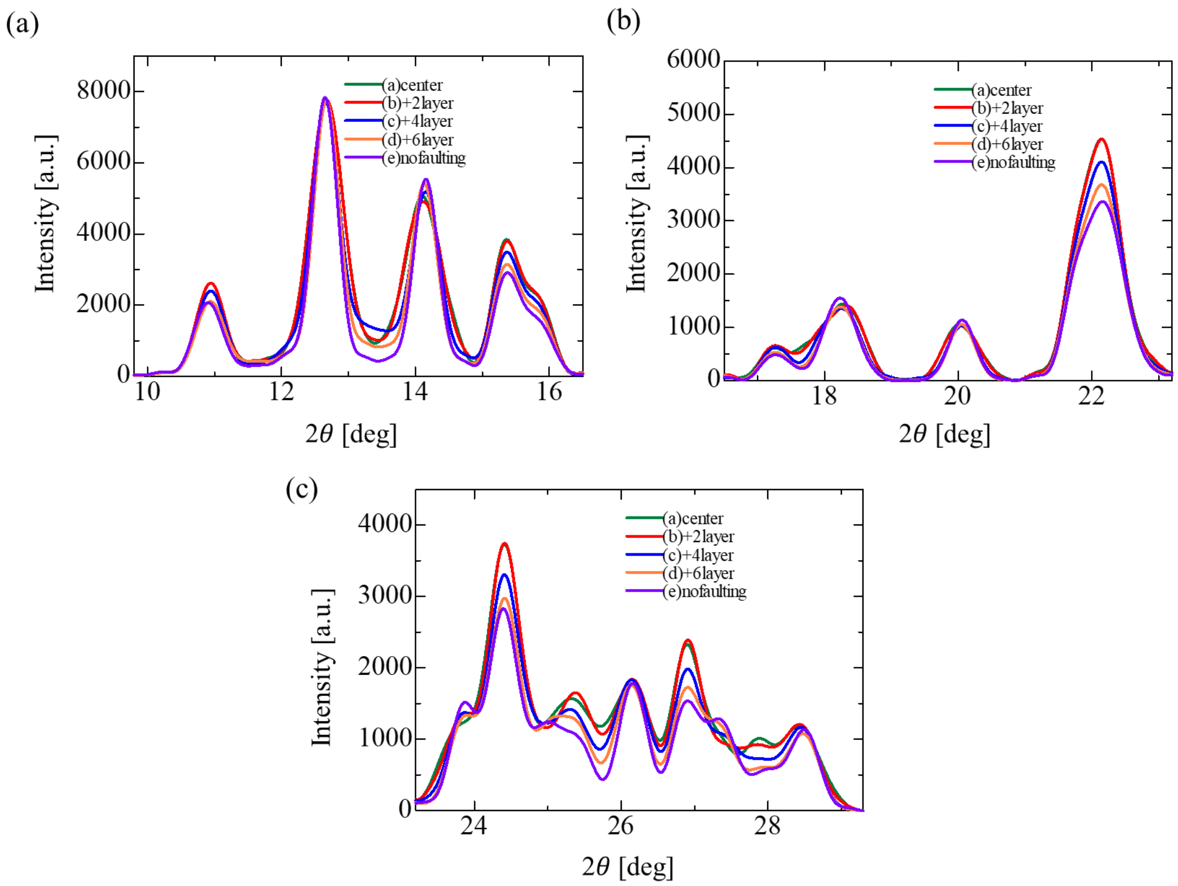

Figure 3.6.26 Powder profiles of the structure models (a) 9.8 ° to 16.5 °, (b) 16.5 ° to 23.2 °, (c) 23.2 ° to 29.3 °.

Figure 3.6.26 shows the powder profiles calculated from the structure model. The intensity of powder profiles were normalized to the peak height of -111 reflection at 12.8 °. Figure 3.6.26(a) shows the diffraction angle from 9.8 ° to 16.5 °. The width of the 111 reflection of the structure model of one twin faulting was larger than that of the structure model without faulting by 0.2 °. Figure 3.6.26 (b) shows the diffraction angle from 16.5 ° to 23.2 °. Peak height of 220 reflection at 22.1 ° of the structure model of one twin faulting was lower than that of the structure model without faulting by 1000. Figure 3.6.26 (c) shows the diffraction angle from 23.2 ° to 29.3 °. The peak height of 113 reflection at 26.8 ° of the structure model of one twin faulting was higher than that of the structure model without faulting by 1000. Figure 3.6.26 (d) shows the diffraction angle from 29.3 ° to 38 °. The peak height of 204 reflection at 37 ° of the structure model of one twin faulting was higher than that of the structure model without faulting by 500.

The position of faulting does not mean that all the nanoparticles in powder sample have the twin faulting at the specific position. This probably reflects the fraction of nanoparticles which have the twin faulting, since the powder profiles of the structure models with faulting shifted by 2, 4 and 6 layers can be expressed as the linear combination of powder profiles of the model without faulting and the model with faulting at the center.

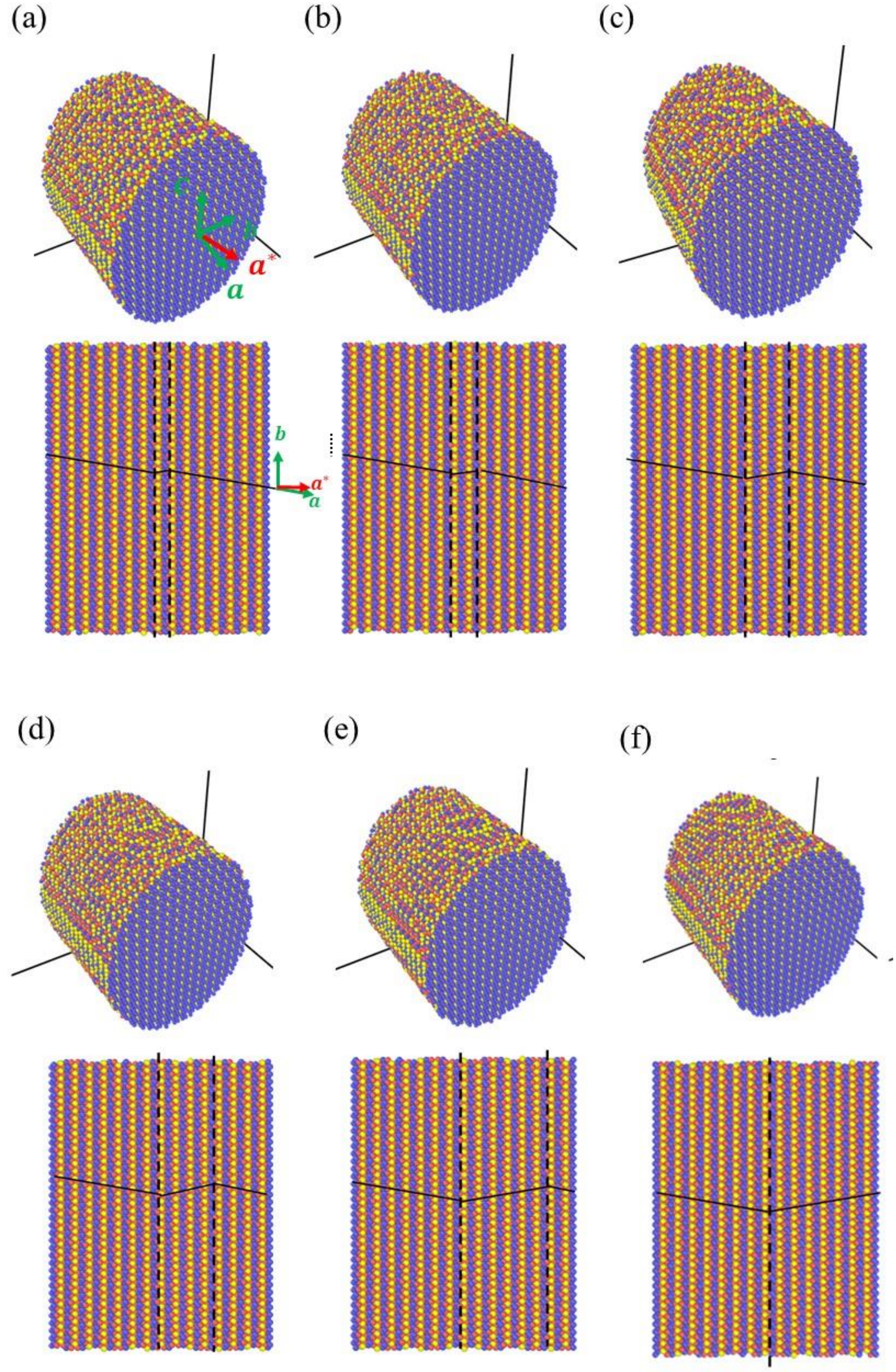

Figure 3.6.27 Structure models of ZrO_2 nanoparticle with the different separation between two twin faulting. (a) Two layers of twin faulting, (b) two twin layers of faulting with the separation by one layer, (c) two layers, (d) three layers, (e) five layers, (f) one layer of twin faulting.

Figure 3.6.27 shows the structure models of ZrO_2 nanoparticle. Definitions of the colored spheres and arrows are the same as Figure 3.6.23. Shape and crystal structure of structure models are the same as Figure 3.6.23. Upper figures show the structure models. Lower figures show the cutting surface by ac plane. Height of is 7.8 nm. Short axis is 8.2 nm. Long axis is 10.2 nm. Number of atoms is 43612.

Figure 3.6.27(a) shows the structure model with two twin faulting at the center. Black lines show the direction of the stacking sequence of zirconium atoms. Black dashed line shows the position of twin faulting. Figure 3.6.27(b) shows the structure model with two layers of twin faulting separated by one layer of zirconium atoms. Figure 3.6.27(c) shows the structure model with two layers of twin faulting separated by two layers of layers of zirconium atoms. Figure 3.6.27(d) shows the structure model with two layers of twin faulting separated by three layers of zirconium atoms. Figure 3.6.27(e) shows the structure model with two layers of twin faulting separated by five layers of zirconium atoms. Figure 3.6.27(e) shows the structure model with one layer of twin faulting.

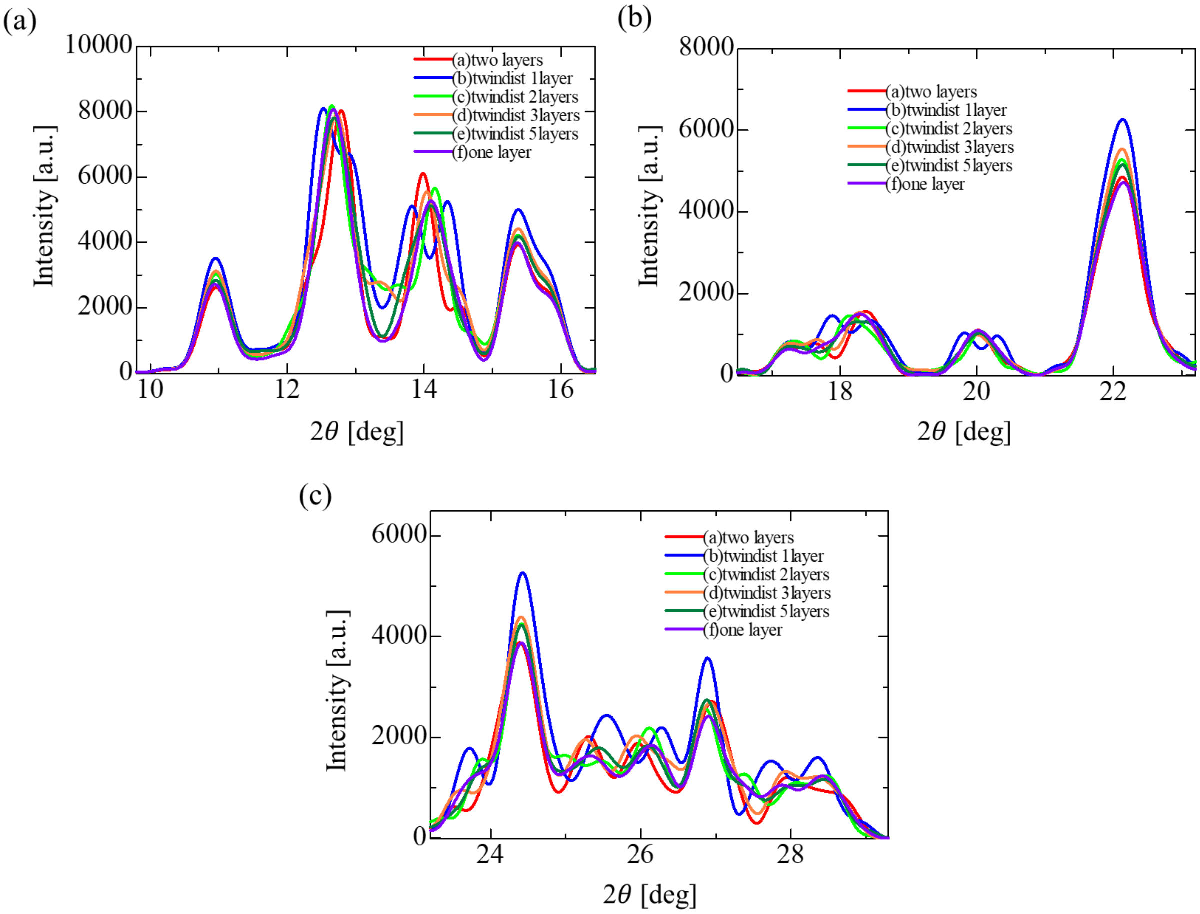

Figure 3.6.28 Powder profiles of the structure models (a) 9.8 ° to 16.5 °, (b) 16.5 ° to 23.2 °, (c) 23.2 ° to 29.3 °.

Figure 3.6.28 shows the powder profiles calculated from the structure model. The intensity of powder profiles were normalized to the peak height of -111 reflection at 12.8 °. Figure 3.6.28 (a) shows the diffraction angle from 9.8 ° to 16.5 °. The -111 and 111 reflection of the model with the separation by one layer was split. The width of the 111 reflection of the structure model of one layer twin faulting was larger than that of the model with one layer of twin faulting by 0.2 °. Figure 3.6.28(b) shows the diffraction angle from 16.5 ° to 23.2 °. Peak height of 220 reflection at 22.1 ° of the model with one layer of twin faulting was lower than that of the of the model with one layer of twin faulting by 1000. Figure 3.6.28 (c) shows the diffraction angle from 23.2 ° to 29.3 °. The peak height of 113 reflection at 26.8 ° of the structure model of one layer twin faulting was higher than that of the model with one layer of twin faulting by 1000.

The effects of twin faulting to the powder profiles of ZrO_2 nanoparticles were systematically investigated by the powder profiles of the structure models with twin faulting. The peak around 18 ° was shifted by 0.3 ° in the positive direction of the diffraction angle by inserting the twin faulting in the structure model. The peak height at 26.8 ° has increased by inserting the twin faulting in the structure model. The separation between twin faulting caused the split, shift and complex broadening of Bragg peaks.

3.6.2.3 HfO_2

The effect of the size and the lattice defect of nanoparticles to the powder profile were investigated by DSE. The structure models of monoclinic HfO_2 were constructed for the analysis. Crystal structure by Whittle *et al.* used for the structure model [77]. The shape of structure model was assumed as the elliptic cylinder. The height, short axis and long axis of the elliptic cylinder were changed for investigating the effect of the size. The powder profiles were calculated from the structure models by DSE. We especially focused on the intensity of powder profiles from 16.8 ° to 21.2 ° where the deviations were found in the Rietveld refinement.

3.6.2.3.1 Effect of size of HfO_2 nanoparticles

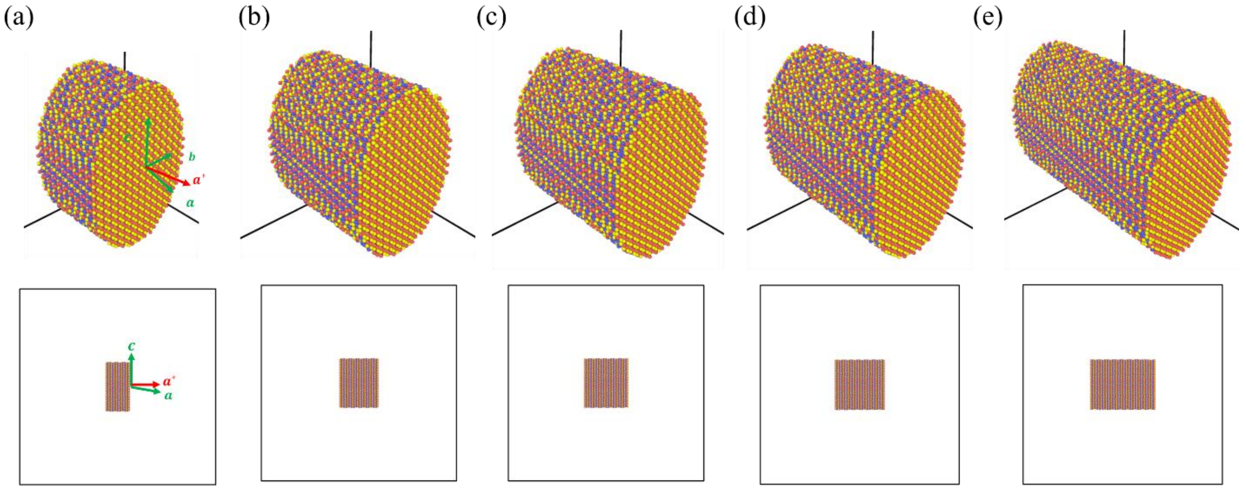

Figure 3.6.29 Structure models of HfO_2 nanoparticle. Height of the elliptic cylinders are (a) 5 nm, (b) 7nm, (c) 9 nm, (d) 11 nm, and (e) 13 nm.

Figure 3.6.29 shows the structure models of HfO_2 nanoparticle. Red spheres show hafnium atoms. Blue and yellow spheres are oxygen atoms. Green arrows show the direction of axes of the unit cell. Red arrow shows the direction of *a** axis of reciprocal lattice vector. Upper figures show structure models. Lower figures show structure models from *b* direction. Short axis is parallel to *b* direction. Long axis is parallel to c direction. Short axis is 7 nm. Long axis is 10 nm. Number of atoms in the structure model with the height of 5 nm was 23104. Number of atoms in the structure model with the height of 7 nm was 32664. Number of atoms in the structure model with the height of 9 nm was 42224. Number of atoms in the structure model with the height of 11 nm was 51782. Number of atoms in the structure model with the height of 13 nm was 61332.

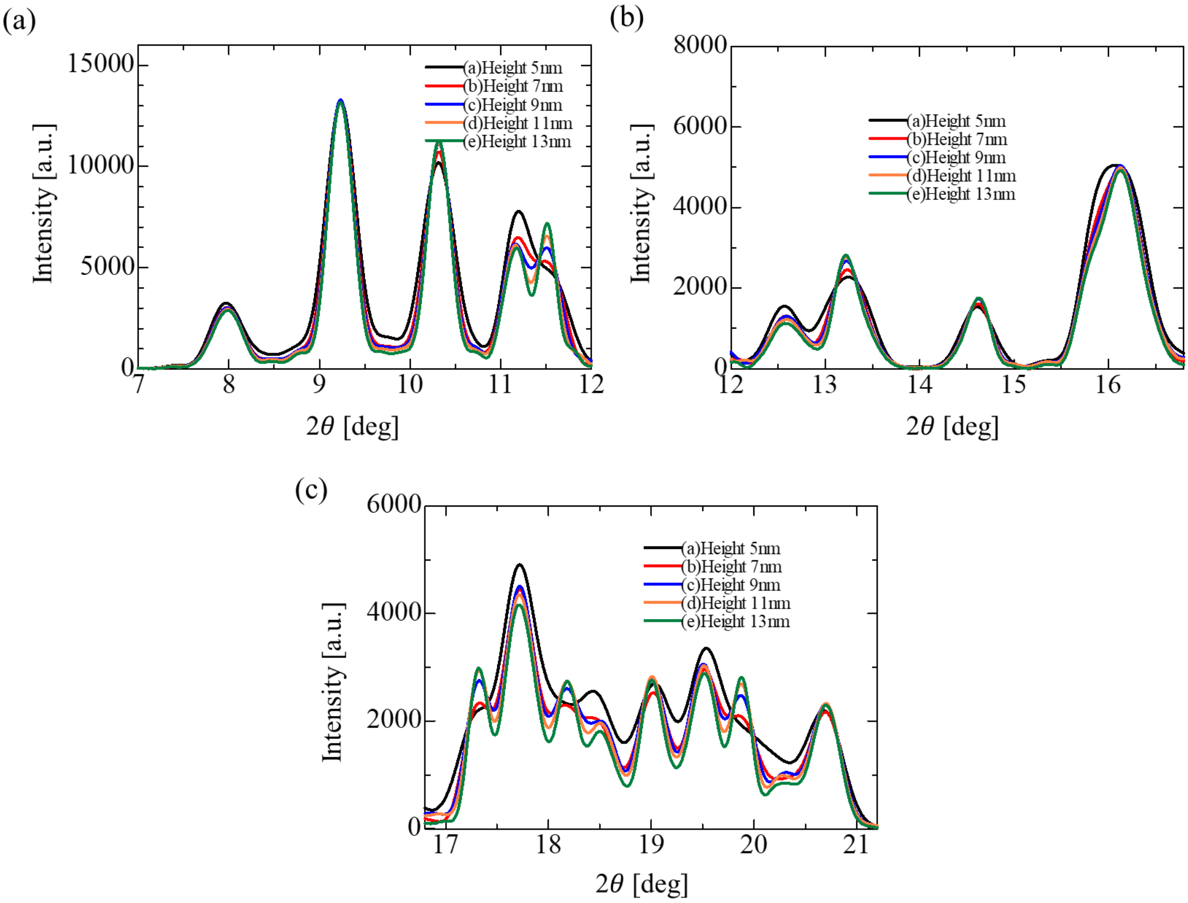

Figure 3.6.30 Powder profiles of the structure models (a) 7 ° to 12 °, (b) 12 ° to 16.8 °, (c) 16.8 ° to 21.2 °.

Figure 3.6.30 shows the powder profiles calculated from the structure models. The intensity of powder profiles were normalized to the peak height of -111 reflection at 9.2 °. Figure 3.6.30(a) shows the diffraction angle from 7 ° to 12 °. The peak of 200 reflection has not appeared at 11.5 ° in the powder profile of the model with the height of 5 nm. Figure 3.6.30(b) shows the diffraction angle from 12 ° to 16.8 °. The shift of peak around 13.5 ° was less than 0.1 ° with the change of the height. The change of the peak height of 022 reflection at 21.8 ° was less than 200 with the increase of the height of 8 nm. Figure 3.6.30(c) shows the diffraction angle from 16.8 ° to 21.2 °. The peak height of -113 reflection at 17.7 ° has decreased by 800 with the increase of the height by 8 nm. The peak height at 19.5 ° has decreased only by 500 with the increase of the height by 8 nm.

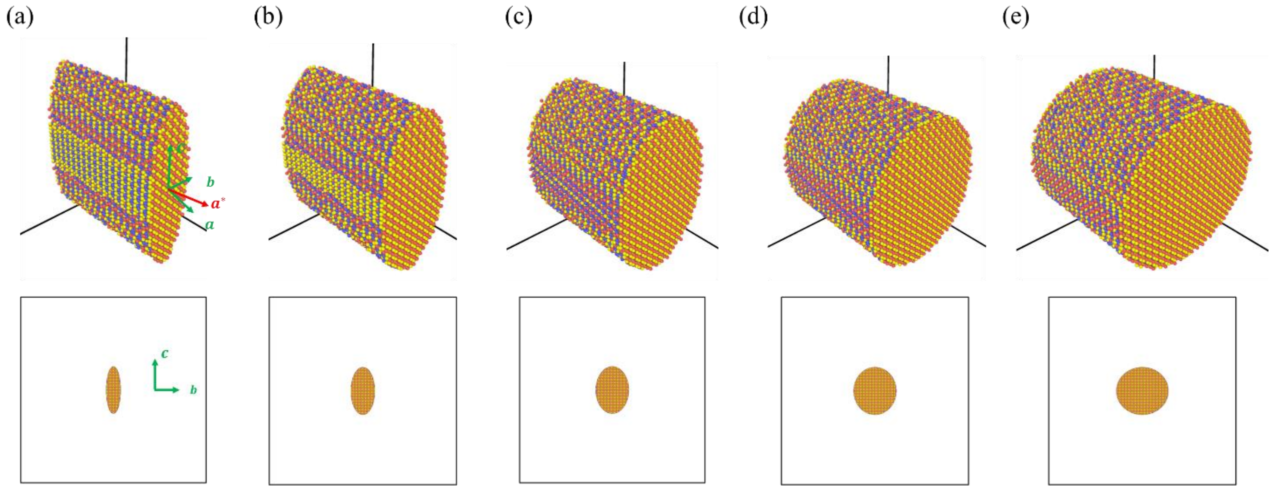

Figure 3.6.31 Structure models of HfO_2 nanoparticle. Short axis of elliptic cylinders are (a) 3 nm, (b) 5 nm, (c) 7 nm, (d) 9 nm and (e) 11 nm.

Figure 3.6.31 shows structure models of HfO_2 nanoparticle. Definitions of colored spheres and arrows are the same as Figure 3.6.29. Shape and crystal structure of structure models are the same as Figure 3.6.29. Upper figures show the structure models. Lower figures show the structure models from *a** direction. Height of the elliptic cylinder is 9 nm. Long axis is 10 nm.

Figure 3.6.31 (a) shows the structure model with the short axis of 3 nm. Number of atoms was 18174. Figure 3.6.31 (b) shows the structure model with the short axis of 5 nm. Number of atoms was 30212. Figure 3.6.31 (c) shows the structure model with the short axis of 7 nm. Number of atoms was 42224. Figure 3.6.31(d) shows the structure model with the short axis of 9 nm. Number of atoms was 54294. Figure 3.6.31 (e) shows the structure model with the short axis of 11 nm. Number of atoms was 66440.

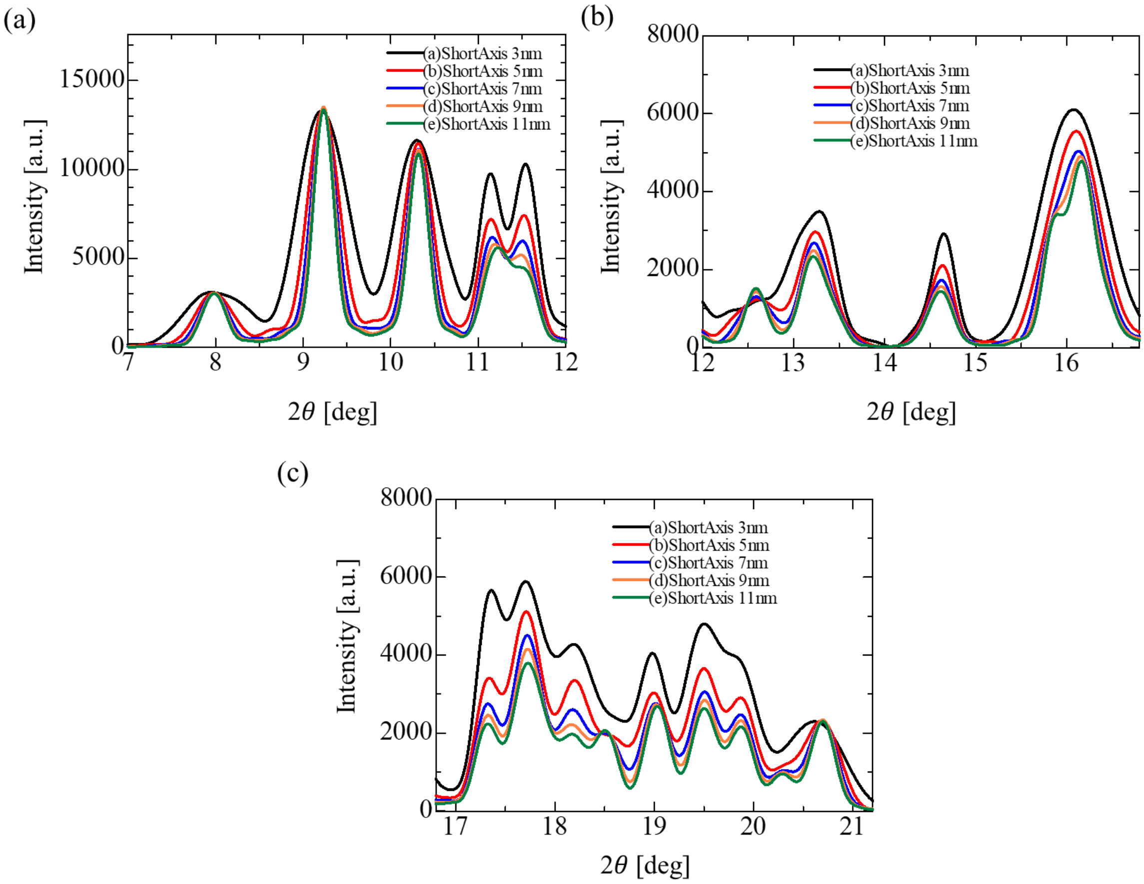

Figure 3.6.32 Powder profiles of the structure models. (a) 7 ° to 12 °, (b) 12 ° to 16.8 °, (c) 16.8 ° to 21.2 °.

Figure 3.6.32 shows the powder profiles calculated from the structure model. The intensity of powder profiles were normalized to the peak height of -111 reflection at 9.2 °. Figure 3.6.32 (a) shows the diffraction angle from 7 ° to 12 °. The peak height of 200 reflection at 11.5 ° has decreased by 6000 with increase of the short axis by 8 nm. Figure 3.6.32 (b) shows the diffraction angle from 12 ° to 16.8 °. The peak shifted around 13.3 ° was less than 0.1 ° by changing the short axis. The peak height of 220 reflection at 16.2 ° has decreased by 1000 with increase of the short axis by 8 nm. Figure 3.6.32 (c) shows the diffraction angle from 16.8 ° to 21.2 °. The peak height of 400 reflection at 17.3 ° has decreased by 3000 with increase of the short axis by 8 nm. The peak height around 19.5 ° has decreased by 500 with increase of the short axis by 8 nm. In this case, the difference of the intensity at 17.4 ° and 17.7 ° was less than 500.

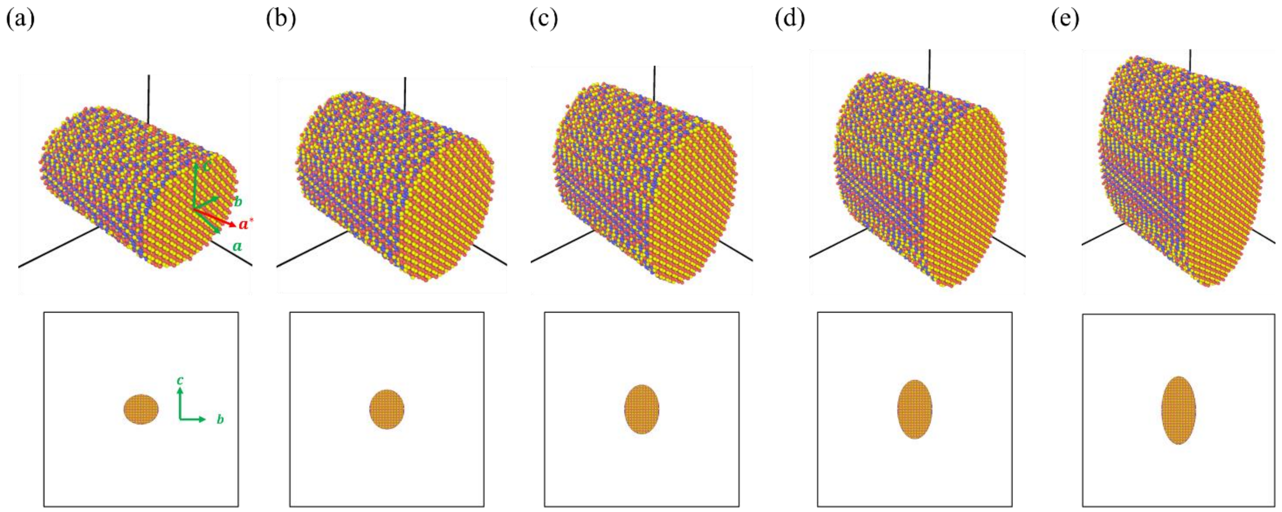

Figure 3.6.33 Structure models of HfO_2 nanoparticle. Long axis of elliptic cylinders are (a) 6 nm, (b) 8 nm, (c) 10 nm, (d) 12 nm, and (e) 14 nm.

Figure 3.6.33 shows structure models of HfO_2 nanoparticle. Definitions of colored spheres and arrows are the same as Figure 3.6.29. Shape and crystal structure of structure models are the same as Figure 3.6.29. Upper figures show the structure models. Lower figures show the structure models from a* direction. Height of the elliptic cylinder is 9 nm. Short axis is 7 nm.

Figure 3.6.33 (a) shows the structure model with the long axis of 6 nm. Number of atoms was 25320. Figure 3.6.33 (b) shows the structure model with the long axis of 8 nm. Number of atoms was 33754. Figure 3.6.33 (c) shows the structure model with the long axis of 10 nm. Number of atoms was 42224. Figure 3.6.33 (d) shows the structure model with the long axis of 12 nm. Number of atoms was 50644. Figure 3.6.33 (e) shows the structure model with the long axis of 14 nm. Number of atoms was 59082.

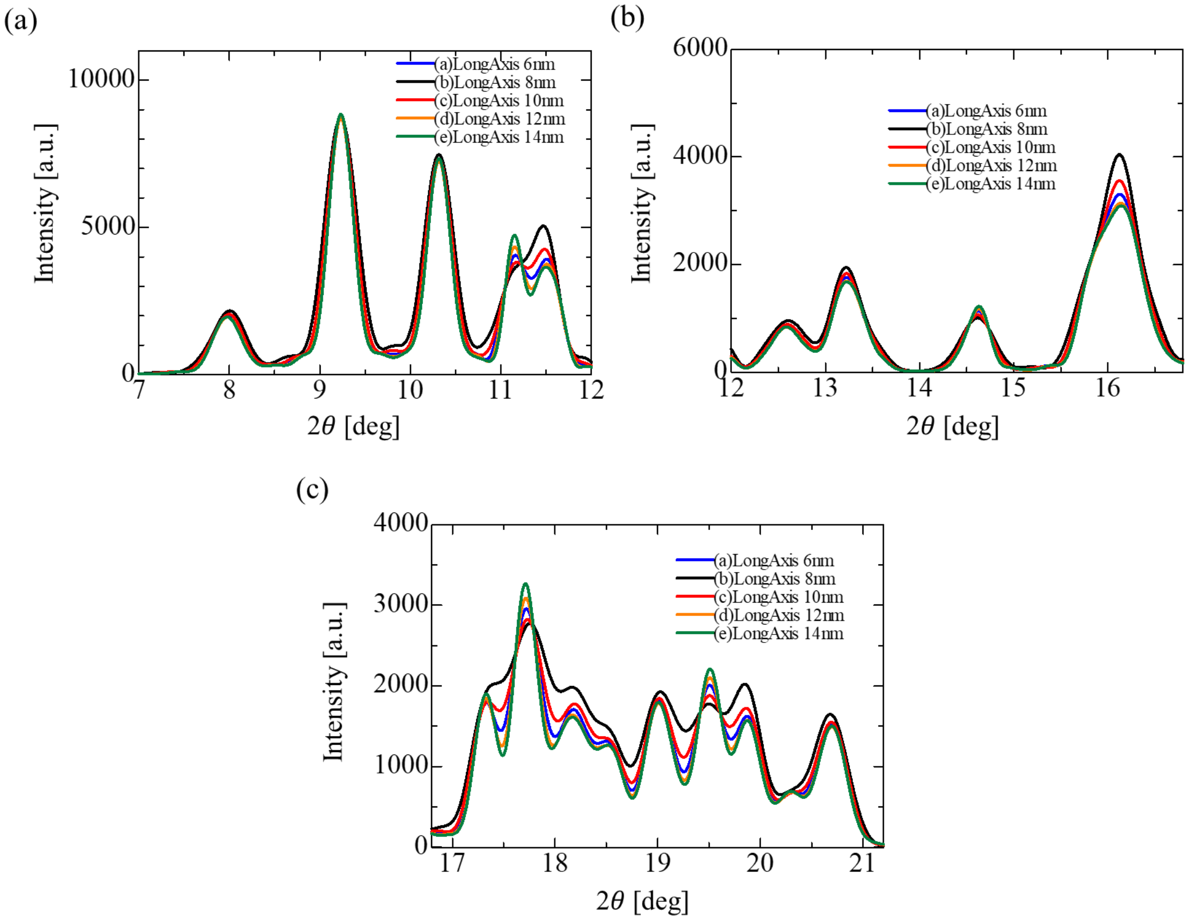

Figure 3.6.34 Powder profiles of the structure models. (a) 7 ° to 12 °, (b) 12 ° to 16.8 °, (c) 16.8 ° to 21.2 °.

Figure 3.6.34 shows the powder profiles calculated from the structure model. The intensity of powder profiles were normalized to the peak height of -111 reflection at 9.2 °. Figure 3.6.34 (a) shows the diffraction angle from 7 ° to 12 °. The peak height of 200 reflection at 11.5 ° has increased by 500 with increase of the long axis by 8 nm. Figure 3.6.34 (b) shows the diffraction angle from 12 ° to 16.8 °. The shift of peak around 13.3 ° was less than 0.05° by the change of the long axis. The peak height of 220 reflection at 16.2 ° has decreased by 1000 with increase of the long axis by 8 nm. Figure 3.6.34 (c) shows the diffraction angle from 16.9 ° to 21.2 °. The peak height at 17.8 ° has increased by 500 with increase of the long axis by 8 nm. The peak height at 19.5 ° has increased by 300 with increase of the long axis by 8 nm.

The size effects to the powder profiles of HfO_2 nanoparticles were investigated by changing the height, the short axis and the long axis of the structure model. The shift of the peak around 13.3 ° were less than 0.1 ° by changing the height, the short axis and the long axis by 8 nm. The peak height at the 19.5 ° has increased by the increase of the long axis, the decrease of the short axis or the decrease of the height of the elliptic cylinder. 200 peak at the 15.8 ° has vanished by the decrease of the height. The peak height at 17.3 ° became close to that at 17.8 ° by the decrease of the short axis. The peak height of 200 peak at 11.5 ° became smaller than that of 002 peak at 11.2 ° by the increase of the long axis.

3.6.2.3.2 Effect of twin faulting in HfO$_2$ nanoparticles

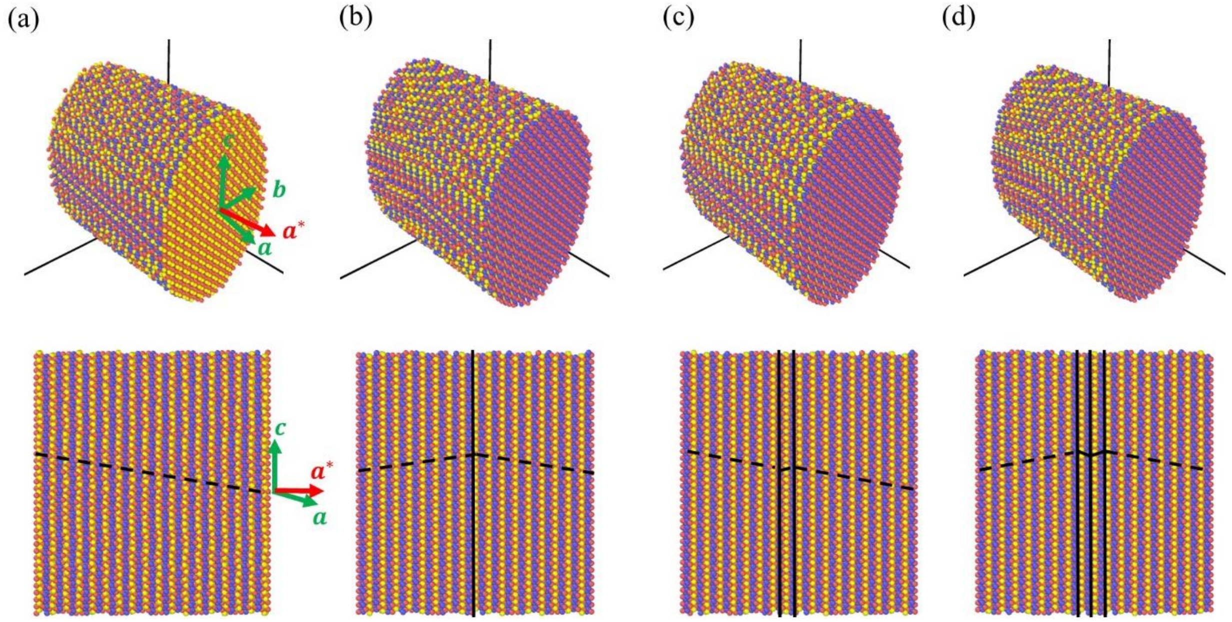

Figure 3.6.35 Structure models of HfO$_2$ nanoparticle. (a) No faulting, (b) one layer, (c) two layers, (d) three layers.

Figure 3.6.35 shows the structure models of HfO$_2$-nanoparticle. Red spheres are hafnium atoms. Blue and yellow spheres are oxygen atoms. Crystal structure by Whittle *et al*. used for the structure model [76]. The lattice parameters were obtained from the Rietveld refinement. Green arrows show the direction of axes of unit cell. Red arrow shows the direction of *a** axis of reciprocal lattice vector. Upper figures show structure model. Lower figures show the cutting surface of structure model by ac plane. Length was 9 nm. Short axis was 7 nm. Long axis was 10 nm. Number of atoms in the model was 42220.

Figure 3.6.35(a) shows the structure model with no faulting. Black dashed line shows the direction of stacking sequence of zirconium atoms. Figure 3.6.35(b) shows the structure model with one layer of twin faulting. Black line shows the position of twin faulting. Figure 3.6.35(c) shows the structure model with two layers of twin faulting. Figure 3.6.35(d) shows the structure model with three layers of twin faulting.

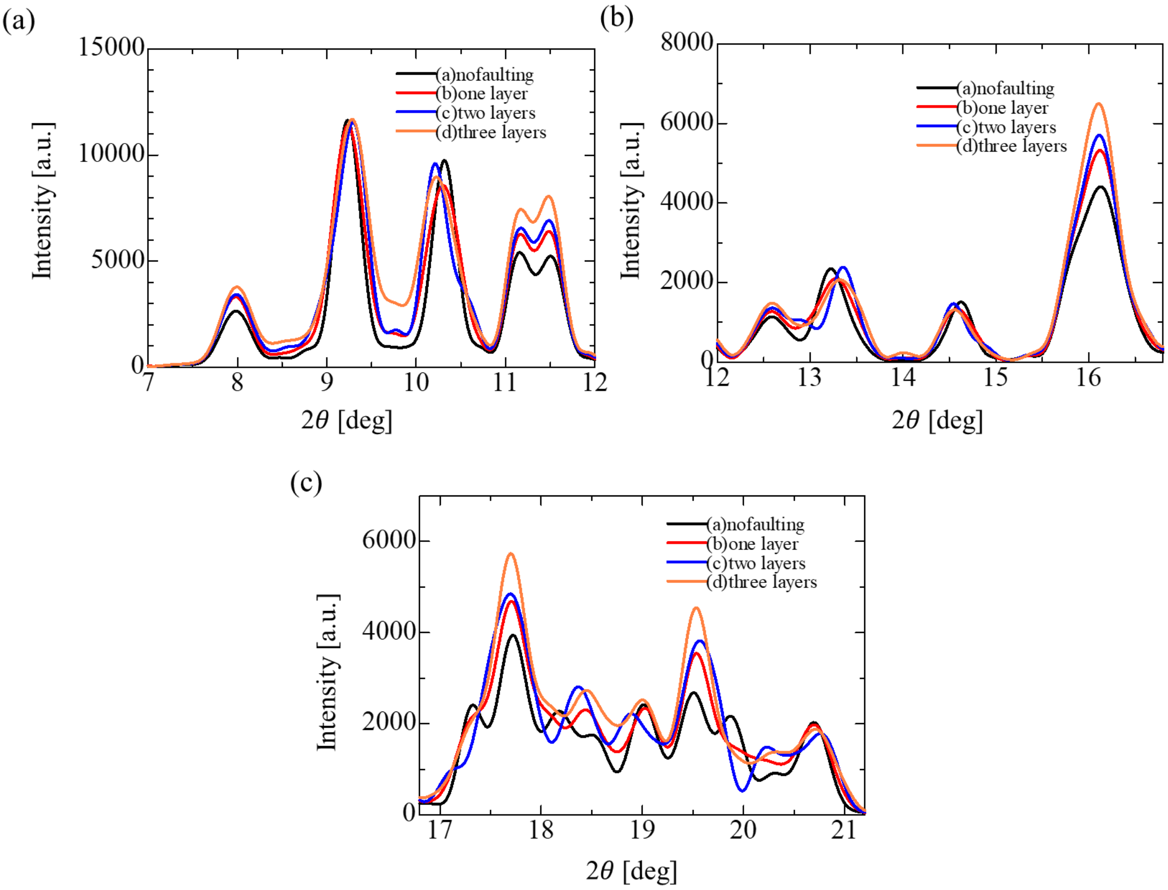

Figure 3.6.36 Powder profiles of the structure models. (a) 7 ° to 12 °, (b) 12 ° to 16.8 °, (c) 16.8 ° to 21.2 °.

Figure 3.6.36 shows the powder profiles calculated from the structure models. Figure 3.6.36(a) shows the diffraction angle from 7 ° to 12 °. The positions of 111 reflection of the structure models with two and three twin faulting were shifted by 0.2 ° in the positive direction compared with that of the model without faulting. Figure 3.6.36 (b) shows the diffraction angle from 12 ° to 16.8 °. The peak around 13.3 ° of the structure models with twin faulting were at the higher angle by 0.1 ° compared with that of the structure model without faulting. Figure 3.6.36 (c) shows the diffraction angle from 16.8 ° to 21.2 °. The peak height at 19.5 ° of the models with twin faulting was higher than that of the model without faulting by 1000. The peak has not appeared at 19.8 ° in the powder profiles of the models with twin faulting.

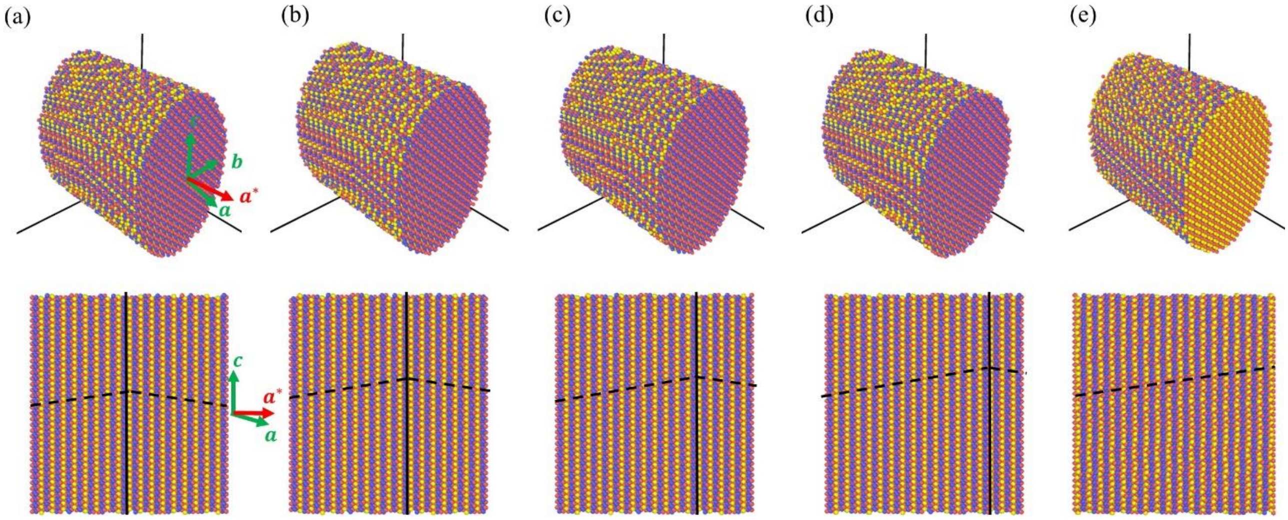

Figure 3.6.37 Structure models of HfO_2 nanoparticle with different positions of the twin faulting. (a) Twin faulting at the center, (b) shifted by two layers, (c) shifted by four layers, (d) shifted by six layers, (e) no faulting.

Figure 3.6.37 shows the structure models of HfO_2 nanoparticle. Definitions of the colored spheres and arrows are the same as Figure 3.6.35. Shape and crystal structure of the models are the same as Figure 3.6.35. Upper figures show the structure models. Lower figures show the cutting surface by ac plane. Height was 9 nm. Short axis was 7 nm. Long axis was 10 nm. Number of atoms was 42220.

Figure 3.6.37(a) shows the structure model with twin faulting at the center. Black lines show the direction of the stacking sequence of zirconium atoms. Black dashed line shows the position of twin faulting. Figure 3.6.37(b) shows the structure model with twin faulting. Position of the twin faulting was shifted by two layers from the center in the positive direction of a^* axis. Figure 3.6.37(c) shows the structure model with twin faulting shifted by four layers. Figure 3.6.37(d) shows the structure model with twin faulting shifted by six layers. Figure 3.6.37(e) shows the structure model with no faulting.

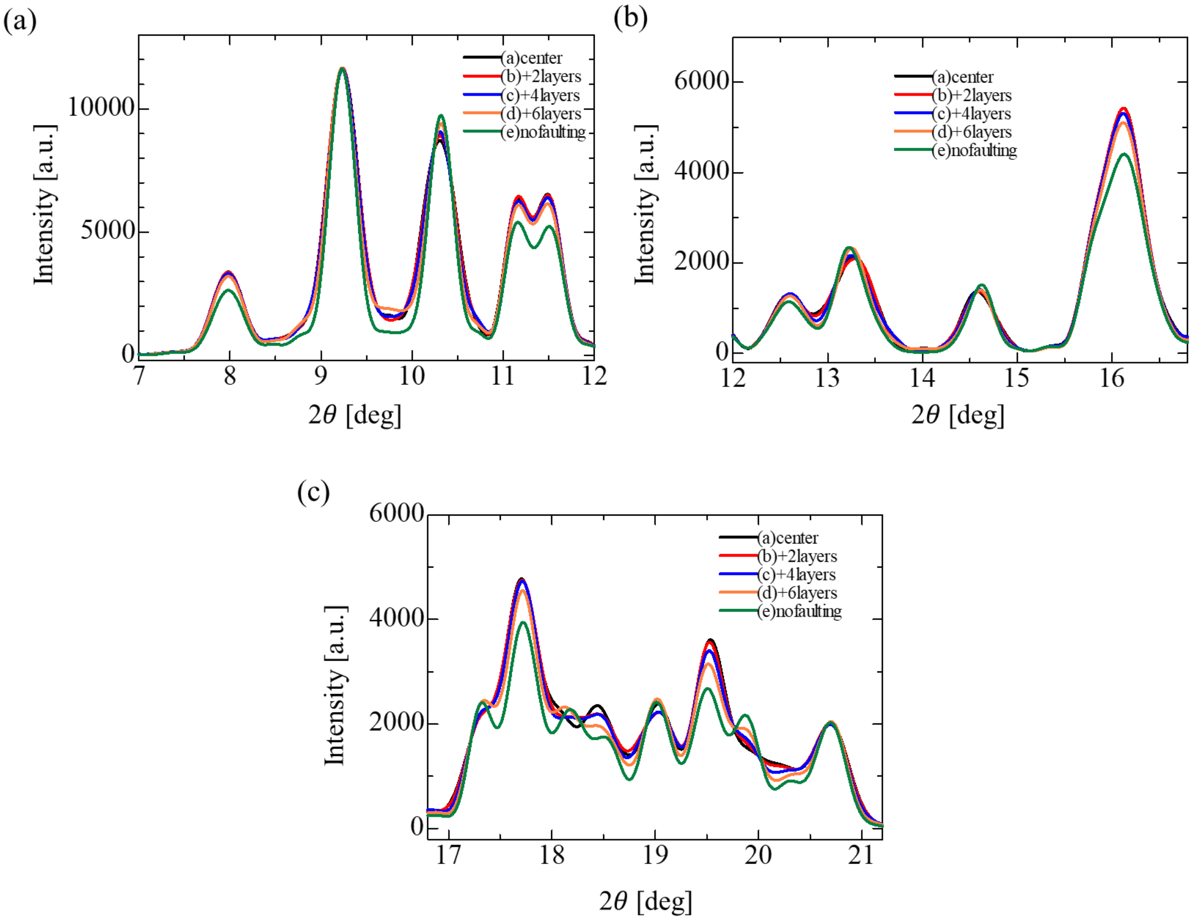

Figure 3.6.38 Powder profiles of the structure models. (a) 7 ° to 12 °, (b) 12 ° to 16.8 °, (c) 16.8 ° to 21.2 °.

Figure 3.6.38 shows the powder profiles calculated from the structure model. The intensity of powder profiles were normalized to the peak height of -111 reflection at 9.2 °. Figure 3.6.38 (a) shows the diffraction angle from 7 ° to 12 °. The width of the 111 reflection of the structure model of one layer of twin faulting was larger than that of the structure model without faulting by 0.1 °. Figure 3.6.38 (b) shows the diffraction angle from 12 ° to 16.8 °. Peak height of 220 reflection at 22.1 ° of the structure model of one twin faulting was lower than that of the structure model without faulting by 800. Figure 3.6.38 (c) shows the diffraction angle from 16.8 ° to 21.2 °. The peak height at 19.5 ° of the structure model of one layer of twin faulting was higher than that of the structure model without faulting by 800. The intensity of powder profiles were continuously changed between the powder profile of the model with one layer of twin faulting and that of the model without faulting.

The position of faulting does not mean that all the HfO_2 nanoparticles in powder sample have the twin faulting at the specific position. This probably reflects the fraction of nanoparticles which have the twin faulting, since the powder profiles of the structure models with faulting shifted by 2, 4 and 6 layers can be expressed as the linear combination of powder profiles of the model without faulting and the model with faulting at the center.

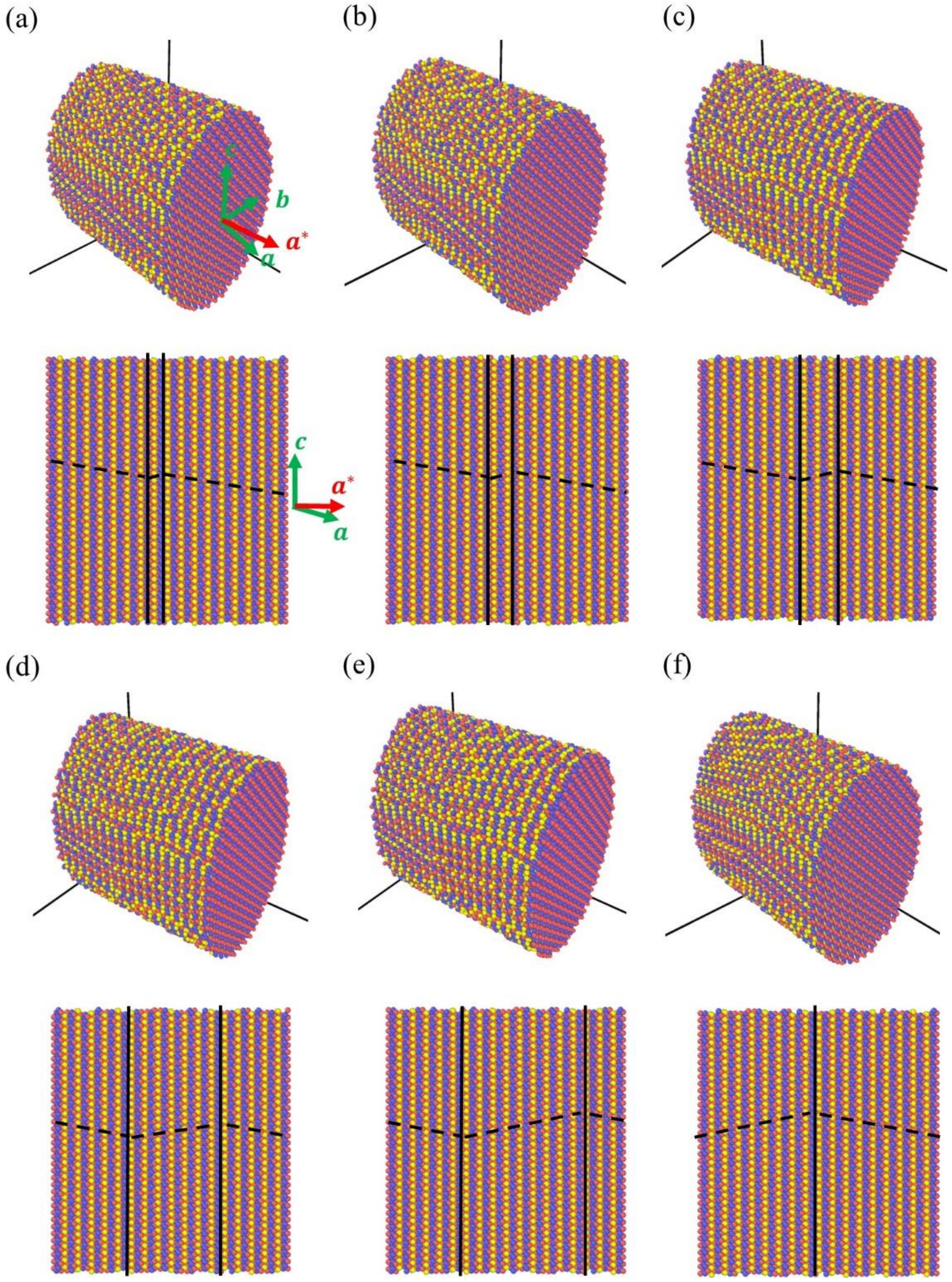

Figure 3.6.39 Structure models of HfO_2 nanoparticle with the different separation between two twin faulting. (a) Two layers of twin faulting, (b) two layers of twin faulting with the separation by one layer, (c) two layers, (d) three layers, (e) five layers, (f) one layer of twin faulting.

Figure 3.6.39 shows the structure models of HfO_2 nanoparticle. Definitions of the colored spheres and arrows are the same as Figure 3.6.35. Shape and crystal structure of structure models are the same as Figure 3.6.35. Upper figures show the structure models. Lower figures show the cutting surface by ac plane. Height was 9 nm. Short axis was 7 nm. Long axis was 10 nm. Number of atoms was 42220.

Figure 3.6.39(a) shows the structure model with two layers of twin faulting at the center. Black lines show the direction of the stacking sequence of zirconium atoms. Black dashed line shows the position of twin faulting. Figure 3.6.39(b) shows the structure model with two layers of twin faulting separated by one layer of zirconium atoms. Figure 3.6.39(c) shows the structure model with two layers of twin faulting separated by two layers of zirconium atoms. Figure 3.6.39(d) shows the structure model with two layers of twin faulting separated by three layers of zirconium atoms. Figure 3.6.39(e) shows the structure model with two layers of twin faulting separated by five layers of zirconium atoms. Figure 3.6.39(e) shows the structure model with one layer of twin faulting.

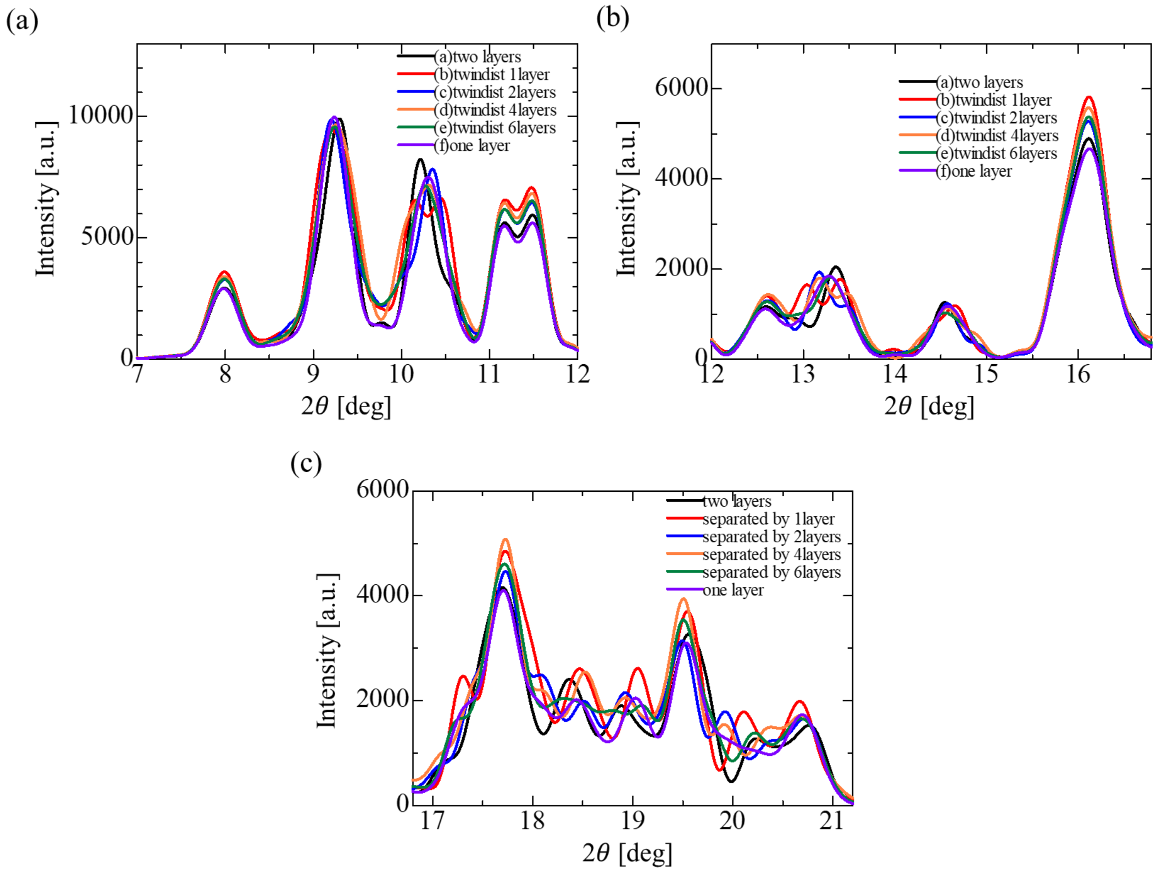

Figure 3.6.40 Powder profiles of the structure models. (a) 7 ° to 12 °, (b) 12 ° to 16.8 °, (c) 16.8 ° to 21.2 °.

Figure 3.6.40 shows the powder profiles calculated from the structure model. The intensity of powder profiles were normalized to the peak height of -111 reflection at 9.2 °. Figure 3.6.40 (a) shows the diffraction angle from 7 ° to 12 °. 111 reflection of the model with the separation by one layer was split. The intensity ratio at 11.2 ° and 11.5 ° showed almost no change. Figure 3.6.40 (b) shows the diffraction angle from 12 ° to 16.5 °. Peak height of 220 reflection at 22.1 ° of the model with one layer of twin faulting was lower than that of the model with one layer of twin faulting by 900. Figure 3.6.40 (c) shows the diffraction angle from 16.8 ° to 21.2 °. The peak height of the model with the separation by 4 layers was higher than that of other models by 100.

The effects of twin faulting to the powder profiles of ZrO_2 nanoparticles were systematically investigated by the powder profiles of the structure models with twin faulting. The peak around 13.3 ° was shifted by 0.1 ° in the positive direction of the diffraction angle by the twin faulting in the structure model. The peak height at 26.8 ° has increased by inserting the twin faulting in the structure model. The separation between twin faulting caused the split, shift and complex broadening of diffraction profiles.

3.6.3 Analysis of powder profiles of nanoparticles with twin faulting by DSE

The usefulness and the effectiveness of DSE for modelling the effects of the size and the twin faulting to the powder profiles were systematically investigated for Ag, ZrO_2 and HfO_2 nanoparticles. Several changes appeared in the powder profiles of Ag nanoparticles indicated that the powder profiles calculated from the structure models of nanoparticles with twin faulting can provide the better expression for the powder diffraction data of nanoparticles. For example, the broadening of 200 reflection was obtained by twin faulting in the structure model of Ag nanosphere. A satellite peak appeared in the powder profile of the model with three layers of twin faulting. It was consistent with the peculiar shape of 111 reflection in the powder diffraction data.

For the ZrO_2 nanoparticles, it was also indicated that the powder profile calculated from the structure model with twin faulting can provide the better expression for the powder diffraction data. The structure model with twin faulting showed the shift of a peak around 18.5 ° in the positive direction of the diffraction angle. The peak height at 26.8 ° has increased by inserting the twin faulting in the structure model. It was also indicated that only the size change of a structure model doesn't provide the better expression for the powder diffraction data. For example, the increase of long axis of nanoparticles increased the peak height at 26.8 °, but it also resulted in the large decrease of the peak height of 200 reflection at 15.8 °.

For the HfO_2 nanoparticles, it was also indicated that the powder profile calculated from the structure model with twin faulting can provide the better expression for the powder diffraction data. The structure model with twin faulting showed the peak shift at 1.3 ° compared with the powder profile of the model without faulting. The peak height at 19.5 ° has increased by twin faulting. The peak has not appeared around 19.8 ° in the powder profiles. These expressions were not appeared at the same time in the powder profiles of the model without twin faulting.

We analyzed the powder diffraction data by the powder profiles calculated from the structure models of nanoparticles with twin faulting. The structure models were constructed for Ag, ZrO_2 and HfO_2 nanoparticles. The powder profiles were calculated from the structure models by DSE. The profile fitting was carried out for the powder diffraction data. Agreement between diffraction data and powder profile were compared with that of Rietveld refinement. Section 3.6.3.1 shows the analysis of diffraction data of Ag nanoparticles. Section 3.6.3.2 shows analysis of diffraction data of ZrO_2 nanoparticles. Section 3.6.3.3 shows analysis of diffraction data of HfO_2 nanoparticles.

3.6.3.1 Ag 10 nm nanosphere

Powder diffraction data were analyzed by the profile fitting. Ozawa investigated the angular dependence of peak widths of Ag 10 nm nanosphere. Ozawa found that the angular dependence can be expressed by the powder profile of Ag nanoparticles with twin faulting [29]. The effect of twin faulting of Ag nanoparticles to the powder profile was described in Section 3.6.2.1.

The powder profile of Ag nanoparticles was calculated from the structure model. The structure model of Ag nanosphere with diameter 11 nm was constructed for the analysis. Three layers of twin faulting were inserted at the center of structure model. The powder profile of the quartz capillary was used in the analysis. The intensity of powder profiles of Ag nanoparticles and the quartz capillary was optimized in the analysis.

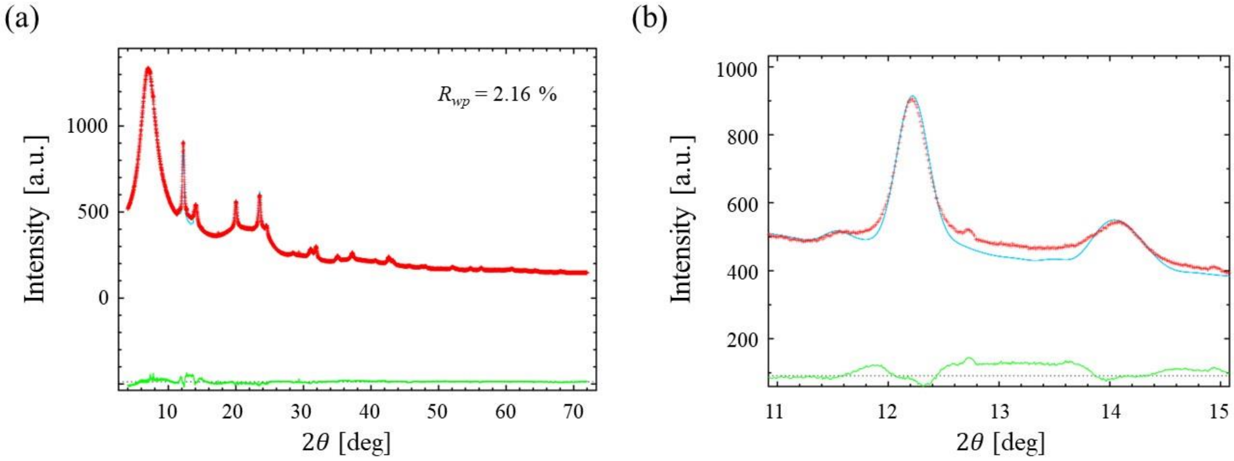

Figure 3.6.41 Powder diffraction data of Ag nanoparticle and the sum of powder profiles. (a) 10 ° to 72 °, (b) 11 ° to 15 °.

Figure 3.6.41 shows powder diffraction data of Ag nanoparticle and the sum of powder profiles. Figure 3.6.41(a) shows the diffraction angle from 4 ° to 72 °. R_{wp} was 2.16 %. R_{wp} of the profile fitting was lower than that of Rietveld refinement by 0.96 %. Figure 3.6.41(b) shows the diffraction angle from 11 ° to 15 °. The shape of peak around 11.5 ° was expressed by the satellite peak of the powder profile of Ag nanoparticle with twin faulting. The difference in the peak height of 200 reflection at 14.2 ° was less than 20. The difference in the peak height of 200 reflection at 14.2 ° was less than 30.

The profile fitting with powder profile of Ag nanosphere with twin faulting provided the better expression for powder diffraction data than Rietveld refinement. Diameter of nanosphere was 11 nm. It was found that Ag nanospheres have three layers of twin faulting in the structure.

3.6.3.2 ZrO_2

3.6.3.2.1 Powder diffraction data at supercritical water

Powder diffraction data of ZrO_2 nanoparticle collected at supercritical water condition was analyzed by the profile fitting. The structure models of monoclinic ZrO_2 nanoparticle with twin faulting were constructed for the analysis. The powder profiles were calculated by DSE. The powder profiles of tetragonal ZrO_2 were calculated by Rietveld refinement since the peaks of tetragonal phase in the powder diffraction data were expressed by the powder profile of the average structure model in the Rietveld refinement. The powder profile of fused silica capillary and the powder profile of supercritical water at 673 K and 30 MPa was used in the analysis. The intensity of powder profiles of ZrO_2 nanoparticles, supercritical water and fused silica capillary were optimized in the analysis. Scale factor, lattice constants and peak width parameter w of tetragonal phase of ZrO_2 were optimized in the refinement.

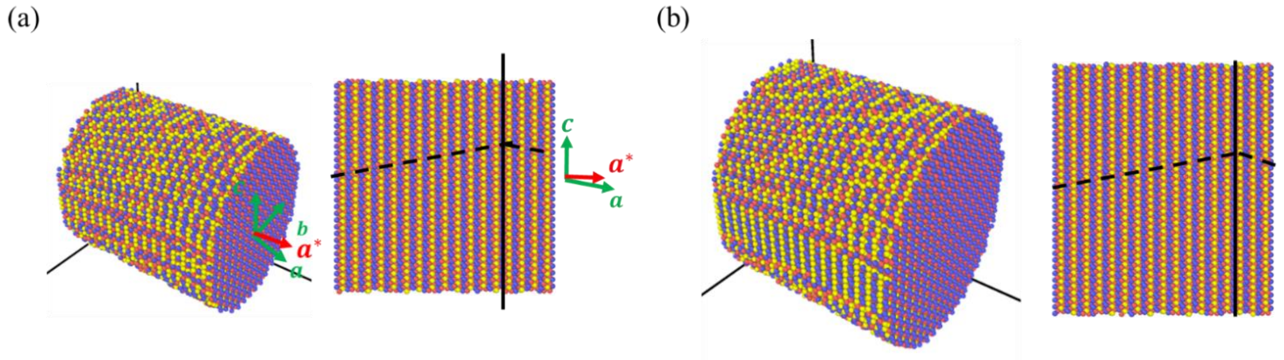

Figure 3.6.42 Structure models of monoclinic ZrO_2 nanoparticle. (a) initial 5 min, (b) 25 to 30 min and 55 to 60 min.

Figure 3.6.42 shows the structure models of monoclinic ZrO_2 nanoparticle. The shape of structure models was elliptic cylinder. Figure 3.6.42(a) shows the structure model for profile fitting of data at initial 5 min. Height was 8.6 nm. Short axis was 7.6 nm. Long axis was 8.4 nm. Number of atoms was 36742. One layer of twin faulting was inserted in the structure model. Position of twin faulting was shifted by 5 layers from the center of elliptic cylinder. Figure 3.6.42(b) shows the structure model of nanoparticle for the profile fitting of data from 25 to 30 min and that of data from 55 to 60 min. Height was 8.6 nm. Short axis was 8.8 nm. Long axis was 10.0 nm. Number of atoms was 50637. One layer of twin faulting was inserted in the structure model. Position of layer was shifted by 6 layers from the center of elliptic cylinder.

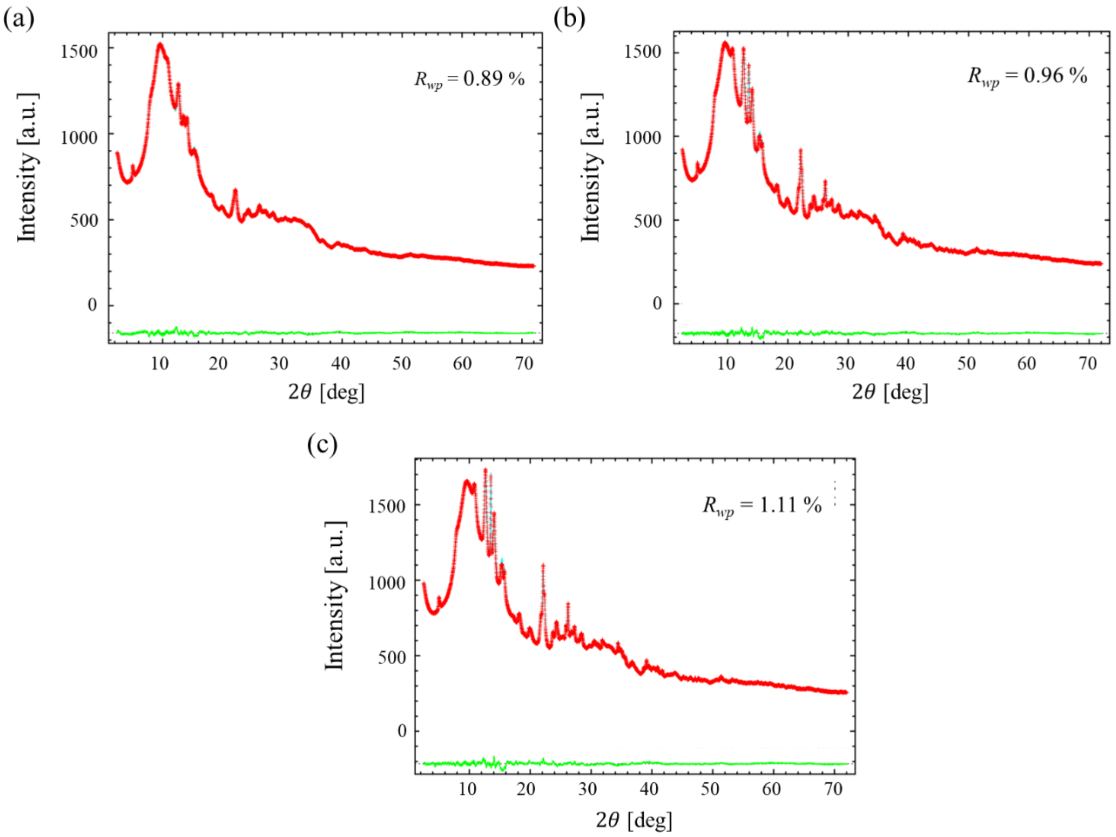

Figure 3.6.43 Powder diffraction data and the sum of powder profiles from 4 ° to 72 °. (a) Initial 5 min, (b)

25 to 30 min, (c) 55 to 60 min.

Figure 3.6.43 shows the powder diffraction data of at 673 K and 30 MPa and the sum of powder profiles. The diffraction angle from 4 ° to 72 °was shown in the figure. Figure 3.6.43(a) shows the powder diffraction data and the sum of powder profiles at initial 5 min. R_{wp} was 0.89 %. R_{wp} of the profile fitting was lower than that of Rietveld refinement by 0.05 %. Figure 3.6.43(b) shows the powder diffraction data and the sum of powder profiles from 25 to 30 min. R_{wp} was 0.96 %. R_{wp} of the profile fitting was lower than that of Rietveld refinement by 0.07 %. Figure 3.6.43(c) shows the powder diffraction data and the sum of powder profiles from 55 to 60 min. R_{wp} was 1.11 %. R_{wp} of the profile fitting was lower than that of Rietveld refinement by 0.02 %.

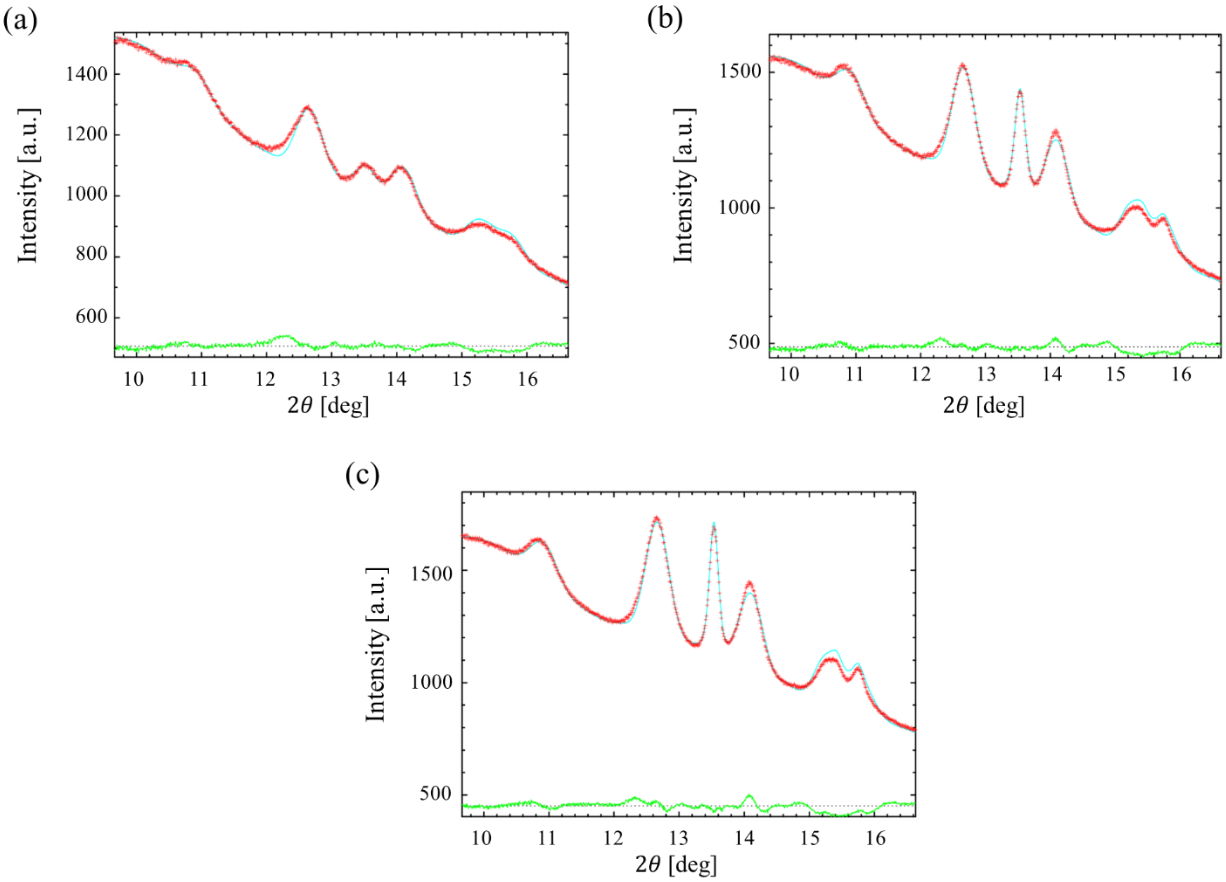

Figure 3.6.44 Powder diffraction data and the sum of powder profiles from 9.8 ° to 16.5 °. (a) Initial 5 min, (b) 25 to 30 min, (c) 55 to 60 min.

Figure 3.6.44 shows the powder diffraction data of at 673 K and 30 MPa and the sum of powder profiles. The diffraction angle from 9.8 ° to 16.5 ° was shown in the figure. Figure 3.6.44(a) shows the powder diffraction data and the sum of powder profiles at the initial 5 min. The difference of intensity in this angle was less than 50. Figure 3.6.44(b) shows the powder diffraction data and the sum of powder profiles from 25 to 30 min. The difference of intensity in this angle was less than 50. Figure 3.6.44(c) shows the powder diffraction data and the sum of powder profiles from 55 to 60 min. The difference of intensity in this angle was less than 50.

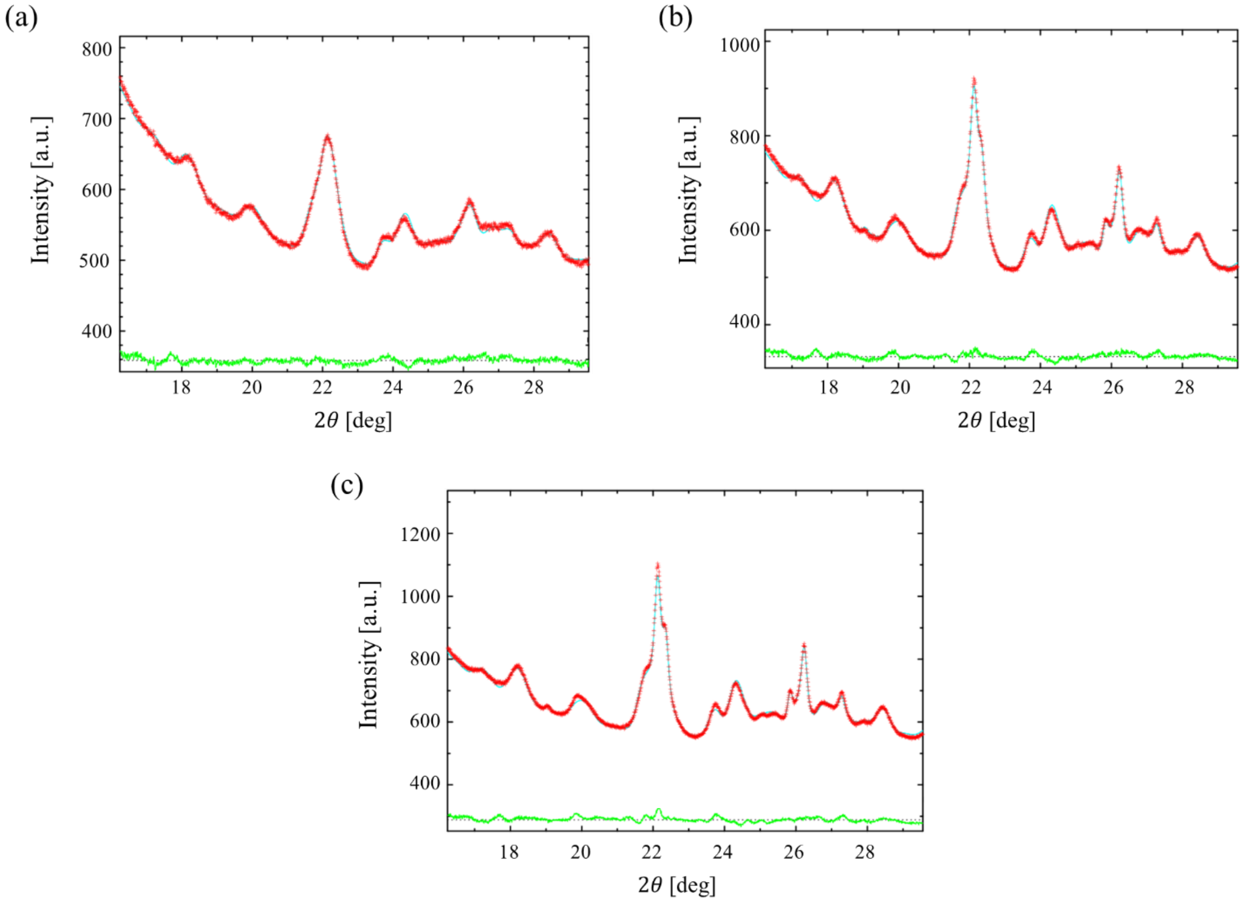

Figure 3.6.45 Powder diffraction data and the sum of powder profiles from 16.5 ° to 29.3 °. (a) Initial 5 min, (b) 25 to 30 min, (c) 55 to 60 min.

Figure 3.6.45 shows the powder diffraction data of at 673 K and 30 MPa and the sum of powder profiles. The diffraction angle from 16.5 ° to 29.3 ° was shown in the figure. Figure 3.6.45 (a) shows the powder diffraction data and the sum of powder profiles at initial 5 min. The difference of intensity at 18 ° was less than 10. The difference of intensity at 26.8 ° was less than 10.

Figure 3.6.45 (b) shows the powder diffraction data and the sum of powder profiles from 25 to 30 min. The difference of intensity at 18 ° was less than 10. The difference of intensity at 26.8 ° was less than 10. Figure 3.6.45 (c) shows the powder diffraction data and the sum of powder profiles from 55 to 60 min. The difference of intensity at 18 ° was less than 10. The difference of intensity at 26.8 ° was less than 10.

The profile fitting with powder profiles of monoclinic ZrO_2 elliptic cylinder with twin faulting provided the better expression for powder diffraction data than Rietveld refinement. Height, short axis and long axis of elliptic cylinder were 8.6 nm, 7.6 nm and 8.4 nm for 5 min data. Height, short axis and long axis were 8.6 nm, 8.8 nm and 10.0 nm for 30 min data and 60 min data. It was found that monoclinic ZrO_2 nanoparticles in supercritical water have twin faulting in the structure.

3.6.3.2.2 Powder diffraction data at room temperature

Powder diffraction data of ZrO_2 nanoparticle collected at room temperature was analyzed by the profile fitting. The structure models of monoclinic ZrO_2 nanoparticle with twin faulting were constructed for the analysis. The powder profiles were calculated by DSE. The powder profile of fused silica capillary and the powder profile of water at 300 K and 30 MPa was used in the analysis. The intensity of powder profiles of ZrO_2 nanoparticles, supercritical water and fused silica capillary were optimized in the analysis.

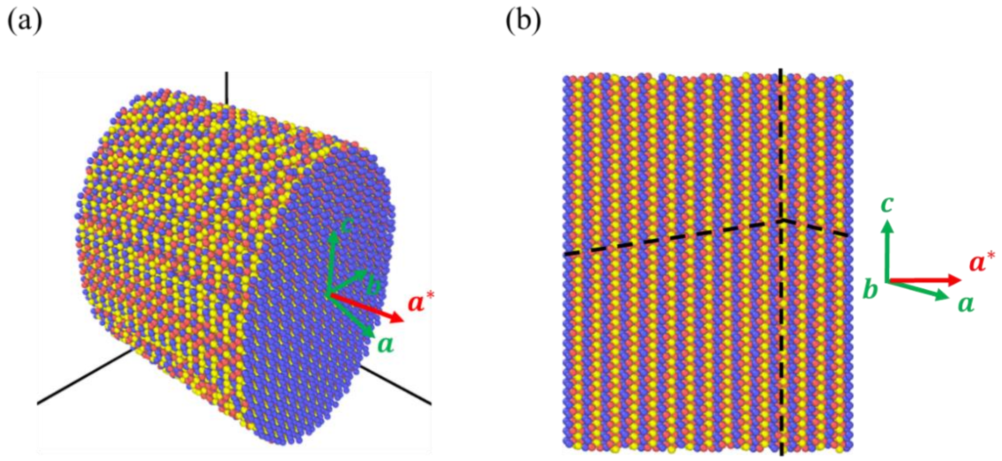

Figure 3.6.46 Structure model of monoclinic ZrO_2 nanoparticle.

Figure 3.6.46 shows the structure model of monoclinic ZrO_2 nanoparticle used for calculation of powder profile. The shape of structure model was elliptic cylinder. Figure 3.6.46(a) shows the structure model used for profile fitting of the powder diffraction data. Height was 7.8 nm. Short axis was 8.2 nm. Long axis was 10.2 nm. Number of atoms was 43602. Figure 3.6.46(b) shows cutting surface of structure model by ac plane. One layer of twin faulting was inserted in the model. Position of twin faulting was shifted by 4 layers from the center of elliptic cylinder.

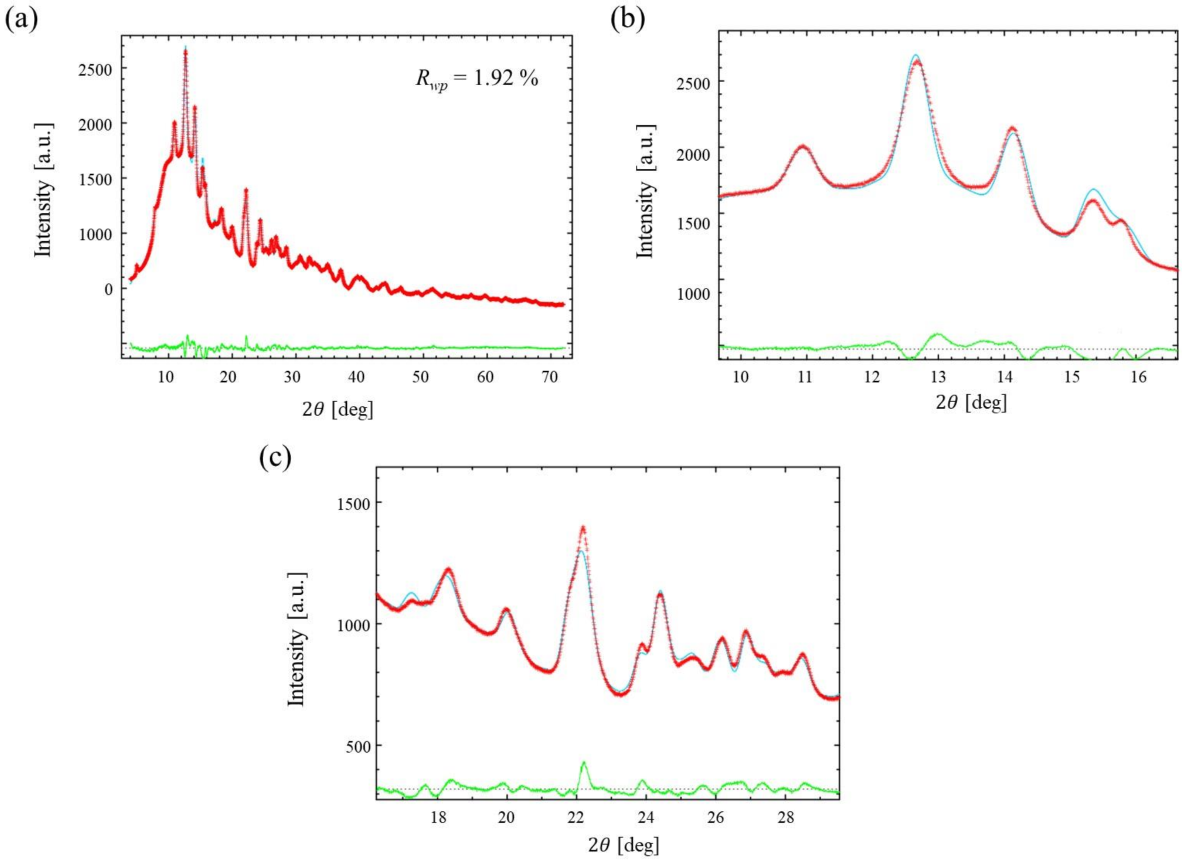

Figure 3.6.47 Powder diffraction data and the sum of powder profiles. (a) 4 ° to 72 °, (b) 23.2 ° to 29.2 °.

Figure 3.6.47 shows the powder diffraction data and the sum of powder profiles. Figure 3.6.47(a) shows the diffraction angle from 4 ° to 72 °. R_{wp} was 1.92 %. R_{wp} of the profile fitting was lower than that of Rietveld refinement by 0.39 %. Figure 3.6.47(b) shows the diffraction angle from 9.8 ° to 16.5 °. The difference of the intensity between the powder diffraction data and the powder profile at 11 ° was less than 20. The difference of the intensity between the powder diffraction data and the powder profile at 13.5 ° was less than 50. Figure 3.6.47(c) shows the diffraction angle from 23.2 ° to 29.2 °. R_{wp} in this angle was 1.98 %. R_{wp} of the profile fitting was lower than that of Rietveld refinement by 0.92 %. Difference of intensity was less than 50 in 18 ° . The difference of intensity was less than 30 in 26.8 ° .

The profile fitting with powder profile of monoclinic ZrO_2 elliptic cylinder with twin faulting provided the better expression for powder diffraction data than Rietveld refinement. Height, short axis and long axis of elliptic cylinder were 7.8 nm, 8.2 nm and 10.2 nm. It was found that ZrO_2 nanoparticles at room temperature have twin faulting in the structure.

3.6.3.3 HfO_2

Powder diffraction data of HfO_2 nanoparticle collected at supercritical water condition was analyzed by the profile fitting. The structure model of HfO_2 nanoparticle with twin faulting was constructed for the analysis. The powder profile of HfO_2 nanoparticles were calculated by DSE. The powder profiles of fused silica capillary and the powder profile of supercritical water at 673 K and 30 MPa were used in the analysis. The intensity of powder profiles of HfO_2 nanoparticles, supercritical water and fused silica capillary were optimized in the analysis.

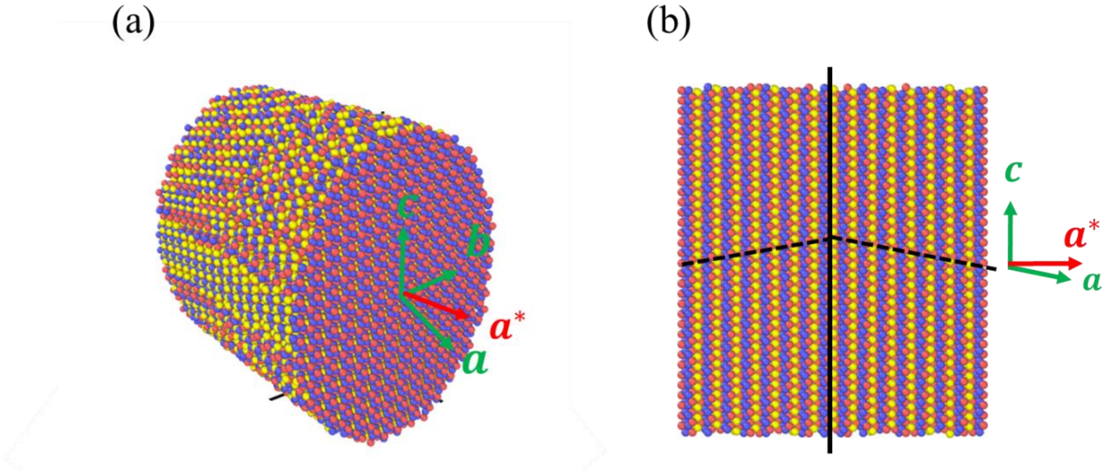

Figure 3.6.48 Structure models of monoclinic HfO_2 nanoparticles. (a) elliptic cylinder, (b) cutting surface by *ac* plane.

Figure 3.6.48 shows the structure model of monoclinic HfO_2 nanoparticle. Red spheres are hafnium atoms. Yellow and blue spheres are oxygen atoms. Lattice constants were obtained from the result of Rietveld refinement at Section 3.6.1.3. The fractional coordinates of atoms were obtained from the structure model by Whittle et al [77]. Green arrows show the directions of the axes of unit cell. The shape of the structure model was elliptic cylinder. Short axis is parallel to *b* direction. Long axis is parallel to *c* direction.

Figure 3.6.48(a) shows structure model used for profile fitting. Height was 8.0 nm. Short axis was 7.0 nm. Long axis was 9.0 nm. Number of atoms was 43602. Figure 3.6.48(b) shows cutting surface by ac plane. One layer of twin faulting was inserted at the center of structure model. Black dashed line shows position of twin faulting and directions of stacking sequence of hafnium atoms.

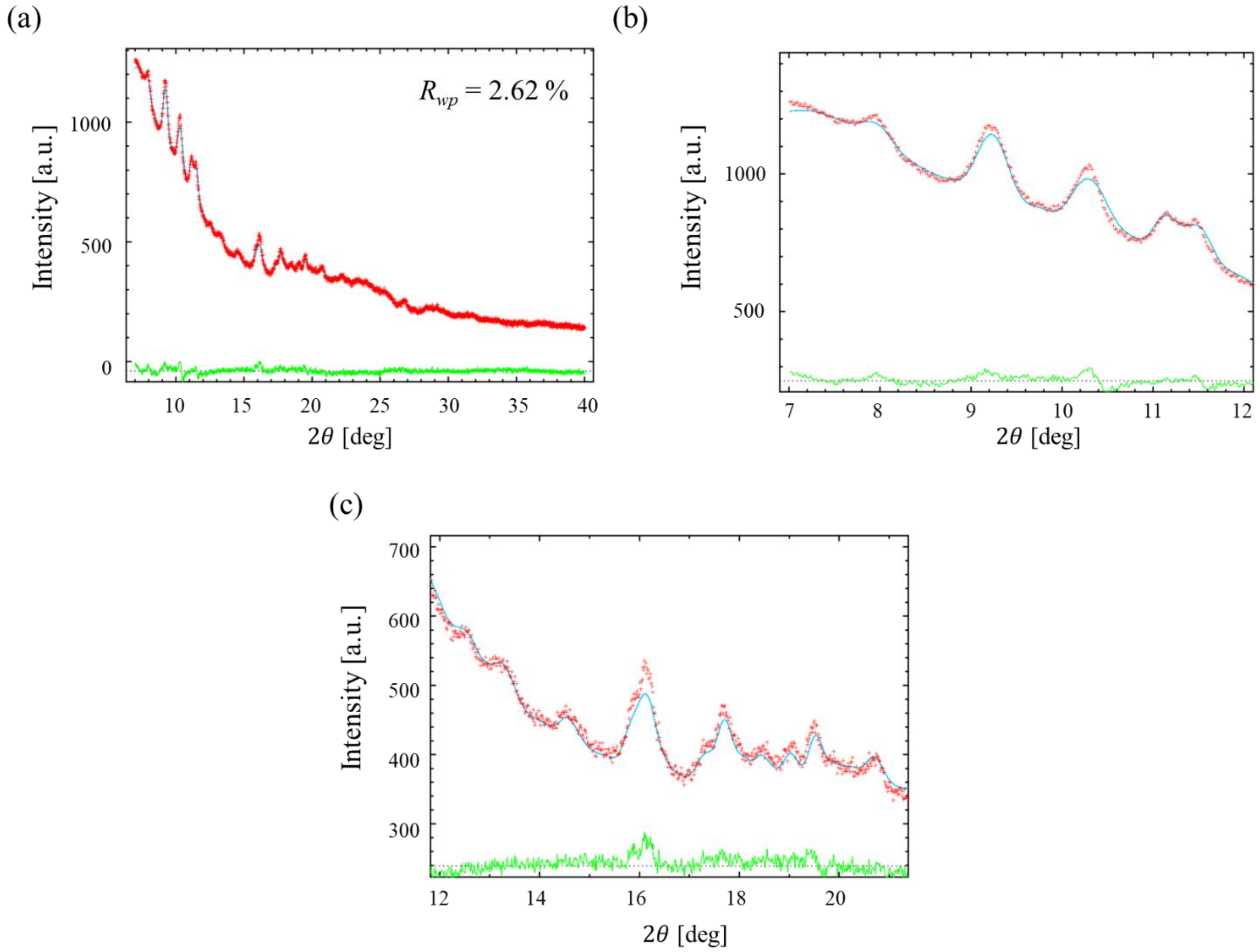

Figure 3.6.49 Powder diffraction data and the sum of powder profiles. (a) 7 ° to 40 °, (b) 16.8 ° to 21.2 °.

Figure 3.6.49 shows the powder diffraction data and the sum of powder profiles. Figure 3.6.49(a) shows the diffraction angle from 7 ° to 40 °. R_{wp} was 2.62 %. R_{wp} was lower than that of Rietveld refinement by 0.13 %. Figure 3.6.49(b) shows the diffraction angle from 7 ° to 12 °. The peak of 200 reflection at 11.6 ° has appeared in the powder profile. The intensity of the powder profile at 7.9 ° was lower than that of the powder diffraction data by 30. Figure 3.6.49(c) shows the diffraction angle from 16.8 ° to 21.2 °. The difference of the intensity between the powder diffraction data and the sum of powder profiles were less than 20 in this angle. No Bragg peak appeared in the sum of powder profiles at 19.8 °.

The profile fitting with powder profile of monoclinic HfO_2 elliptic cylinder with twin faulting provided the better expression for powder diffraction data than Rietveld refinement. Height, short axis and long axis of elliptic cylinder was 8.0 nm, 7.0 nm and 9.0 nm. It was found that HfO_2 nanoparticles synthesized in supercritical water have twin faulting in the structure.

3.6.4 Development of method for analysis of powder diffraction data of nanoparticles

A method was developed for the analysis of the powder diffraction data of nanoparticles. At first, the powder diffraction data of nanoparticles were analyzed by Rietveld refinement. The powder profile was calculated from the average structure model of crystals. The deviations of the intensity were found between the powder diffraction data and the calculated powder profiles. For examples, the powder profile of fcc Ag showed 200 reflection with the larger peak height and smaller FWHM than the powder diffraction data. Several peaks of the powder diffraction data of ZrO_2 nanoparticles and HfO_2 nanoparticles were not expressed by the powder profiles.

These deviations came from the effect of small size or the lattice defect of nanoparticles. We systematically investigated the effect of size and twin faulting to the powder profiles. The powder profiles were calculated from the structure models of nanoparticles by DSE. It was found that several desirable expression were obtained from the powder profiles of nanoparticles with twin faulting. The twin faulting in the structure of Ag nanosphere provided not only the broadening of 200 reflection but also a satellite peak at the lower angle region of 111 reflection. Twin faulting in the structure of ZrO_2 nanoparticles and HfO_2 nanoparticles caused the shift and the increase of the peak height for several peaks where the deviations of the intensity were found in Rietveld refinement. It was also confirmed that only size change cannot express these changes in the powder profiles.

The powder diffraction data of nanoparticles were analyzed by the powder profiles calculated by DSE. The structure models of nanoparticles with twin faulting was constructed for Ag, ZrO_2 and HfO_2 nanoparticles. The powder profiles calculated from the structure models provided the lower reliability factors and the better expression for the powder diffraction data of nanoparticles than Rietveld refinement.

3.7 Summary

We developed a method for the analysis of *in-situ* SR-PXRD data. The powder profiles of a fused silica capillary and pure water were determined for extracting the diffraction of nanoparticles from the powder diffraction data. The powder diffraction data of nanoparticles were not expressed by the powder profiles calculated from the averaged structure models of Rietveld refinement. DSE was used for the analysis of the structure of nanoparticles. The effects of the size and the local lattice defects to the powder profile were systematically investigated. The powder profile calculated from the structure model with twin faulting provided the better expression for the powder diffraction data of Ag, HfO_2 and ZrO_2 nanoparticles.

4. Phase and size selective crystal growth of ZrO_2 nanoparticle in supercritical water

4.1 Purpose of *in-situ* SR-PXRD study

The mechanism of the phase stability of the tetragonal and the monoclinic phase of ZrO_2 nanoparticles remained unsolved, even though many studies have been performed about that. We carried out the *in-situ* SR-PXRD study of the synthesis of ZrO_2 nanoparticles in supercritical water for the investigation of the relation between the crystalline phases of ZrO_2 nanoparticles and the synthesis conditions. *In-situ* SR-PXRD data collected at thirteen conditions were used for the analysis. It should be noted that we used the identical precursor for all the measurements and the difference of synthesis conditions were only temperature and pressure. The crystalline phases of the synthesized nanoparticles were identified by Rietveld refinement. The size of nanoparticles were estimated from the width of Bragg peaks. The time dependence of scale factor were determined by the analysis.

We investigated the dependence of the crystalline phases of nanoparticles on the synthesis conditions. At first, the size and crystalline phases of end product were obtained by analyzing the last frames of *in-situ* SR-PXRD experiment. The crystalline phases of end products showed the complex dependence on temperature and pressure. Next, we investigated the crystalline phases of nanoparticles during the synthesis. Two types of the time dependence of the intensity of Bragg peaks were found for the monoclinic phase and the tetragonal phase. The crystalline phases of nanoparticles which were stably synthesized during the reaction were investigated by using the time dependences of the intensity of Bragg peaks. It was found that the crystalline phases during the synthesis also showed the complex dependence on temperature and pressure.

We focused on properties of water as the parameters which are varied with temperature and pressure. The dependence of crystalline phases were investigated in terms of density of water, dielectric constant of water and ion product of water. These properties of water described the dependence of crystalline phases of nanoparticles in twelve conditions. Among three properties, we selected ion product of water as the appropriate scale to describe the crystalline phases of ZrO_2 nanoparticles. Ion product scale were applied for the size of synthesized nanoparticles. Ion product scale also described a series of results reported on the previous papers.

Section 4.2 summarizes the reported studies of ZrO_2 nanoparticles synthesis. Section 4.3 explains the estimation of the size of synthesized nanoparticles. Section 4.4 shows the crystalline phases of end products. Section 4.5 describes the crystalline phases of nanoparticles during the synthesis. Section 4.6 explains the dependence of crystalline phases on properties of the water. Section 4.7 describes ion product scale of the crystalline phases. Ion product scale was applied for the size of nanoparticles. Ion product scale was also applied for the crystalline phases of nanoparticles on previous papers. Section 4.8 summarizes this chapter.

4.2 Previous studies of the phase stability for the crystalline phases of ZrO_2 nanoparticles

This section summarizes the previous studies on the phase stability of the monoclinic phase and the tetragonal phase of ZrO_2 materials. For bulk materials, only monoclinic phase is available at room temperature [80]. In the case of nanoparticles, the metastable tetragonal phase can coexist with the monoclinic phase [81]. The mechanisms for the stabilization of the tetragonal phase at room temperature were reviewed by Shukla *et al.* [8]. They noted that no single mechanism can satisfactorily explain all the experimental results. Several studies suggested that the size of nanoparticle affects the phase stability. For example, Garvie *et al.* suggested an upper limit of the size for the stabilization of the tetragonal phase [82], [83].

Table 4.2.1 Crystalline phases and the synthesis conditions of ZrO_2 nanoparticles.

Precursor	Temperature [K]	Crystalline phase	Reference
$ZrO(NO_3)_2$・$2H_2O$	473	*m* + *t*	[84]
	523	*m* + *t*	
$ZrO(NO_3)_2$	473	*m* + *t*	[85]
$ZrO(NO_3)_2$ + KOH	473	*m* + *t*	
$ZrOCl_2$・$8H_2O$ + TMAHC/TMAH	423	*m*	[86]
$ZrOCl_2$・$8H_2O$ + $KHCO_3$/KOH	423	*t*	
$ZrOCl_2$・$8H_2O$ + NH_4OH/KOH + NaOH	423	*t*	[87]
	473	*m*	
	523	*m*	
$ZrOCl_2$・$8H_2O$ + NaOH	523	*m*	[88]
$ZrO(NO_3)_2$・$2H_2O$	483	*m*	[89]
$Zr(CH_3COO)_4$	473	*m*	[90]
$Zr(CH_3COO)_4$	723	*m* + *t*	[55]
$ZrO(CH_3COO)_2$	673	*m* + *t*	[54]

Many studies have been reported about the synthesis of ZrO_2 nanoparticles in the reaction field of water including supercritical conditions. Table 4.2.1 summarizes the crystalline phases and synthesis conditions of ZrO_2 nanoparticles in the previous studies. Columns of table are: the precursor, temperature, crystalline phases of synthesized nanoparticles and index of reference. *m* shows the synthesis of the monoclinic phase nanoparticles. *t* shows the synthesis of the tetragonal phase nanoparticles. The crystalline phases of synthesized nanoparticles showed the complex dependence on the synthesis conditions. Noh *et al*. reported the synthesis of the tetragonal phase at 473 K and the synthesis of monoclinic phase at 523 K and 573 K [87]. Taguchi *et al.* reported the synthesis of the monoclinic phase and the synthesis of the tetragonal phase of ZrO_2 nanoparticles at 523 K and 573 K [84].

Other factors such as the chemical composition and pH of the precursor can affect the stability of crystalline phases. Sato *et al.* controlled the crystalline phases of ZrO_2 nanoparticles by changing the surfactants [86]. The surface modification by the mixture of tetramethyl hydrogen carbonate and tetramethyl ammonium hydroxide provided the monoclinic phase. The surface modification by the mixture of potassium bicarbonate and potassium hydroxide provided the tetragonal phase.

Denkewicz *et al.* carried out the synthesis by changing the amount of potassium hydroxide. Monoclinic phase and tetragonal phase nanoparticles were obtained in the synthesis. The ratio of the amount of the monoclinic phase and the tetragonal phase nanoparticles were different at an acidic condition and at alkaline conditions [85]. *In-situ* SR-PXRD studies of the synthesis of ZrO_2 nanoparticles in water were performed only on one condition [89], [90]. ZrO_2 nanoparticles synthesis were carried out by various reaction time. The synthesis with batch-type reactor takes from one hour to ten days [84], [88]. The synthesis by the flow type reactor typically completed within one minute

[54], [55]. The relation between the crystalline phases of synthesized nanoparticles and the synthesis conditions remains unsolved.

4.3 Estimation of size of nanoparticles

The powder diffraction data of ZrO_2 nanoparticles in the present study were analyzed by Rietveld refinement. The results of Rietveld refinement were described in Section 3.6.1.2. The powder diffraction data of nanoparticles were expressed as the sum of powder profiles of the structure models of monoclinic phase and tetragonal phase of ZrO_2.

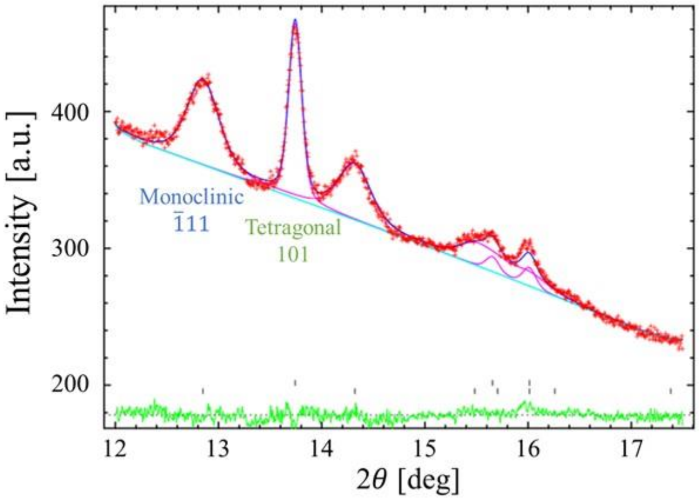

Figure 4.3.1 powder diffraction data and the sum of powder profiles of Rietveld refinement.

Figure 4.3.1 shows the powder diffraction data and the sum of powder profiles of Rietveld refinement. Size of nanoparticles were estimated from the width of Bragg peaks. Scherrer's equation was used for the estimation of the average size of nanoparticles. FWHM of Bragg peaks determined by Rietveld refinement were used for the analysis. FWHM of -111 reflection at 12.8 ° was used for estimating the size of the monoclinic phase nanoparticles. FWHM of 101 reflection at 13.6 ° was used for estimating the size of the tetragonal phase nanoparticles.

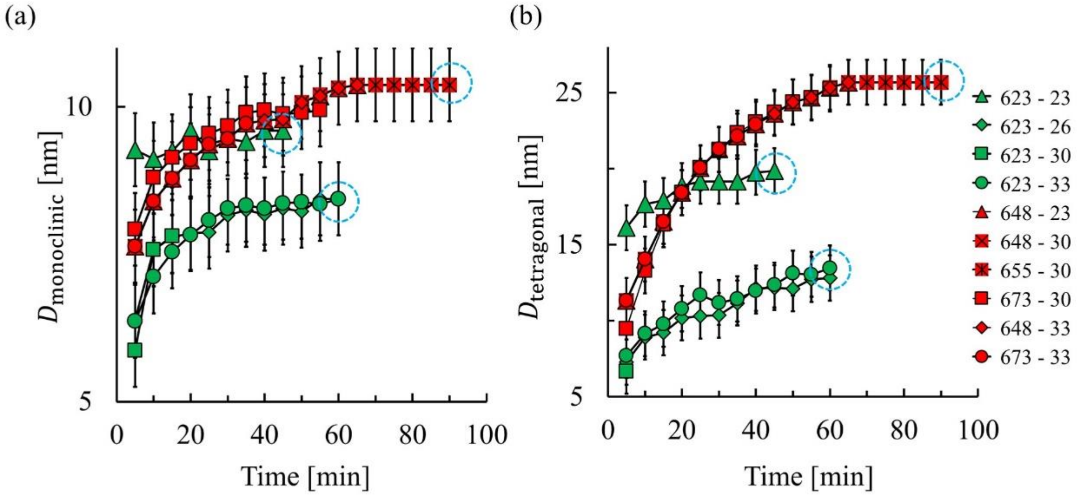

Figure 4.3.2 Time dependence of the size of ZrO_2 nanoparticles. (a) monoclinic phase (b) tetragonal phase.

Blue circles show the size of the end product in several conditions.

Figure 4.3.2 shows the time dependence of the size of ZrO_2 nanoparticles. The horizontal axis is the time in min. The vertical axis is the average size of nanoparticles by Scherrer's equation. The legend shows temperature and pressure of synthesis without units. Green color indicate liquid phase conditions. Red color indicates supercritical water conditions. The size of nanoparticles increased with time in all the conditions. We focused on the size of nanoparticles at the last frame of *in-situ* SR-PXRD experiment. We call nanoparticles at the last frame of *in-situ* SR-PXRD experiment as end product.

Figure 4.3.2 (a) shows the time dependence of size of monoclinic phase nanoparticles. The size of end products was about 8 nm in two conditions. The size of end product was about 9 nm at 623 K and 23 MPa. The size of end product was about 10 nm in other seven conditions. Three types were found for the size of end product of monoclinic phase nanoparticles.

Figure 4.3.2 (b) shows the time dependence of size of tetragonal phase nanoparticles. The size of end products was about 12 nm in two conditions. The size of end products was 20 nm at 623 K and 23 MPa. The size of end products in other seven conditions was about 25 nm. Three types were also found for the size of end products of the tetragonal phase nanoparticles.

4.4 Crystalline phases of end product

The crystalline phases of end products were investigated by Rietveld refinement. The dependence of the crystalline phases of end products on temperature and pressure were investigated in the analysis.

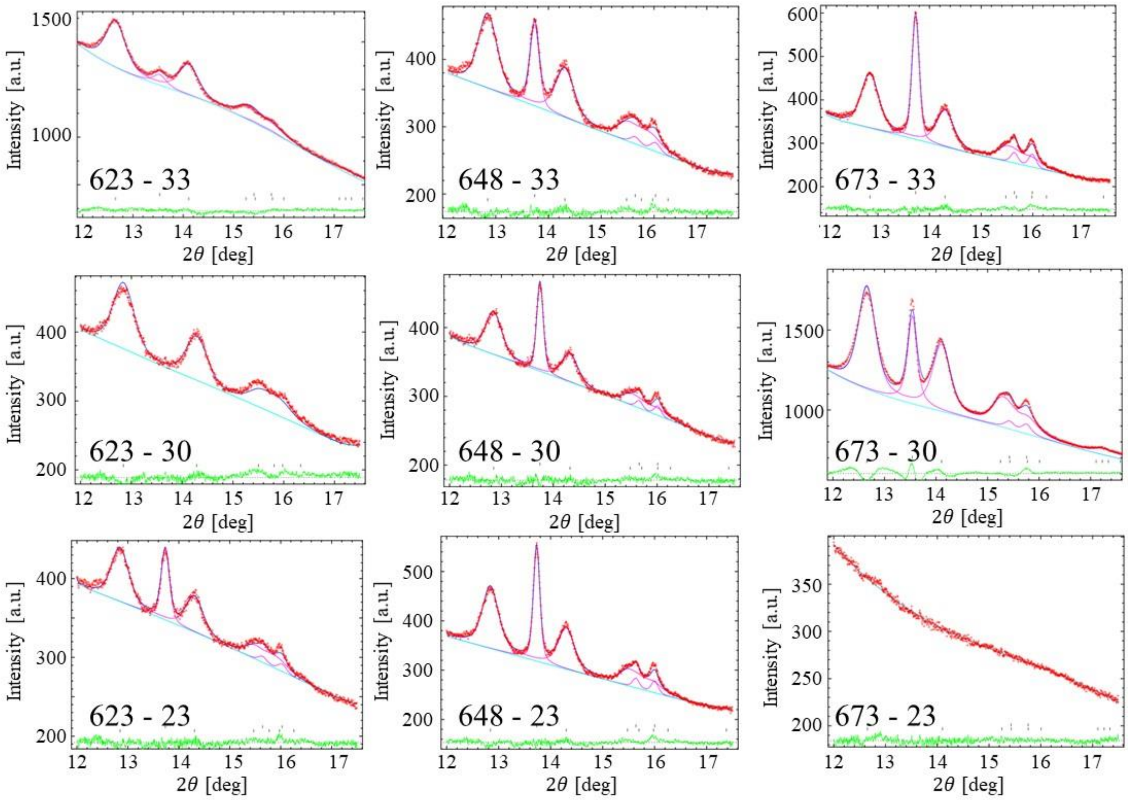

Figure 4.4.1 powder diffraction data of the end product in nine conditions.

Figure 4.4.1 shows the powder diffraction data of end products in nine conditions. The powder diffraction data at temperature of 623 K, 648 K and 673 K and at pressure of 23 MPa, 30 MPa and 33 MPa were shown as representative. The numbers in the figures show temperature and pressure of synthesis without units. Only Bragg peaks of monoclinic phase was observed at 623 K and 30 MPa. No Bragg peaks were observed at 673 K and 23 MPa. In other conditions, Bragg peaks of the monoclinic phase and the tetragonal phase were observed in the powder diffraction data.

The dependence of crystalline phase of end products on synthesis conditions were investigated by the intensity of Bragg peaks in the powder diffraction data. We focused on the intensity ratio of -111 reflection of the monoclinic phase to that of 101 reflection of the tetragonal phase. At temperature of 623 K, the intensity ratio at 23 MPa was higher than those at 30 MPa and 33 MPa. At 673 K, the intensity ratio at 33 MPa was higher than those at 30 MPa and 23 MPa. At 23 MPa and 30 MPa, the intensity ratio at 648 K was higher than those at 623 K and 673 K. At 33 MPa, the intensity ratio at 673 K was higher than those at 623 K and 648 K. The crystalline phases of end products showed the complex dependence on temperature and pressure.

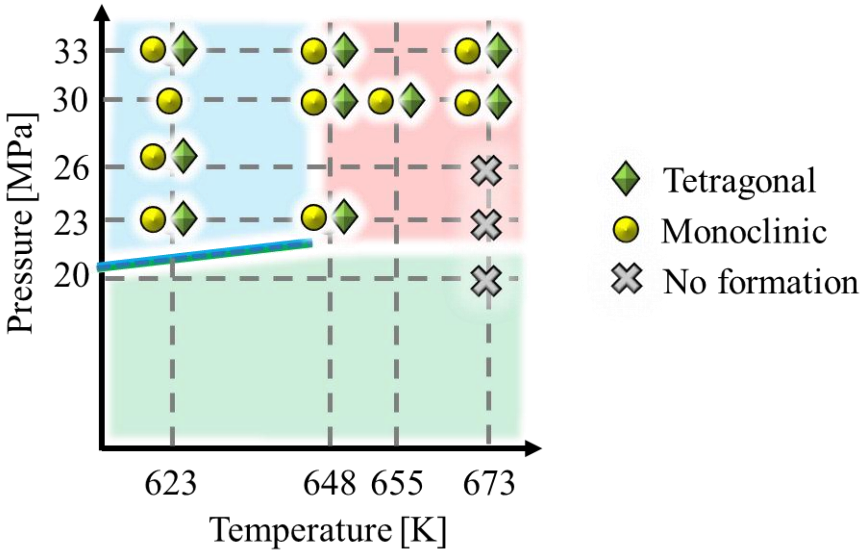

Figure 4.4.2 Dependence of crystalline phases of end products on temperature and pressure.

Figure 4.4.2 summarizes the dependence of crystalline phases of end products on synthesis conditions. The crystalline phases on thirteen conditions including nine conditions in Figure 4.4.1 were shown on the phase diagram. Blue, green and red regions show liquid phase, gas phase and supercritical water. Symbols shows the crystalline phases of nanoparticles observed in the end product. Yellow circle shows the synthesis of monoclinic phase. Green rhombus shows the synthesis of tetragonal phase. Gray cross shows no formation of nanoparticles. At 623 K, only monoclinic phase was observed in the end product at 30 MPa. In other pressure, the monoclinic phase and the tetragonal phase were observed in the end product. At 673 K, nanoparticles were not synthesized at 20, 23 and 26 MPa. In other conditions, the monoclinic phase and the tetragonal phase nanoparticles were observed in the end product.

The crystalline phases of end products showed the complex dependence on synthesis conditions. We found that there is a region on the phase diagram where nanoparticles were not synthesized. It was also suggested that the analysis of crystalline phases of end products is probably not sufficient for the investigation of relation between the crystalline phase and the synthesis conditions. *In-situ* SR-PXRD experiment provided set of the powder diffraction data collected from nanoparticles during synthesis. Next we focused on the crystalline phases of ZrO_2 nanoparticles during synthesis.

4.5 Crystalline phases of nanoparticles during synthesis

The powder diffraction data collected at *in-situ* SR-PXRD experiment were analyzed for investigating the relation between the crystalline phases and synthesis conditions. The time dependence of the intensity of Bragg peaks of the monoclinic phase and the tetragonal phase were investigated for all the conditions. We found that there were two types of the time dependence of the intensity of Bragg peaks for the monoclinic phase and the tetragonal phase. The time dependence of scale factors of Rietveld refinement were used for investigating the relation between the crystalline phases of nanoparticles during reaction and synthesis conditions.

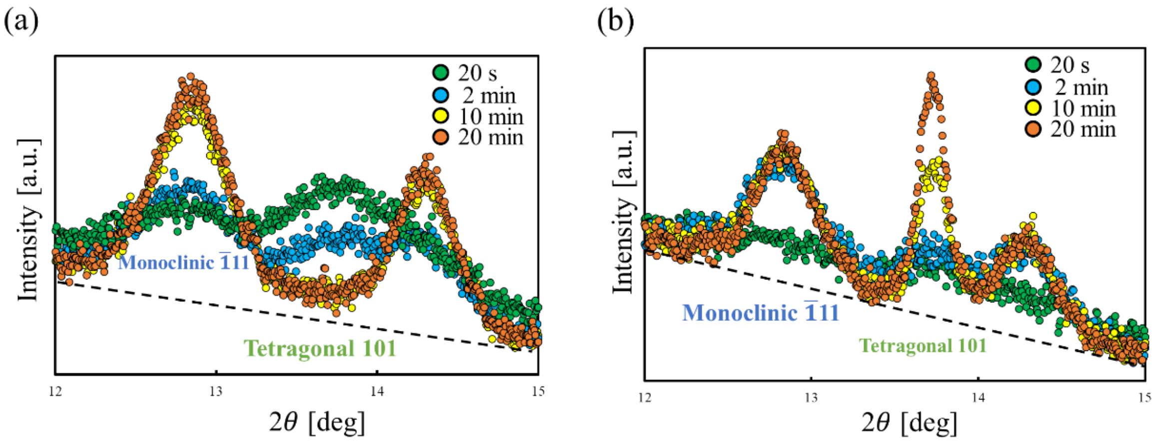

Figure 4.5.1 Powder diffraction data of *in-situ* SR-PXRD experiment. (a) 623 K and 33 MPa(b) 673 K and 33 MPa.

Figure 4.5.1 shows the powder diffraction data of in-situ SR-PXRD experiment. The powder diffraction data collected at 623 K and 33 MPa and 673 K and 33 MPa were shown as representatives. Figure 4.5.1(a) shows the powder diffraction data collected at 623 K and 33 MPa. 101 reflection of tetragonal phase was observed at 20 s from the start of the experiment. The intensity at 13.6 ° has decreased at 2 min and the peak has vanished at 10 min. The intensity of -111 reflection of monoclinic phase has increased at 20 min. It was indicated that tetragonal phase nanoparticles were synthesized at the lower temperature during the initial heating and vanished at the target temperature. In this condition, monoclinic ZrO2 nanoparticles were stably synthesized during the measurement.

Figure 4.5.1(b) shows the powder diffraction data collected at 673 K and 33 MPa. The monoclinic -111 reflection and tetragonal 101 reflection were observed at 2 min. The intensity of -111 reflection of monoclinic phase has increased at 10 min and showed no change after 15 min. The intensity of 101 reflection of tetragonal phase has increased at 20 min. In this condition, tetragonal ZrO_2 nanoparticles were stably synthesized during the measurement.

Two types of the time dependences were observed for the intensity of Bragg peaks of the monoclinic phase and the tetragonal phase nanoparticles. One type showed the stable synthesis of monoclinic phase nanoparticles. Tetragonal phase nanoparticles were destabilized at the target temperature in this type of synthesis. Another type showed the stable synthesis of tetragonal phase nanoparticles. The monoclinic phase nanoparticles were also synthesized in this type of synthesis, but the synthesis was almost stopped after 10 min.

For investigating the relation between the crystalline phase of stably synthesized nanoparticles and synthesis conditions, we used the scale factors determined by Rietveld refinement. The time dependence of scale factor of the monoclinic phase and the tetragonal phase in ten conditions were used in the analysis. The time dependences of scale factor were compared in terms of temperature and pressure.

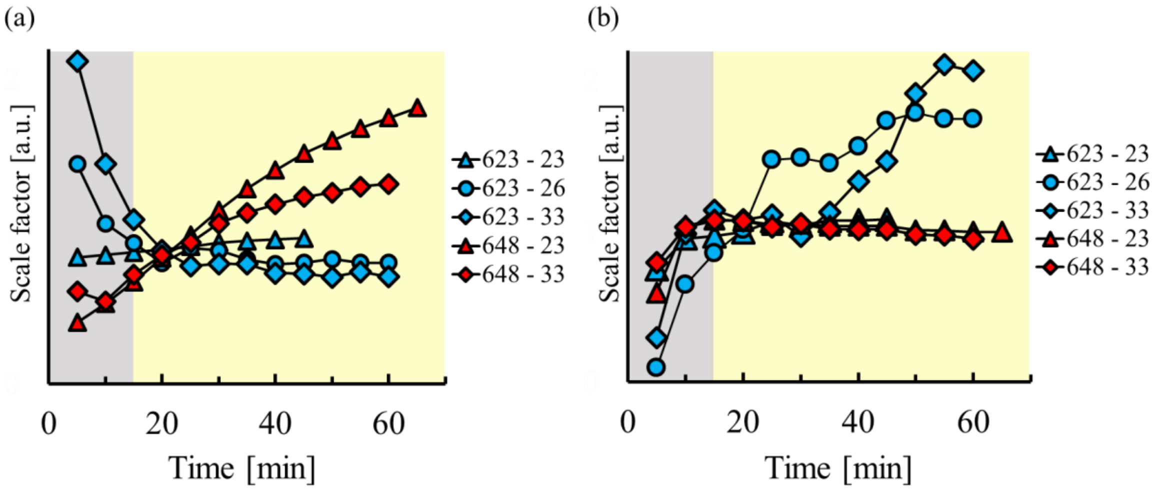

Figure 4.5.2 Time dependence of scale factor of five conditions. (a) monoclinic phase (b) tetragonal phase.

Figure 4.5.2 shows the time dependence of the scale factor. The horizontal axis is time in min. The vertical axis is scale factor. The scale factors in five conditions were shown as representative. We focused on the time dependence of scale factor after 10 min. Yellow colored area shows the time range after 15 min. Figure 4.5.2(a) shows the time dependence of scale factor of the tetragonal phase. The scale factors at 623 K and 33 MPa and at 623 K and 26 MPa showed almost no change or the slight decrease after 15 min. The scale factors at 623 K and 23 MPa has increased after 15 min. The scale factors at 648 K and 23 MPa and at 648 K and 33 MPa were increased with time after 15 min.

Figure 4.5.2(b) shows the time dependence of scale factor of the monoclinic phase. The scale factor at 623 K and 33 MPa and 623 K and 26 MPa increased with time after 15 min. The scale factor at 623 K and 23 MPa has increased with time after 15 min. The scale factor at 648 K and 23 MPa and at 648 K and 33 MPa showed almost no change after 15 min. For four conditions, it was found that only one of the crystalline phases has synthesized after 15 min. Only monoclinic phase nanoparticles were synthesized at 623 K and 33 MPa and at 623 K and 26 MPa. Only tetragonal phase nanoparticles were synthesized at 648 K and 23 MPa and 648 K and 33 MPa. The monoclinic phase and the tetragonal phase nanoparticles were selectively synthesized after 15 min of these four conditions. We investigated the relation between the crystalline phases after 15 min and the synthesis conditions for all the conditions.

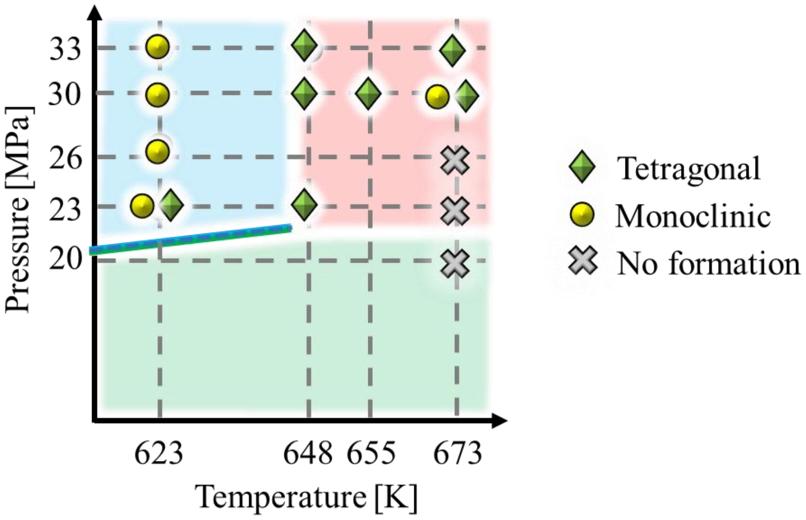

Figure 4.5.3 Dependence of crystalline phases of stably synthesized nanoparticles on temperature and pressure.

Figure 4.5.3 shows the dependence of crystalline phases of nanoparticles after 15 min on temperature and pressure. Crystalline phases of the synthesized nanoparticles were shown as symbol on the phase diagram. It should be noted that in this figure, these symbols show the crystalline phases which were stably synthesized after 15 min. Yellow circle shows the synthesis of monoclinic phase. Green rhombus shows the synthesis of tetragonal phase. Gray cross shows no formation of nanoparticles.

At 623 K, the monoclinic phase and the tetragonal phase nanoparticles were stably synthesized at 23 MPa. The crystalline phase of stably synthesized nanoparticles became monoclinic phase by additional pressure of 3 MPa. At 648 K, tetragonal phase nanoparticles were stably synthesized at 23 MPa. Crystalline phase of stably synthesized nanoparticles were not changed by additional pressure. At 33 MPa, only monoclinic phase nanoparticles were synthesized at 623 K. The crystalline phase of stably synthesized nanoparticles became tetragonal phase by additional temperature of 50 K. At 23 MPa, monoclinic phase and tetragonal phase nanoparticles were stably synthesized in the synthesis. No crystalline phases were observed by additional temperature of 50 K. The crystalline phases of stably synthesized nanoparticles after 15 min showed the complex dependence on temperature and pressure.

4.6 Dependence of crystalline phases on properties of water

The crystalline phases of stably synthesized nanoparticles showed the complex dependence on the synthesis conditions. As noted in the section 4.1, the difference of the synthesis conditions were only temperature and pressure. We focused on density of water, dielectric constant of water and ion product of water as the parameters which are varied with temperature and pressure.

The dependences of crystalline phases were investigated for density of water, dielectric constant of water and ion product of water. Density of water was calculated based on the IAPWS-IF97 [30]. Dielectric constant was calculated by the equation of Uematsu and Franck [31]. Ion product of water was calculated by the equation of Marshall and Franck [32].

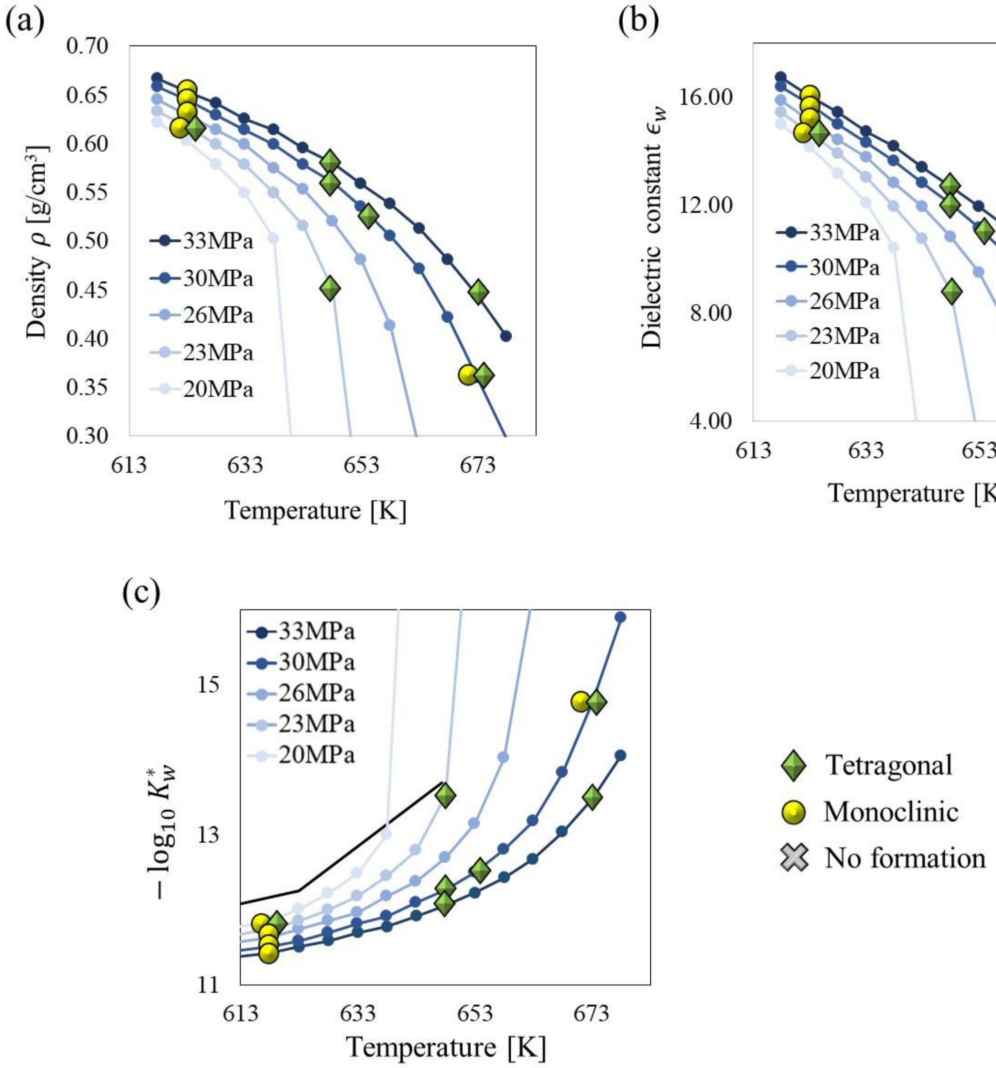

Figure 4.6.1 The dependences of crystalline phases of nanoparticles on properties of water. (a) density, (b) dielectric constant, (c) ion product.

Figure 4.6.1 shows the dependence of crystalline phases of synthesized nanoparticles on density of water, dielectric constant of water and ion product of water. The horizontal axis is temperature. The symbol on the plot shows the crystalline phase of the synthesized nanoparticles after 15 min. Yellow circle shows the synthesis of monoclinic phase. Green rhombus shows the synthesis of tetragonal phase. Gray cross shows no formation of nanoparticles.

Figure 4.6.1 (a) shows the dependence of the crystalline phases on density of water. The monoclinic phase nanoparticles were synthesized above density of 0.62 g/cm^3. The tetragonal phase nanoparticles were synthesized in density from 0.36 to 0.62 g/cm^3. Nanoparticle was not synthesized below density of 0.19 g/cm^3.

Figure 4.6.1 (b) shows the dependence of the crystalline phases on dielectric constant of water. The monoclinic phase nanoparticles were synthesized above dielectric constant of 14.69. The tetragonal phase nanoparticles were synthesized in dielectric constant from 5.99 to 14.69. Nanoparticle was not synthesized below dielectric constant of 2.72.

Figure 4.6.1 (c) shows the dependence of the crystalline phases on ion product of water. The monoclinic phase nanoparticles were synthesized above ion product of $10^{-11.8}$ mol^2L^{-2}. The tetragonal phase nanoparticles were synthesized in ion product from 10^{-15} to $10^{-11.8}$ mol^2L^{-2}. Nanoparticle was not synthesized below ion product of $10^{-18.6}$ mol^2L^{-2}.

The monoclinic phase nanoparticles and tetragonal phase nanoparticles were synthesized at 623 K and 23 MPa and 673 K and 30 MPa. Density of water, dielectric constant of water and ion product of water at 623 K and 23 MPa were placed between the range of synthesis of the monoclinic phase and that of synthesis of the tetragonal phase. The crystalline phases of 673 K and 30 MPa was not consistent with these properties of water. This condition was located in the neighborhood of Nishikawa-Widom line [35]. Further studies may be required for the investigation of phase stability of ZrO_2 nanoparticles around Nishikawa-Widom line. Except 673 K and 30 MPa, the crystalline phases of ZrO_2 nanoparticles in twelve conditions were explained by density of water, dielectric constant of water and ion product of water.

4.7 Ion product scale of crystalline phase and size of nanoparticles

The crystalline phases in twelve conditions were described by density of water, dielectric constant of water and ion product of water. Several studies were reported about the crystalline phases of ZrO_2 nanoparticles and the role of water on the phase stability. We examined the discussion on these studies and selected ion product of water as the scale to describe the crystalline phases of ZrO_2 nanoparticles.

A part of the tetragonal phase of nanoparticles were destabilized in three conditions of *in-situ* SR-PXRD experiment. Monoclinic phase nanoparticles were stably synthesized in these conditions. These observations indicated the possibility of tetragonal-to-monoclinic phase transition of ZrO_2 nanoparticles. The roles of water on tetragonal-to-monoclinic were reported by several studies [8], [91].

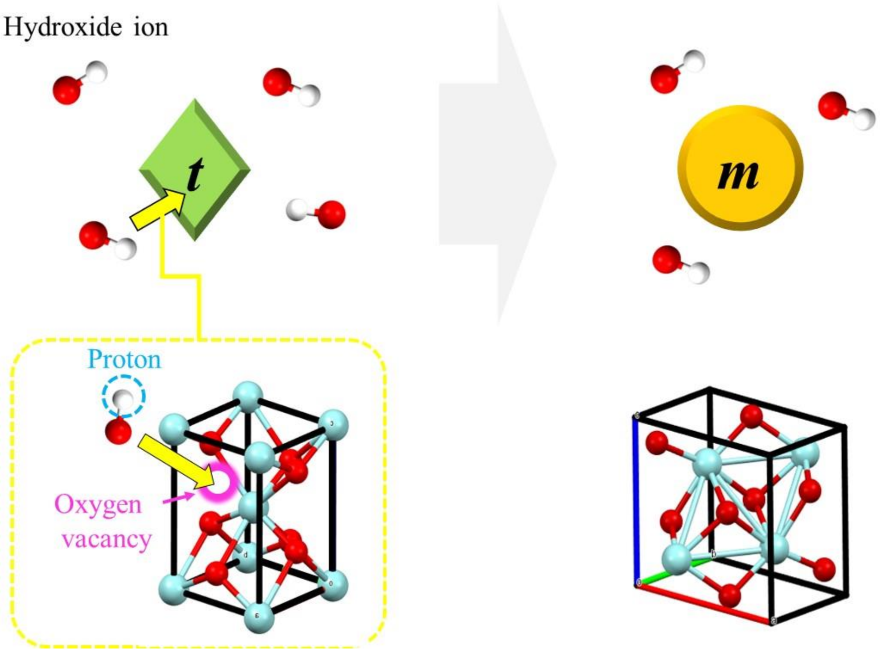

Figure 4.7.1 Schematic of tetragonal-to-monoclinic phase transition of ZrO_2 by the diffusion of hydroxide ions in the lattice. This mechanism was suggested by Guo for bulk materials [51].

Guo reviewed a series of studies on the previous papers and discussed the mechanism of tetragonal-to-monoclinic phase transition of the bulk ZrO_2 [51]. Guo concluded that the phase transition is caused by the diffusion of hydroxide ions in the tetragonal lattice which has the oxygen vacancies. Figure 4.7.1 shows the schematic of Guo's mechanism of tetragonal-to-monoclinic phase transition. Hydroxide ions were incorporated in the lattice of tetragonal phase nanoparticles. Oxygen vacancies were replaced with the diffused hydroxide ions and the proton defects are formed in the lattice. The accumulation of proton defects in the lattice destabilizes the tetragonal phase. Hydroxide ions were detected on the surface of ZrO_2 by X-ray photoemission spectroscopy and infrared adsorption spectroscopy [92]–[95]. The relation between the thickness of the degraded area of bulk material on SEM image by Kim *et al.* and concentration of hydroxide ions supported the diffusion of hydroxide ions in the lattice [93]. The evaluation of concentration of proton defect and oxygen vacancy by Kruse *et al.* with the elastic recoil detection analysis method supported the scenario of filling oxygen vacancies with hydroxide ions [96]. The destabilization of tetragonal phase of ZrO_2 nanoparticles supported this mechanism of tetragonal-to-monoclinic phase transition.

The scale to describe the crystalline phases of ZrO_2 nanoparticles were examined based on this mechanism. Both of dielectric constant of water and ion product of water is related to the ionic nature of water. The ion product of water is more appropriate than dielectric constant of water as the scale for the atomic-scale structure, since ion product explicitly treats the hydroxide ion but dielectric constant is the macroscopic property.

The comparison between density of water and ion product of water is complicated. It depends on the mechanism of the incorporation of hydroxide ions in the lattice. It is unclear whether the dissociative adsorption of a water molecule on an oxygen vacancy forms a hydroxide ion in the lattice or a hydroxide ion in water is directly incorporated in the lattice. No observation is reported on the incorporation of hydroxide ions into the ZrO_2 lattice. All the experimental evidences in Guo's paper are obtained from *ex-situ* characterization of bulk ZrO_2 sample. We selected ion product of water which is explicitly related to the hydroxide ion as the scale for the crystalline phases of ZrO_2 nanoparticles [97].

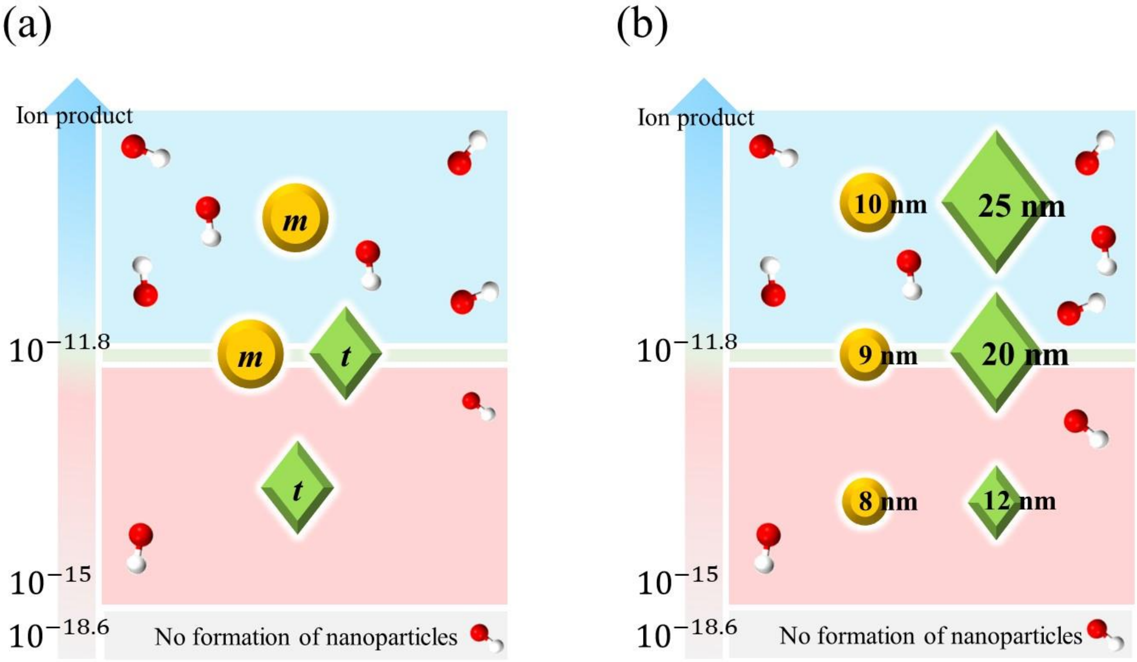

Figure 4.7.2 Ion product scale of the crystal growth of ZrO_2 nanoparticles. (a) ion product and the crystalline phases of nanoparticles synthesized after 15 min, (b) ion product and the size of the end products.

Figure 4.7.2 summarizes the ion product scale of the crystal growth of ZrO_2 nanoparticles. Figure 4.7.2 (a) shows the ion product of water and the crystalline phases of nanoparticles synthesized after 15 min. Only tetragonal phase nanoparticles were synthesized in the range of ion product from 10^{-15} to $10^{-11.8}$. Only monoclinic phase nanoparticles were synthesized in ion product above $10^{-11.8}$. Both of the monoclinic phase and the tetragonal phase nanoparticles were synthesized at ion product of $10^{-11.8}$.

The ion product scale can also explain the size of the synthesized nanoparticles in section 4.3. The size of end product of monoclinic phase was about 10 nm in the range of ion product from 10^{-15} to $10^{-11.8}$. The size of end product of tetragonal phase was about 25 nm in these conditions. The size of end product of monoclinic phase was about 8 nm in ion product above $10^{-11.8}$. The size of end product of tetragonal phase was about 12 nm in these conditions. The size of end product of monoclinic phase was about 9 nm in ion product of $10^{-11.8}$. The size of end product of tetragonal phase was about 20 nm in this condition.

Table 4.7.1 List of the previous studies which were qualitatively consistent with the present study.

Precursor	Temperature [K]	Crystalline phase	Reference
$ZrO(NO_3)_2 \cdot 2H_2O$	473	*m* + *t*	[84]
	523	*m* + *t*	
$ZrO(NO_3)_2$	473	*m* + *t*	[85]
$ZrO(NO_3)_2$ + KOH	473	*m* + *t*	
$ZrOCl_2 \cdot 8H_2O$ + TMAHC/TMAH	423	*m*	[86]

$ZrOCl_2 \cdot 8H_2O + KHCO_3/KOH$	423	*t*	
$ZrOCl_2 \cdot 8H_2O + NH_4OH/KOH + NaOH$	423	*t*	[87]
	473	*m*	
	523	*m*	
$ZrOCl_2 \cdot 8H_2O + NaOH$	523	*m*	[88]
$ZrO(NO_3)_2 \cdot 2H_2O$	483	*m*	[89]
$Zr(CH_3COO)_4$	473	*m*	[90]
$Zr(CH_3COO)_4$	723	*m* + *t*	[55]
$ZrO(CH_3COO)_2$	673	*m* + *t*	[54]

The ion product scale explained the several results of the previous studies. Yellow colored rows in Table 4.7.1 show the list of previous studies which were qualitatively consistent with ion product scale in the present study. Temperature dependence of the crystalline phases in the previous studies were qualitatively described by ion product scale. Noh *et al.* reported the synthesis of tetragonal phase at 473 K at ion product $10^{-11.64}$, and the synthesis of monoclinic phase at temperature of 523 K and 573 K at the higher ion product $10^{-11.31}$ and $10^{-11.19}$ [87]. Taguchi *et al.* reported the increase of the intensity of tetragonal phase with time at ion product of $10^{-11.31}$ and the decrease of the intensity of tetragonal phase at ion product of $10^{-11.19}$ [84]. The ion product scale was consistent with the previous *in-situ* studies of the synthesis of ZrO_2 nanoparticles. Dippel *et al.* showed the decrease of the intensity of tetragonal phase at ion product of $10^{-11.14}$ [89]. Bremholm *et al.* reported the synthesis of pure monoclinic phase at ion product of $10^{-11.16}$ [90].

The ion product scale also provided the additional possible insight to the several observations in the previous studies. Denkewicz *et al.* reported a series of synthesis of ZrO_2 nanoparticles in an acidic and an alkaline conditions [85]. The decrease of the amount of tetragonal phase nanoparticles with the reaction time were observed in all the conditions where tetragonal phase nanoparticles were synthesized. The faster decrease of the amount of tetragonal phase nanoparticles at an alkaline condition than that at an acidic condition can be simply interpreted as the facilitation of the tetragonal-to-monoclinic phase transition by higher concentration of hydroxide ions in the reaction field. Faster decrease of the tetragonal phase in alkaline condition was also observed by Bućko *et al.* [88].

4.8 Summary

The relation between the crystalline phases of ZrO_2 nanoparticles and synthesis conditions were investigated by *in-situ* SR-PXRD experiment. Powder diffraction data collected at thirteen conditions were used for the analysis. The difference of synthesis conditions were only temperature and pressure. The powder diffraction data were analyzed by the Rietveld refinement. The powder diffraction data were expressed as the sum of powder profiles of the monoclinic phase and the tetragonal phase. The size of nanoparticles were estimated by Scherrer's equation.

The crystalline phases of end product were investigated in the analysis. It showed the complex dependence on the synthesis conditions. Next, we focused on the crystalline phases of nanoparticles during synthesis. The two types of the time dependence of intensity of Bragg peaks were found for the monoclinic and tetragonal phase. It was found that only one of the crystalline phases were selectively synthesized in several conditions after 10 min. We investigated the relation between the crystalline phases of nanoparticles after 15 min of synthesis and synthesis conditions. The crystalline phases of nanoparticles after 15 min also showed the complex dependence on synthesis conditions.

We focused on properties of water as the parameter which are varied with temperature and pressure. Density of water, dielectric constant of water and ion product of water were calculated for all the synthesis conditions. The crystalline phases of twelve conditions were explained by density of water, dielectric constant of water and ion product of water. Ion product of water was selected as the scale for the crystalline phases of ZrO_2 nanoparticles based on the discussion on the mechanism of tetragonal-to-monoclinic phase transition by Guo. The size of synthesized nanoparticles were explained by ion product scale. The crystalline phases of ZrO_2 nanoparticles reported in the previous papers were also described by ion product scale.

5. Conclusions

Phase and size selective crystal growth of ZrO_2 nanoparticles in supercritical water was revealed from the analysis of the powder diffraction data. The powder diffraction data at thirteen conditions were analyzed by Rietveld refinement. The observed crystalline phases were identified as the monoclinic phase and the tetragonal phase. The relation between the time dependence of crystal growth of each crystalline phase and the synthesis conditions were investigated. The ion product of water was selected as the scale to describe the crystalline phases of synthesized nanoparticles. Monoclinic nanoparticles were stably synthesized in ion product higher than $10^{-11.8}$. Tetragonal nanoparticles were destabilized in these conditions. Tetragonal nanoparticles were stably synthesized in ion product from $10^{-11.8}$ to 10^{-15}. The ion product scale also explained the size of nanoparticles.

The present study showed that *in-situ* SR-PXRD experiment provided new findings in crystal growth of ZrO_2 nanoparticle in supercritical water. Time dependence of crystal growth provided a direct evidence of stability of ZrO_2 polymorphs in supercritical water. It was found that the results reported on previous papers were also described by ion product scale. Such a finding will be a clue for understanding some important issues of ZrO_2 materials related to tetragonal-to-monoclinic phase transition such as Low Temperature Degradation.

A method was developed for the analysis of the powder diffraction data of nanoparticles in the reaction vessel. The powder profiles of reaction vessel and reaction field were modelled for extracting the powder data of nanoparticles. DSE was employed for calculating the powder profiles of nanoparticles. The powder profiles of nanoparticles by DSE flexibly expressed the effect of the small size or the lattice defects in the structure of nanoparticles. The powder diffraction data of Ag, ZrO_2 and HfO_2 nanoparticles were analyzed by the powder profiles of nanoparticles with twin faulting. These powder profiles provided better expression of the powder diffraction data than the powder profiles of Rietveld refinement which was often used for the analysis of powder data of bulk materials.

The system for *in-situ* SR-PXRD experiment was developed to investigate how the structure of nanoparticles in supercritical water can be controlled. System was composed of the sample holder, the pump section and the heater. Powder diffraction data were successfully collected from the synthesis of ZrO_2 and HfO_2 nanoparticles by *in-situ* SR-PXRD experiment at SPring-8 BL02B2. SR-PXRD experiment was performed to measure the powder diffraction data of fused silica capillary and pure water.

Present study showed that *in-situ* SR-PXRD experiment is an effective tool to investigate the mechanism of the structure control of nanoparticles. The parameter which can describe not only the present result but also the results of the previous papers was found from the monitoring of the nanoparticle synthesis. Such finding provides a strategy for the selective synthesis of nanomaterials. The structure of nanoparticles inside the reaction vessel were analyzed by the developed method. The crystal structure, the size and the lattice defect of nanoparticles were simultaneously characterized from the powder diffraction data. Many unknown processes and the structural changes can be found by *in-situ* experiment of the synthesis of nanoparticles. We believe that the combination of *in-situ* SR-PXRD measurement and the analysis method of the powder diffraction data of nanoparticles will be a powerful tool for developing a new area of the material science of nanoparticles, since the structure control is essential for the preparation of the highly functional nanomaterials.

Further research is required for the phase stability of ZrO_2 nanoparticles around Nishikawa-Widom line. It is an interesting topic whether ion product scale can be observed for the other polymorphic metal oxide nanoparticles such as TiO_2. In the present study, the batch-type reactor was used for the experiment. The minimum data collection time was 20 s. Understanding the mechanisms of nucleation or the structure control in flow-type reactor will provide the important clues to prepare the highly functional nanoparticles in supercritical water. This will require X-ray source with the ultrahigh brilliance such as undulator or X-ray Free Electron Laser for collecting the diffraction data in femtoseconds to milliseconds time scales. The dedicated measurement system is essential for *in-situ* experiment. DSE will also be a useful tool for characterizing the non-crystalline nucleuses or the ultrafine nanoparticles with the disordered structure.

References

[1] T. Adschiri, K. Kanazawa, and K. Arai, "Rapid and Continuous Hydrothermal Crystallization of Metal Oxide Particles in Supercritical Water," *J. Am. Ceram. Soc.*, vol. 75, pp. 1019–1041, 1992, doi: 10.1111/j.1151-2916.1992.tb04179.x.

[2] Q. X. Zheng *et al.*, "Synthesis of YVO4 and rare earth-doped YVO4 ultra-fine particles in supercritical water," *J. Supercrit. Fluids*, vol. 46, pp. 123–128, 2008, doi: 10.1016/j.supflu.2008.04.014.

[3] H. Hayashi and Y. Hakuta, "Hydrothermal Synthesis of metal oxide nanoparticles in supercritical water," *Materials*, vol. 3, no. 7, pp. 3794–3817, 2010, doi: 10.3390/ma3073794.

[4] T. Adschiri and A. Yoko, "Supercritical fluids for nanotechnology," *J. Supercrit. Fluids*, vol. 134, pp. 167–175, 2018, doi: 10.1016/j.supflu.2017.12.033.

[5] R. C. Garvie, R. H. Hannink, and R. T. Pascoe, "Ceramic steel?," *Nature*, vol. 258, pp. 703–704, 1975, doi: 10.1038/258703a0.

[6] J. Panpranot, K. Kontapakdee, and P. Praserthdam, "Effect of TiO2 crystalline phase composition on the physicochemical and catalytic properties of Pd/TiO2 in selective acetylene hydrogenation," *J. Phys. Chem. B*, vol. 110, pp. 8019–8024, 2006, doi: 10.1021/jp057395z.

[7] Z. Wang, D. Xia, G. Chen, T. Yang, and Y. Chen, "The effects of different acids on the preparation of TiO2 nanostructure in liquid media at low temperature," *Mater. Chem. Phys.*, vol. 111, pp. 313–316, 2008, doi: 10.1016/j.matchemphys.2008.04.015.

[8] S. Shukla and S. Seal, "Mechanisms of room temperature metastable tetragonal phase stabilisation in zirconia," *Int. Mater. Rev.*, vol. 50, pp. 45–64, 2005, doi: 10.1179/174328005X14267.

[9] Z. Fang, H. Assaaoudi, H. Lin, X. Wang, I. S. Butler, and J. A. Kozinski, "Synthesis of nanocrystalline SnO2 in supercritical water," *J. Nanopart. Res.*, vol. 9, pp. 683–687, 2007, doi: 10.1007/s11051-006-9171-9.

[10] N. Talebian and F. Jafarinezhad, "Morphology-controlled synthesis of SnO2 nanostructures using hydrothermal method and their photocatalytic applications," *Ceram. Inter.*, vol. 39, pp. 8311–8317, 2013, doi: 10.1016/j.ceramint.2013.03.101.

[11] K. Sue, K. Kimura, K. Murata, and K. Arai, "Effect of cations and anions on properties of zinc oxide particles synthesized in supercritical water," *J. Supercrit. Fluids*, vol. 30, pp. 325–331, 2004, doi: 10.1016/j.supflu.2003.09.009.

[12] S. Mangel, L. Houben, and M. Bar Sadan, "The effect of atomic disorder at the core-shell interface on stacking fault formation in hybrid nanoparticles," *Nanoscale*, vol. 8, pp. 17568–17572, 2016, doi: 10.1039/c6nr04867f.

[13] M. Ibáñez *et al.*, "Crystallographic control at the nanoscale to enhance functionality: Polytypic Cu2GeSe3 nanoparticles as thermoelectric materials," *Chemistry of Materials*, vol. 24, no. 23, pp. 4615–4622, Dec. 2012, doi: 10.1021/cm303252q.

[14] P. M. Diehm, P. Ágoston, and K. Albe, "Size-dependent lattice expansion in nanoparticles: Reality or anomaly?," *ChemPhysChem*, vol. 13, pp. 2443–2454, 2012, doi: 10.1002/cphc.201200257.

[15] C. Weidenthaler, "Pitfalls in the characterization of nanoporous and nanosized materials," *Nanoscale*, vol. 3, pp. 792–810, 2011, doi: 10.1039/c0nr00561d.

[16] H. Akiba *et al.*, “Nanometer-Size Effect on Hydrogen Sites in Palladium Lattice,” *J. Am. Chem. Soc.*, vol. 138, pp. 10238–10243, 2016, doi: 10.1021/jacs.6b04970.

[17] I. Lignos, S. Stavrakis, A. Kilaj, and A. J. deMello, “Millisecond-Timescale Monitoring of PbS Nanoparticle Nucleation and Growth Using Droplet-Based Microfluidics,” *Small*, vol. 11, pp. 4009–4017, 2015, doi: 10.1002/smll.201500119.

[18] R. I. Walton and D. O’Hare, “Watching solids crystallise using in situ powder diffraction,” *Chem. Commun.*, pp. 2283–2291, 2000, doi: 10.1039/b007795j.

[19] K. M. Ø. Jensen, C. Tyrsted, M. Bremholm, and B. B. Iversen, “In situ studies of solvothermal synthesis of energy materials,” *ChemSusChem*, vol. 7, pp. 1594–1611, 2014, doi: 10.1002/cssc.201301042.

[20] H. Jensen *et al.*, “In situ high-energy synchrotron radiation study of sol-gel nanoparticle formation in supercritical fluids,” *Angew. Chem. Int. Ed.*, vol. 46, pp. 1113–1116, 2007, doi: 10.1002/anie.200603386.

[21] J. L. Mi, Y. Shen, J. Becker, M. Bremholm, and B. B. Iversen, “Controlling allotropism in ruthenium nanoparticles: A pulsed-flow supercritical synthesis and in situ synchrotron x-ray diffraction study,” *J. Phys. Chem. C*, vol. 118, pp. 11104–11110, 2014, doi: 10.1021/jp501229p.

[22] T. Friščić *et al.*, “Real-time and in situ monitoring of mechanochemical milling reactions,” *Nat. Chem.*, vol. 5, pp. 66–73, 2013, doi: 10.1038/nchem.1505.

[23] O. Aalling-Frederiksen, M. Juelsholt, A. S. Anker, and K. M. Ø. Jensen, “Formation and growth mechanism for niobium oxide nanoparticles: Atomistic insight from: In situ X-ray total scattering,” *Nanoscale*, vol. 13, pp. 8087–8097, 2021, doi: 10.1039/d0nr08299f.

[24] B. E. Warren and E. P. Warekois, “Stacking faults in cold worked alpha-brass,” *Acta Metall. Mater.*, vol. 3, pp. 473–479, 1955, doi: 10.1016/0001-6160(55)90138-3.

[25] H. L. Andersen, E. D. Bøjesen, S. Birgisson, M. Christensen, and B. B. Iversen, “Pitfalls and reproducibility of in situ synchrotron powder X-ray diffraction studies of solvothermal nanoparticle formation,” *J. Appl. Cryst.*, vol. 51, pp. 526–540, 2018, doi: 10.1107/S1600576718003552.

[26] A. Leonardi and P. Scardi, “Dislocation Effects on the Diffraction Line Profiles from Nanocrystalline Domains,” *Metall. Mater. Trans. A*, vol. 47, pp. 5722–5732, 2016, doi: 10.1007/s11661-015-2863-y.

[27] F. Bertolotti *et al.*, “Crystal Structure, Morphology, and Surface Termination of Cyan-Emissive, Six-Monolayers-Thick CsPbBr3 Nanoplatelets from X-ray Total Scattering,” *ACS Nano*, vol. 13, pp. 14294–14307, 2019, doi: 10.1021/acsnano.9b07626.

[28] A. Parakh *et al.*, “Nucleation of Dislocations in 3.9 nm Nanocrystals at High Pressure,” *Phys. Rev. Lett.*, vol. 124, p. 106104, 2020, doi: 10.1103/PhysRevLett.124.106104.

[29] H. Ozawa, “X線散乱に基づく粒子の原子配列解析法の開発,” 2018.

[30] W. Wagner *et al.*, “The IAPWS Industrial Formulation 1997 for the Thermodynamic Properties of Water and Steam,” *J. Eng. Gas Turb. Power*, vol. 122, pp. 150–182, 2000.

[31] M. Uematsu and E. U. Franck, “Static Dielectric Constant of Water and Steam,” *J. Phys. Chem. Ref. Data*, vol. 9, pp. 1291–1306, 1980, doi: 10.1063/1.555632.

[32] W. L. Marshall and E. U. Franck, “Ion Product of Water Substance, 0-1000℃, 1-10,000 Bars New International Formulation and Its Background,” *J. Phys. Chem. Ref. Data*, vol. 10, pp. 295–304, 1981, doi:

10.1063/1.555643.

[33] M. Fisher and B. Widom, "Decay of Correlations in Linear Systems," *J. Chem. Phys.*, vol. 50, p. 3756, 1969, doi: 10.1063/1.1671624.

[34] T. Morita, K. Kusano, H. Ochiai, K.-I. Saitow, and K. Nishikawa, "Study of inhomogeneity of supercritical water by small-angle x-ray scattering," *J. Chem. Phys.*, vol. 112, pp. 4203–4211, 2000, doi: 10.1063/1.480965.

[35] N. Yoshida, M. Matsugami, Y. Harano, K. Nishikawa, and F. Hirata, "Structure and Properties of Supercritical Water: Experimental and Theoretical Characterizations," *J*, vol. 4, pp. 698–726, 2021, doi: 10.3390/j4040049.

[36] Y. Hakuta, S. Onai, H. Terayama, T. Adschiri, and K. Arai, "Production of ultra - fine ceria particles by hydrothermal synthesis under supercritical conditions," *J. Mater. Sci. Lett.*, vol. 17, pp. 1211–1213, 1009, doi: 10.1023/A:1006597828280.

[37] J. Zhang, S. Ohara, M. Umetsu, T. Naka, Y. Hatakeyama, and T. Adschiri, "Colloidal ceria nanocrystals: A tailor-made crystal morphology in supercritical water," *Adv. Mater.*, vol. 19, pp. 203–206, 2007, doi: 10.1002/adma.200600964.

[38] N. Aoki *et al.*, "Kinetics study to identify reaction-controlled conditions for supercritical hydrothermal nanoparticle synthesis with flow-type reactors," *J. Supercrit. Fluids*, vol. 110, pp. 161–166, 2016, doi: 10.1016/j.supflu.2015.11.015.

[39] Y. Hakuta, T. Adschiri, H. Hirakoso, and K. Arai, "Chemical equilibria and particle morphology of boehmite(AlOOH) in sub and supercritical water," *Fluid Phase Equilibr.*, vol. 158–160, pp. 733–742, 1999, doi: 10.1016/S0378-3812(99)00118-1.

[40] J. Becker *et al.*, "Experimental setup for in situ X-ray SAXS/WAXS/PDF studies of the formation and growth of nanoparticles in near-and supercritical fluids," *J. Appl. Cryst.*, vol. 43, pp. 729–736, 2010, doi: 10.1107/S0021889810014688.

[41] S. Kawasaki, Y. Xiuyi, K. Sue, Y. Hakuta, A. Suzuki, and K. Arai, "Continuous supercritical hydrothermal synthesis of controlled size and highly crystalline anatase TiO2 nanoparticles," *J. Supercrit. Fluids*, vol. 50, pp. 276–282, 2009, doi: 10.1016/j.supflu.2009.06.009.

[42] F. H. Gjørup, J. v. Ahlburg, and M. Christensen, "Laboratory setup for rapid in situ powder X-ray diffraction elucidating Ni particle formation in supercritical methanol," *Rev. Sci. Instrum.*, vol. 90, p. 073902, 2019, doi: 10.1063/1.5089592.

[43] Y. Yang *et al.*, "In Situ X-ray Absorption Spectroscopy of a Synergistic Co-Mn Oxide Catalyst for the Oxygen Reduction Reaction," *J. Am. Chem. Soc.*, vol. 141, pp. 1463–1466, 2019, doi: 10.1021/jacs.8b12243.

[44] M. Bremholm, H. Jensen, S. B. Iversen, and B. B. Iversen, "Reactor design for in situ X-ray scattering studies of nanoparticle formation in supercritical water syntheses," *J. Supercrit. Fluids*, vol. 44, pp. 385–390, 2008, doi: 10.1016/j.supflu.2007.09.029.

[45] E. Bøjesen and B. Iversen, "The chemistry of nucleation ," *CrystEngComm*, vol. 18, pp. 8332–8353, 2016.

[46] S. J. Moorhouse, N. Vranje, A. Jupe, M. Drakopoulos, and D. O'Hare, "The oxford-diamond in situ cell for studying chemical reactions using time-resolved x-ray diffraction," *Rev. Sci. Instrum.*, vol. 83, p. 084101,

2012, doi: 10.1063/1.4746382.

[47] J. S. O. Evans *et al.*, "An apparatus for the study of the kinetics and mechanism of hydrothermal reactions by *in situ* energy dispersive x-ray diffraction," *Rev. Sci. Instrum.*, vol. 66, pp. 2442–2445, 1995, doi: 10.1063/1.1146451.

[48] E. Nishibori *et al.*, "The large Debye Scherrer camera installed at SPring-8 BL02B2 for charge density studies," *Nucl. Instr. Meth.*, vol. A467, p. 1045, 2001.

[49] S. Kawaguchi *et al.*, "High-throughput powder diffraction measurement system consisting of multiple MYTHEN detectors at beamline BL02B2 of SPring-8," *Rev. Sci. Instrum.* , vol. 88, p. 085111, 2017, doi: 10.1063/1.4999454.

[50] T. Fujita, H. Kasai, and E. Nishibori, "Hydrothermal reactor for in-situ synchrotron radiation powder diffraction at SPring-8 BL02B2 for quantitative design for nanoparticle," *J. Supercrit. Fluids*, vol. 147, pp. 172–178, 2019, doi: 10.1016/j.supflu.2018.10.016.

[51] X. Guo, "Property degradation of tetragonal zirconia induced by low-temperature defect reaction with water molecules," *Chem. Mater.*, vol. 16, pp. 3988–3994, 2004, doi: 10.1021/cm040167h.

[52] C. Piconi and G. Maccauro, "Zirconia as a ceramic biomaterial," *Biomaterials*, vol. 20, pp. 1–25, 1999, doi: 10.1016/s0142-9612(98)00010-6.

[53] V. Lughi and V. Sergo, "Low temperature degradation -aging- of zirconia: A critical review of the relevant aspects in dentistry," *Dent. Mater.*, vol. 26, pp. 807–820, 2010, doi: 10.1016/j.dental.2010.04.006.

[54] Y. Hakuta, T. Ohashi, H. Hayashi, and K. Arai, "Hydrothermal synthesis of zirconia nanocrystals in supercritical water," *J. Mater. Res.*, vol. 19, pp. 2230–2234, 2004, doi: 10.1557/JMR.2004.0314.

[55] J. Becker *et al.*, "Critical size of crystalline ZrO2 nanoparticles synthesized in near- and supercritical water and supercritical isopropyl alcohol," *ACS Nano*, vol. 2, pp. 1058–1068, 2008, doi: 10.1021/nn7002426.

[56] J. Qi and X. Zhou, "Formation of tetragonal and monoclinic-HfO2 nanoparticles in the oil/water interface," *Colloid. Surface A*, vol. 487, pp. 26–34, 2015, doi: 10.1016/j.colsurfa.2015.09.037.

[57] A. Sahraneshin, S. Takami, D. Hojo, K. Minami, T. Arita, and T. Adschiri, "Synthesis of shape-controlled and organic-hybridized hafnium oxide nanoparticles under sub- and supercritical hydrothermal conditions," *J. Supercrit. Fluids*, vol. 62, pp. 190–196, 2012, doi: 10.1016/j.supflu.2011.10.019.

[58] A. Sahraneshin *et al.*, "Surfactant-assisted hydrothermal synthesis of water-dispersible hafnium oxide nanoparticles in highly alkaline media," *Cryst. Growth Des.*, vol. 12, pp. 5219–5226, 2012, doi: 10.1021/cg3005739.

[59] H. M. Rietveld, "A Profile Refinement Method for Nuclear and Magnetic Structures," *J. Appl. Cryst.*, vol. 2, pp. 65–71, 1969, doi: 10.1107/S0021889869006558.

[60] H. Toraya, "Array-Type Universal Profile Function for Powder Pattern Fitting," *J. Appl. Cryst*, vol. 23, pp. 485–491, 1990, doi: 10.1107/S002188989000704X.

[61] E. Nishibori *et al.*, "Accurate structure factors and experimental charge densities from synchrotron X-ray powder diffraction data at SPring-8," *Acta Cryst.* , vol. A63, pp. 43–52, 2007, doi: 10.1107/S0108767306047210.

[62] P. Debye, "Scattering from non-crystalline substances," *Ann. Physik*, pp. 809–823, 1915.

[63] F. Bertolotti, D. Moscheni, A. Guagliardi, and N. Masciocchi, “When Crystals Go Nano – The Role of Advanced X-ray Total Scattering Methods in Nanotechnology,” *Eur. J. Inorg. Chem.*, vol. 2018, pp. 3789–3803, 2018, doi: 10.1002/ejic.201800534.

[64] A. P. Thompson *et al.*, “LAMMPS - a flexible simulation tool for particle-based materials modeling at the atomic, meso, and continuum scales,” *Comput. Phys. Commun.*, vol. 271, p. 108171, 2022, doi: 10.1016/j.cpc.2021.108171.

[65] L. Martinez, R. Andrade, E. G. Birgin, and J. M. Martínez, “PACKMOL: A package for building initial configurations for molecular dynamics simulations,” *J. Comput. Chem.*, vol. 30, pp. 2157–2164, 2009, doi: 10.1002/jcc.21224.

[66] A. Stukowski, “Visualization and analysis of atomistic simulation data with OVITO-the Open Visualization Tool,” *Model. Simul. Mater. Sc.*, vol. 18, p. 015012, 2010, doi: 10.1088/0965-0393/18/1/015012.

[67] S. Narioka, 2004.

[68] P. Scherrer, “Bestimmung der Grösse und der inneren Struktur von Kolloidteilchen mittels Röntgenstrahlen,” *Nachrichten von der Gesellschaft der Wissenschaften*, pp. 98–100, 1918.

[69] M. Leoni, J. Martinez-Garcia, and P. Scardi, “Dislocation effects in powder diffraction,” *J. Appl. Cryst.*, vol. 40, pp. 719–724, 2007, doi: 10.1107/S002188980702078X.

[70] F. Bertolotti *et al.*, “A total scattering Debye function analysis study of faulted Pt nanocrystals embedded in a porous matrix,” *Acta Cryst.*, vol. A72, pp. 632–644, 2016, doi: 10.1107/S205327331601487X.

[71] S. K. Huang, N. Li, Y. H. Wen, J. Teng, S. Ding, and Y. G. Xu, “Effect of Si and Cr on stacking fault probability and damping capacity of Fe-Mn alloy,” *Mater. Sci. Eng. A*, vol. 479, pp. 223–228, 2008, doi: 10.1016/j.msea.2007.06.063.

[72] K. R. Beyerlein, R. L. Snyder, and P. Scardi, “Faulting in finite face-centered-cubic crystallites,” *Acta Cryst.* , vol. A67, pp. 252–263, 2011, doi: 10.1107/S0108767311009482.

[73] G. Hura, J. M. Sorenson, R. M. Glaeser, and T. Head-Gordon, “High-quality X-ray scattering experiment on liquid water at ambient conditions,” *J. Chem. Phys.*, vol. 113, pp. 9140–9148, 2000, doi: 10.1063/1.1319614.

[74] K. Nishikawa and N. Kitagawa, “X-Ray Diffraction Study of Liquid Water,” *Bull. Chem. Soc. Jpn.*, vol. 53, pp. 2804–2808, 1980.

[75] M.-C. Bellissent-Funel, “Structure of Supercritical Water,” *J. Mol. Liq.*, vol. 90, pp. 313–322, 2001, doi: 10.1016/S0167-7322(01)00135-0.

[76] C. J. Howard, R. J. Hill, and B. E. Reichert, “Structures of the ZrO2 Polymorphs at Room Temperature by High-Resolution Neutron Powder Diffraction,” *Acta Cryst.* , vol. B44, pp. 116–120, 1988, doi: 10.1107/S0108768187010279.

[77] K. R. Whittle, G. R. Lumpkin, and S. E. Ashbrook, “Neutron diffraction and MAS NMR of cesium tungstate defect pyrochlores,” *J. Solid State Chem.*, vol. 179, pp. 512–521, 2006, doi: 10.1016/j.jssc.2005.11.011.

[78] T. Kiguchi, T. Shiraishi, T. Shimizu, H. Funakubo, and T. J. Konno, “Domain orientation relationship of orthorhombic and coexisting monoclinic phases of YO1.5-doped HfO2 epitaxial thin films,” *Jpn. J. Appl. Phys.*, vol. 57, pp. 11–16, 2018, doi: 10.7567/JJAP.57.11UF16.

[79] D. A. Navarro, S. W. Depner, D. F. Watson, D. S. Aga, and S. Banerjee, “Partitioning behavior and

stabilization of hydrophobically coated HfO2, ZrO2 and Hf xZr1-xO2 nanoparticles with natural organic matter reveal differences dependent on crystal structure," *J. Hazard. Mater.*, vol. 196, pp. 302–310, 2011, doi: 10.1016/j.jhazmat.2011.09.028.

[80] Q. Mahmood, A. Afzal, H. M. Siddiqi, and A. Habib, "Sol-gel synthesis of tetragonal ZrO2 nanoparticles stabilized by crystallite size and oxygen vacancies," *J. Sol-Gel Sci. Techn.*, vol. 67, pp. 670–674, 2013, doi: 10.1007/s10971-013-3112-8.

[81] A. S. Barnard, R. R. Yeredla, and H. Xu, "Modelling the effect of particle shape on the phase stability of ZrO 2 nanoparticles," *Nanotechnology*, vol. 17, no. 12, pp. 3039–3047, 2006, doi: 10.1088/0957-4484/17/12/038.

[82] R. C. Garvie, "Stabilization of the Tetragonal Structure in Zirconia Microcrystals," *J. Phys. Chem.*, vol. 82, pp. 218–223, 1978, doi: 10.1021/j100491a016.

[83] R. C. Garvie, "The occurrence of metastable tetragonal zirconia as a crystallite size effect," *J. Phys. Chem.*, vol. 69, pp. 1238–1243, 1965, doi: 10.1021/j100888a024.

[84] M. Taguchi *et al.*, "One-pot synthesis of monoclinic ZrO2 nanocrystals under subcritical hydrothermal conditions," *J. Supercrit. Fluids*, vol. 85, pp. 57–61, 2014, doi: 10.1016/j.supflu.2013.11.001.

[85] R. P. Denkewicz, K. S. TenHuisen, and J. H. Adair, "Hydrothermal Crystallization Kinetics of m-ZrO2 and t-ZrO2," *J. Mater. Res.*, vol. 5, pp. 2698–2705, 1990, doi: 10.1557/JMR.1990.2698.

[86] K. Sato, H. Abe, and S. Ohara, "Selective growth of monoclinic and tetragonal zirconia nanocrystals," *J. Am. Chem. Soc.*, vol. 132, pp. 2538–2539, 2010, doi: 10.1021/ja910712r.

[87] H. J. Noh, D. S. Seo, H. Kim, and J. K. Lee, "Synthesis and crystallization of anisotropic shaped ZrO2 nanocrystalline powders by hydrothermal process," *Mater. Lett.*, vol. 57, pp. 2425–2431, 2003, doi: 10.1016/S0167-577X(02)01248-X.

[88] M. Bucko, K. Haberko, and M. Faryna, "Crystallization of Zirconia under Hydrothermal Conditions," *J. Am. Ceram. Soc.*, vol. 78, pp. 3397–3400, 1999, doi: 10.1111/j.1151-2916.1995.tb07985.x.

[89] A. C. Dippel *et al.*, "Towards atomistic understanding of polymorphism in the solvothermal synthesis of ZrO2 nanoparticles," *Acta Cryst.*, vol. A72, pp. 645–650, 2016, doi: 10.1107/S2053273316012675.

[90] M. Bremholm, J. Becker-Christensen, and B. B. Lversen, "High-pressure, high-temperature formation of phase-pure monoclinic zirconia nanocrystals studied by time-resolved in situ synchrotron X-ray diffraction," *Adv. Mater.*, vol. 21, pp. 3572–3575, 2009, doi: 10.1002/adma.200803431.

[91] Y. Murase and E. Kato, "Preparation of Zirconia Whiskers from Zirconium Hydroxide in Sulfuric Acid Solutions under Hydrothermal Conditions at 200°C," *J. Am. Ceram. Soc.*, vol. 84, pp. 2705–2706, 2001, doi: 10.1111/j.1151-2916.2001.tb01076.x.

[92] X. Guo, "On the degradation of zirconia ceramics during low-temperature annealing in water or water vapor," *J. Phys. Chem. Solids*, vol. 60, pp. 539–546, 1999, doi: 10.1016/S0022-3697(98)00301-1.

[93] Y. S. Kim, C. H. Jung, and J. Y. Park, "Low temperature degradation of yttria-stabilized tetragonal zirconia polycrystals under aqueous solutions," *Journal of Nucl. Mater.*, vol. 209, pp. 326–331, 1994, doi: 10.1016/0022-3115(94)90271-2.

[94] J.-F. Li, R. Watanabe, B.-P. Zhang, K. Asami, and K. Hashimoto, "X-ray Photoelectron Spectroscopy

Investigation on the Low-Temperature Degradation of 2 mol% Y2O3-ZrO2 Ceramics,” *J. Am. Chem. Soc.*, vol. 79, pp. 3109–3112, 1996, doi: 10.1111/j.1151-2916.1996.tb08084.x.

[95] M. Yoshimura, T. Noma, K. Kawabata, and S. Somiya, “Role of H2O on the degradation process of Y-TZP,” *J. Mater. Sci. Lett.*, vol. 6, pp. 465–467, 1987, doi: 10.1007/BF01756800.

[96] O. Kruse, H. Carstanjen, Kountouros. P., H. Schubert, and G. Petzow, “Characterization of H2O-Aged TZP by Elastic Recoil Detection Analysis (ERDA),” in *Science and Technology of Zirconia V*, S. Badwal, M. Bannister, and R. Hannink, Eds. Lancaster: Technomic Publishing Company, Inc., 1993, p. 163.

[97] T. Fujita, H. Kasai, and E. Nishibori, “Ion Product Scale for Phase and Size Selective Crystal Growth of Zirconia Nanoparticles,” *Cryst. Growth Des.*, vol. 20, pp. 5589–5595, 2020, doi: 10.1021/acs.cgd.0c00765.

Acknowledgements

I would like to express my sincere gratitude to all the professors, the students and the people who supported this study. I would like to express my sincere gratitude to my supervisor Professor Eiji Nishibori for continuous support, encouragement and patience for my Ph.D research. This research was accomplished by the invaluable guidance from Professor Nishibori. I express my deepest gratitude to Professor Nishibori for accepting me in the laboratory, introducing to me the basics of research of natural science and providing me the great environment for concentrating on scientific research using state-of-the art technologies. I would like to thank my Ph.D thesis committee: Professor Yutaka Moritomo, Professor Akinobu Kanda and Professor Michio Ikezawa for their insightful and critical questions, suggestions, advices and comments on my Ph.D thesis. I express a deep sense of gratitude. My sincere gratitude also goes to assistant professor Dr. Hidetaka Kasai and assistant professor Dr. Galica Tomasz of Nishibori laboratory. Dr. Kasai guided me and supervised me for five years in Nishibori laboratory. I learnt much things from Dr. Kasai from the basics of experiment to the attitude as a scientist. Dr. Kasai and Dr. Tomasz also carefully checked the manuscript and gave me helpful suggestions on the insufficient parts of my writing. I thank all my labmates who worked with me in University of Tsukuba: Dr. Tomoaki Sasaki, Mr. Hantaro Ozawa, Mr. Shuichi Karatsu, Mr. Atsushi Nakamura, Ms. Yuka Deguchi, Mr. Yanyan Zheng, Mr. Ryunosuke Nakamura, Mr. Seiya Takahashi, Mr. Takashi Nishioka, Ms. Mibuki Hayashi and Mr. Kazuya Maeda. I had a wonderful time working with you. Thank you very much! Finally, I would like to offer my special thanks to my parents and my grandmother who always warmly supported me and encouraged me during my Ph.D program even under the pandemic of COVID-19.